THE UNIVERSITY *of* EDINBURGH

THE UNIVERSITY
of EDINBURGH

Simulating the impact of wind and radiation on snow dynamics across linear disturbances in boreal forests.

Rosa L. Milodowski B.A.(Hons) M.Sci.

Ph.D. Atmospheric and Environmental Sciences

University of Edinburgh

2022

Declaration

I declare that this thesis has been composed solely by myself and that it has not been submitted, either in whole or in part, in any previous application for a degree or professional qualification. Except where otherwise acknowledged, the work presented is entirely my own.

Rosa Milodowski

January, 2022

Acknowledgments

This thesis has felt a long time in the making and there are so many people who, over the last seven (or so) years have given me their time, expertise, advice and friendship. I am incredibly grateful for all the support that I have received during this time; this thesis wouldn't be here without it.

Firstly, I would like to thank my principal supervisor, Richard Essery. Thank you for introducing me to the world of snow modelling. Your encouragement and guidance throughout my PhD has been invaluable. Thank you for your patience and always taking time to explain things to me. A lot has happened during this time and your support and understanding throughout the project is much appreciated; it has made it feel possible to balance the demands of undertaking a PhD with raising a young family. Thanks also to my second supervisor, Genevieve Patenaude, for those early conversations that helped shape the direction of my project. I am also grateful to the School of GeoSciences PGR team, in particular Stephanie Robin for your support and reassurance.

I am thankful to the funding bodies who made this research possible. The Natural Environment Research Council (NERC) provided the main funding through the Edinburgh Earth and Environment Doctoral Training Partnership (E3 DTP). I am also very grateful for the The Derek and Maureen Moss 2014 PhD Scholarship, which generously provided research funds that supported the invaluable opportunities to travel

to Canada and Finland. I am also grateful to the Research Councils UK (RCUK, now UK Research and Innovation (UKRI)) for the incredible opportunity to spend three months working on a policy briefing note with the team at the Parliamentary Office of Science and Technology in Westminster.

I would also like to thank everyone who helped with my research, in the field or with the modelling work. Thank you to John Pomeroy and the research group at the University of Saskatchewan Coldwater Laboratory in Alberta, Canada. My visits to the Canadian Rockies were incredible immersive experiences in all things snow and provided a great start to the PhD. Thanks also to the research team at FMI-ARC for welcoming me to Sodankylä and facilitating my field work. Thank you to Andrew Ross for sharing your BLASIUS code that underpins the wind modelling in my thesis. Thank you to Clare Webster for your support and assistance.

I am so grateful for all the wonderful people that I have had the chance to meet through doing this PhD. Sandra, Paula, Becky, Jamie, Sara, Pedro, Emma and Amelia -thank you. And thank you to Vanessa and Nicole for your friendship outside of my PhD bubble. I have so many happy memories from my time spent doing my PhD; a lot of that is down to you all, and I'm grateful for having such a wonderful support network.

And finally, I could not have seen this PhD to its completion without the unconditional love and support of my family. Thank you to Fiona and Tony for helping me get to the finish line. Thank you to my sister and my parents, for your constant support and encouragement. I will forever be grateful to my parents for fostering my love for learning from a young age.

Thomas and Rowan, you have provided the most wonderful distraction from my work and remind me every day what is most important in life. Stay curious little ones!

David, I love you. You are the best team mate that I could ask for. Thank you for

always being there to listen to me, and for the many words of advice and encouragement. You kept me going through what turned out to be an eventful seven years and have always believed in me, even when I haven't. I couldn't have done this without you.

Abstract

Boreal forests are Earth's second largest forest biome, covering an area of 12.0–14.7 million km^2. Winters are typically long, cold and dry, creating ideal conditions for sustaining snowpacks throughout this period. The spatial and temporal distribution of snow cover in boreal forest environments plays a crucial role in hydrological and ecological processes at local and regional scales. The dynamics of snow accumulation and melt reflect the interplay between such processes as the wind-driven redistribution of snow and the net energy balance at the snowpack surface. The presence of a forest canopy exerts a modifying effect on these processes; snow on the forest floor is typically sheltered from wind and direct solar radiation, whilst receiving enhanced longwave radiation from the surrounding canopy. However, the balance between these effects can be complex, particularly in the case of discontinuous forest canopies where clearings allow wind and light to penetrate down to the underlying snowpack. Understanding how the interplay between environmental factors drives spatially and temporally varying patterns of snow cover across forest edges is of particular importance and relevance in boreal regions where rates of climate change are high and forest fragmentation is increasing.

In this thesis I explore how linear clearings, such as roads and tracks, may alter patterns of wind flow and incoming radiation, and consequently modify the dynamics of snow accumulation and melt across discontinuous forest canopies. This investigation uses field data collected during this research project and observations from long-running

monitoring at the Arctic Research Centre of the Finnish Meteorological Institute (FMI-ARC), in northern Finland.

Using a Met Office wind flow model (BLASIUS) I simulate patterns of wind flow across forest discontinuities and show that the clearing width is a key influence on these dynamics. There is less drag on the wind flow within the clearing relative to the forest canopy. Sufficient distance (approx. 100 m) is required for the wind flowing across the gap to adjust to this change in the boundary conditions. A region of reversed flow as the wind enters the gap was found for all gap widths. Within the 100 m gap, the wind speed then increases with distance across the gap until it is slowed by the presence of the downwind canopy edge. Narrow gaps ($<$30 m wide) have less impact on sub-canopy wind speeds as there is insufficient distance for the flow to fully adjust to the change in conditions. The influence of a forest gap on sub-canopy wind dynamics becomes negligible for very narrow gaps (approx. 3 m wide). Canopy height and density have a second-order effect on the wind flow dynamics across the gap. Increasing the canopy height accentuates the region of reversed flow, and faster flowing air above the canopy is not drawn down as deeply down into the gap. A denser forest canopy results in greater vertical velocities at the canopy edges. Reducing the canopy density results in greater overall wind speeds across the model domain.

The wind flow model was coupled to a forest snow model (a simplified version of FSM2) using a linear scaling relationship observed between above- and below- canopy wind speeds, and similarly for surface friction velocity. This coupled model was used to explore the interactions between forest canopy, wind, and the surface energy balance on snow accumulation and melt across a range of forest gap scenarios. The simulated snow mass accumulates sooner and at a greater rate within the gap compared to under the forest canopy. In wider gaps ($\geq$ 50 m) there is an asymmetric pattern of snowmelt, with melt occurring sooner towards the exposed downwind edge of the

gap and persisting for up to a month longer towards the sheltered upwind edge. Snow melts more evenly across narrower gaps. In the simulated scenarios I show that turbulent heat fluxes drive the spatial pattern of snowmelt across a gap. Simulated snowmelt patterns in the wider gaps correlate with sub-canopy wind speeds across the gap; higher wind speeds lead to greater fluxes of sensible heat and therefore earlier onset of melting and higher melt rates. Radiative fluxes provide a secondary influence on snow melt and have most impact on the melt dynamics towards the upwind edge where wind speeds are lowest. The canopy density influences the amount of sub-canopy snow accumulation and modulates the snowmelt patterns set by the energy fluxes across the gap. In the widest gap (100 m), increasing the LAI leads to later snow disappearance.

The findings from this thesis demonstrate that introducing clearings into boreal forests produces a significant change in the local wind flow dynamics and snow hydrology. The width of the clearing is important, with canopy characteristics providing a secondary, modulating effect. The modifications to wind and snow induced by the presence of a gap in the canopy are greatest in the widest gaps. However, even narrow canopy gaps may have a significant impact if their orientation aligns closely with the prevailing wind direction. While the effects of an individual gap may be localised, they could become regionally significant in areas of boreal forest undergoing extensive fragmentation.

Lay summary

Boreal forests are found in some of the northernmost regions of the world such as Canada, Scandinavia and Russia, and cover approximately 11% of the Earth's land surface. Winters in boreal forests are typically long, cold and dry, creating ideal conditions for sustaining snow on the ground. Understanding snow in boreal forests is important because the accumulation and melting of snow in boreal forest environments play crucial roles in the hydrology and ecology of these regions.

The overall impact of forests on snow cover can be variable. As snow falls, some may land on the branches and leaves of the forest canopy. This interception of snow reduces the amount of snow on the ground when compared to nearby open areas. Snow on the forest floor is sheltered from the wind and shaded from the sun by the overlying canopy, which has the effect of preserving the snow for longer. On the other hand, trees emit longwave radiation, which provides energy for melting.

Where there are gaps in the canopy, less snow is intercepted and so greater amounts of snow can accumulate on the ground. There is the potential for greater wind speeds within the gap when compared to the surrounding canopy. The snow in the gap is also more exposed to radiation from the sun and may still receive the enhanced longwave radiation from surrounding trees, both of which act to bring on melting of the snow sooner and faster. The interactions between these processes are central to understanding how changes in forest cover impact on the snowpack in boreal

forests.

In this thesis I explore how linear clearings may alter patterns of wind flow and incoming radiation, and consequently change snow accumulation and melt across the clearing. Linear clearings can be natural features, such as rivers, or generated by human activity, such as road-building, forestry practices, and oil and gas exploration.

As the evolution of snow within the boreal landscape is dependent in part on the wind at the snow surface, it was necessary to use a computational model to explore how clearings in forest canopies affect the local wind flow. I use a computational model of wind flow developed by the Met Office, alongside measurements made at the Arctic Research Centre of the Finnish Meteorological Institute (FMI-ARC), in northern Finland, to simulate wind flowing across forest clearings with different clearing widths and canopy characteristics. I show that the width of the clearing is a key influence on local wind speeds. Forest clearings are associated with higher wind speeds below the height of the trees than in intact forest. This is because the leaves and branches of trees act to slow the wind down (canopy drag), whereas within the gap there is less drag on the air flow. However, this is only the case if there is sufficient distance (approx. 100 m) for the wind flow to adjust to the lower drag in the clearing. For narrow gaps (less than 30 m wide), the effect of a forest clearing on wind speeds is reduced, becoming negligible for very narrow gaps (3 m wide). A zone of recirculating air was found as the wind enters the gap, and is enhanced when there are taller trees surrounding the gap. Reducing the density of the forest canopy (e.g. if there are fewer leaves) leads to higher overall wind speeds across the forest and gap.

To understand snow accumulation and melting in fragmented boreal forests, I combine the wind flow model with a second model that simulates snow accumulation and melting, alongside further measurements from FMI-ARC. I use the combined model to explore how snow accumulation and melting are controlled by the interactions

between the forest canopy, wind, and the melting energy received by the snow surface, across a range of different forest gap scenarios. I show that snow accumulates earlier and faster within the gaps compared to within the forest. In wider gaps ($\geq$ 50 m) there is an asymmetric pattern of snowmelt, with melt occurring sooner towards the exposed downwind edge of the gap and persisting for up to a month longer towards the sheltered upwind edge. This melting pattern is created because away from the sheltered forest edge higher wind speeds help to maintain a temperature difference between the snow surface and the air immediately above it. In narrow gaps, snow lasts longer and melts more evenly, as the wind speeds are much lower compared to wider clearings.

The findings in this thesis demonstrate that gaps in forest canopies impact both local wind flow and snow dynamics. There is a global trend towards increasingly fragmented forests, often linked to human development. As a result, linear clearings may become increasingly prevalent within these landscapes. Therefore, by revealing the role that these clearings play in modifying the local environment, this thesis contributes towards future forest management aiming to mitigate as far as possible any negative impacts of existing and future boreal forest fragmentation.

Contents

List of Figures

List of Tables

Chapter 1

Introduction

1.1 Thesis context and rationale

Boreal forests are Earth's second largest forest biome, with a spatial extent covering 12.0 – 14.7 million km^2 (Baldocchi et al. 2000). Boreal forests play an important role in the global carbon cycle and are estimated to contain 32% of global forest carbon stocks (272 ± 23 Pg C), with 20% of this stored in live biomass, 20% in deadwood and litter and 60% in soil (Pan et al. 2011). They are located in the circumpolar region between 50 and 70 degrees north, predominantly in Canada, Russia and Scandinavia (Johnson & Miyanishi 2012, Gauthier et al. 2015). Winters are typically long, cold and dry, creating ideal conditions for sustaining snowpacks throughout this period (Bonan & Shugart 1989, Brandt n.d.).

The spatial and temporal distribution of snow cover plays an important role in the ecology, hydrology and economies of seasonally snow-covered landscapes (Pomeroy & Goodison 1997, Barnett et al. 2005, Bokhorst et al. 2016, Sturm et al. 2017, Penczykowski et al. 2017, Slatyer et al. 2021). The accumulation and subsequent melting of the snowpack are key processes that affect a wide range of environmental

factors such as: soil temperature and moisture (Zhang 2005, Lawrence & Slater 2010, Hardy et al. 2001); biogeochemical cycling (Brooks & Williams 1999, Jones 1999, Brooks et al. 2011); streamflow timing and amount (Lundquist & Dettinger 2005, Sun et al. 2018); vegetation dynamics (Wipf et al. 2009, Rasmus et al. 2011, Trujillo et al. 2012); surface albedo (Warren 1982, Flanner et al. 2011).

The low thermal conductivity of snow protects tree seedlings and understory species from cold winter temperatures (Penczykowski et al. 2017). Snow cover also insulates the underlying soil, and so the accumulation and the melting of snow has an important influence on the timing of soil thaw and the subsequent release of available soil moisture (Zhang 2005, Bartlett et al. 2006). The timing of spring thaw and availability of soil moisture are strong controls on the start of leaf-out and photosynthesis (Barichivich et al. 2014). The length of the growing season is linked to the strength of the boreal forest carbon sink, with earlier snowmelt linked to enhanced carbon uptake in boreal forests (Black et al. 2000, Jarvis & Linder 2000, Barr et al. 2002, Pulliainen et al. 2017, Ahmed et al. 2021). Longer growing seasons in forest ecosystems may increase carbon availability in the form of labile litter, enhancing microbial respiration and thereby reducing net carbon uptake (Brooks et al. 2005). Additionally, soil respiration is an important contributor to annual CO_2 fluxes (Valentini et al. 2000) and as soil temperature is a primary control on soil microbial activity, snow cover can facilitate the continuation of microbial activity during the winter (Brooks et al. 1996). Patterns of snow cover distribution can also impact on the availability of nutritious food for herbivores (Mårell et al. 2006, Penczykowski et al. 2017). Furthermore, up to one-third of annual precipitation may be stored within the snowpack until melting in the spring, which has an important influence on streamflow timing and magnitude (Pomeroy & Granger 1997, Barnett et al. 2005, Bartlett et al. 2006, Sturm et al. 2017).

Boreal forests are typically dominated by coniferous tree species, such as pine, spruce

and fir, that retain their needle-shaped leaves during the winter and as such are an important influence on the amount and duration of underlying snow (Pomeroy & Dion 1996, Gauthier et al. 2015). Understanding the interactions between forests and snow is key to producing accurate snow accumulation and melt predictions, which are necessary for the effective management of forested water-sheds and improving land surface schemes for climate modelling (Essery et al. 2009, Rutter et al. 2009, Wang et al. 2010, Ellis et al. 2013, Dickerson-Lange et al. 2021, Malle et al. 2021).

Forest canopies influence both the accumulation and ablation (removal) of snow on the underlying forest floor (Essery et al. 2009). Interception of falling snow by the canopy acts to reduce the snow mass on the ground, a process enhanced by the needle-shaped leaves of conifers that increase the surface area of the canopy (Lundquist et al. 2013). The snow may be held in the canopy for a period before it is unloaded or sublimates, giving rise to greater heterogeneity in the distribution of snow mass and properties compared to snow in open environments (Wilm & Dunford 1948, Troendle & King 1985, Pomeroy & Schmidt 1993, Hedstrom & Pomeroy 1998, Varhola et al. 2010, Schelker et al. 2013, Moeser et al. 2016, Lundberg et al. 2016). Wind flowing through a forest is slowed by the aerodynamic drag exerted on it by canopy elements such as leaves and branches (Finnigan 2000). As such, the typically low wind speeds under a forest canopy mean that turbulent fluxes tend to constitute a minor contribution towards snowmelt energetics and the net radiation balance is the dominant component of the surface energy balance (Link & Marks 1999*a*).

Incoming shortwave and longwave radiation to the snow surface is strongly modified by the presence of a forest canopy, which produces different spatial and temporal patterns of melt compared to those observed in open environments (Musselman et al. 2015). Shading by the canopy reduces the amount of direct shortwave radiation reaching the forest floor, which acts to enhance snow retention and is a key influence on snow-melt variability (Harding & Pomeroy 1996, Metcalfe & Buttle 1998, Hardy

et al. 2004, Sicart et al. 2004, Talbot et al. 2006, Musselman et al. 2012, Malle et al. 2019). In contrast, longwave radiation to the underlying snow surface tends to be enhanced under forest cover relative to adjacent open areas, due to the greater emissivity of forest canopies (Sicart et al. 2006, Essery et al. 2008, Lawler & Link 2011, Webster et al. 2017). As a consequence of absorbing solar radiation, the canopy may reach substantially higher temperatures than the overlying air (Webster et al. 2016). This results in greater transmissions of energy to the snow surface and acts to advance the onset of melting (Link et al. 2004, Sicart et al. 2004, Pomeroy et al. 2009).

Forest disturbance is a key driver of heterogeneity in eco-hydrological systems across landscapes (Dale et al. 2001, Johnson & Miyanishi 2010, Turner 2010, Mitchell 2013). The cause of disturbance may be abiotic (e.g. drought); biotic (e.g. pathogens) or anthropogenic (e.g. forestry practices) in origin, or a combination of these (e.g. fires) (Turner 2010). Disturbance to forest ecosystems can have far-reaching impacts, for example affecting crucial ecosystem services such as carbon storage and water provision (Seidl et al. 2016, Thom & Seidl 2016).

In boreal forests, human activity such as road-building, forestry practices, and oil and gas exploration, can produce linear forest clearings. Road networks can form extensive networks through the forest landscape, which are often extended to allow greater access for logging and extractive industries (Kuklina et al. 2021). Linear features can also result from the creation of drainage ditches in forested wetlands (Hasselquist et al. 2018). This practice is used within the forestry industry to improve forest productivity and in some locations leads to highly fragmented landscapes (Lohmus et al. 2015). Seismic lines are long linear clearings created as part of the oil and gas exploration process (Lee & Boutin 2006, Van Rensen et al. 2015). They often form dense gridded networks of clearings and can become pervasive features in many boreal forests that overlay large hydrocarbon deposits (Machtans 2006, Pasher et al.

2013).

The increasing fragmentation of forest landscapes has significantly expanded the length of forest edges and the proportion of forested areas within close proximity to an edge (Haddad et al. 2015). As such, understanding environmental responses to forest edges and gaps is increasingly important; of particular interest in boreal forests is the impact of this on snow accumulation and melting.

The overall impact of forests on snow cover can be variable: although canopies intercept snow and emit longwave radiation, thus acting to reduce snow cover, forests can simultaneously shelter snow from wind and solar radiation, which acts to preserve snow cover (Chen et al. 1993, Pomeroy et al. 2002, Varhola et al. 2010). The trade-off between these processes is central to understanding how changes in forest cover impact on the snow pack and how this is likely to vary with factors such as size and orientation of forest gap (Golding & Swanson 1978, Ellis et al. 2011, 2013, Lundquist et al. 2013). Snow in forest gaps exhibits a high degree of variability that is related to gap-specific spatial patterns of interception, wind-driven redistribution and compaction, and energy inputs, therefore it is important to capture this variation in forest snow models (Golding & Swanson 1986, Murray & Buttle 2003, Essery et al. 2009, Lawler & Link 2011).

Snow within and adjacent to forest gaps can be more exposed to higher wind speeds than within a closed canopy, and so may be redistributed and the the surface can become more compacted (Liston et al. 2007, Stern et al. 2018, Currier & Lundquist 2018). The presence of a clearing within the forest opens up the underlying snow to direct shortwave radiation, an effect further modified by the size of gap and its orientation relative to the position of the sun (Lawler & Link 2011, Seyednasrollah & Kumar 2014, Musselman et al. 2015). The snow surface is also more exposed to atmospheric longwave radiation within a gap than under closed canopy, and may still receive thermal energy emitted by surrounding trees at the gap edge (Lawler & Link

2011, Seyednasrollah & Kumar 2014, Webster et al. 2017). Which of these processes dominate depends on multiple factors, including gap size and orientation.

This thesis aims to improve our understanding of the spatial and temporal patterns of snow accumulation and melt across linear forest gaps and how the gap width and orientation may further modify these dynamics. This will be achieved through the use of observational meteorological, snow and canopy data collected at a field site in northern Finland, combined with a wind flow model (BLASIUS (Wood & Mason 1993, Ross & Vosper 2005)) and a forest snow model (simplified version of FSM2 (Mazzotti et al. 2020a). First, BLASIUS is used to explore how wind flow through a forest canopy may be modified by a linear clearing of varying width and surrounding canopy structure. Observational wind speed data and canopy metrics are then used to evaluate the ability of BLASIUS to capture the flow dynamics across a real forest edge and to obtain a simple model of sub-canopy wind speed and surface friction velocity based on measured above-canopy wind speeds. A simple model of sub-canopy snow accumulation is calibrated using observational meteorological and snow data, and then extended to include the snow surface energy balance. Finally, the wind and snow modelling work is drawn together to simulate spatial and temporal patterns of snow accumulation and melting in different hypothetical forest gap scenarios.

1.2 Thesis structure

The structure of the thesis is outlined as follows:

Chapter 1: Introduction

This current chapter introduces boreal forests, the importance of seasonal snow processes within these environments, and how they may be modified by the presence of canopy discontinuities.

Chapter 2: Literature Review

This chapter provides context to the driving research questions of this thesis through a summary of the current state of knowledge regarding linear disturbances in boreal forests, canopy wind flow dynamics, and sub-canopy snow accumulation and melting processes.

Chapter 3: Simulating wind dynamics across canopy gaps using the BLASIUS wind flow model

This chapter investigates how wind flow through a simulated forest canopy may be affected by a linear clearing of varying width and surrounding canopy structure, using the BLASIUS wind model. A combination of forest structure and clearing width scenarios are presented that are hypothetical but representative of real-world canopy discontinuities.

Chapter 4: Data collection and calibration of the BLASIUS wind flow model

Observational wind speed and canopy structure data collected from a forest-edge site in northern Finland are used to evaluate the ability of the BLASIUS model to represent wind flow across a real forest edge. This chapter also presents a scaling relationship between measured above-canopy wind speeds and modelled sub-canopy wind speeds.

Chapter 5: Calibration of a simplified snow accumulation model using observational data from forest and open sites

This chapter focuses purely on snow accumulation processes. Seven years of observational meteorological and snow data from forest and open sites in northern Finland are used to calibrate a simplified version of the forest snow model FSM2.

Chapter 6: Modelling direct and diffuse radiation to sub-canopy snow

This chapter sets out the modelling methodology used in the subsequent chapter to extend the simplified FSM2 model to include direct and diffuse radiation inputs to the snowpack energy balance. Observational data along a forest gap transect in northern Finland is used to evaluate the chosen models of direct and diffuse radiation to sub-canopy snow.

Chapter 7: Simulating snow accumulation and melt across linear forest clearings

Here the preceding research chapters are drawn together to produce a model of forest gap snow dynamics, encompassing the accumulation, wind-driven redistribution and compaction, and melting of snow. The model is calibrated using observational meteorological and snow data from northern Finland to evaluate simulations of snow melt. Hypothetical scenarios with varying forest gap width and orientation are explored and the impacts on snow accumulation and melting are discussed.

Chapter 8: Conclusion

This chapter synthesises the key findings from Chapters 3 – 7 and presents the main thesis conclusions, its wider implications and scope for further work.

Chapter 2

Literature review

2.1 Introduction

This chapter provides an overview of the current knowledge in canopy wind flow interactions, and forest snow accumulation and melt processes, with a particular focus on the influence of forest canopy discontinuities. The chapter begins with an overview of forest disturbance and edge creation within a more general context, before narrowing to a discussion of linear edge creation in boreal forests. Next, an evaluation of the current understanding of canopy modifications to wind and the additional influence of canopy discontinuities on forest wind flow is presented. Snow accumulation processes are then discussed, particularly considering wind-blown snow transport and the environmental conditions necessary for this to take place. Finally the snowpack energy balance is discussed, with a particular focus on the shortwave and longwave radiation input to snowmelt energetics. The chapter concludes with an overview of the thesis objectives and underlying research questions.

2.2 Forest disturbance and linear clearings

2.2.1 Forest disturbance

Forest disturbance represents a key driver of spatial and temporal heterogeneity in physical and ecological systems across landscapes (Dale et al. 2001, Johnson & Miyanishi 2010, Turner 2010, Mitchell 2013). Forest ecosystems can be disturbed in a number of ways and disturbances may be abiotic (e.g. hurricanes, volcanic eruptions, drought) or biotic (e.g. spread of pests or pathogens) in origin, or a combination of both (e.g. fires) (Turner 2010). Disturbance may also be anthropogenically generated, for instance as a result of road-building, and spatial patterns of discontinuities in forest landscapes resulting from human activity often have no historical analogue in that ecosystem (Pickell et al. 2015). For instance, regimes of thinning, clearcutting and planting in intensively managed forests have largely replaced irregular and unpredictable forest disturbance regimes to which the ecosystem has adapted to (Schelhaas et al. 2003).

Natural disturbances often interact with human-driven environmental change (Dale et al. 2001). Changes in climate and human activity at local, regional and global scales are altering the frequency and intensity of natural disturbances (Becknell et al. 2015). Furthermore, disturbances can interact and create "cascades of disturbance" where one disturbance event enhances the likelihood of another occurring, potentially stimulating domain shifts (Paine et al. 1998, Dale et al. 2001). Crucially, disturbance to forest ecosystems can produce substantial socioeconomic costs and impact on the wider provision of important ecological services, such as carbon storage and water purification (Schelhaas et al. 2003, Gardiner et al. 2013, Seidl et al. 2014).

Landscape fragmentation has increased the length of forest edges and the proportion of forest area that lies in close proximity to an edge. It is estimated that 70% of

forests globally are located within 1 km of an edge (Haddad et al. 2015). Edges can have both positive and negative impacts on the wider environment and are an important influence on: ecosystem structure and processes (e.g. productivity and decomposition); microclimatic conditions; understory species; and wildlife habitat, composition and distribution (Chen et al. 1993, Cadenasso & Pickett 2000, Harper et al. 2005, Latimer & Zuckerberg 2017). In landscape ecology, a patch represents a basic analysis unit that is conceptualised as a homogeneous area that is distinct from its surroundings (Forman 1995) and the "edge effect" reduces with distance from the boundary of a patch in a landscape towards its core (Baskent & Jordan 1995, Zeng et al. 2009).

2.2.2 Linear forest clearings and seismic lines

This thesis focuses specifically on clearings in boreal forests. Boreal forests are Earth's second largest forest biome, with a spatial extent covering 12.0 – 14.7 million km^2 (Baldocchi et al. 2000). Boreal forests play an important role in the global carbon cycle and are estimated to contain 32% of global forest carbon stocks (272 $\pm$ 23 Pg C), with 20% of this stored in biomass and 60% in soil (Pan et al. 2011). They are located in the circumpolar region between 50 and 70 degrees north, predominantly in Canada, Russia and Scandinavia. Winters are typically long, cold and dry, creating ideal conditions for sustaining snowpacks throughout this period (Bonan & Shugart 1989, Brandt n.d.). Snow plays an important role in regional hydrology, storing up to one-third of annual precipitation until melting in the spring (Bartlett et al. 2006). Furthermore, the distribution of snow cover and timing of melting (onset and duration) have important influences on: biogeochemical cycling (Brooks & Williams 1999, Brooks et al. 2011); soil moisture; groundwater recharge; stream flow and chemistry (Williams & Melack 1991, Pomeroy & Granger 1997); and plant phenology, growth and reproduction (Black et al. 2000, Wipf et al. 2009, Trujillo et al. 2012).

Human activity, such as road-building, forestry practices, and oil and gas exploration, has produced linear clearings through boreal forests. Natural features such as rivers may also produce near-linear clearings through forest areas.

The construction of road networks can create extensive linear clearings through forests that are maintained as permanent features in the landscape (Laurance & Arrea 2017, Wells et al. 2020). Furthermore, the extent of reported road networks can be inaccurate as there may be roads that are not reported on maps and databases. As a results, some regions of boreal forest that appear roadless can actually have extensive networks of roads and access tracks that are unmapped. For example, using landscape observations Kuklina et al. (2021) found that 88% of the total road length in their study area in a Siberian boreal forest landscape consists of uncharted informal roads. Road routes are often extended through the boreal forest to allow greater access for logging and extractive industries.

The drainage of forested wetlands and peatlands can also create linear features within the boreal landscape (Figure 2.1a.). Ditches lower the groundwater level to create improved growing conditions for trees. This practice is used within the forestry industry as a management technique to improve forest productivity and is employed across boreal forests (Hasselquist et al. 2018). It requires intensive thinning of trees and regular ditch maintenance (Kojola et al. 2012). The highest rates of drainage are in countries such as Finland, the Baltic states and Sweden; in these places, 20-25% of forested areas are drained, leading to highly fragmented forested wetlands (Lohmus et al. 2015).

Seismic lines are long corridors cleared through forests as part of the oil and gas exploration process (MacFarlane 2003, Lee & Boutin 2006, Van Rensen et al. 2015) (Figure 2.1b.). These linear clearings are pervasive features in many forest landscapes that overlay large hydrocarbon deposits (Machtans 2006, Pasher et al. 2013). In north-eastern Alberta, Canada, the mean density of seismic lines can be as high as

10 km per km^2(Lee & Boutin 2006). Historically, seismic lines were created as 5–10 m wide clearings using bulldozers (Latham et al. 2011). More recently, lines tend to be 3–5 m wide and can be $<$ 2 m wide in ecologically sensitive areas, where methods such as hand-cutting have been employed (Lankau et al. 2013, Dabros et al. 2017). After use, seismic lines are typically left to regenerate naturally, although this may not occur, especially where there are continued levels of high human activity or due to poor growing conditions because of factors such as soil compaction, altered light regimes, and changes in soil moisture (Revel et al. 1984, Lee & Boutin 2006, Caners & Lieffers 2014, Van Rensen et al. 2015, Dabros et al. 2017).

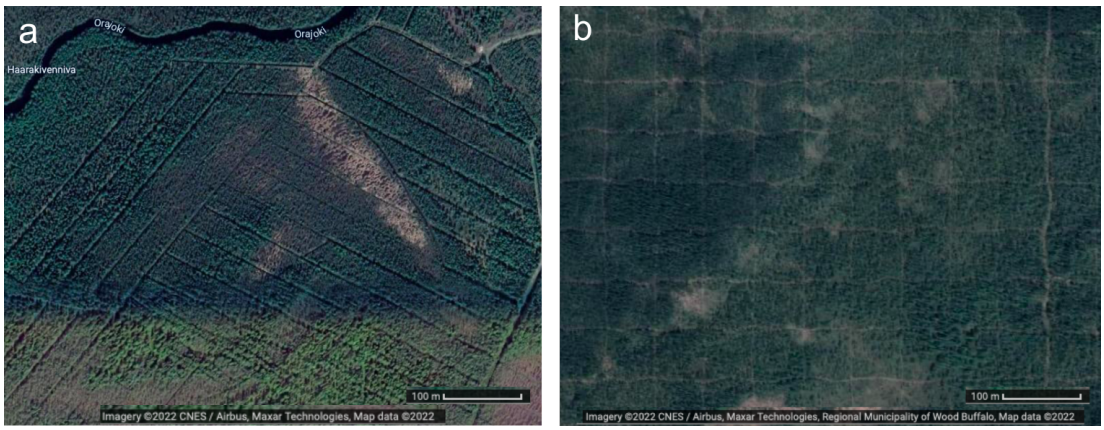

Figure 2.1: Linear features in boreal forest landscapes: (a) Drainage channels used to increase forest productivity in northern Finland; (b) Network of seismic lines for oil and gas exploration in Alberta, Canada. Images are from Google Maps: `https://goo.gl/maps/qR9c4Rqj3usX9QvG7` *and* `https://goo.gl/maps/9vLJEcHpsMEbmd8HA` *respectively.*

There are concerns that the large amounts of forest edges created by linear clearings, such as roads and seismic lines, are reducing core interior habitats (Lankau et al. 2013, Haddad et al. 2015). Edge effects can have a wider area of influence than the immediate boundary edge between forest and clearing (Matlack 1993, Cadenasso et al. 1997); the impacts of linear clearings is not necessarily related to how visible in the landscape they are. Hence, there has been a push towards developing further indicators of their impact that incorporate an understanding of how different types of linear clearings may influence the surrounding environment (Lankau et al. 2013, Kuklina et al. 2021).

Linear features in boreal forest landscapes have been shown to impact the behaviour and population dynamics of a range of boreal wildlife, including wolves (James & Stuart-Smith 2000, Latham et al. 2011, Whittington et al. 2011, Pattison et al. 2020), bears (Linke et al. 2005, Stewart et al. 2013, Tigner et al. 2014), woodland caribou (James & Stuart-Smith 2000, Dyer et al. 2001, 2002, Sorensen et al. 2008, Leblond et al. 2013), and ovenbirds (Bayne et al. 2005, Machtans 2006, Lankau et al. 2013). In addition, linear corridors through forests enhance access to people and vehicles (Kuklina et al. 2021). This can promote the transfer of invasive and non-native species, with important impacts on native biota and regeneration processes (Cameron et al. 2007, Mortensen et al. 2009, Sanderson et al. 2012).

While the myriad ecological impacts of linear clearings in boreal forests have been well investigated, there are far fewer studies on the impact of these disturbances on the physical environment. It has been shown more generally that gaps in forest canopies can produce spatial and temporal variations in sub-canopy wind flow patterns, and snow accumulation and melting processes (see sections 2.3.4 and 2.5.3). This would suggest that linear clearings in forests have the potential to alter local snow hydrology, with important consequences for the wider environmental system. How linear and near-linear clearings through forests, produced by human activity such as seismic exploration and road building, or resulting from natural features in the landscape such as rivers, modify wind and snow processes remains a topic for further investigation.

The following sections present an overview of the current understanding of canopy wind flow interactions (Section 2.3), forest snow accumulation (Section 2.4) and the sub-canopy energy balance for snow melt (Section 2.5), particularly focused within the context of discontinuous forest canopies.

2.3 Forest canopy wind flow

Forests cover approximately one-third of earth's terrestrial surface and can strongly influence local and regional wind dynamics (Belcher et al. 2003, FAO 2016, Finnigan 2000). Forest landscapes often exhibit a large degree of spatial variability, for instance due to the presence of clearings (Section 2.2) or natural diversity in canopy characteristics such as height or density. Canopy elements (such as leaves and branches) increase the drag forces on air as it flows through a forest and so spatial variations in the canopy structure and properties can introduce corresponding variations in wind flow patterns (Finnigan 2000). Understanding how canopy heterogeneities modify wind flow through forest environments is of importance for a range of applications such as: modelling snow transport and melt dynamics (Pomeroy et al. 1998, Essery & Pomeroy 2004, Gelfan et al. 2004, Liston & Elder 2006, Essery et al. 2009); the prediction of wind damage to trees (Gardiner et al. 2016, Panferov & Sogachev 2008, Schwartz et al. 2017); optimising wind turbine siting (Lopes da Costa et al. 2006, Rodrigo et al. 2007, Ayotte 2008, Dellwik et al. 2014, Arnqvist et al. 2015); calculating carbon fluxes (Belcher et al. 2012); modelling pollen dispersal (Dupont et al. 2006); understanding wildfire propagation and VOC emissions (Coen 2005, Sun et al. 2009, Conan et al. 2015).

This section introduces the principles of canopy-modified wind flow, discusses how this may be altered by the presence of canopy discontinuities and outlines previous approaches to studying canopy wind flow dynamics, with a particular focus on flow across forest edges.

2.3.1 Principles of canopy wind flow

Consider a simplified scenario where air is flowing over a flat homogeneous surface. The atmospheric boundary layer may also be considered horizontally homogeneous and its properties can then be described using Monin–Obukhov scaling laws (Kaimal & Finnigan 1994). This means that the vertical profile of the streamwise wind velocity may be described using the log-law wind profile (see also figure 2.2.a.):

$$\bar{u}(z) = \frac{u_*}{\kappa} ln \frac{z}{z_0} \tag{2.1}$$

where $\bar{u}(z)$ is the streamwise velocity, u_* is the friction velocity, κ is the von Karman constant (0.4), z is the height above the surface and z_0 is the aerodynamic roughness length, which is a representative length-scale of the roughness of a particular surface.

Surface	**Roughness length, z_0 (m)**
Snow	0.5–10.0 x 10^{-4}
Soil	0.001 – 0.01
Grass	0.003 – 0.10
Agricultural crops	0.04 – 0.20
Forest	1.0 – 6.0

Table 2.1: Typical roughness lengths for different land surface types (from Oke (1978))

In reality, the Earth's surface consists of a patchwork of land surface types with varying roughness lengths (see Table 2.1 for examples). As the wind flows from one surface to another, the streamwise velocity profile adjusts with the new roughness length and a new internal boundary layer (IBL) develops from the surface upwards (Irvine et al. 1997). The properties of this internal boundary layer are influenced by the properties of the underlying surface. Over a forest canopy, an internal boundary layer called the roughness sub-layer develops and may extend upwards to three times the canopy height (Belcher et al. 2012).

Within the roughness sublayer, Monin-Obukhov scaling tends not to apply and canopy-scale turbulent eddies dominate the flow. The mean wind profile above the canopy may still be represented approximately by the log profile (Figure 2.2.b.), which is displaced upwards (accounted for by the addition of a displacement height term, d, to Equation 2.1). However, it is more complex within the canopy due to the additional aerodynamic drag that slows the flow and variations in the distribution of canopy elements. The modified log-law wind profile (which may be applied above the canopy) is as follows:

$$\bar{u}(z) = \frac{u_*}{\kappa} ln \frac{(z-d)}{z_0} \tag{2.2}$$

Whereas an exponential function may be used to represent the sub-canopy velocity profile (Figure 2.2.b.):

$$\frac{\bar{u}(z)}{\bar{u}_h} = e^{-\upsilon_e(1-\frac{z}{h})} \tag{2.3}$$

where $\bar{u}_h$ is the mean wind speed at the canopy top, υ_e is the extinction coefficient (which increases with leaf area index) and h is the canopy height (Kaimal & Finnigan 1994). Depending on the vertical distribution of foliage, the wind velocity may deviate from this, for instance if the lower canopy is relatively open and a sub-canopy jet of faster air is able to flow through at this level (Dupont et al. 2011).

The two canopy wind profiles blend together at the canopy top, producing an inflection point that creates instabilities in the flow (Kelvin-Helmholtz instabilities). This generates mixing of the air and gives rise to a turbulent layer, which is dominated by large coherent eddy structures that drive the transport of mass, momentum and energy in the roughness sub-layer (Raupach et al. 1996, Finnigan 2000, Finnigan et al. 2009).

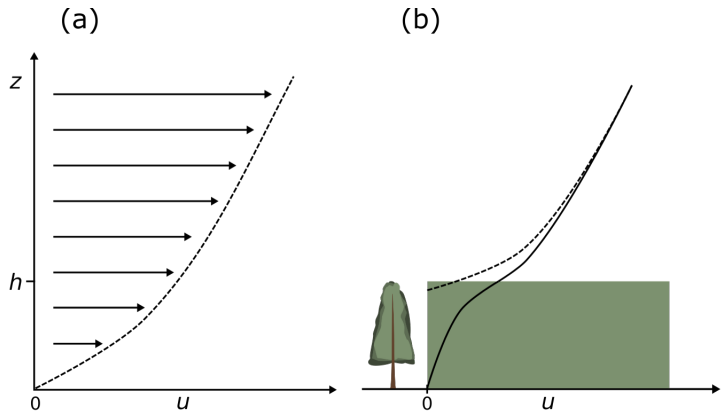

Figure 2.2: Vertical profiles of streamwise velocity (u) over: (a) flat terrain, following the log-law relationship (Eq. 2.1); and (b) forest canopy, where the streamwise velocity profile may be approximated by a modified log-law relationship above the canopy (Eq. 2.2) and an exponential relationship below (Eq. 2.3).

Wind flow over homogeneous canopies has been extensively studied, through a range of methods including: wind tunnel experiments (Raupach et al. 1986, Ruck & Adams 1991); field experiments (Raupach 1979, Baldocchi & Meyers 1988, Amiro 1990); numerical simulations (Dwyer et al. 1997, Ross & Vosper 2005, Dupont et al. 2008, Finnigan et al. 2009, Ross & Harman 2015). More recently, attention has also been applied to spatially varying canopies and the behaviour of wind as it flows across a forest edge (Belcher et al. 2012).

2.3.2 Wind flow across edges

At the transition between un-forested and forested land cover, the wind flow adjusts to the presence of the forest canopy (Belcher et al. 2012, Dellwik et al. 2014). As the displacement height of a forest canopy is significantly larger than that of a short grass canopy or rough ground (which has negligible displacement height), the wind flow must enter or exit out of a canopy (Dupont & Brunet 2008*a*, Cassiani et al. 2008, Detto et al. 2008, Markfort et al. 2014). The impact of a forest edge on the wind flow has been studied via a variety of methods, including: wind tunnel and flume experiments (Rominger & Nepf 2011, Markfort et al. 2014); field experiments (Gash

1986, Flesch & Wilson 1999, Mammarella et al. 2008, Dellwik et al. 2014, Grant et al. 2015); analytical models and numerical models (Belcher et al. 2003, Cassiani et al. 2008, Dupont & Brunet 2008*a*, Ross & Baker 2013, Boudreault et al. 2017).

The two main types of numerical models used are Reynolds-Averaged Navier-Stokes (RANS) based models and models that run Large-Eddy Simulations (LES). LES can simulate canopy turbulence in greater detail than RANS type models, which only simulate the mean profiles of the flow (e.g. of wind speed or shear stress). However, whilst LES provide more information than RANS type models, they are more computationally expensive to run and more difficult to implement in heterogeneous canopies. It has also been shown that simpler RANS models are still able to produce similar results to those obtained by LES or wind tunnel experiments (Ross 2008).

2.3.2.1 The characteristic regions of canopy wind flow

Belcher et al. (2003) identified the main development regions as the wind flow enters and adjusts to a canopy (Figure 2.3).

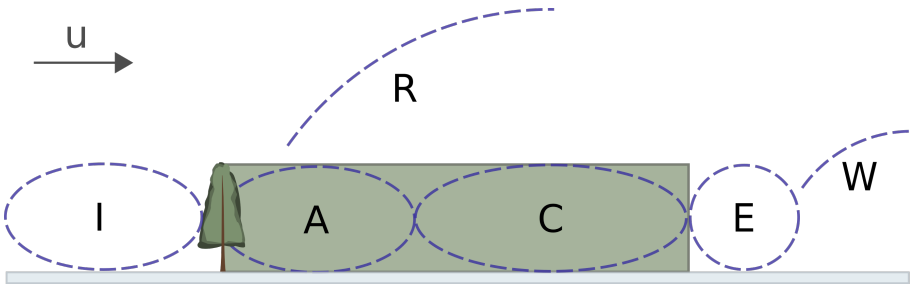

Figure 2.3: Schematic showing the adjustment zones as wind flows through a canopy from left to right (as according to Belcher et al. (2003)): impact region (I); adjustment region (A); roughness change region (R); canopy flow region (C); exit region (E); wake region (W).

Impact region (I): Canopy drag creates a pressure gradient, which causes the flow to decelerate ahead of the forest edge (Belcher et al. 2003).

Adjustment region (A): The main forces acting on an air parcel in this region are:

(i) canopy drag; (ii) advective deceleration; (iii) pressure gradient (Belcher et al. 2003, Yang et al. 2006, Rominger & Nepf 2011). Canopy drag decelerates the wind in the streamwise direction, which leads to a vertical mass flux out of the top of the canopy in order to conserve momentum. However, there may also be a jet of faster moving air close to the ground in canopies that have a lower density trunk space, i.e. if the tree foliage is concentrated in the upper canopy levels (Dupont et al. 2011). Turbulence in the canopy decreases as canopy elements produce small wake eddies, which enhances energy dissipation. Work against drag also acts to make canopy turbulence more isotropic as energy is preferentially removed from the streamwise component of the wind velocity and transferred to the crosswind components (Belcher et al. 2012). The length of the adjustment region is typically $\sim$ 8–10h or $\sim$3L_c, where L_c is the adjustment length scale for momentum and depends on the canopy properties such that:

$$L_c = \frac{1}{C_d a} \tag{2.4}$$

where C_d is the canopy drag coefficient and a is the leaf area density; denser canopies can be expected to have shorter adjustment regions and vice versa (Dupont & Brunet 2008*a*).

Roughness change region (R): The wind flow above the canopy adjusts to the greater roughness of the canopy and an internal boundary layer develops, growing with distance downwind. The whole boundary layer may adjust to the presence of the forest if the canopy is very long (fetch $\approx$10 km) (Belcher et al. 2012). Further downstream, a more turbulent layer develops within the internal boundary layer and above the canopy.

Canopy flow region / Equilibrium region (C): The wind flow is fully adjusted to the canopy and the form of the wind profile now matches that for a homogeneous

canopy (Belcher et al. 2003). There is a well developed shear layer at the canopy top that is characterised by coherent eddies, which are responsible for most of the momentum, mass and heat exchange between the canopy and the atmosphere. New eddies are constantly forming and their size is characterised by the shear scale at the top of the canopy, which is approximately the canopy height (Finnigan 2000).

Exit region (E): An exit region occurs at the downwind edge of the canopy for a distance on the order of h downwind. As the wind exits the canopy there is a sudden increase in the mean wind speed and a concurrent downward motion of air to conserve mass.

Wake region (W): The vertical profile of the wind flow exiting the canopy returns to the log form. If the canopy is sufficiently dense, a recirculation region may be established in the lee of the canopy, analogous to flow observed downwind of a backward facing step (Cassiani et al. 2008, Detto et al. 2008).

The characteristic regions of wind flow across canopy edges, as described by Belcher et al. (2003), applies to relatively uniform canopies. In reality, canopies are likely to be spatially heterogeneous, with varying heights, densities and vertical distribution of foliage Boudreault et al. (2017). There may also be clearings and gaps within the canopy, which can occur naturally, due to varying environmental conditions and natural disturbance patterns, or anthropogenically, such as for roads, oil and gas exploration, or vineyards (Bergeron et al. 2014, Laurance et al. 2009, Pickell et al. 2015, Chahine et al. 2014).

2.3.3 Influence of canopy characteristics on flow dynamics

Several studies have investigated the influence of forest morphology on wind flow over a forest edge. Cassiani et al. (2008) used LES to show that a greater plant area index

(PAI, i.e. a denser canopy) encourages the formation of recirculating zones of airflow at the leeside canopy edge and just into the canopy preceding it. Dupont & Brunet (2008*a*) also used LES to model wind flow across a forest edge and found that flow entering a canopy adjusts faster with a denser canopy.

2.3.4 Influence of canopy discontinuities on flow dynamics

Compared to wind flow through continuous canopies or across a single edge, wind flow through canopies with a gap or clearing has been relatively less explored. Schlegel et al. (2012) used a LES combined with high resolution plant area distribution (PAD) data from terrestrial laser scanning (TLS) to investigate the impact of canopy structure on the local flow structure. They found that plant-scale heterogeneities introduced further complexities to the spatial pattern of wind velocities and turbulence, particularly within the forest stand. The modelled canopy included a 60 m clearing and the flow contours across the clearing followed a similar pattern in both the case of a homogeneous canopy (i.e. uniform vertical and horizontal distribution of PAD) and the heterogeneous canopy based on the TLS (both with a 60 m gap). Analysis of the flow streamlines showed a recirculation zone extending across most of the width of the clearing and into the downwind canopy section. The presence of a recirculation zone within the clearing is consistent with other studies investigating wind flow across canopy gaps and clearings (Banerjee et al. 2013, Kiefer et al. 2016, Queck et al. 2014, Schlegel et al. 2015). Vertical velocities were positive (directed upwards) at the first canopy edge (i.e. as the flow enters the gap) and negative towards the second canopy edge. There was also movement of faster flowing air from above the canopy down into the gap and penetrating into the second canopy section.

Kiefer et al. (2016) modelled wind flow across a gap for the purpose of understanding the influence of canopy discontinuities on forest fire dynamics. Similarly to Schlegel

et al. (2012), they found that the presence of a gap led to updrafts at the first canopy edge and downdrafts at the second canopy edge, producing a clockwise recirculation pattern. They also found that the presence of a gap produced greater downstream mean wind speeds compared to a homogeneous canopy with no gap.

Panferov & Sogachev (2008) used a wind flow model to perform a series of numerical experiments with canopy gap sizes from 3–75 tree heights (h) in order to interpret spatial patterns of wind damage to trees. As part of their study they considered the impact of gaps on the streamwise wind velocity; similar to Schlegel et al. (2012) and Kiefer et al. (2016), their results also showed the movement of faster flowing air from above the canopy down into the gap. Furthermore, they found that within the gap (and at $z < h$), the mean wind speed increased with gap size but that the rate of increase was not linear. The mean wind speed increased most rapidly between gap diameters of 3–15 h, after which the rate of increase remained almost constant.

Chahine et al. (2014) used LES and field measurements to investigate wind flow dynamics over a vineyard, which comprises structured rows of vegetation. They found that the wind-direction relative to the row orientation was important as they observed channelling of wind down the rows when the streamwise wind direction was parallel to the rows, whereas if the wind direction was cross-row or diagonal to the rows, the mean flow over the vineyard was approximately similar to that observed in uniform canopies. Canopy metrics such as displacement height and roughness length varied with the aspect ratio (of rows to wind direction), for instance if the wind flow is directed down the rows then the canopy appears more open than if the flow is directed across rows.

In boreal forests, one way in which clearings may potentially impact on the surrounding environment is through changes in the spatial distribution of snow on the forest floor due to altered wind dynamics. Wind modelling studies have the potential to be utilised to predict situations where we might expect blowing snow events to occur

and, conversely, where we might expect to observe accumulation of wind-blown snow. The following section presents an overview of snow accumulation processes, with a particular focus on the redistribution of snow by wind.

2.4 Snow accumulation and redistribution in forest environments

Snow dynamics are determined by a range of processes that contribute towards the accumulation, redistribution and removal of snow from the landscape. Key processes that contribute towards the spatial distribution of snow mass within a boreal forest environment include canopy interception and un-loading of snow, and the wind driven transport of snow.

2.4.1 Interception of snow

Interception processes are an important influence on the spatial distribution of snow accumulation and the wider hydrology of forest environments (Wilm & Dunford 1948, Troendle & King 1985, Varhola et al. 2010, Schelker et al. 2013, Moeser et al. 2016, Lundberg et al. 2016). Forest canopies intercept up to 60% of cumulative snowfall, which is then retained in the canopy before it is released through sublimation or unloading processes (Hedstrom & Pomeroy 1998). In contrast to temperate forests, snow may be held in boreal forest canopies for several days to a month (Pomeroy & Schmidt 1993). The canopy structure (e.g. canopy density) is an important influence on sub-canopy patterns of snow accumulation and melt timing (Golding & Swanson 1986, Boon 2012, Moeser et al. 2015, 2016, Varhola et al. 2013, Winkler & Moore 2006).

2.4.1.1 Interception efficiency

The amount of falling snow that is intercepted by a forest canopy ranges widely from 0-60% of the total annual snowfall in forested areas (Storck et al. 2002, Hedstrom & Pomeroy 1998). The efficiency with which a branch accumulates snow is equal to all the individual efficiencies of individual branches in the canopy within a particular time period, less any unloading (Hedstrom & Pomeroy 1998). The interception efficiency of falling snow depends on:

(i) The branch collection area, which is the horizontal plan area of the branch and depends on both the tree species and the temperature. As the temperature decreases the branch becomes less elastic, which increases its plan area (Schmidt & Gluns 1991, Schmidt & Pomeroy 1990).

(ii) The combined branch and snow collection area, which depends on how thick the existing snow load is and the formation of any snow bridges across branches as the load increases (which extend the collection area) (Schmidt & Gluns 1991).

Hedstrom & Pomeroy (1998) developed an interception model that uses an exponential model as the underlying efficiency distribution. It is based on the assumption that interception efficiency decreases with increasing snow load and increases with increasing canopy density. This model was the first to directly include canopy parameterisations, which it does through the leaf area index (LAI) and canopy closure. Most subsequent interception models use either or both of these parameters to describe the canopy (Essery et al. 2009, Rutter et al. 2009).

Empirical methods of quantifying interception include:

(i) Taking direct measurements; a destructive method where a tree is cut and attached to a scale that measures the snow load intercepted over time (Hedstrom & Pomeroy 1998, Nakai et al. 1994, Schmidt & Gluns 1991, Storck et al. 2002, Lundberg &

Halldin 2001).

(ii) Optical (indirect) methods, such as time lapse photography, to gain a visual measurement of the intercepted snow load, which can then be related to field measurements (Bründl et al. 1999, Garvelmann et al. 2013, Parajka et al. 2012).

2.4.1.2 Sublimation and unloading of canopy snow

Snow is held in the canopy until it either sublimates or it is unloaded and falls to the ground. The unloading of snow from the canopy is influenced by the following counteracting effects. If any of these factors fail, the canopy snow is released to the ground:

(i) Snow cohesion from branches, due to micro-scale ice or liquid bonds that form rapidly between snow crystals and tree needles and stems. As temperatures rise, the snow wetness increases, which enhances the level of cohesion (Kobayashi 1987).

(ii) The strength of the snow mass, due to inter-crystal bonding. In general, bonds are stronger at cold temperatures and become weaker as the melting point is approached (Langham 1981).

(iii) Branch support; branches are elastic near melting temperatures and so are less able to support snow (Schmidt & Pomeroy 1990).

Sublimation is the process by which snow crystal mass becomes water vapour; when the vapour pressure at the snow particle‘s surface exceeds that in the air it loses mass (Schmidt 1972). Intercepted snow has a relatively large surface area, as it is spread out across the tree branches. As such, a large proportion of snowfall over boreal forests never actually reaches the ground and instead sublimates directly from the canopy (Schmidt & Troendle 1992, Pomeroy & Gray 1995, Lundberg & Halldin 2001).

2.4.2 Wind-driven transport of snow

The wind-driven transport of snow introduces spatial variation in snow depth and density (Liston et al. 2007, Mott et al. 2018). Snow in open and exposed sites may be eroded and redistributed by the wind to sheltered areas, such as forests (Essery & Pomeroy 2004). Furthermore, sublimation losses during blowing snow events can be substantial and may remove up to 40% of annual snowfall depending on climatic conditions (Pomeroy et al. 1993). The resultant variability in the amount and distribution of accumulated snow can produce patchy cover during snow melt, thereby affecting the surface energy exchange, snowmelt dynamics and the local water balance (Marsh & Pomeroy 1996, Mott et al. 2018, Pomeroy & Li 2000). Wind-driven snow transport also has important ecological impacts, for instance through the transport of nutrients across a landscape and the insulation of snow-covered vegetation and soil (Sturm et al. 2001).

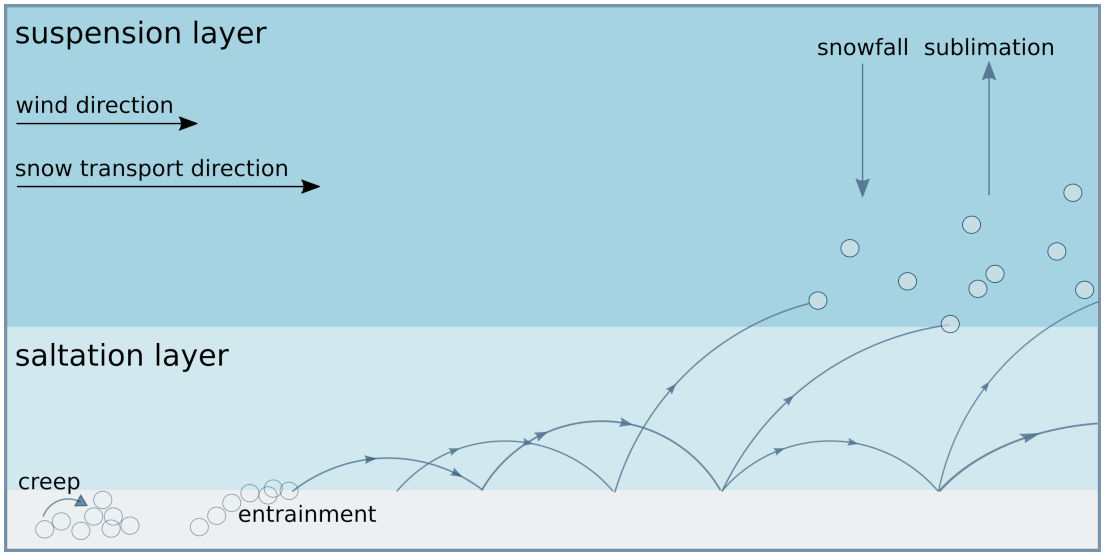

Figure 2.4: Schematic of blowing snow processes. Creep is the wind-driven movement of large snow particles across the snow surface. Saltating snow particles bounce and skip across the snow surface and eject further particles into the saltation layer. Above the saltation layer, snow particles (originating from falling or saltating snow) may be held in suspension and transported downwind.

There are three possible methods of snow transport (Figure 2.4): (i) Creep, where the force of the wind rolls large particles across the snow surface; (ii) Saltation, where

snow particles skip along the surface and eject further particles; (iii) Suspension, where atmospheric turbulence supports snow particles in the air. Saltation and suspension are the main modes of snow transport and suspension typically dominates, particularly when wind speeds are high. Periods of blowing snow always start with saltation, which can then act as a source of particles for turbulent diffusion into the suspension layer, although falling snow may also feed into the suspension layer (Pomeroy et al. 1997).

2.4.2.1 Saltation

The word 'saltation' is derived from 'saltare', which means 'to dance'; saltating snow comprises blowing snow particles that skip and bounce over the snow surface with curved trajectories (Figure 2.4). Saltation involves the erosion and entrainment of the snow surface to form a two-phase flow layer that is several centimetres thick (Kobayashi 1972, Schmidt 1986, Pomeroy & Gray 1990). As snow particles saltate and collide with the surface, they shatter the surface snow crystals and eject further particles into the saltation layer. Sublimation and abrasion processes change the form of saltating particles so that they are broadly spherical, with a mean diameter of 200 µm, although sizes range widely from tens to hundreds of micrometres in diameter (Schmidt 1981).

The threshold wind speed is a metric typically defined as the wind speed at the cessation of particle movement. This is because fluid forces alone are not sufficient to initiate particle movement, rather the impact of saltating particles is needed to eject further particles from the surface (Schmidt 1980). These particle impacts may be initiated by a turbulent sweep that produces flurries of saltating snow particles, hence in terms of wind speed it is clearer to define the end of particle movement than the start (Nickling 1988). Li & Pomeroy (1997) recorded threshold wind speeds of 7–14 m s^{-1} for wet snow (average = 9.9 m s^{-1}) and generally lower speeds of

4–11 m s^{-1} for dry snow (average = 7.7 m s^{-1}). The threshold wind speed may be related to the threshold friction speed as follows:

$$u_{*c} = \frac{u_c k}{ln(z/z_0)} \tag{2.5}$$

where u_{*c} is the threshold friction speed (m s^{-1}), u_c is the threshold wind speed (m s^{-1}) at height z (m), k is von Karman's constant (0.4) and z_0 is the roughness length (m).

However, rather than threshold wind speed, a threshold surface shear stress better encapsulates the force required for particle ejection and thus to initiate snow movement. The threshold shear stress may also be expressed as a friction velocity:

$$u_{*c} = \sqrt{\frac{\tau_c}{\rho_a}} \tag{2.6}$$

where ρ_a is the density of air (kg m^{-3}) and τ_c is the wind shear stress at the snow surface (kg m^{-1} s^{-2} = Pa), which depends on the wind speed and the aerodynamic roughness of the surface. For a given wind speed, a rougher surface will generate more turbulence and shear stress. The presence of vegetation increases the roughness of a surface and some of the force of the wind is expended on the vegetation rather than towards snow transport (Pomeroy & Gray 1995, Raupach et al. 1993). Kind (1981, as cited in Pomeroy & Gray (1990)) found threshold friction velocities in the range 0.07–0.25 m s^{-1} for fresh, loose, dry snow, and during snowfall, whereas for old, wind-hardened, dense and/or wet snow, thresholds were higher and ranged from 0.25–1.0 m s^{-1} .

Threshold conditions are dynamic and are strongly influenced by the degree of surface cohesion and bonding (He & Ohara 2017, Schmidt 1980). In contrast to the saltation

of sediment, saltating snow involves interactions with a surface comprised of bonded crystals that form a cohesive matrix (vs. non-cohesive sediment grains). The inter-crystal strength of this matrix is important in determining the force required to eject a particle from the surface (Schmidt 1980). The strength of cohesive bonding depends upon the snow surface history, specifically its: (i) age; (ii) temperature history; (iii) friction properties; and (iv) elastic properties. These factors are described in more detail as follows:

Age of snowpack The threshold wind speed increases with time since deposition as the density of snow increases as it ages (due to metamorphism, see below) (Schmidt 1980, Gray & Morland 1995). Snow that is more densely packed has more contact points per unit mass from which to form bonds between particles. Although the strength of bonds is not necessarily enhanced by this process, the overall strength of the snow increases. Li & Pomeroy (1997) observed higher typical threshold wind speeds for aged snow (from 8.0 m s^{-1}) compared to fresh snow (from 7.5 m s^{-1}).

Temperature history of snowpack The structure of snow may undergo metamorphism and thereby change over time (Sommerfeld & LaChapelle 1970, Colbeck 1987). There are two types of metamorphism that are of particular importance to snow transport: (i) temperature gradient metamorphism; (ii) equi-temperature metamorphism. Temperature gradient metamorphism occurs when there are vertical gradients in temperature. Water vapour pressure decreases with decreasing temperature and so water vapour will move via diffusion from warmer to colder sections of the snowpack where it condenses and promotes crystal growth. In contrast, equi-temperature metamorphism occurs where there are very small or no variation in snowpack temperature with depth and is instead driven by pressure differences across snow crystals. The vapour pressure is greatest at the convex parts of an ice crystal and lowest in the con-

cave parts, stimulating diffusion of vapour across the crystal and the growth of ice bonds through sintering, which forms strong inter-crystal bonds. Snowpack cohesion may also be enhanced due to viscous forces between thin layers of liquid that form on snow crystals under warm conditions and this effect increases exponentially with increasing temperature (Schmidt 1980, Conklin & Bales 1993).

Frictional properties of snow The frictional properties of snow are related to temperature. Plates of snow crystals can slide past each other, similar to graphite. Langham (1981) found that the sliding friction force increased by 60 % when temperatures fell from 0°C to -25°C.

Elastic properties of snow The greater the elasticity of snow, the greater the force required to break inter-particle bonds and thus shatter and eject snow particles. The Young's modulus of elasticity for snow is a function of snow temperature. Mellor (1975, cited in Li & Pomeroy (1997)) found that elasticity increased by approximately 30 % when temperatures decreased from -1°C to -40°C.

While it is difficult to directly measure the bond strength of the snow surface, the main factors controlling snow bonding and cohesion (detailed above) are strongly related to temperature. Li & Pomeroy (1997) related the threshold wind speed to the snow temperature, which is assumed to be related to the air temperature in windy and exposed locations (because the snow surface is well-mixed with the overlying air). They found that for air temperatures above -25°C, the threshold wind speed increases non-linearly with air temperature. However, this is unlikely to apply in forest environments where the snow surface is sheltered from the wind and therefore less mixing occurs.

The mean horizontal velocity of saltating particles is typically proportional to the threshold friction velocity. The trajectories of saltating particles are less than a few

centimetres in height and typically follow a non-uniform path, with a near vertical ascent and a descent that is close to horizontal (Maeno et al. 1985). In the lower saltation layer, most saltating particles are relatively unaffected by turbulence however in the upper saltation layer there is more disturbance of particle trajectories by turbulence. This "modified saltation" connects the saltation phase of wind-driven snow transport with the suspension phase.

2.4.2.2 Suspension

Atmospheric turbulence supports snow crystals in the suspension layer, which extends upwards from the top of the saltation layer and can reach several tens of metres above the snow surface (Budd 1966, Schmidt 1982*a*, Pomeroy & Male 1992). Suspended snow particles originate from falling snow or are entrained snow from the surface (via saltation) and their radii range from 10–170 µm (Budd 1966, Schmidt 1982*b*). The snow particles flow downwind as their mass is transported with the mean horizontal component of the wind speed (Pomeroy & Male 1992). The mass concentration of the suspended layer is lower than that in the saltation layer and decreases exponentially with height but increases exponentially with the atmospheric friction velocity (Pomeroy & Male 1992).

The suspension transport rate increases with the fourth power of wind speed and so increases more rapidly with wind speed than saltation transport, which increases linearly with wind speed (Pomeroy et al. 1997). Therefore, suspension typically dominates blowing snow transport and especially so at high wind speeds; suspension constitutes more than 90% of total snow transport when 10 m wind speeds are greater than 17 m s^{-1} (Pomeroy & Male 1992).

2.4.2.3 Sublimation of blowing snow

In comparison to snow on the ground, wind blown snow particles have a high ratio of surface area to mass and are well ventilated, which results in higher sublimation losses. Furthermore, there is often a high atmospheric vapour deficit due to strong atmospheric mixing during large blowing snow events and on clear-sky days there is an additional solar energy input, both of which further promotes sublimation of blowing snow (DeWalle & Rango 2008). When snow particles sublimate, they cool and the air layer in contact with the particle reduces in temperature slightly (0.5–1.0°C), which removes sensible heat from the surrounding air. As a result, the air vapour content gradually increases and, consequently, this may inhibit sublimation rates downwind unless further dry air is mixed in. The distance of heterogeneous terrain upwind is termed the 'fetch' and, in addition to climatic conditions, also influences how much blowing snow accumulates or is lost through sublimation. Sublimation is a vertical flux and so snow mass loss increases with the horizontal distance travelled, whereas snow transport (via saltation or suspension) is a horizontal flux and so mass does not increase with fetch (Pomeroy et al. 1997). As a result, for longer fetches (>1000 m), sublimation losses dominate (Pomeroy et al. 1993).

2.5 Sub-canopy energy balance and snow melting

In high latitude boreal environments, where there is a persistent snowpack for over five months of the year, the annual snowmelt is a hydrologically significant event (Gray & Male 1981). Boreal forests are dominated by coniferous tree species, such pine, spruce and fir, that retain their needles during the winter and as such are an important influence on the timing and magnitude of snow melt (Pomeroy & Dion 1996). Understanding the interactions between forests and snow is key to producing accurate snow melt predictions, which are necessary for the effective management of

forested watersheds and improving land surface schemes for climate modelling (Wang et al. 2010, Ellis et al. 2013).

In boreal forest landscapes, the main components of the forest snow energy balance (Figure 2.5) are:

$$Q_{net} = R_{net} + THF + PHF + GHF + PCH \tag{2.7}$$

where Q_{net} is the total amount of energy to the snow, R_{net} is the net radiation (comprised of shortwave (SWR) and longwave (LWR) radiation), THF are the turbulent heat fluxes (sensible (H_s) and latent (H_l)), PHF is the heat flux from precipitation, GHF is the heat exchange between the ground and snow subsurface, and PCH is the energy from snowpack phase changes.

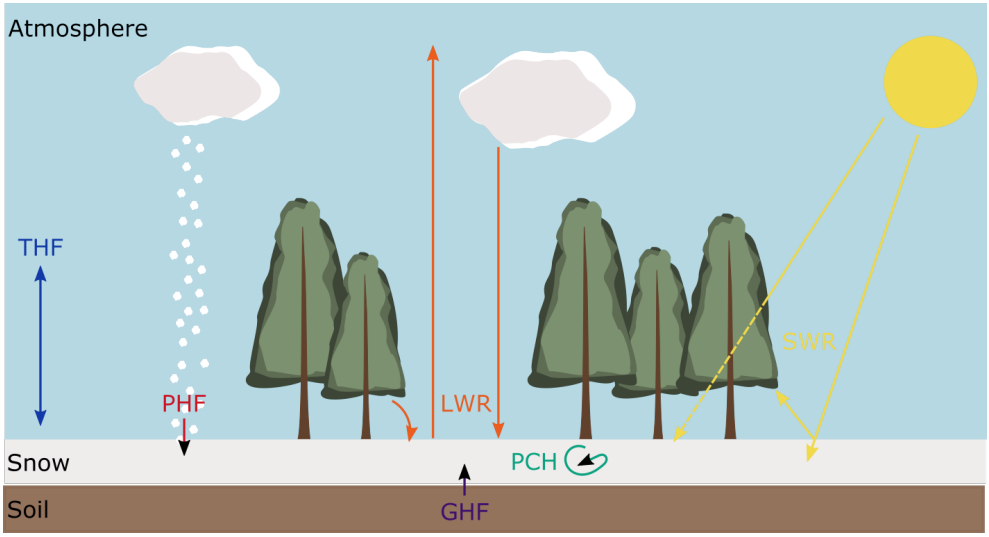

Figure 2.5: Schematic of the energy balance of sub-canopy snow (redrawn from Jonas & Essery (2011)), including: shortwave solar radiation (SWR); atmospheric and canopy longwave radiation (LWR); turbulent heat fluxes (THF); precipitation heat flux (PHF); ground heat flux (GHF); energy from snowpack phase changes (PCH).

Forests shelter underlying snow from the wind, thereby reducing turbulent energy fluxes to snow and elevating the importance of radiative fluxes for snowmelt (Harding & Pomeroy 1996, Link & Marks 1999*b*). The balance between incoming and outgoing

shortwave and longwave radiation determines the net radiation to the sub-canopy snow (R_{net}), which is calculated as:

$$R_{net} = (\downarrow SWR - \uparrow SWR) + (\downarrow LWR - \uparrow LWR) \tag{2.8}$$

Net radiation is the dominant influence on the sub-canopy snow cover energy balance and accounts for 60-90% of snowmelt energy, (Hardy et al. 2004, Lawler & Link 2011, Link & Marks 1999*a*, Male & Granger 1981). Incoming shortwave and longwave radiation to the snow surface is strongly modified by the presence of a forest canopy, which produces different spatial and temporal patterns of melt compared to those observed in open environments (Musselman et al. 2015). For instance, shading by the canopy reduces the shortwave radiation reaching the forest floor whilst solar heating of the canopy enhances the longwave radiation to snow. (Sicart et al. 2004) (Figure 2.6). The combination of these effects form a 'radiative paradox', which means that the presence of a forest canopy has the potential to both delay snowmelt through the reduction of shortwave radiation and turbulent energy fluxes (common in dense canopies) and to accelerate the onset of melting due to increased longwave radiation emissions (particularly in discontinuous canopies where canopy elements (e.g. trunks) are more exposed to solar heating) (Lawler & Link 2011).

2.5.1 Sub-canopy shortwave radiation

Shortwave radiation (0.2–2.8 μm) is the dominant component of sub-canopy net radiation with regards to snowmelt. Shortwave radiation is at its maximum value at the top of the atmosphere (1367 W m^{-2}). It is attenuated and split into diffuse and direct components through absorption and scattering processes as it passes through the atmosphere and canopy (Hay 1976). The exact proportion of sub-canopy shortwave

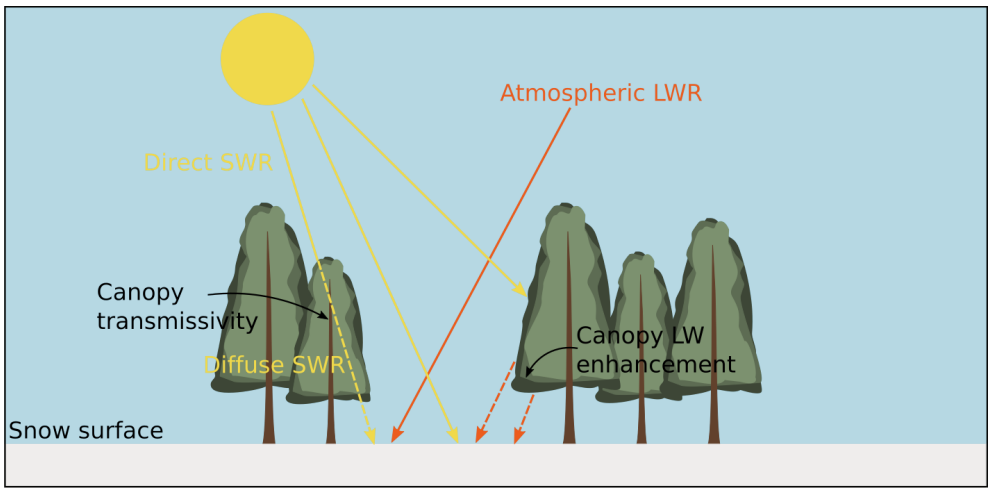

Figure 2.6: Schematic of the incoming shortwave and longwave radiation within forest canopy clearings

radiation incident to the snow surface that is direct or diffuse depends on factors such as the time of year, the solar angle, canopy properties and topography (Seyednasrollah et al. 2013).

Shortwave radiation may be reflected, transmitted or absorbed by a forest canopy and may further be reflected by the underlying snow. The reflectance of a surface is indicated by its albedo (α), which is the dimensionless ratio of reflected to incoming shortwave radiation at the surface (Eq. 2.9). The energy difference between incoming and reflected shortwave radiation is considered to be absorbed by the surface.

$$\alpha = \frac{\uparrow SWR}{\downarrow SWR} \tag{2.9}$$

In the case of a boreal forest canopy in the winter, this absorbed energy can include both shortwave radiation transmitted through the canopy but not reflected back from the snow, and shortwave radiation that is reflected by the snow but that is not then transmitted back out of the canopy. Coniferous canopies in boreal forests have low albedos, even with an intercepted snow load in winter, due to the multiple scattering of light between canopy and snow (Harding & Pomeroy 1996, Nijssen & Lettenmaier

1999). Snow albedo tends to decrease as it ages, as over time snow grain size increases and contaminants accumulate in the snow, both of which increase the absorption of radiation (Jonas & Essery 2011). Typical albedo values for a boreal forest canopy and the underlying snow surface are given in Table 2.2.

Surface	Albedo	
Boreal forest canopy	0.08 - 0.18	Pomeroy & Dion (1996); Betts & Ball (1997)
Sub-canopy snow surface	0.8 - 0.9	Melloh et al. (2002)

Table 2.2: Typical boreal forest albedos

The transmission of shortwave radiation through a forest canopy is dependent on the solar angle and canopy structure. The transmissivity τ_{SWR}, is the ratio between incoming shortwave radiation above and below the canopy, and is used as a measure of the degree to which the canopy transmits shortwave radiation. The lower the density of a forest canopy the greater the shortwave transmissivity, which can be $>$ 50% in sparse discontinuous canopies, whereas in very dense and continuous canopies, τ_{SWR} can be close to zero (Pomeroy et al. 2008, Reid et al. 2014).

The simplest and most common model for shortwave transmissivity applies Beer's Law, such that

$$\tau_{SWR} = exp(-\kappa \cdot LAI) \tag{2.10}$$

where κ is an extinction coefficient, which is an empirically determined parameter that describes the clumping and orientation of canopy elements, and LAI is the leaf area index, which is the total projected leaf area per unit ground area. Direct measurements of LAI are destructive and time-consuming, and so effective leaf area index (LAI') is often used instead as it can be estimated from measurements of canopy gap fraction (which may be obtained through indirect optical methods such as hemispherical photography) (Chen et al. 1997).

The Beer's Law approach treats the canopy as horizontally homogeneous and predicts

the average radiation. In the case of heterogeneous canopies and cloudy conditions, a more detailed approach can be taken to determine the direct and diffuse components of transmitted shortwave radiation. Using a probabilistic approach, the transmission of direct shortwave radiation at the forest floor may be calculated as

$$\tau_{dir} = \cos(\theta)P \tag{2.11}$$

$$P = e^{-G\lambda L_{path}} \tag{2.12}$$

where θ is the solar angle (the angle between the sun and normal to the surface), P is the probability of a solar beam passing through the canopy unobstructed, G is a projection function of leaf orientation ($G = 0.5$ if a random orientation is assumed), λ is the effective foliage area volume density, and L_{path} is the length of the path taken by the solar beam through the canopy (Seyednasrollah et al. 2013).

The transmission of diffuse shortwave radiation may then be taken as equivalent to the sky-view fraction (υ_f):

$$\tau_{diff} = \upsilon_f \tag{2.13}$$

where υ_f describes the fraction of the hemispherical sky that is unobscured by canopy elements.

Pomeroy & Dion (1996) measured transmissivity through a boreal jack pine forest in Saskatchewan, Canada, and found that the strong seasonality in solar angles at high latitudes is matched in the seasonality of radiative fluxes to sub-canopy snow. The typically horizontal orientation of pine tree branches result in relatively high shortwave transmission at low solar angles. The transmissivity fell as the solar angle increased, up to a solar angle of $\approx 50^{\circ}$, after which it began to increase again.

2.5.2 Sub-canopy longwave radiation

Forest snow receives diffuse longwave radiation (2.8–100 μm) from the surrounding canopy and the atmosphere (via gaps in the canopy) (Figure 2.6). Compared to open environments, incoming longwave radiation to the snow surface is enhanced due to thermal emissions from heated canopy elements. The contribution that this longwave enhancement makes to the net radiation balance is particularly significant under dense canopies during sunny periods (which heats the canopy) and for snow in close proximity to tree trunks (Lawler & Link 2011, Sicart et al. 2006, Webster et al. 2016). Of particular significance to snow melt timing and rate, Lundquist et al. (2013) found that the net longwave radiation flux is positive (i.e. directed towards the snow surface) in dense forest environments, whereas in open environments the flux is negative.

During clear-sky conditions, shortwave radiation is the dominant radiative flux to snow. In contrast, during cloudy conditions, or in close proximity to trees receiving high levels of shortwave radiation, or underneath a high density canopy, the contribution to the net sub-canopy energy balance from the longwave radiation component of the sub-canopy energy balance can exceed that from shortwave (Sicart et al. 2004).

The net sub-canopy longwave radiation balance is mainly influenced by: (i) the hemispherical sky-view fraction (υ_f); (ii) atmospheric and canopy temperatures; (iii) atmospheric and forest emissivities (Lawler & Link 2011, Sicart et al. 2006).

The incoming above-canopy longwave radiation can be calculated using the Stefan-Boltzmann law as:

$$\downarrow LWR_{atm} = \epsilon_a \sigma {T_a}^4 \tag{2.14}$$

Where ϵ_a is the dimensionless atmospheric emissivity (which depends on air temperature, percentage cloud cover and relative humidity), σ is the Stefan-Boltzmann constant (5.67×10^{-8} W m^{-2} K^{-4}) and T_a is air temperature (K).

The canopy contribution to the net sub-canopy longwave radiation can be calculated similarly to the atmospheric longwave radiation, such that:

$$\downarrow LWR_{can} = \epsilon_c \sigma \ {T_c}^4 \tag{2.15}$$

Where ϵ_c is the canopy emissivity and T_c is the canopy temperature (K).

Combining equations 2.14 and 2.15, sub-canopy longwave radiation may be calculated using a two-part model consisting of incoming longwave radiation received from the sky (the sky view fraction, v_s) and from the surrounding canopy (1 - v_s), such that:

$$\downarrow LWR_{can} = v_s(\epsilon_a \sigma {T_a}^4) + (1 - v_s)(\epsilon_c \sigma \ {T_c}^4) \tag{2.16}$$

When modelling the sub-canopy radiation balance, one option is to calculate the $\downarrow LWR_{atm}$ using the formulation presented by Liston & Elder (2006). However, it has been found that using a locally measured value of $\downarrow LWR_{atm}$ from above the canopy or at an open site nearby produces more accurate estimates of sub-canopy incoming longwave radiation compared to using a calculated values (Essery et al. 2008). Calculated values of $\downarrow LWR_{atm}$ fail to capture spatial and temporal variations, particularly in discontinuous canopies.

Typical ϵ_c values used in previous studies range from 0.9 – 1 (Essery et al. 2008, Pomeroy et al. 2009, Price & Petzold 1984, Seyednasrollah et al. 2013, Webster et al. 2016), which implies that canopy emissions of longwave radiation are strongly

dependent on T_c. Therefore, it is often assumed that the emitting temperature of the canopy is equivalent to the local air temperature, which is more easily measured (e.g. Essery et al. 2008, Lawler & Link 2011). While this assumption has been shown to hold for dense canopies, under cloudy skies or with low solar angles, vertical variations in canopy temperatures have been observed (Sicart et al. 2004, Pomeroy et al. 2009). Furthermore, uneven solar heating of tree elements can lead to significantly higher values of T_c at the edges of canopy discontinuities compared to the locally measured air temperature and the surrounding canopy temperature; Webster et al. (2016) observed tree trunk temperatures up to 25°C higher than the local air temperature. To avoid equating T_c to T_a, some modelling studies have divided the canopy into different emitting components (e.g. Seyednasrollah et al. 2013) or found statistical relationships between canopy and air temperatures to find an effective canopy temperature based on site-specific measurements (e.g. Essery et al. 2008).

2.5.3 Spatial and temporal variations in sub-canopy net radiation

A challenge with modelling the sub-canopy radiation balance is that shortwave and longwave radiation fluxes vary over small temporal and spatial scales due to shading, reflection, absorption and transmission processes that vary with canopy structure. The presence of discontinuities, in the form of gaps and clearings, in forest canopies provide further complexity to forest-snow interactions (Lawler & Link 2011, Musselman et al. 2015).

The influence of solar position on snowmelt energetics becomes particularly pronounced when considering discontinuous canopies. Lawler & Link (2011) discuss two paradoxes of incoming radiation that can occur in discontinuous forests with small gaps:

1. When solar elevation angles are low, the snow surface may be shaded by the surrounding canopy throughout the day while longwave radiation enhancement is minimal due to a relatively high sky view fraction (when compared to a continuous canopy). This results in an all-wave radiative minima, a 'cold hole' (Bernier & Swanson 1993), compared to an open or continuous forest site.

2. When solar elevation angles are high, there are similar levels of shortwave radiation in the gap as in an open site, and similar levels of longwave radiation as in a continuous forest site (due to a relatively small sky view fraction). As such, there are higher all-wave radiation levels in the gap compared to both an open site and a continuous canopy site. This leads to a radiative 'hotspot' in the gap that may be further enhanced by heated trunks, which increase longwave radiation emissions to the snow surface.

Previous studies have typically considered broadly circular gaps in forest canopies. Golding & Swanson (1978) observed greater variability in snow melt rates in forest gaps compared to dense forest stands, furthermore they found melt rates to be a function of gap size: melt rates were lowest in small gaps where $D/h \approx 0.75$–1 (D = gap diameter; h= canopy height), and highest in large gaps of size $D/h \approx 5$–6. Berry & Rothwell (1992) observed the smallest rates of ablation in small gaps (where $D \approx h$), when compared to both dense forest and open areas. Bernier & Swanson (1993) similarly found very low snowmelt rates in gaps of this size compared to a large clearing ($D/h \approx 40$). Typically, in clear sky conditions, as gaps become larger the net shortwave radiation increases and the net longwave radiation decreases, due to the higher exposure to direct and diffuse shortwave radiation. However, Seyednasrollah & Kumar (2014) noted that for gaps $D/h < 0.5$, as gap size increases, the net longwave radiation reduces at a faster rate than the rate of increase in net shortwave radiation. This results in decreasing net all-wave radiation to snow until gap sizes reach $D/h = 0.5$, where the lowest seasonal average radiation was observed to occur.

For gaps with $D/h > 0.5$, net all-wave radiation increases with size until $D/h > 10$, when changes in shortwave and longwave net radiation become broadly similar and the net all-wave radiation balance becomes less sensitive to the gap size. Seyednasrollah & Kumar (2014) described gaps where $D/h \leq 4$ as 'dark', as they receive less seasonal net radiation than open areas. In contrast, the seasonal net radiation received in large gaps ($D/h > 10$) exceeded that in open areas.

In the northern hemisphere, radiative minima occur at the south edges of gaps and may persist into late spring. In contrast, radiative maxima are found at the northern edge of gaps, and the smaller the gap, the later in the year this maxima occurs due to the higher solar elevation angles necessary to penetrate in to smaller gaps (Lawler & Link 2011).

The presence of complex topography within a landscape introduces further spatial variability to the surface energy balance, producing differences in snowmelt timing and intensity according to the slope and aspect of the terrain (Essery & Marks 2007, Ellis et al. 2011, Marsh et al. 2012). Field observations in pine and spruce forest in the Rocky Mountains, Canada, showed that, in general, south-facing forest slopes receive lower total radiation (compared to open areas) and so experience a delay to snowmelt, whereas, total radiation to snow is higher on north-facing slopes and so the onset of snowmelt is advanced (Ellis et al. 2011). Ellis et al. (2013) used the Cold Regions Hydrological Modeling (CRHM) platform (Pomeroy et al. 2007), a physically based snow model, to investigate the impact of thinning regimes in forested slopes on snowmelt and found contrasting results where there were gaps in the forest. They found that forest clear-cuts on north-facing slopes experienced a delay in melt onset, primarily due to reductions in longwave radiation. Whereas enhanced levels of shortwave radiation to gaps on south-facing slopes resulted in earlier and faster snowmelt. Seyednasrollah & Kumar (2014) similarly observed that net all-wave radiation was lowest in gaps on north-facing slopes and greatest on

south-facing slopes. The terrain slope angle also influences the surface energy balance through changes to the solar incidence angle, shading fraction and sky view fraction: Seyednasrollah & Kumar (2014) found that all-wave net radiation increased with slope angle for all gap sizes.

2.5.4 Turbulent heat fluxes

Turbulent fluxes of sensible and latent heat occur because of the turbulent mixing of air which transports heat and moisture between the land surface and the atmosphere (Bonan 2015). Turbulence creates eddies that mix the air, so that air from above is moved downward and air from below is moved upward. Vertical motions of air by turbulence can be generated mechanically due to drag at the surface that causes shear, leading to instability and turbulent eddies, or due to surface heating that creates warm buoyant air, which rises and carries heat and moisture away from the surface.

The turbulent fluxes of heat and water vapour to and from the snowpack play an important role in the snow surface energy and mass balances. However, turbulent fluxes to snow in forest environments has not been subject to much attention. They are often considered to be of minor importance (relative to radiation) due to typically low sub-canopy wind speeds that attenuate turbulent mixing (Conway et al. 2018, Hardy et al. 1998, Link & Marks 1999*a*, Marks et al. 2008).

Turbulent fluxes can be measured directly using eddy covariance instrumentation, although this is challenging under forest canopies due to factors such as low wind speeds and heterogeneous canopy structure (Conway et al. 2018, Mahat et al. 2013, Marks et al. 2008). There are also challenges in modelling and validating sub-canopy turbulent exchange processes, for example due to the complex spatial patterns of turbulence generated by canopy elements (Marks et al. 2008). The representation of turbulent fluxes within a physically based snow model can be evaluated by using

observational data to assess the models ability to simulate snowmelt and snow surface temperatures accurately (Conway et al. 2018).

2.6 Summary and research questions

The above review highlights the myriad processes involved in the accumulation and removal of snow. The accumulation of snow is influenced by processes such as interception and redistribution; factors impacting the subsequent removal of snow include the net energy balance to the snowpack and sublimation. Wind plays a significant role in snow dynamics, both directly – through the redistribution of snow, and as a driver of turbulent fluxes – and indirectly, since the redistribution of snow determines spatial patterns in snow accumulation, and therefore the efficacy of processes driving snow loss. Many of these processes are impacted by heterogeneities and discontinuities in forest canopies, thus increasing the complexity of the snow mass and energy balances in these environments.

This thesis aims to provide a better understanding of how patterns of sub-canopy wind flow and radiative fluxes vary across linear clearings in forests, and the impact of these dynamics on the spatial and temporal distribution of snow accumulation and melt processes.

The research questions underlying this research project are as follows:

Chapter 3:

1. How are the dynamics of wind flow through forested canopies affected by the presence of a clearing?

2. How does clearing width modulate these changes in wind velocities?

3. What is the impact of forest canopy structure on these wind velocities?

Chapter 4:

1. How reliably may field measurements of wind speed across boreal forest edges be reproduced by the BLASIUS wind flow model?

2. How do sub-canopy wind speeds and friction velocities across discontinuous forest landscapes scale with above-canopy wind speeds?

Chapter 5:

1. Can a simple snow model capture the temporal patterns of snow accumulation over multiple winter periods?

Chapter 6:

1. How well can simple models of direct and diffuse radiation match observations across a forest discontinuity?

Chapter 7:

1. How do spatial and temporal patterns of snow accumulation and melt vary across gaps of different widths?

2. How sensitive is the modelled melt behaviour to the different energy fluxes to the snowpack across the gap?

3. What is the impact of changing the canopy density on these snow dynamics?

4. How is the pattern of snowmelt across the gap altered by changing its orientation?

These questions will be addressed using a Met Office wind flow model (BLASIUS (Wood & Mason 1993, Wood 1995)) and a forest snow model (a simplified version of

FSM2 (Mazzotti et al. 2020a)) in conjunction with observational meteorological and snow data from a boreal forest setting at the Arctic Research Centre of the Finnish Meteorological Institute (FMI-ARC) research station in northern Finland.

Chapter 3

Simulating wind dynamics across canopy gaps using the BLASIUS wind flow model

3.1 Introduction

This chapter aims to investigate the modifying impact of forest discontinuities on canopy wind flow and any compounding effects of clearing width and canopy structure.

Forest canopies are well-known to modify local wind flow patterns through an increase in aerodynamic drag due to canopy elements such as branches and leaves (Belcher et al. 2003, Finnigan 2000). The presence of canopy discontinuities, for instance clearings resulting from road-building, introduce further complexity to canopy-wind interactions (Banerjee et al. 2013, Panferov & Sogachev 2008, Schlegel et al. 2012).

For further information on canopy wind flow, please refer to the more detailed review in section 2.3.

This chapter seeks to explore how canopy clearings of varying widths may alter the wind flow and considers the potential consequences of this within the context of snow accumulation, in particular wind-driven transport and compaction processes. To fulfil this aim, the research questions driving this chapter were as follows:

1. How are the dynamics of wind flow through forested canopies affected by the presence of a clearing?

2. How does clearing width modulate these changes in wind velocities?

3. What is the impact of forest canopy structure on these wind velocities?

To answer these questions, a Reynolds-Averaged Navier Stokes model with a 1.5 order closure scheme (BLASIUS) was used to simulate a combination of forest structure and clearing width scenarios, which are hypothetical but representative of real-world canopy fragmentation scenarios.

First, the BLASIUS model is presented (Section 3.2). Then wind flow is simulated across hypothetical forest canopies with varying structures and gap sizes (Section 3.3). The results are then discussed (Section 3.4) and conclusions presented (Section 3.5).

3.2 Methodology

3.2.1 Model description

Wind flow simulations were performed using the BLASIUS (Boundary Layer Above Stationary, Inhomogeneous Uneven Surfaces) model from the UK Met Office (Wood & Mason 1993, Wood 1995), which has been used for a number of canopy flow studies previously (Ross & Vosper 2005, Ross 2008, Ross & Baker 2013, Ross & Harman 2015). For all simulations, BLASIUS was run as a Reynolds-Averaged Navier-Stokes (RANS) model using a one-and-a-half order mixing length turbulence closure scheme, which uses a prognostic equation for the turbulent kinetic energy (TKE). The model is available to use from the Met Office under a research license and modifications to the code to include canopy effects (not included in the official model) were made available to me by Dr Andrew Ross (University of Leeds).

The model was run under neutral atmospheric conditions and periodic boundary conditions were used for all simulations, which means that an infinite series of forest-gap-forest patterns were simulated. The modelled terrain is flat (i.e. no hills) and a surface roughness of $z_0 = 0.001$ m was used for all simulations (the typical range for snow covered surfaces is z_0 = 0.5 – 10.0 $\times 10^{-4}$ (Oke 1978). A domain depth of 100 m and length of 600 m is used for all simulations in this chapter. There are 40 grid-points in the vertical direction and stretching of the model grid by a factor of 1.05 allows for relatively higher resolution within and just above the canopy (the height of the lowest grid point is at $z = 0.15$ m). A 0.5 m horizontal resolution resolves the flow at canopy edges sufficiently and at significantly lower computational expense than higher resolutions. The horizontal wind velocity at the upper boundary of the model domain is used to drive the model flow; a driving velocity of 20 m s^{-1} was used for the following simulations, unless otherwise stated, and the model is run to equilibrium. To help the two-dimensional (2D) simulation of wind flow for a given

canopy scenario converge more quickly, it is helpful to provide an approximate solution as a starting point. This is achieved by first running a one-dimensional model of wind flow through the canopy to provide an estimate of the velocity profile before then running the 2D model. Parameter adjustments to simulate the presence of a forest canopy are described below; all other model parameters not detailed here remained as described in Ross & Vosper (2005).

3.2.2 Simulating forest clearings

3.2.2.1 Canopy parameters

A forest canopy is represented in the BLASIUS model through two modifications to the original code (as described by Ross & Vosper (2005)). Firstly, the aerodynamic drag exerted by leaves and branches on the air flowing through the canopy is modelled through the inclusion of an additional drag term ($\rho C_d a \boldsymbol{U}|\boldsymbol{U}|$) in the momentum equation:

$$\rho \frac{D\boldsymbol{U}}{Dt} = -\Delta p + \Delta \cdot \boldsymbol{\tau} - \rho C_d a \boldsymbol{U}|\boldsymbol{U}| \tag{3.1}$$

where ρ is the air density, U is the velocity, p is the pressure, τ is the Reynolds stress tensor C_d is the canopy drag coefficient of individual canopy elements, a is the leaf area per unit volume.

The mixing length (used in the turbulence closure scheme) is also modified by the canopy. Within the canopy, the mixing length is taken as constant and scales with height above the canopy. The dissipation term in the prognostic equation for TKE is also modified to account for the enhanced dissipation of energy due to canopy drag, which converts energy from large scales to smaller wake scales that dissipate more

rapidly.

The forest canopy structure may be specified via adjustment of canopy parameters within the BLASIUS model (see Table 3.1). These parameters are assumed to be constant with height within the canopy but can be varied in the horizontal direction on a grid-point by grid-point basis so that canopy heterogeneities, such as gaps, may be simulated. The canopy values used for this investigation are similar to those used in previous studies that have used BLASIUS to model canopy wind flow (e.g. Ross & Vosper (2005), Ross & Baker (2013), Ross & Harman (2015)) and are within a realistic range based on empirical boreal forest metrics (Mayhead 1973, Amiro 1990, Finnigan 2000).

A fixed canopy drag of $C_d = 0.2$ was used for all simulations ($C_d \approx 0.1$–0.3 for most vegetation (Katul et al. 2004)). A uniform canopy height (h) and displacement height (d) were prescribed for a given canopy. The displacement height is the height at which the mean surface drag appears to act on the canopy and so is always $< h$ (Jackson 1981). A displacement height of 0.76 h was chosen according to the value given in Jarvis et al. (1976) for Scots pine, which is a common evergreen boreal tree species and the dominant tree species at the Finnish field site described in later chapters (e.g. see 4.2.1.1). Furthermore, Jarvis et al. (1976) give a mean of 0.78 h based on data from eleven forests, including a variety of pine, fir and spruce species (d/h ranged from 0.61 – 0.92). Therefore the value used in this study can also be considered a reasonable approximation for a range of typical boreal evergreen species. A leaf area density (a) of 0.1 or 0.4 was used. The leaf area density is the leaf area per unit volume of tree and these values correspond to a leaf area index (LAI: a commonly used index of leaf area, defined as one-half of the total foliage surface area per unit area of ground (Chen & Black 1992)) of 0.8–0.9 and 3.2–3.6, respectively, for a canopy of height 10 m for instance ($LAI = (0.8\text{–}0.9) * LAD * h$, (Gower et al. 1999)).

	Forest 1	Forest 2	Forest 3
Canopy height, h (m)	10	20	10
Drag coefficient, C_d (m)	0.2	0.2	0.2
Leaf-area density, a (m^{-1})	0.4	0.4	0.1
Displacement height, d (m)	7.6	15.2	7.6

Table 3.1: Canopy parameter settings for the BLASIUS model.

3.2.2.2 Linear clearing widths

Simulated clearing widths of 3 m, 10 m, 30 m and 100 m were chosen as realistic clearing widths that could be observed in boreal forests, for example:

- A 3 m gap approximates narrow (modern) seismic lines (Dabros et al. (2018)) and forest tracks
- A 10 m gap corresponds to a wide (conventional) seismic line (Dabros et al. (2018)) or a small road
- A 30 m gap could be created by wider roads and small rivers
- A 100 m clearing may result from a large river or area of felled forest

A clearing is simulated within the model by setting the canopy parameters to zero at the appropriate grid points. As a result, simulated clearing edges are clearly defined and abrupt, and so are a simplification of naturally occurring clearings and where there may be regrowth following edge creation. However, for the purposes of this investigation this may be considered a reasonable approximation.

3.3 Results

This section presents the results from the wind flow modelling using the BLASIUS model outlined in section 3.2.1. The results show the changes in wind flow across

gaps in forest canopies, highlighting the impact of gap width on these dynamics. Also presented are the results of varying canopy characteristics such as height and leaf area density.

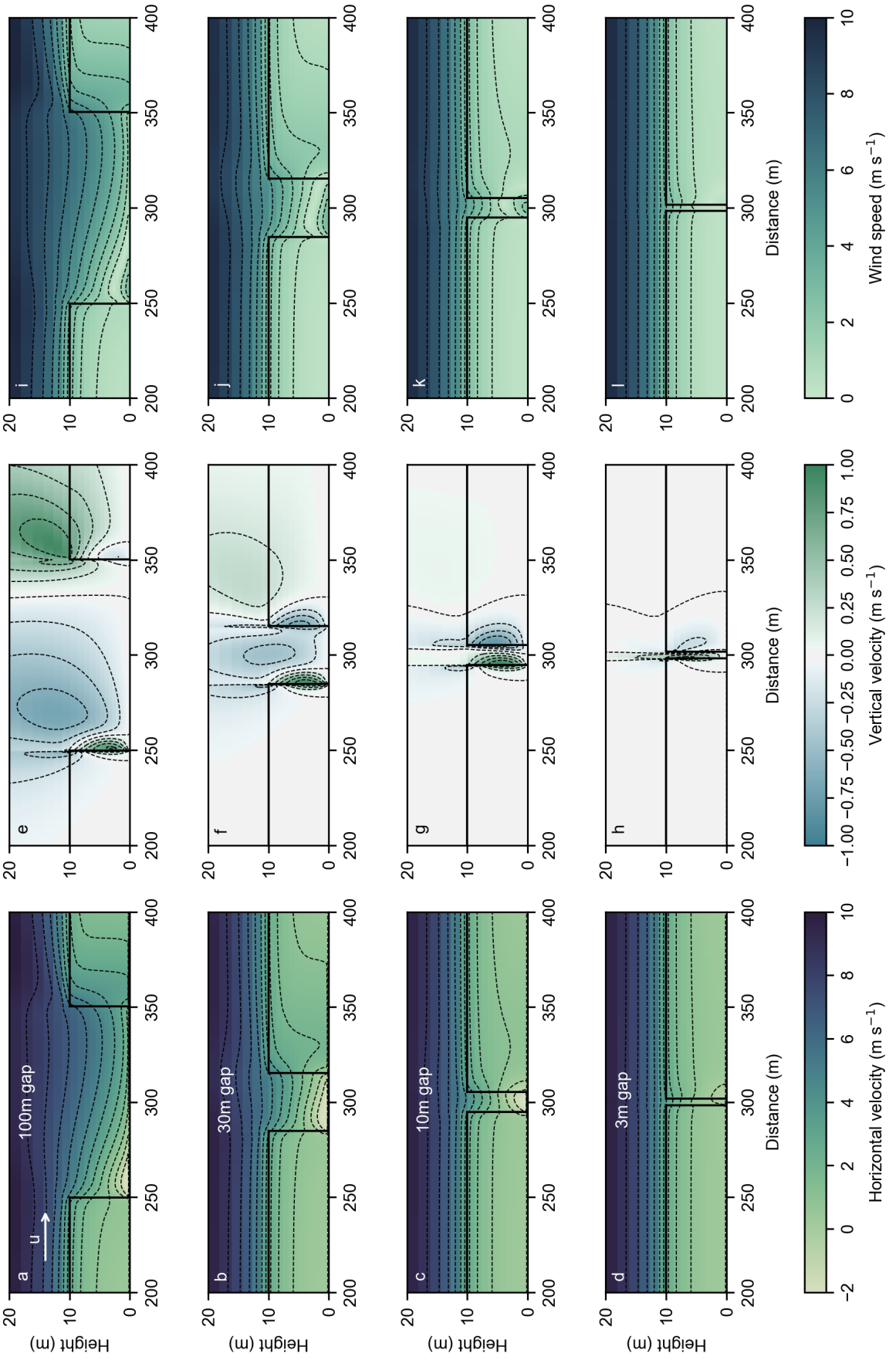

Figure 3.1: Wind velocities and speeds across forest clearings for four different gap sizes: 100 m, 30 m, 10 m and 3 m. The simulated canopy has height of $h = 10$ m and a leaf area density of $a = 0.4$ m^{-1}. The canopy extent is shown by the solid black lines. The driving wind velocity at the upper boundary $= 20$ m s^{-1} and flows from left to right. The dashed black lines are isolines of constant velocity or speed. The horizontal scale is such that 1 gridpoint $= 0.5$ m and the vertical resolution decreases with height non-linearly.

3.3.1 Impact of gap width on wind flow

First, considering the case of a 100 m gap (Figure 3.1a., e., & i., and Figure 3.2 for vertical profiles at the edges): on exiting the canopy, there is a reversal of the flow at the lower levels shown by the area of negative horizontal velocity. Outside of this area of flow reversal and below the height of the canopy, u increases with x distance until a distance of approximately 10 m from the windward canopy edge. The flow appears to be reaching a new adjusted flow pattern within the gap after approximately 75 m, indicated by the approach to parallel lines of velocity. On approaching the canopy edge, the horizontal velocity starts to decrease at heights $>$1.9 m and increases below this height. Figure 3.3 shows the flow in this canopy-gap scenario over a greater horizontal distance. The horizontal velocity flow readjusts to the presence of the canopy over a distance of approximately 100 m (Figure 3.3.a).

There is a distinct region of positive vertical velocity (maximum $= 0.82$ m s^{-1}) located at the exit point from the canopy into the 100 m gap. Above this and into the gap is a region of negative vertical velocity as the air flow enters the space created by the gap. The peak downward velocities of -0.69 m s^{-1} are located 20 m beyond the first canopy edge. As the flow approaches the downwind canopy edge, the vertical velocity is negative in the mid-lower canopy ($z <$ 4.2 m) and positive in the mid-upper canopy and above the canopy.

Figure 3.4 illustrates the effect of changing the driving wind speed at the upper boundary ($z =$ 100 m) on the modelled horizontal and vertical velocities, with the 100 m gap case as an example. The wind flow features described above are spatially consistent across the different driving speeds but decrease in intensity with decreasing driving wind speed.

The zone of reversed flow seen with the 100 m gap is present in the case of the narrower 30 m gap and occupies the full width of this gap. As such, the flow does

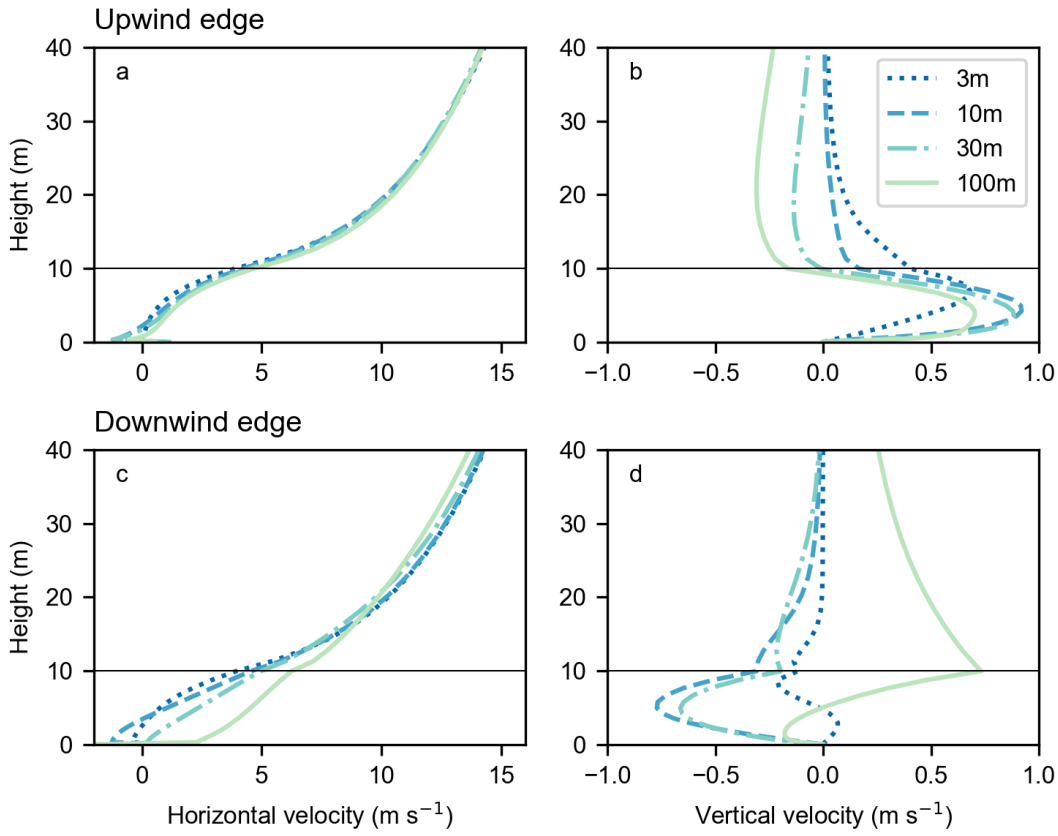

Figure 3.2: Vertical wind profiles for horizontal and vertical velocities at the upwind and downwind edges for four different gap sizes: 100 m, 30 m, 10 m and 3 m. The simulated canopy has height of $h = 10$ m and a leaf area density of $a = 0.4$ m^{-1}. The canopy top is shown by the solid black line.

not have the space to adjust to the gap. Compared to the 100 m gap scenario, there is a similar but less marked increase in horizontal velocity at the mid-upper canopy ($z > 5$ m) and decrease at lower heights on entering the second canopy edge. The horizontal velocity adjusts to the presence of the canopy more rapidly than when entering from the 100 m gap, with an adjustment length of approximately 85 m.

The general spatial patterns of vertical velocity values seen with a 100 m gap are repeated with a 30 m gap but with the peak downward velocities ($w = -0.67$ m s^{-1}) occurring at the second canopy edge in this case. The upward vertical velocities observed at and above the canopy top as the flow entered the canopy following the 100 m gap are also seen here but displaced further along the length of the canopy and

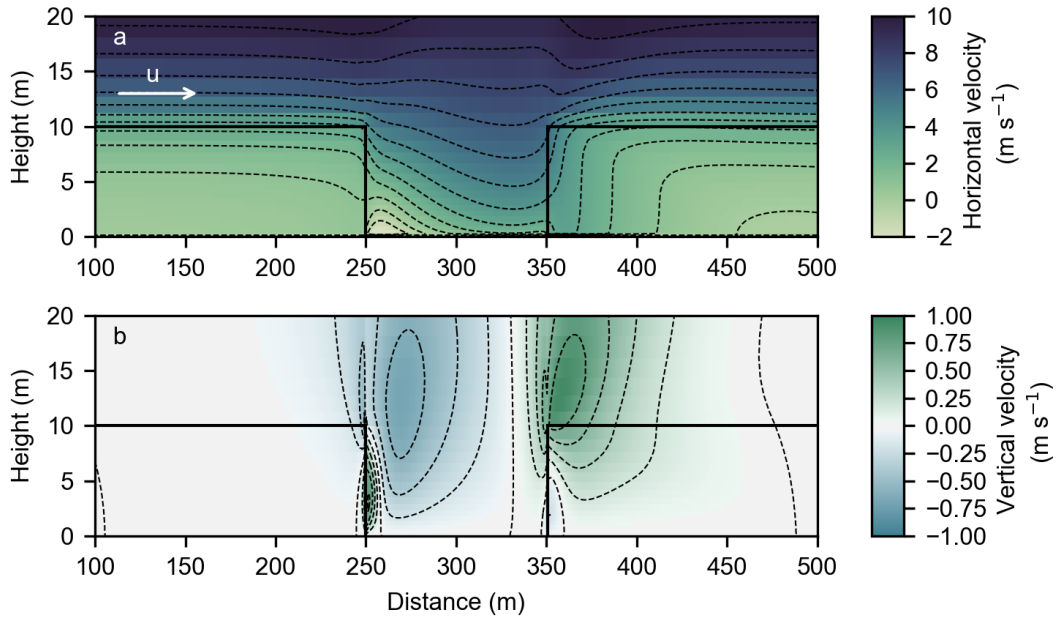

Figure 3.3: Horizontal and vertical wind velocities across a 100 m gap. The simulated canopy has height of $h = 10$ m and a leaf area density of $a = 0.4$ m^{-1}. The canopy extent is shown by the solid black lines. The driving wind velocity at the upper boundary = 20 m s^{-1} and flows from left to right. The dashed black lines are isolines of constant velocity.

are smaller in magnitude (max $w = 0.29$ m s^{-1}, compared to max $w = 0.95$ m s^{-1} following the 100 m gap).

The reversed horizontal flow feature persists in the 10 and 3 m gaps, although it becomes less pronounced and starts to extend into the second canopy section as the gap size decreases. In general, the canopy flow is less perturbed by the presence of the narrower gaps and on entering the downwind canopy, the flow adjusts to the canopy after approximately 77.5 m and 3.5 m following the 10 and 3 m gaps respectively.

With the 10 m gap scenario, the upward vertical velocities as the flow exits the canopy (max $w = 0.94$ m s^{-1}) extend over a similar horizontal distance (approximately 10 m) as in the cases of the wider gaps and so occupy a larger proportion of the gap itself. As the flow enters the second canopy edge, a downward vertical velocity component dominates (min $w = -0.79$ m s^{-1}) and a reduced region of upward vertical velocity

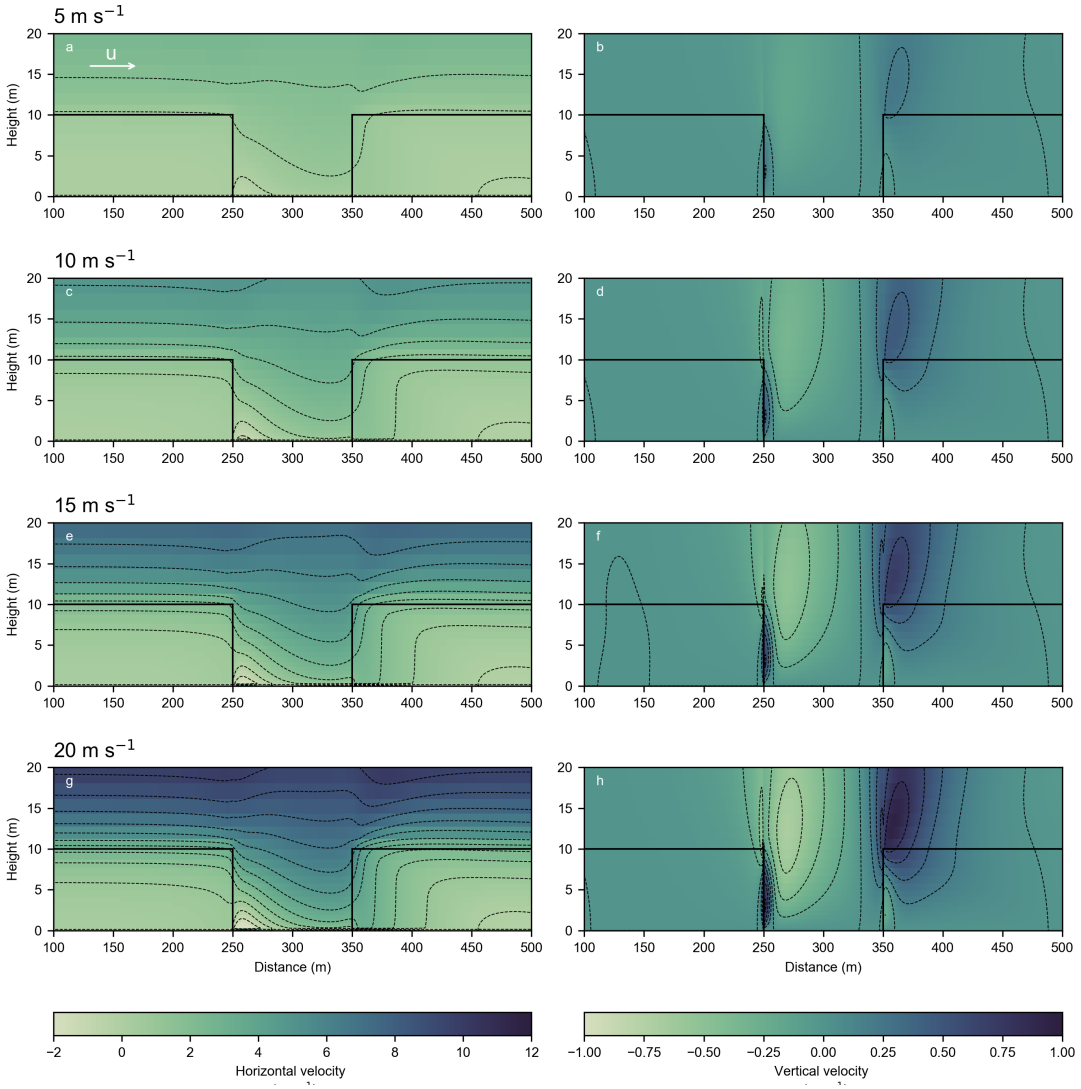

Figure 3.4: Horizontal and vertical wind velocities across a 100 m gap with four different driving wind speeds at the upper boundary (flowing left to right): 5 m s^{-1} (a. & b.); 10 m s^{-1} (c. & d.); 15 m s^{-1} (e. & f.); 20 m s^{-1} (g. & h.). The canopy height = 10 m, leaf area density = 0.4 m^{-1} and the canopy extent is shown by the solid black lines. The dashed black lines are isolines of constant velocity.

occurs at a greater horizontal distance from the edge when compared to the 30 and 100 m gap scenarios.

In the case of the 3 m gap, the vertical velocity values are largely positive and located within the gap (max $w = 0.68$ m s^{-1}), with a region of negative velocities as the flow enters the second canopy edge (min $w = -0.24$ m s^{-1}). The magnitude of the vertical velocity at a given height is generally smallest in this case and the perturbations to

the vertical velocity are more spatially concentrated when compared to the wider gap scenarios.

Across all gap width scenarios, the wind speed generally increases with height. However, in the 100, 30 and 10 m gap scenarios there is a region of relatively higher wind speed concentrated at the forest floor (at heights $\leq$ 1.5 m) and corresponding to the region of reversed horizontal flow.

3.3.2 Impact of canopy height on wind flow

Increasing the canopy height from 10 m to 20 m accentuated the region of reversed flow described above. In the 100 m gap scenario, this region extends over most of the horizontal distance of the gap (commencing 7 m before the first canopy edge and finishing 1 m before the second canopy edge) and up to a maximum height of 4.2 m (Figure 3.5.a.). The region of positive vertical velocity on exiting the canopy is still observed and begins within the canopy approximately 15 m before the edge. The subsequent negative vertical velocity as the air flows through the gap is observed with both canopy heights but there is a further distinctive region of negative vertical velocity as the flow re-enters the taller (20 m) canopy, which is seen to a lesser degree in the shorter (10 m) canopy case (maximum downward velocity of -0.67 m s^{-1} when $h = 20$ m, compared to -0.2 m s^{-1} when $h = 10$ m). In contrast, the region of positive vertical velocity at and above the downwind canopy top is more spatially concentrated in the vertical when $h = 20$ m and velocities are generally lower (maximum vertical velocity of 0.62 m s^{-1}, compared to 0.95 m s^{-1} when $h =$ 10 m).

3.3.3 Impact of leaf area density on wind flow

Lowering the leaf area density (a) from 0.4 m^{-1} to 0.1 m^{-1} increases the horizontal velocity at a given height within the canopy and gap but the general spatial patterns of horizontal velocity change across the gap are similar (Figures 3.6 (a–d) and 3.7 (a & c)). As with the case where $a = 0.4$ m^{-1}, there is a region of reversed flow on entering the 100 m gap when $a = 0.1$ m^{-1}, although it begins 6.5 m into the gap rather than directly at the canopy edge and is reduced in spatial extent. A similar pattern of delayed onset and reduced extent of the reversed flow region is seen in the 30 m and 10 m gaps. On leaving the gap, the horizontal velocity takes longer to readjust to the canopy when $a = 0.1$ m^{-1}, with adjustment lengths of 160 m, 150 m, 120 m and 24 m for the 100 m, 30 m, 10 m and 3 m gap scenarios respectively (compare to 100 m, 85 m, 77.5 m and 3.5 m when a $= 0.4$ m^{-1}).

The lower leaf area density results in lower magnitudes of vertical velocity across all gap sizes, although again the general spatial patterns of velocity change are similar (Figures 3.6 (e–h) and 3.7 (b & d)). A notable difference is that the region of positive vertical velocity observed when the flow exits the canopy and enters the gap is displaced further into the gap when $a = 0.1$ m^{-1} in all cases except the 3 m gap.

These changes in the velocity components on lowering the leaf area density resulted in higher overall wind speeds through the canopy and gaps (Figure 3.6 (i–l)).

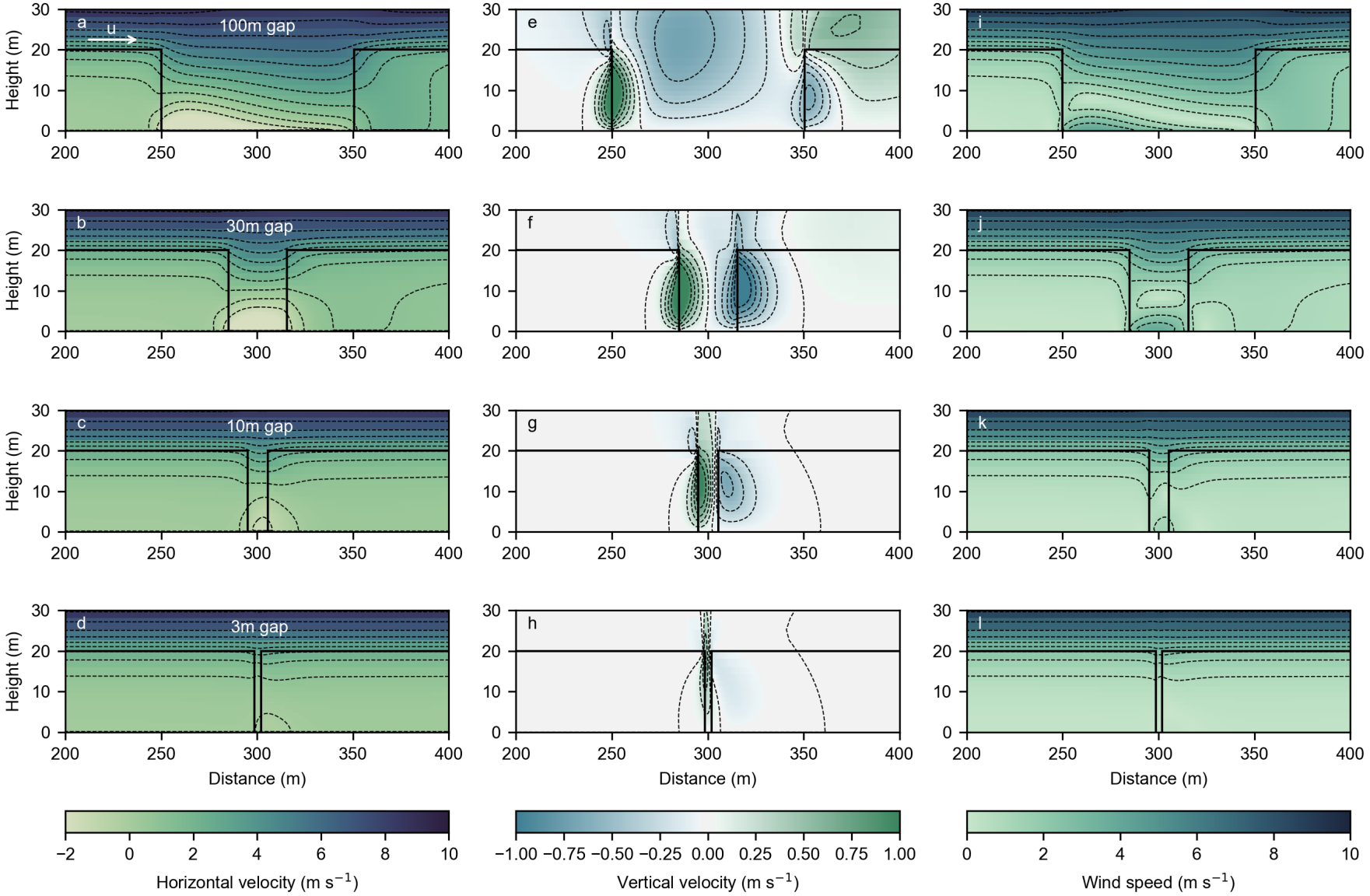

Figure 3.5: Wind velocities and speeds across forest clearings for four different gap sizes: 100 m, 30 m, 10 m and 3 m. The simulated canopy has height of $h = 20$ m and a leaf area density of $a = 0.4$ m^{-1}. The canopy extent is shown by the solid black lines. The driving wind velocity at the upper boundary = 20 m s^{-1} and flows from left to right. The dashed black lines are isolines of constant velocity or speed. The horizontal scale is such that 1 grid point = 0.5 m and the vertical resolution decreases with height non-linearly.

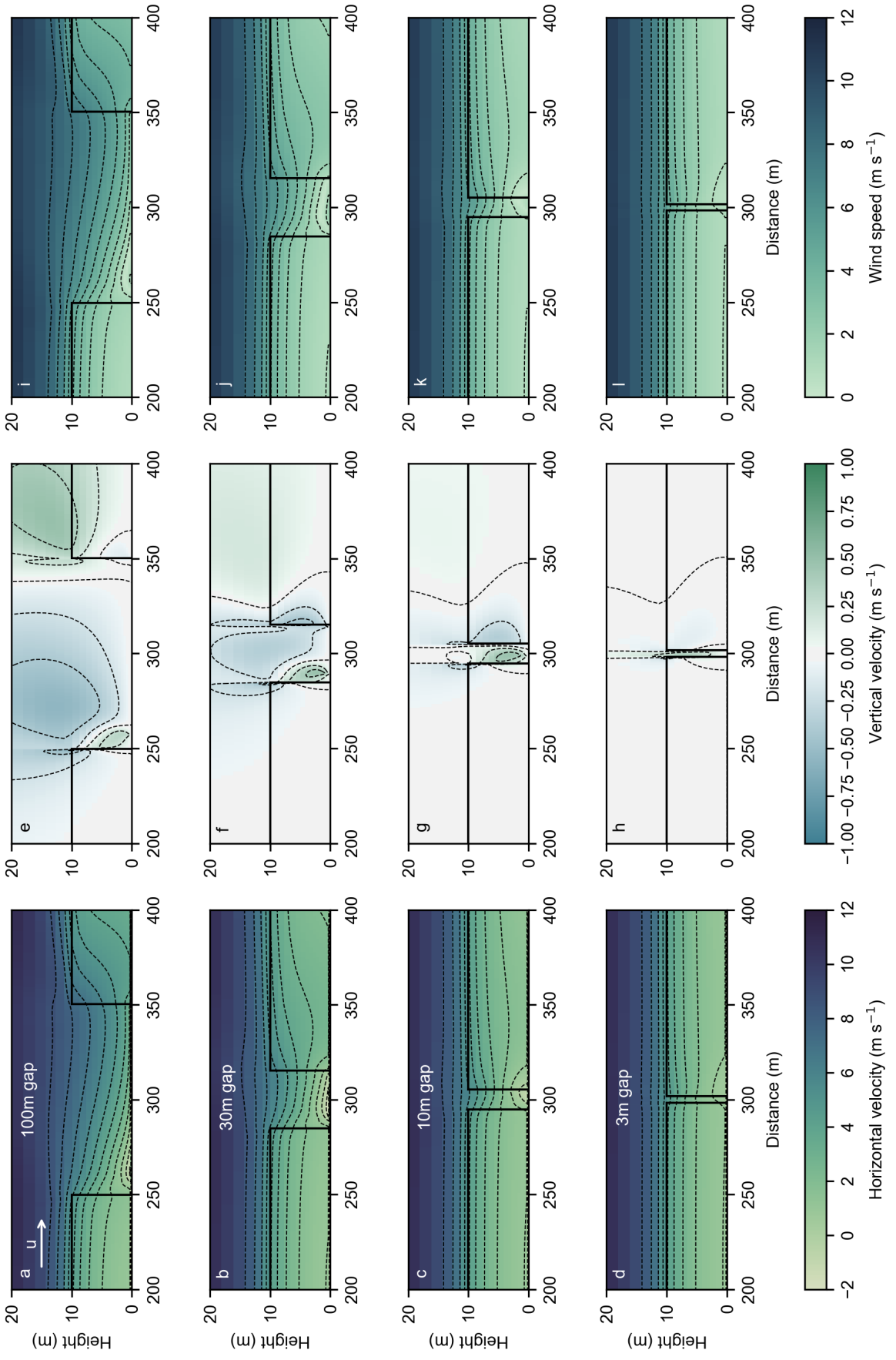

Figure 3.6: Wind velocities and speeds across forest clearings for four different gap sizes: 100 m, 30 m, 10 m and 3 m. The simulated canopy has height of $h = 10$ m and a leaf area density of $a = 0.1$ m^{-1}. The canopy extent is shown by the solid black lines. The driving wind velocity at the upper boundary $= 20$ m s^{-1} and flows from left to right. The dashed black lines are isolines of constant velocity or speed. The horizontal scale is such that 1 grid point $= 0.5$ m and the vertical resolution decreases with height non-linearly.

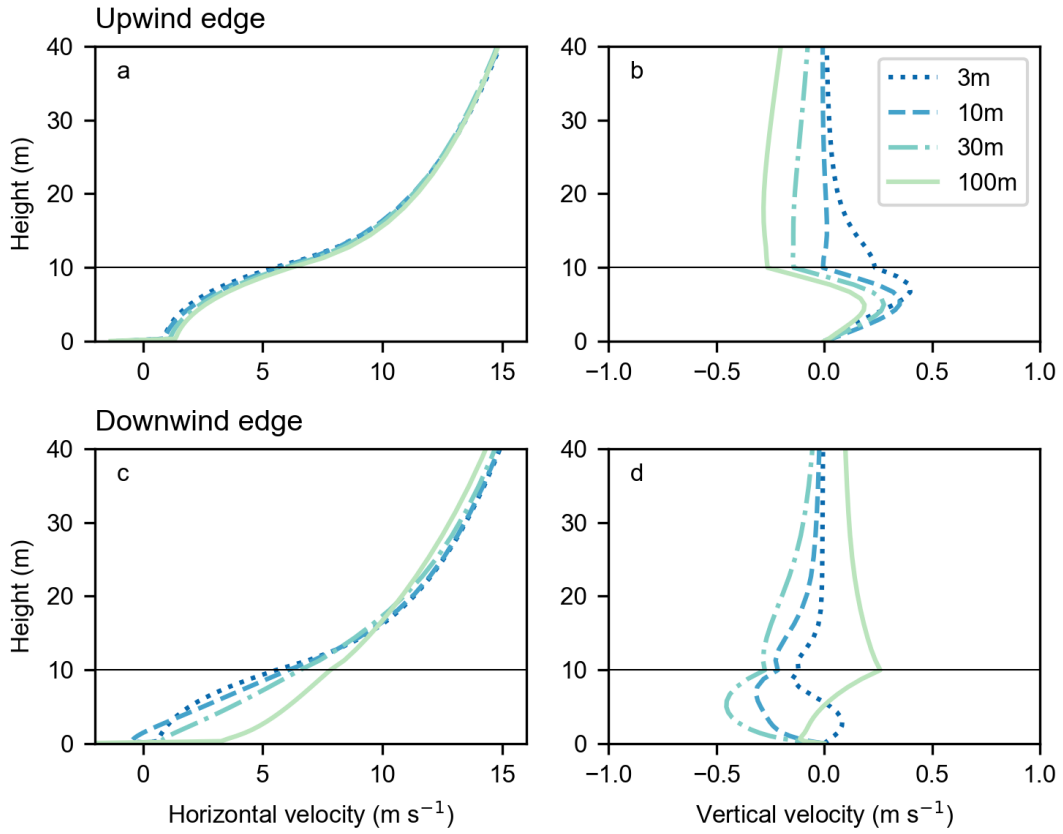

Figure 3.7: Vertical wind profiles for horizontal and vertical velocities at the upwind and downwind edges for four different gap sizes: 100 m, 30 m, 10 m and 3 m. The simulated canopy has height of $h = 10$ m and a leaf area density of $a = 0.1$ m^{-1}. The canopy top is shown by the solid black line.

3.4 Discussion

Using the BLASIUS wind flow model, spatial patterns of wind velocities and speeds were investigated across a range of canopy and clearing width scenarios. It was found that the clearing width produced the most pronounced differences in the observed dynamics. Canopy characteristics such as height and leaf area density had a second-order effect on these dynamics, predominantly influencing the strength and extent of velocity gradients and regions of reversed flow. The following section discusses the implications and limitations of these results. It ends with a discussion on the potential modifying effect of gap width and canopy structure on the spatial distribution of snow accumulation across a discontinuous boreal forest landscape.

In their modelling study of canopy flow, Belcher et al. (2003) described a series of characteristic adjustment zones as wind flows through a forest canopy (see section 2.3.2.1 for further details). We see all of these exhibited in the case of the largest clearing simulated (Figure 3.8).

As the flow exits the first canopy section the horizontal velocity increases and just beyond the edge there is a downward movement of air, to conserve mass (Exit region (E); see Figure 3.8). A region of flow recirculation on exiting the canopy was observed with all four clearing sizes (shown by the directional streamlines in Figure 3.9), a feature also observed by a number of other studies ((Bergen 1975, Cassiani et al. 2008, Detto et al. 2008, Banerjee et al. 2013)). The 100 m gap was sufficiently long that the flow had adjusted to the new boundary condition before decelerating ahead of the next canopy edge (Impact region (I); Figure 3.8). Within the canopy adjustment zone (A) we see the effect of the canopy drag decelerating the horizontal flow and the associated upward movement of air to conserve momentum. There was insufficient distance within the narrower gaps (i.e. < 100 m) for the flow to readjust to the new lower boundary condition. As a result, the perturbation to the canopy

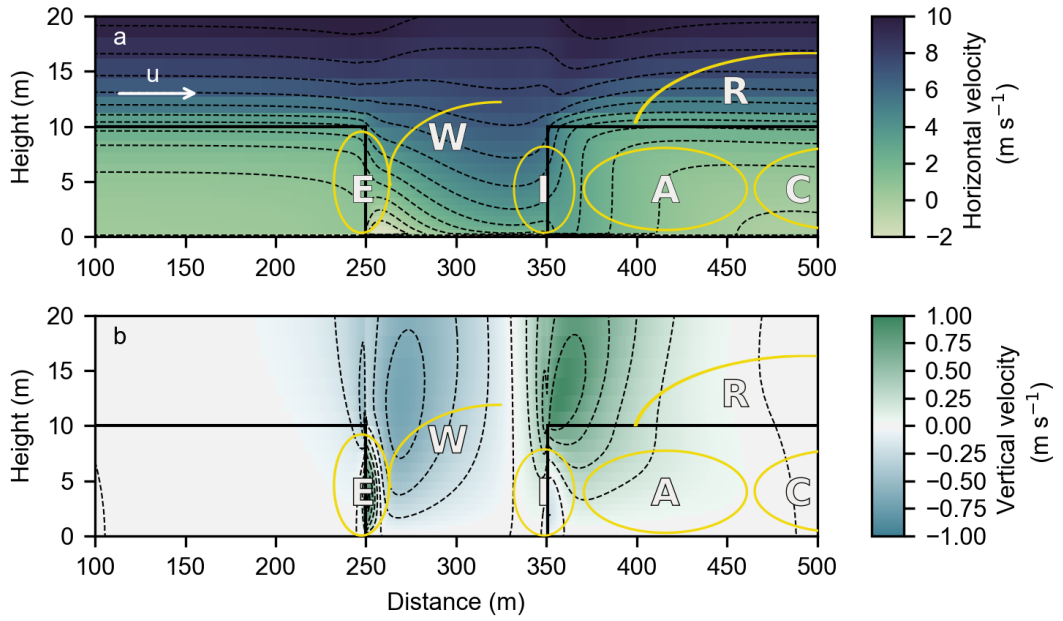

Figure 3.8: Contour plots of the evolution of the (a) horizontal velocity, and (b) vertical velocity across a 100 m forest clearing. The simulated canopy has height of $h = 20$ m and a leaf area density of $a = 0.4$ m^{-1}. The canopy extent is shown by the solid black lines. The driving wind velocity at the upper boundary = 20 m s^{-1} and flows from left to right. Overlain are yellow lines representing a schematic of the adjustment of the flow as it exits and enters the canopy (adapted from Belcher et al. 2003), showing the: adjustment region (A); canopy flow region (C); exit region (E); impact region (I); roughness change region (R); wake region (W).

wind flow was smaller and we do not see all of the same well-defined zones described above.

Dupont et al. (2011) observed a jet of faster moving air close to the ground in canopies where the foliage is concentrated in the upper canopy levels (e.g. in pine forests). This was not observed here as the BLASIUS model assumes constant leaf-area density with height, which does not allow for such flow features to form (although a canopy displacement height is specified and may be varied by the user). Boreal forests are typically comprised of such tree species as spruce, pine, fir, birch and aspen. Some of these species, such as spruce and fir, have a relatively low vertical variation in leaf area density and so the way that the canopy is represented by the model as a homogeneous column is fairly realistic. Broadleaf trees such as birch and aspen do not maintain their foliage over winter but this is less problematic as it is a spatially

complete loss of foliage so that a very low leaf area density could be applied uniformly over the vertical canopy space. However, as mentioned, pine trees tend to have a more variable vertical distribution of foliage, with greater leaf area density in the upper levels of the canopy. Therefore the spatial patterns described in this study may not be a complete description of wind flow in forest canopies with a high vertical variation in foliage distribution. Significantly, the area of reversed flow observed here in the canopy gaps could be expected to be weakened or absent in canopies with a sparse trunk space where there is less aerodynamic drag on the wind flow (compared to higher up in the canopy) and therefore a weaker contrast between canopy and gap conditions at this height.

Canopy height and canopy density both impacted on the flow across the canopy gap, however they did not change the first-order flow dynamics observed across the gaps in the first experiments. Increasing the canopy height serves to accentuate the region of reversed flow, so that it now extends over most of the 100 m gap (Figure 3.10). There is also a more pronounced region of downward air flow at the entrance to the second canopy section. Finally, the faster above-canopy wind speeds are not drawn as deeply down into the gap with a taller canopy.

The spatial patterns are broadly similar across the canopies with differing leaf area density but the spatial gradients in vertical velocity are more pronounced with higher a and the overall wind speeds are slightly greater across the domain when a is lower (Figure 3.11).

The canopies modelled here are uniform homogeneous canopies either side of the gap. This is a simplification and does not reflect natural variations in canopy metrics such as height and leaf area density that are likely to occur in real-life forests, and particularly so in mixed-species forests. It is possible with the model used here to vary the canopy metrics horizontally to represent a more heterogeneous canopy. However, as seen in the modelling results, the 3 m gap, which is of a similar horizontal length

scale to variations we may expect in a natural canopy, has very little influence on the wind flow pattern. As such, it is reasonable to suggest that variations at the individual tree level are unlikely to significantly alter spatial patterns in the modelled wind velocities seen here. A potential avenue for future work would be to consider how larger patches of canopy with varying structures would influence the wind flow patterns observed from the model runs described here.

This study only considered scenarios with a single canopy gap; it would be interesting to explore how multiple gaps, with varying distances between them, would alter the flow and potentially modify the effect of further downwind gaps. It would be expected that a minimum distance between gaps would be needed in order to see any additional effects on the flow behaviour, as it has been shown in this study that the effect of the gap reduces with decreasing gap size and so the converse may be expected that a case where there is a narrow section (e.g. < 10 m) of canopy between two gaps may not look significantly different to a case where there is a single gap of a size equivalent to the two smaller gaps. This is relatively unexplored in the literature and previous studies into this predominantly focus on investigating wind flow through vineyards, which are of a smaller scale in terms of canopy height, in addition to gap width and spacing, compared to typical canopy and linear disturbance structures in boreal forests (Weiss & Allen Jr 1976, Chahine et al. 2014).

The scenarios modelled in this chapter are simplified versions of real-life forest clearings. One simplification is that the horizontal wind flow direction is perpendicular to the line of the canopy-clearing edge. In reality, the likelihood is that the horizontal wind direction at any given time will be oblique to the line of the canopy-clearing edge. Consequently, the distance the wind flows through the clearing rather than the canopy would be lengthened, by a factor equal to $\frac{1}{\cos\theta}$ (Figure 3.12), where θ is the angle between the wind direction and a line perpendicular to the canopy edge. For instance, the effective path length of a parcel of air travelling through a 10 m gap is

10 m when the wind direction is at an angle of 0° to the line perpendicular to the canopy edge, whereas it becomes 29.24 m when the wind direction is at an angle of 70°.

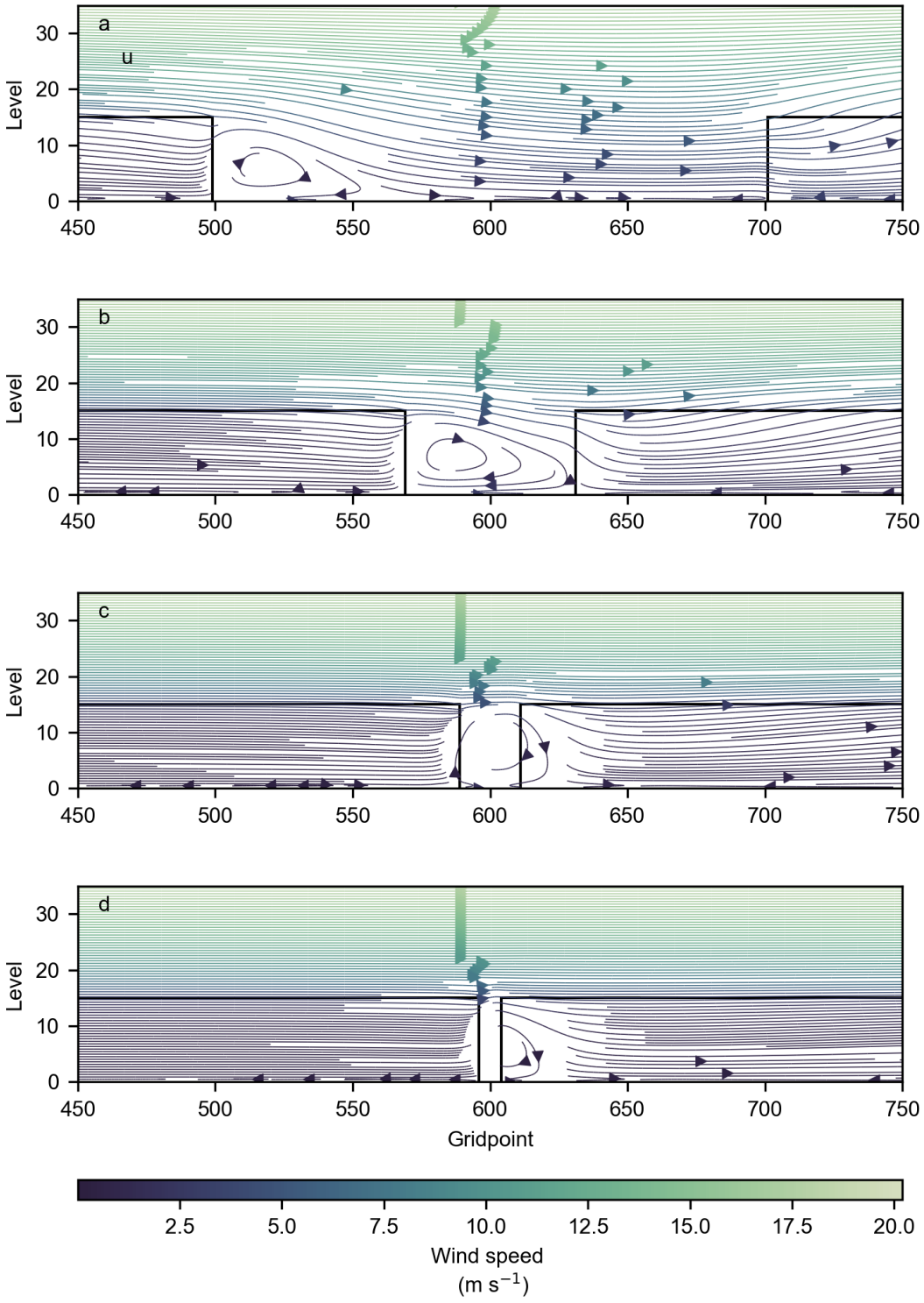

Figure 3.9: Streamplots indicating wind flow direction (arrows) and speed (colour) across forest clearings for four different gap sizes: (a) 100 m; (b); 30 m; (c) 10 m; and (d) 3 m. The simulated canopy has height of $h = 10$ m and a leaf area density of $a = 0.4$ m^{-1}. The canopy extent is shown by the solid black lines. The driving wind velocity at the upper boundary = 20 m s^{-1} and flows from left to right.

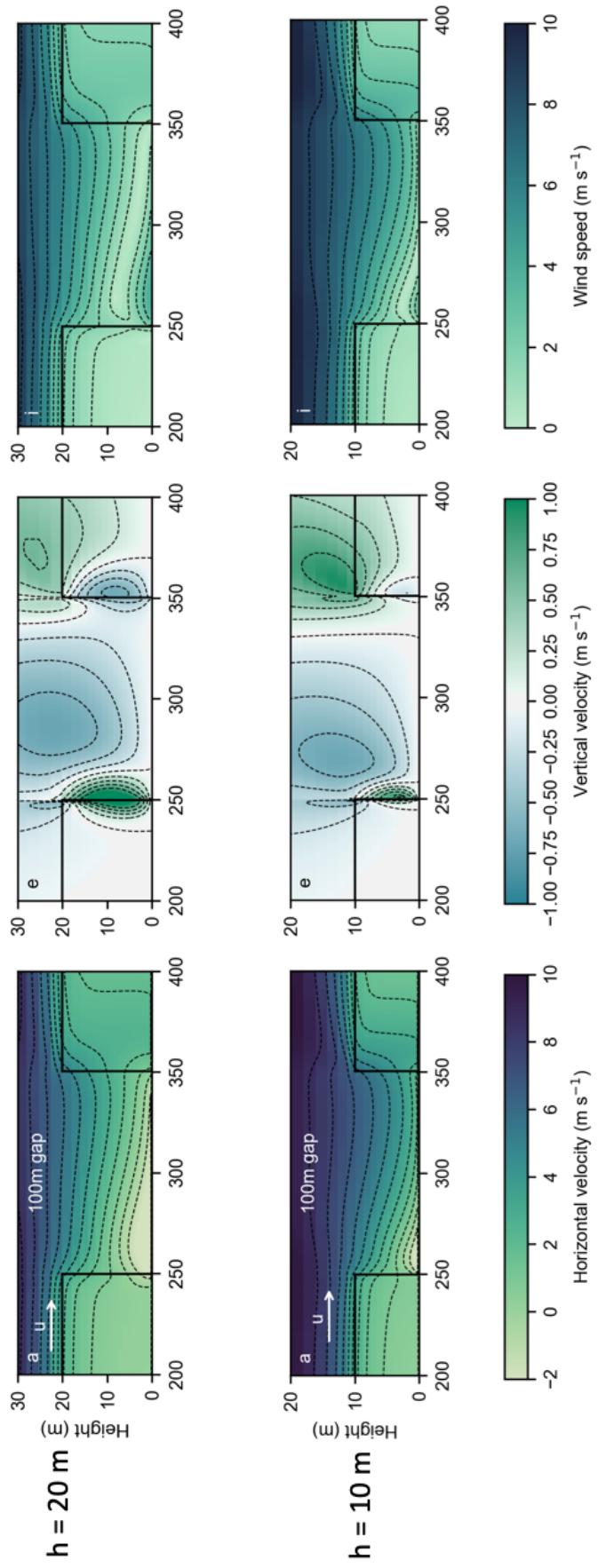

Figure 3.10: Impact of canopy height on wind flow dynamics across a 100 m gap. The top panels show horizontal velocities, vertical velocities and wind speeds across a forest gap with a canopy height of 20 m. The lower panels show the same but for a 10 m high canopy. The canopy extent is shown by the solid black lines. The driving wind velocity at the upper boundary = 20 m s^{-1} and flows from left to right. The dashed black lines are isolines of constant velocity or speed. The horizontal scale is such that 1 grid point = 0.5 m and the vertical resolution decreases with height non-linearly.

Figure 3.11: Impact of canopy density on wind flow dynamics across a 100 m gap. The top panels show horizontal velocities, vertical velocities and wind speeds across a forest gap with a canopy leaf area density of 0.1 m^{-1}. The lower panels show the same but for a canopy with a leaf area density of 0.4 m^{-1}. The canopy extent is shown by the solid black lines. The driving wind velocity at the upper boundary = 20 m s^{-1} and flows from left to right. The dashed black lines are isolines of constant velocity or speed. The horizontal scale is such that 1 grid point = 0.5 m and the vertical resolution decreases with height non-linearly.

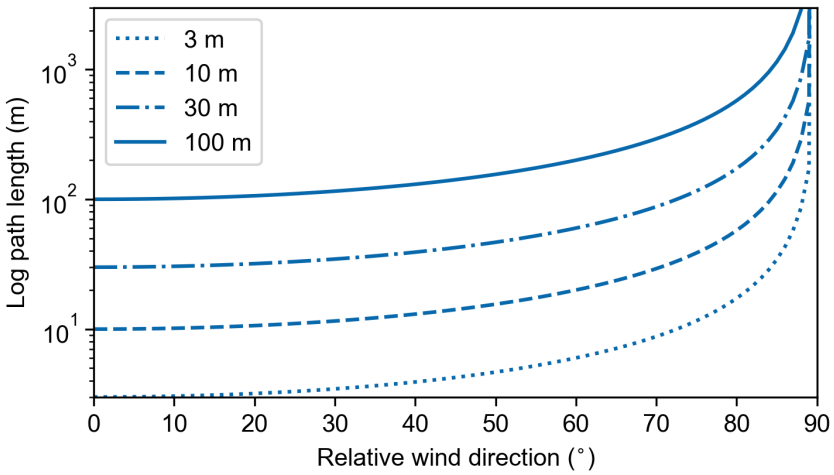

Figure 3.12: Log path lengths travelled by the wind across four different clearing widths (100 m, 30 m, 10 m and 3 m) depending on the wind direction relative to the line of the canopy edge. A relative wind direction of 0° corresponds to flow perpendicular to the edge; a relative wind direction of 90° flows parallel to the edge and travels through the clearing only

3.4.1 Implications for snow transport across canopy clearings

In boreal forests, one way in which clearings may potentially impact on the surrounding environment is through changes in the spatial distribution of snow on the forest floor due to altered wind flow dynamics. Of particular interest for this research project was to further our understanding of the forest clearing scenarios in which we can expect wind-driven movement of snow. The wind modelling described in this chapter can be used to indicate the situations where we might expect snow redistribution to occur and, conversely, where we might expect to observe deposition of wind-blown snow.

Surface friction velocity may be calculated from simulated surface stresses as

$$u_\star = \sqrt{\frac{\tau}{\rho}} \tag{3.2}$$

where ρ is the air density (kg m^{-3}) and τ is the magnitude of the wind shear stress at the surface (kg m^{-1} s^{-2} = Pa).

Figure 3.13 shows modelled friction velocities for all the gap and canopy structure scenarios presented in the results section of this chapter (Section 3.3). Also shown are example threshold friction velocities for snow transport (green lines in Figure 3.13) calculated using formulations in Liston et al. (2007). The thresholds are dependent on the snow density, such that surface snow with the lowest density (e.g. fresh, uncompacted snow) requires the least applied stress for movement to occur (see Table 3.2 for common snow densities). For snow densities between 50 – 300 kg m^{-3}

$$u_{\star t} = 0.10 \exp(0.003\rho_s), \text{ if } 50 < \rho_s \leq 300 \tag{3.3}$$

where $u_{\star t}$ is the threshold friction velocity and ρ_s is the snow density. For higher snow

densities:

$$u_{\star t} = 0.005 \exp(0.013 \rho_s), \text{ if } 300 < \rho_s \leq 450 \tag{3.4}$$

Snow type	Density (kg m^{-3})
New snow	50–70
Damp new snow	100–200
Settled snow	200–300
Wind packed snow	350–400

Table 3.2: Common densities of snow (values from Paterson (1994))

In the 100 m gap scenario (Figure 3.13.a.) with h = 10 m and a = 0.4 m^{-1} (case 1) there is the potential for transport of fresh snow just after the first canopy edge and into the gap, although this spike in the friction velocity is followed by a very low trough suggesting that any snow movement would cease soon after it was initiated. The friction velocity rises again towards the downwind side of the gap and just crosses the threshold for 100 kg m^{-3} density snow. Into the second canopy section the friction velocity increases further and exceeds the threshold for 200 kg m^{-3} snow, suggesting movement of snow further into the canopy interior where the modelled friction velocity decreases and falls below the 100 kg m^{-3} density threshold after approximately 40 m from the canopy edge.

A similar pattern is seen with a lower leaf area density (case 2: h = 10 m, a = 0.1 m^{-1}) although in this instance the friction velocity following the first (upwind) canopy edge is too low to suggest any snow movement. However, at the downwind side of the gap and into the second canopy section the modelled friction velocities exceed those observed in case 1 with a higher leaf area density. This implies that movement of older, wet or compacted snow may occur just into the canopy on the downwind side and that this effect extends at least 100 m into the canopy interior.

With a taller canopy (case 3: h = 20 m, a = 0.4 m^{-1}), movement of snow is most likely in the gap just after the first canopy edge and across the first half of the gap. Movement of low density snow may be expected just into the downwind canopy,

further in than with the 10 m canopies and for a shorter distance.

As observed with the modelled wind velocities, the influence of a canopy gap on snow movement reduces as it's width narrows. With a 30 m gap, snow transport may be expected within the gap for the canopies with a leaf area density of 0.4 m^{-1} (case 1 & 3) and in the downwind canopy section approximately 45 m after the edge for the canopy with a lower leaf area density (case 2). Only the modelled friction velocities with the case 1 canopy are high enough to suggest some movement of low density snow when the gap is 10 m across and no movement of snow would be expected in the case of a 3 m gap for all canopy types modelled here.

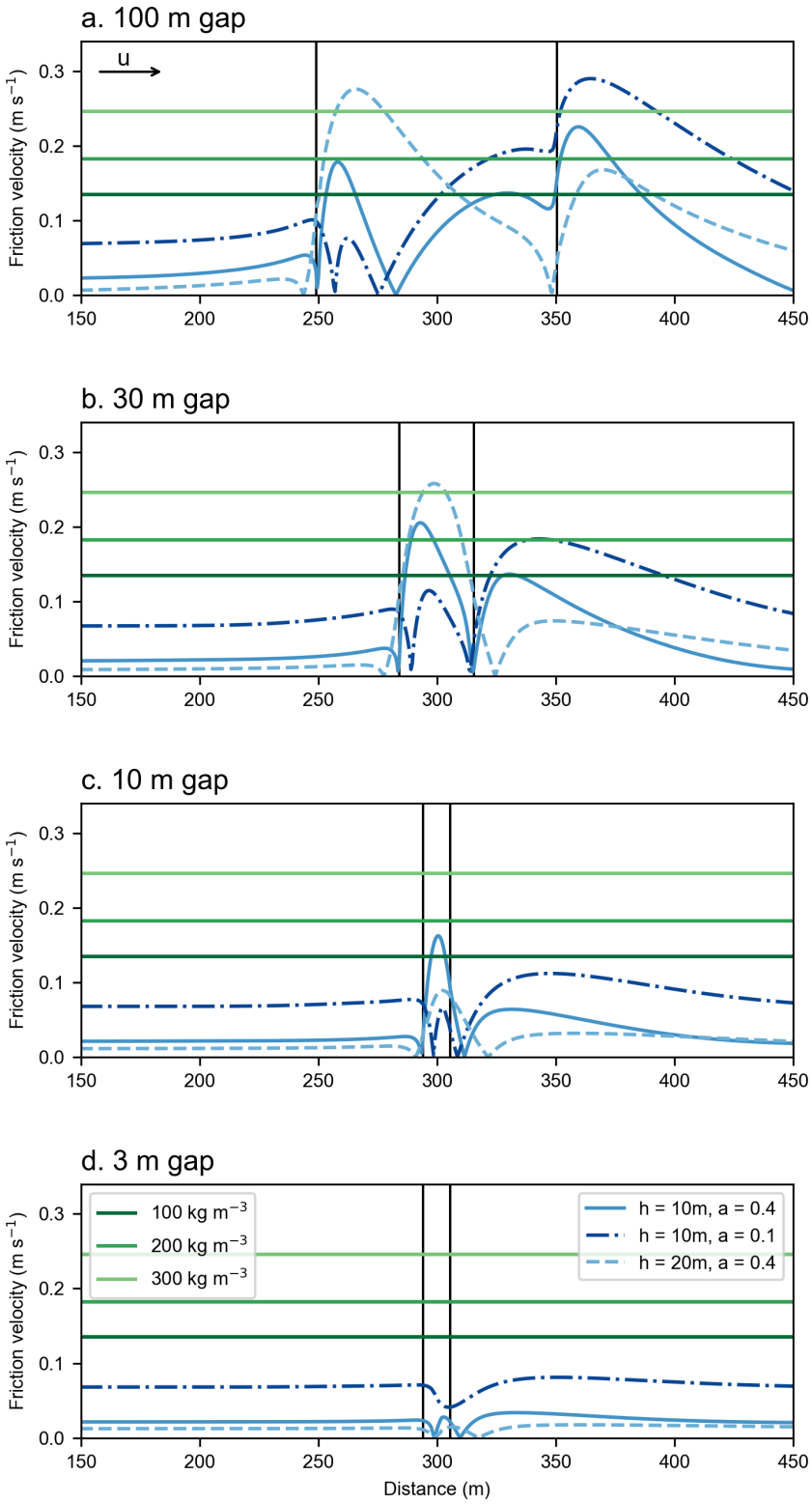

Figure 3.13: Modelled friction velocities for all gap and canopy structure scenarios. The green lines refer to snow density dependent threshold friction velocities for snow transport as proposed by Liston et al. (2007). The wind is flowing from left to right and the solid black vertical lines indicate the canopy edge.

3.5 Conclusion

In this chapter I used a wind flow model (BLASIUS) to simulate patterns of wind flow across forest discontinuities and showed that the clearing width is a key influence on these dynamics.

Sub-canopy wind flow is modified by the presence of a forest gap and sufficient distance (approx. 100 m) is required for the wind flowing across the gap to adjust to the change in the boundary conditions. A region of reversed flow as the wind enters the gap was found for all gap widths. Within the 100 m gap, the wind speed then increases with distance across the gap until it is slowed by the presence of the downwind canopy edge. Narrow gaps ($<$30 m wide) have less impact on sub-canopy wind speeds as there is insufficient distance for the flow to fully adjust. The influence of a forest gap on sub-canopy wind dynamics becomes negligible for very narrow gaps (approx. 3 m wide).

Canopy characteristics have a second-order effect on the wind flow dynamics across the gap. Taller trees accentuate the region of reversed wind flow and faster flowing air above the canopy is not drawn down as deeply down into the gap. A denser forest canopy results in greater vertical velocities at the canopy edges. Reducing the canopy density results in higher overall wind speeds across the domain.

These wind flow scenarios can also be used to explore the potential for wind-driven transport of snow within forest discontinuities. The results presented here suggest that canopy and clearing structures could play a role in the spatial distribution of snow accumulation through modified wind flow dynamics.

Chapter 4

Data collection and calibration of the BLASIUS wind flow model

4.1 Introduction

The previous chapter considered how wind flow through a simulated forest canopy may be affected by a linear clearing of varying width and surrounding canopy structure, using the BLASIUS wind model. Following on from this, this chapter aims to evaluate the ability of the BLASIUS model to represent flow across a real forest edge and to obtain a scaling relationship between measured above-canopy wind speeds and modelled sub-canopy wind speeds and surface friction velocity.

It is important to understand wind flow in boreal forest ecosystems for a number of reasons: firstly, wind blown transport of snow creates areas of relatively deeper and shallower snow, which impacts the timing of snow melt (onset and rate) (Pomeroy et al. 1998, Essery & Pomeroy 2004, Gelfan et al. 2004, Liston & Elder 2006, Essery et al. 2009). When and how quickly snow melts influences hydrological processes, such as river flows and permafrost thaw (Pomeroy & Granger 1997, Williams et al.

2013), and ecological processes, such as photosynthesis (through the availability of soil moisture) (Black et al. 2000, Wipf et al. 2009, Trujillo et al. 2012). Wind flow dynamics also have the ability to determine the spatial and temporal spread of forest fires and airborne particles, including seed dispersal (Coen 2005, Dupont et al. 2006, Sun et al. 2009, Conan et al. 2015). Finally, trees proximal to forest edges may be subject to wind-driven damage, depending on the magnitude of wind speeds and gusts (Dupont & Brunet 2006, 2008*b*, Dupont et al. 2015, Panferov & Sogachev 2008, Schwartz et al. 2017). It is therefore of interest to be able to predict wind speeds in boreal forest settings for a wide number of applications.

To understand how changes in wind flow influence local snow dynamics across forest edges it is necessary to couple a model of wind dynamics with a model that describes the important processes of snow redistribution and melting (e.g. FSM2 (Mazzotti et al. 2020a)). The wind flow model used in this thesis (BLASIUS) is computationally expensive (run-time $\approx$ 1-2 days+ depending on domain size and resolution), which presents a challenge to coupling it with other models. One solution to this general problem is to develop emulators of complex models that capture key relationships in a way that is more readily transferable.

The research questions driving this chapter are as follows:

1. How reliably may field measurements of wind speed across boreal forest edges be reproduced by the BLASIUS wind flow model?

2. How do sub-canopy wind speeds and surface friction velocity across heterogeneous forest landscapes scale with above-canopy wind speeds, as would be measured at a meteorological tower? Can we emulate sub-canopy wind speeds from BLASIUS with a simpler model that captures the fundamental characteristics of the airflow?

To this purpose, the BLASIUS wind flow model is calibrated and evaluated using

observational wind speed and canopy structure data collected from a forest-edge site in northern Finland.

First, the field sites and data collection methods are presented (Section 4.2). Then the model is calibrated and evaluated against field measurements (Section 4.3). The results are then discussed, including the scaling of modelled sub-canopy wind speeds and surface friction velocity to measured above-canopy wind speeds (Section 4.4) and conclusions presented (Section 4.5).

4.2 Methodology

4.2.1 Data collection

4.2.1.1 Field site description

Field measurements were made during April 2016 at the Arctic Research Centre of the Finnish Meteorological Institute (FMI-ARC), which is located in northern Finland at 67.368° N, 26.633° E (approx. 180 m a.s.l.). FMI-ARC is adjacent to the Kitinen River and is situated approximately 7 km south of the nearest town of Sodankylä and 90 km north of the arctic circle (Fig. 4.1.a). The topography is relatively flat and the predominant land cover types comprise boreal forest (dominated by Scots pine (*Pinus sylvestris*) and open peat bog to the east of the site. Continuous meteorological measurements have been made at FMI-ARC since 1908 and instrumentation includes an automatic weather station and radiometer tower (Kivi et al. 1999). Typically, there is snow cover on the ground between October and May, with mean monthly air temperatures < 0°C between November and April, although temperatures can fall < -40°C during the winter (Leppänen et al. 2016). Mean annual precipitation is 527 mm and between 1951–2000 the annual maximum snow depth varied between

62–119 cm, with a median of 83 cm (Essery et al. 2016). Wind speeds are generally low, particularly in forested areas; the monthly mean above-canopy wind speeds range between 2.5–2.9 m s^{-1} and a mean wind speed of 1.17 m s^{-1} was measured over two years during the snow season (mid-September – mid-May) (Leppänen et al. 2016).

Four sites at FMI-ARC were identified as suitable for taking measurements of wind speeds and directions with the purpose of investigating wind behaviour across forest edges: (i) Bog site (67.367° N, 26.647° E); (ii) Road site (67.366° N, 26.635° E); (iii) Forest track site (67.370° N, 26.629° E); (iv) Clearing site (67.362° N, 26.633° E). The measurement sites and their locations are shown in Fig. 4.1 and a brief description of each follows:

4.2.1.2 Bog site

The bog site is within an area of open wetland that is located approximately 1 km east from the main station at FMI-ARC (Fig. 4.1). The water level varies according to precipitation levels and time of year, and snow tends to accumulate on top of a smooth ice layer (Leppänen et al. 2016). As this site is relatively open, redistribution and levelling of snow by the wind often occurs (Leppänen et al. 2016). At the time of measurements, snow depths at this site ranged between 37 – 72 cm, with a mean of 51 cm. A transect was established running approximately north-west from the open bog into a patch of Scots pine and birch (*Betula spp.*) trees (mean canopy height = 5.82 m), with four measurement points along this line (as shown in Fig. 4.2).

The canopy was considered as two sections to reflect the difference in canopy density; the canopy was noticeably sparser in the first 62 m (looking left to right) and so needed to be treated differently to the rest of the canopy patch within the model (through a lower leaf area density and canopy drag coefficient). Figure 4.3 provides a

Figure 4.1: Top: Aerial photograph of FMI-ARC indicating the locations of the study sites and the meteorological mast (yellow dots); inset map showing the location of FMI-ARC (red dot) in Finland. Middle and bottom: Photographs of the four study sites.

more detailed look at the bog site and illustrates the differences between the canopies. Panel (a) shows the canopy as if standing on the left hand side of the schematic in Figure 4.2 and looking towards the canopy patch; (b) shows measurement position K2, which is at the edge of the sparser Canopy 1 section; and (c) shows position K3,

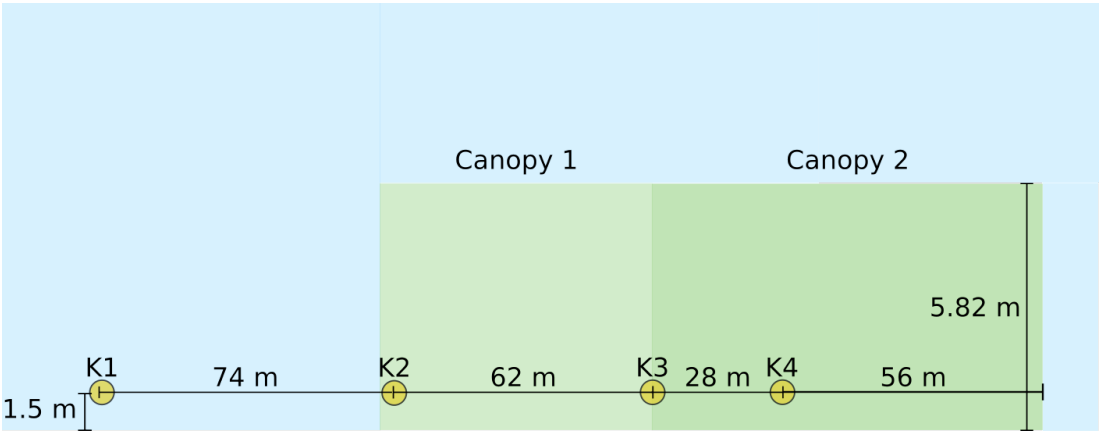

Figure 4.2: Bog site instrumentation setup. Wind measurement points are indicated by the yellow circles and labelled K1–4. The canopy was considered as two distinct sections to account for differences in the canopy density (Canopy 1 was sparser than Canopy 2).

which is located at the transition point between the two canopy sections and looks into the denser Canopy 2 section.

Figure 4.3: Photographic illustration of the difference between the two canopy sections at the bog site. The bog site is shown in (a), looking towards the canopy patch (as if standing on the left hand side of the schematic in Figure 4.2). Measurement position K2 is shown in (b), which is at the edge of the sparser Canopy 1 section, and (c) shows position K3, which is located at the transition point between the two canopy sections and looks into the denser Canopy 2 section.

4.2.1.3 Road site

The measurement transect at this site spanned the main entrance road to the FMI-ARC station, which runs broadly NE-SW and joins onto the main road to the nearest town of Sodankylä. Working with the limitation of a set number of instruments (four anemometers) it was determined that the optimal set up was as follows: two measurement points located on the transect within the planted Scots pine forest (mean canopy height = 11.34 m) on either side of the road and the remaining two instruments located at each edge of the canopy, where the trees meet the road (Fig. 4.4). The distance between the two edge measurement points (i.e. traversing the road) is approximately 19 m.

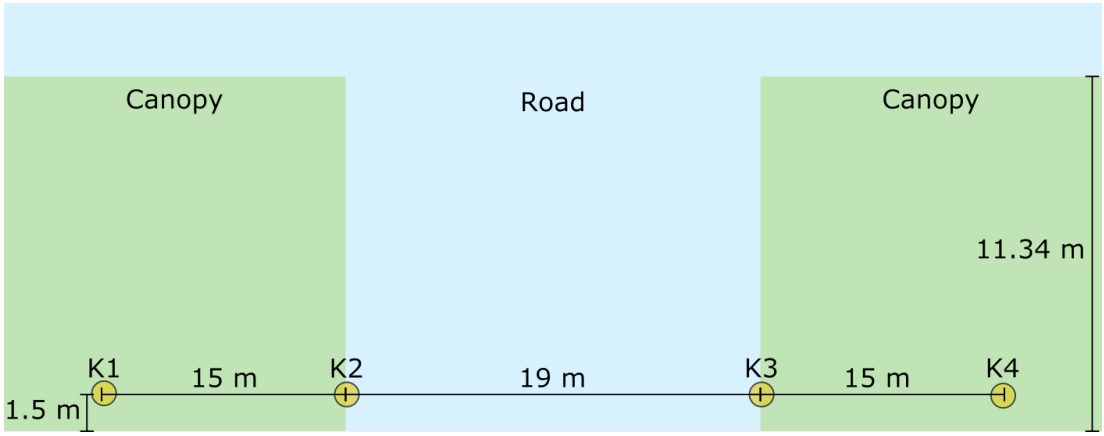

Figure 4.4: Road site instrumentation setup. Wind measurement points are indicated by the yellow circles.

4.2.1.4 Forest track site

Here a measurement transect was established across a narrow track and through a section of planted Scots pine forest (mean canopy height = 12.24 m) with similar canopy characteristics to that at the road site but more extensive in ground area. As at the road site, measurement points were positioned at the canopy edge and 15 m into the canopy on either side (Fig. 4.5). There is a distance of 7.35 m between the two edge measurement points (i.e. traversing the track).

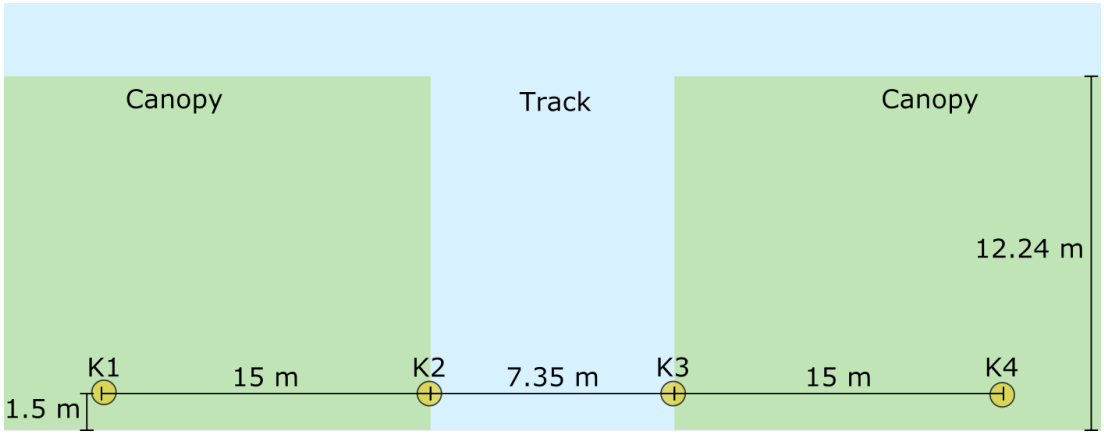

Figure 4.5: Forest track site instrumentation setup. Wind measurement points are indicated by the yellow circles

4.2.1.5 Clearing site

The clearing site is co-located with the FMI-ARC Intensive Observation Area (IOA), a ∼40 m diameter forest clearing that was established in 2006 for conducting snow and meteorological measurements and experiments (Leppänen et al. 2016). The IOA is surrounded by sparse pine forest and is relatively sheltered, so very little wind-driven redistribution of snow occurs. However, this site was chosen as an example of wind flow across a larger size gap in contrast to the narrower openings in the road and forest track sites. The transect at this site was positioned on the northern side of the clearing and so measurements were predominantly of wind entering the canopy, as the prevailing wind direction is from the south. The measurement transect began at the approximate edge of the sparse canopy (mean canopy height ≈ 7.9 m), with the remaining three measurement points located every 15 m along a line perpendicular to the edge and progressing into the trees (see Fig. 4.6).

4.2.1.6 Wind measurements

Wind speed and direction was measured using four commercially available anemometers: three Kestrel 4500 Weather Meters and one Kestrel 5000 Weather Meter

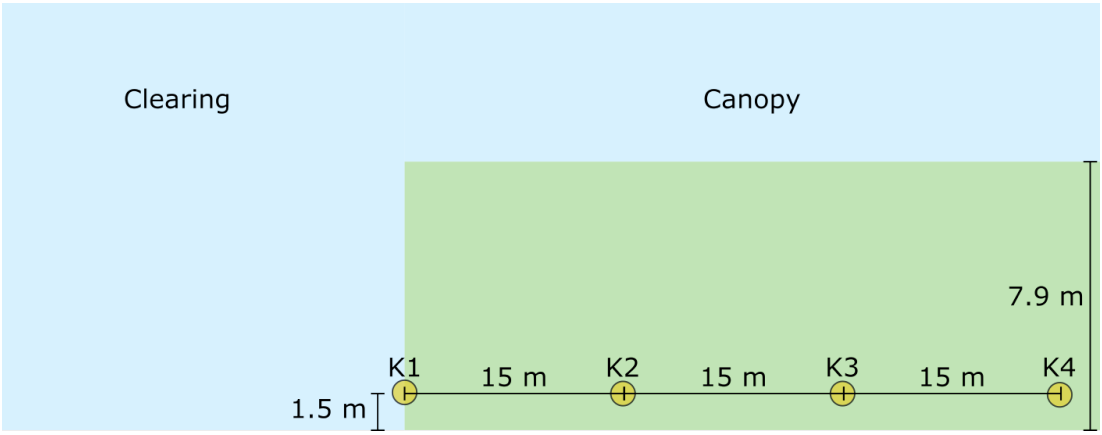

Figure 4.6: Clearing site instrumentation setup. Wind measurement points are indicated by the yellow circles.

(Nielsen-Kellerman, Boothwyn, PA, USA) (Fig. 4.7). The difference in models used was due to stock availability at the time. Each anemometer was mounted on a tripod at a height of 1.5 m (the maximum tripod height) and positioned along the transects described above. Wind speeds were measured by a lightweight impeller, which can operate at low speeds (> 0.6 m s^{-1} (4500 model) or > 0.4 m s^{-1} (5000 model)) and with an accuracy of $\pm$ 0.1 m s^{-1}. The anemometers were fitted with a vane mount and contain an internal compass, comprising a two-axis solid-state magnetoresistive sensor mounted perpendicular to the unit plane with a $\pm$ 5° resolution (NK n.d.). The measured wind direction indicates the direction in which the back of the unit is pointing (when held vertically upright), i.e. the direction from which the wind is blowing. It should be noted that one of the Kestrel 4500 models was unable to record wind direction readings for the duration of this field work. This was taken account of when deciding where to place the instruments along the transects, so that the wind direction was always measured at the canopy edges.

Wind speed and direction measurements were taken automatically every minute. The instruments were checked and data manually downloaded every 24 – 48 hours. Very occasionally the impellers froze overnight but as wind speeds are very low at this time of day, the impact of this on the data collection may be considered negligible. Table 4.1 shows the data collection periods for each of the four measurement sites.

Figure 4.7: A Kestrel 4500 Weather Meter in the field, showing the impeller and weather vane components that are used to measure wind speed and direction, respectively.

4.2.1.7 Canopy measurements

Information about the canopy structure was obtained via measurements of:

- Canopy height (all sites)
- Crown base height (road and forest track sites)
- Crown diameter (road and forest track sites)
- Diameter at breast height (road and forest track sites)
- Tree stocking density (road and forest track sites)

Heights were measured using a Haglöf Vertex III Hypsometer and Transponder T3 (Fig. 4.8), which obtains distances using ultrasonic signals and calculates heights trigonometrically (Haglöf Sweden, Långsele, Sweden). To measure the height of a tree, the transponder (an ultrasonic transmitter/receiver) is first positioned on the trunk at breast height (1.3 m) and the vertex hypsometer sighted to the transponder to measure this distance, then the vertex hypsometer is sighted to the canopy top to obtain the height. The heights of all trees within 2.5 m either side of the transect lines were measured and six height measurements were taken per tree in order to calculate

the mean height for each tree, to which the snow depth at the tree was added to account for the additional height below the surface. The height of the base of each individual tree crown was also measured following this method, taking the crown base to be the height on the tree trunk of the lowest live branch whorl that forms part of the canopy (Forestry Commission 2014*b*). As the air-temperature affects the range of the ultrasonic signals used to determine distances, the vertex hypsometer was allowed at least 10 minutes after removal from a bag or pocket to reach the ambient air temperature before taking measurements, as per the instruction manual advice (Haglöf Sweden n.d.). Furthermore, the instrument was calibrated before each measurement session by manually measuring out a 10 m distance between the vertex hypsometer and the transponder with a tape measure and ensuring that this distance was measured correctly by the vertex hypsometer. The crown diameter of each tree within 2.5 m either side of the transect line was calculated from visual measurements of its extent along a north-south bearing and an east-west bearing (Forestry Commission 2014*b*). The trunk circumference of these trees were measured using a tape measure around the trunk at breast height (1.3 m) (Forestry Commission 2014*a*). To give a measure of tree stocking density, the number of trees were counted within a 15 x 15 m area straddling the transect line on either side of the clearing at the road and forest track sites.

Figure 4.8: The Vertex III Hypsometer and Transponder T3, which were used for measuring tree heights (Haglöf Sweden n.d.)

4.2.2 Model calibration and validation

The BLASIUS wind model is as described in detail in Chapter 3.2.1, and was run with a model domain of length 750 m and a height of 100 m. As with the model runs in Chapter 3, the horizontal resolution is 0.5 m and the model grid is stretched in the vertical by a factor of 1.05 to give higher resolutions closer to the surface (the lowest grid point is at $z = 0.15$ m). The model parameters focused on for calibrating the model are shown in Table 4.2. The calibration and validation of the BLASIUS model was performed using two sets of wind speed data:

1. 10-minute wind speeds, measured at the meteorological mast at FMI-ARC (see figure 4.1 for location). These measurements were taken automatically by a Vaisala WA25 sensor at a height of 48 m (data available here: `http://litdb.fmi.fi/met0002_data.php`) . For the purposes of model calibration and validation, the wind speeds were averaged over a 30-minute period. The average wind speed for a given 30-minute interval was then used to calculate the driving wind speed in the model (described in further detail below).

2. Wind speeds measured every minute by the anemometers described in section 4.2.1.6. These wind speeds were also averaged over a 30-minute period and then compared against modelled wind speeds at the same height of $z = 1.5$ m.

The driving wind speed in the model is prescribed by the parameter $utop$, which is the horizontal velocity component at the top of the model domain (which is at a height of $z = 100$ m in this case). The log wind profile (Eq. 4.1) was used to calculate the expected wind speed at $z = 100$ m based on the wind speed measured at $z = 48$ m on the meteorological mast (Eq. 4.2).

$$\bar{u}(z) = \frac{u_*}{\kappa} ln \frac{(z-d)}{z_0} \tag{4.1}$$

Where $\bar{u}(z)$ is the wind speed at height z, u_* is the friction velocity, κ is the von Karmen constant (0.4), d is the zero plane displacement and z_0 is the roughness length. The zero plane displacement may be calculated as $d = 0.76h$, where h is the canopy height (Jarvis et al. 1976). Values of $h = 15$ m and $z_0 = 0.55$ m were used, based on values used by Essery et al. (2016) as representative of the pine forest at FMI-ARC. Equation 4.1 was written to find the 100 m wind speed as the product of the 48 m wind speed and a ratio of logarithms, such that:

$$\bar{u}_{100} = \bar{u}_{48} \cdot \frac{ln(\frac{(100-d)}{z_0})}{ln(\frac{(48-d)}{z_0})} \tag{4.2}$$

where $\bar{u}_{100}$ is the wind speed at 100 m and $\bar{u}_{48}$ is the wind speed at 48 m.

It was found that when the model was run with the expected speed at $z = 100$ m it did not reproduce the observed wind speed at $z = 48$ m, i.e. the modelled wind profile was not quite a log relationship (see Appendix A.1 Figure A.1 for an example). A further step was therefore necessary, which involved adjusting the driving wind speed in 1D model runs through trial and error until the correct wind speed at $z = 48$ m was reached. This additional step allowed the model runs to be grounded in the meteorological mast observational data.

When selecting suitable 30-minute time periods from the anemometer data it was decided that the following requirements needed to be satisfied:

1. Periods of highest wind speeds for that site: the higher the measured wind speeds the clearer any canopy effects will be and the relative impact of measurement error is reduced

2. Periods where the wind is flowing in or out of the canopy: the wind flow in the Blasius model is directed perpendicular to the line of the canopy edge, therefore periods when the observed wind direction most closely resembled this

were preferable. A threshold condition was applied so that only time periods where the wind direction was within 45° of flowing perpendicular to the canopy edge were considered for use in the calibration and validation process (see Figure 4.9 for a diagrammatic explanation).

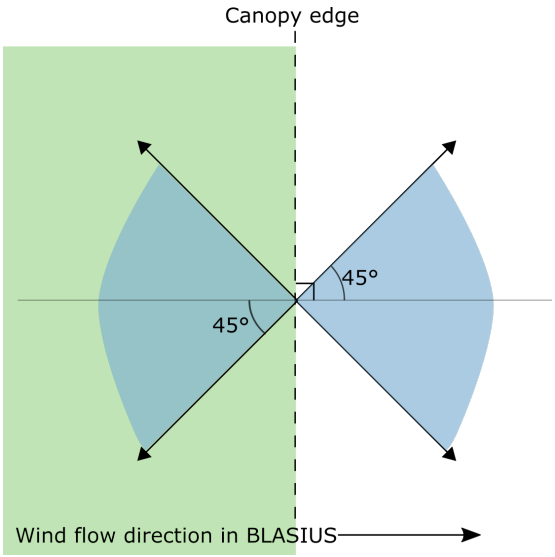

Figure 4.9: Measured wind flow was taken as entering or exiting the canopy if the wind direction was within 45° of flowing perpendicular to the canopy edge, i.e. angles of direction within the blue shaded areas in the figure.

Figures 4.10, 4.11, 4.13 and 4.12 show wind measurements taken at the four field sites (Bog, Road, Clearing and Forest track respectively). They display a subsection of the total data recorded at these sites for clarity of presentation; periods of time where wind speeds were at their highest for each site were chosen, as these were the most likely candidates for modelling. However, aside from at the Bog site (Figure 4.10), wind speeds were still typically low: wind speeds were < 2 m s^{-1} at the Road and Clearing sites (Figures 4.11 and 4.12 respectively) and < 1 m s^{-1} at the Forest track site (Figure 4.13). At the three sites with low wind speeds, it is challenging to discern clear patterns in the wind speeds along the measurement transect. Wind speeds at the Forest track, for example, were typically a little higher at the edges (Figure 4.13; Kestrel 2 & 3) than at the measurement points within the forest canopy (Figure 4.13; Kestrel 1 & 4), but the differences are small. For instance, during the period 11:00 – 16:30 on 21/04/16 at the Forest Track site (Figure 4.13), the mean wind speeds at the

track edges were 0.12 m s^{-1} at Kestrel 2 (σ = 0.14 m s^{-1}) and 0.17 m s^{-1} at Kestrel 3 (σ = 0.20 m s^{-1}), whilst within the forest the mean wind speeds were 0.06 m s^{-1} (σ = 0.11 m s^{-1}) and 0.04 m s^{-1} (σ = 0.10 m s^{-1}), at measurement points 1 and 4 respectively. However, these wind speeds were predominantly $<$0.6 m s^{-1}, which is the threshold operational speed for the Kestrel 4500 models and the differences seen between the measurement points were of a similar scale to the measurement error (0.1 m s^{-1} (NK n.d.)).

Through this exploratory analysis of the data, it was determined that the Road, Forest track and Clearing sites were not suitable for producing a meaningful calibration of the model due to wind speeds that were very low and with a relatively high level of variation (see also Figure 4.14 for wind speed distributions at each field site). Wind speeds were higher and less variable at the Bog site, so measurements taken at this site were selected for the calibration process. One 30 minute period (16:50–17:20 on 07/04/2016) was selected as a calibration data set for fitting the Blasius model to the observational data and two further 30 minute periods (18:30–19:00 and 19:30–20:00 on 07/04/2016) were used as validation data sets once the calibrated parameter set was reached. These three time periods are highlighted by the pale yellow bands in Figure 4.10.

			Mean and (max) wind speeds ($m\ s^{-1}$)			
Site	Measurement period	Hours	K1	K2	K3	K4
Bog	4–6th Apr (14:00–09:30)	43.5	0.52 (5.1)	0.70 (4.2)	0.40 (4.5)	0.22 (4.5)
	6–8th Apr (11:30–10:00)	46.5	2.83 (9.2)	2.27 (7.1)	1.01 (5.7)	0.55 (4.2)
Road	9–11th Apr (11:30–12:00)	24.5	0.22 (2.3)	0.27 (3.4)	0.19 (3.9)	0.13 (2.8)
	11–13th Apr (13:00–09:00)	44	0.28 (2.9)	0.46 (4.9)	0.34 (4.0)	0.26 (2.4)
	13–14th Apr (11:00–09:00)	22	0.41 (3.0)	0.46 (4.9)	0.37 (2.6)	0.32 (2.6)
	14–16th Apr (10:30–10:00)	47.5	0.39 (2.5)	0.37 (4.0)	0.39 (3.7)	0.35 (2.8)
Forest track	16–18th Apr (15:30–08:30)	41	0.08 (2.3)	0.25 (3.1)	0.24 (3.4)	0.12 (2.0)
	18–19th Apr (11:00–08:30)	21.5	0.02 (1.7)	0.10 (1.7)	0.07 (1.8)	0.05 (1.1)
	19–20th Apr (10:00–08:00)	22	0.02 (1.4)	0.14 (1.6)	0.10 (1.5)	0.05 (1.4)
	20th–21st Apr (10:00–09:00)	23	0.21 (2.4)	0.42 (3.0)	0.34 (3.3)	0.24 (2.3)
	21st–22nd Apr (11:00–08:30)	21.5	0.01 (0.9)	0.05 (1.3)	0.03 (1.1)	0.02 (1.2)
Clearing	22nd–24th Apr (14:30–11:00)	44.5	0.51 (3.8)	0.51 (4.0)	0.44 (3.3)	0.37 (3.1)
	24–26th Apr (14:30–07:30)	41	0.60 (5.1)	0.53 (3.9)	0.59 (4.1)	0.57 (4.3)

Table 4.1: Wind measurement periods with mean and maximum measured wind speeds for each measurement point (K1-4) at each site. See Figures 4.2, 4.4, 4.5 and 4.6 for more detail on the relative location of the anemometers at each site

Parameter	**Description**	**Source**
Z_0	Aerodynamic roughness height (m)	Selected within the range for snow recorded by Oke (1978)
UTOP	Horizontal velocity component at the domain top (the driving wind velocity) (m s^{-1})	See Section 4.2.2 (above)
CNPYHT	Canopy height (m)	Mean observed height: see Section 4.2.1.2, and Appendix A.2 for canopy height measurements
DISPHT	Canopy displacement height (m)	$0.76h$ (Jarvis et al. 1976)
CNPYCD	Canopy drag coefficient	Calibration
CNPYDN	Leaf area density (m^{-1})	Calibration

Table 4.2: Key parameters used in the calibration of the Blasius model.

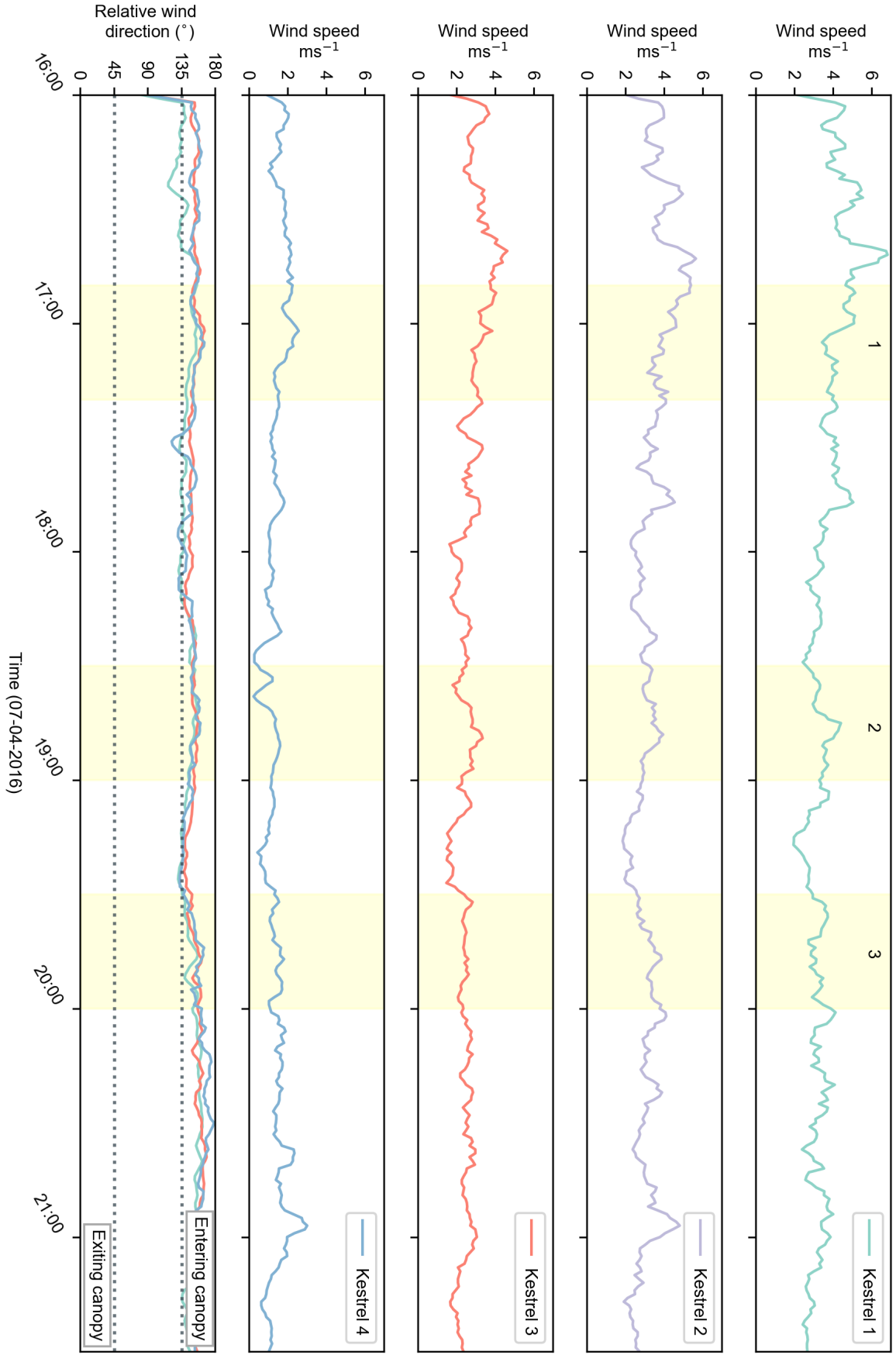

Figure 4.10: Wind speeds and directions measured at the Bog site over a 5.5 hour period on 7th April 2016. Wind speeds at each measurement point are shown separately in the first four panels and represent 5-minute moving averages. Wind directions relative to the main canopy edge are shown together in the bottom panel (directions were not measured by Kestrel 2). A relative direction of 0° corresponds to wind exiting the canopy and a relative direction of 180° corresponds to wind entering the canopy, both flowing perpendicular to the line of the canopy edge. The yellow bands highlight the 30 minute time periods used for the model calibration and validation: period 1 was used for the calibration data set; periods 2 and 3 were used as validation data sets.

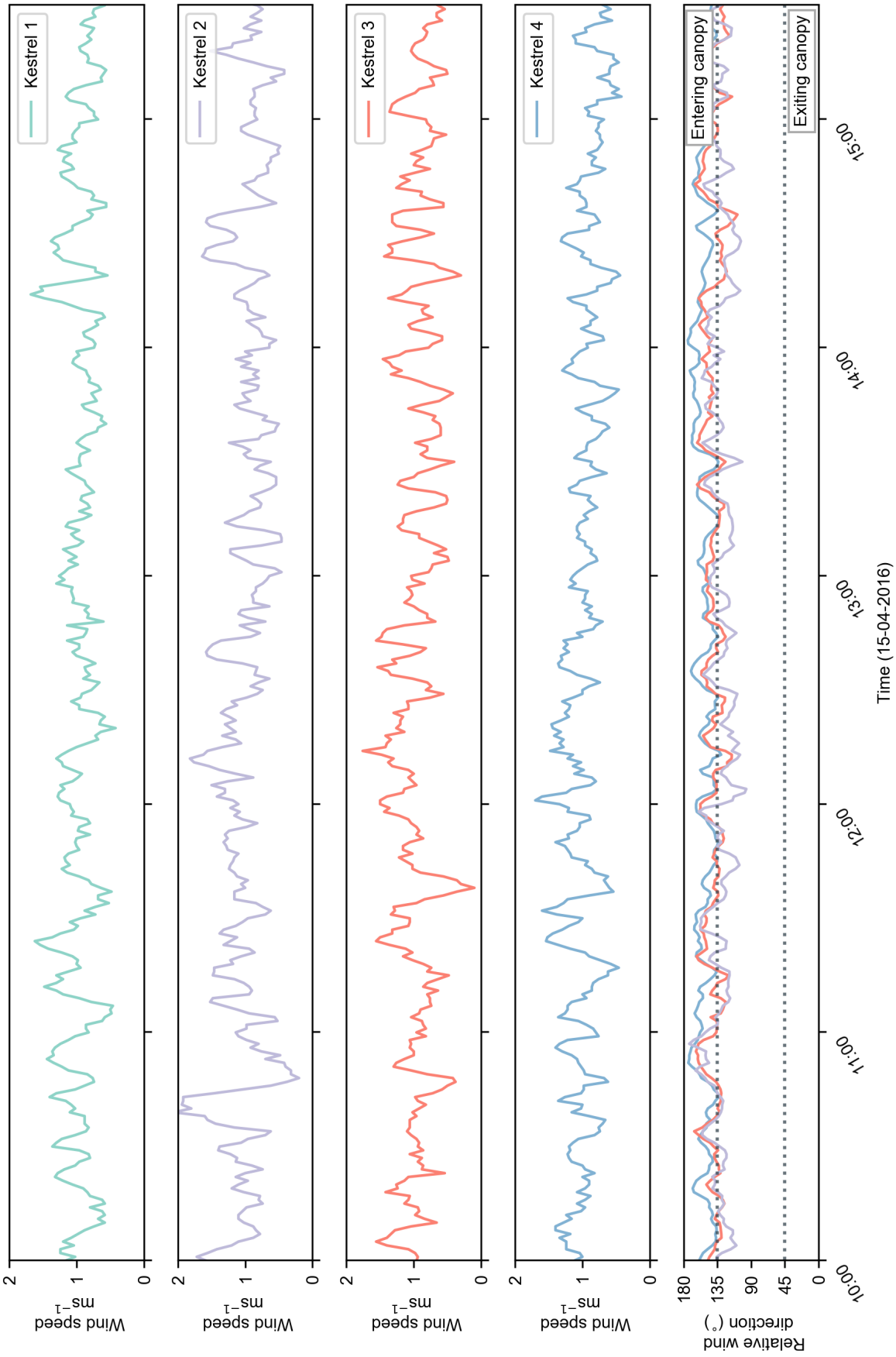

Figure 4.11: Wind speeds and directions measured at the Road site over a 5.5 hour period on 15th April 2016. Wind speeds at each measurement point are shown separately in the first four panels and represent 5-minute moving averages. Wind directions relative to the main canopy edge are shown together in the bottom panel (directions were not measured by Kestrel 1). A relative direction of 0° corresponds to wind exiting the canopy and a relative direction of 180° corresponds to wind entering the canopy, both flowing perpendicular to the line of the canopy edge.

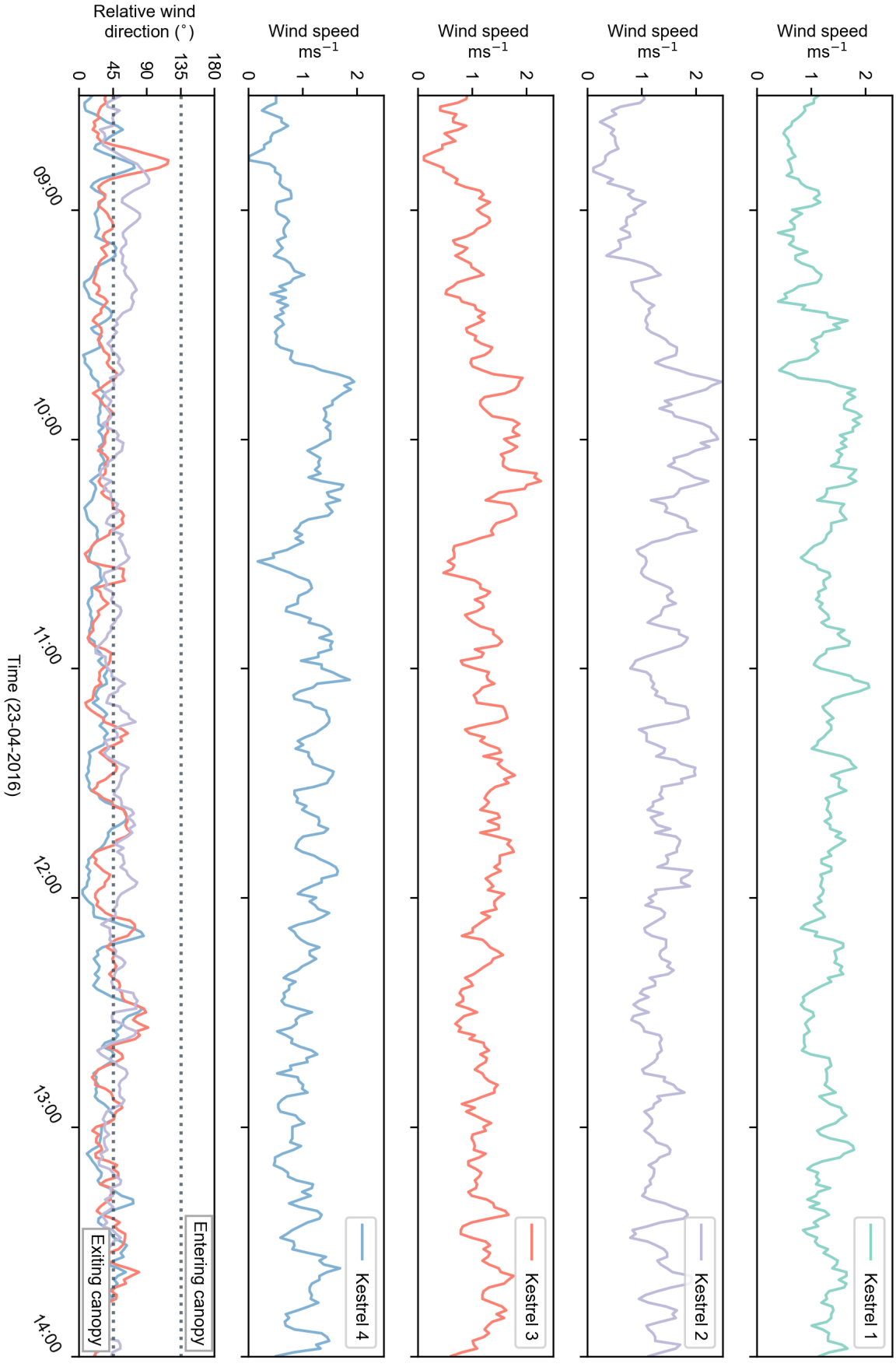

Figure 4.12: Wind speed and direction measured at the Clearing site over a 5.5 hour period on 23rd April 2016. Wind speeds at each measurement point are shown separately in the first four panels and represent 5-minute moving averages. Wind directions relative to the main canopy edge are shown together in the bottom panel (directions were not measured by Kestrel 1). A relative direction of 0° corresponds to wind exiting the canopy and a relative direction of 180° corresponds to wind entering the canopy, both flowing perpendicular to the line of the canopy edge

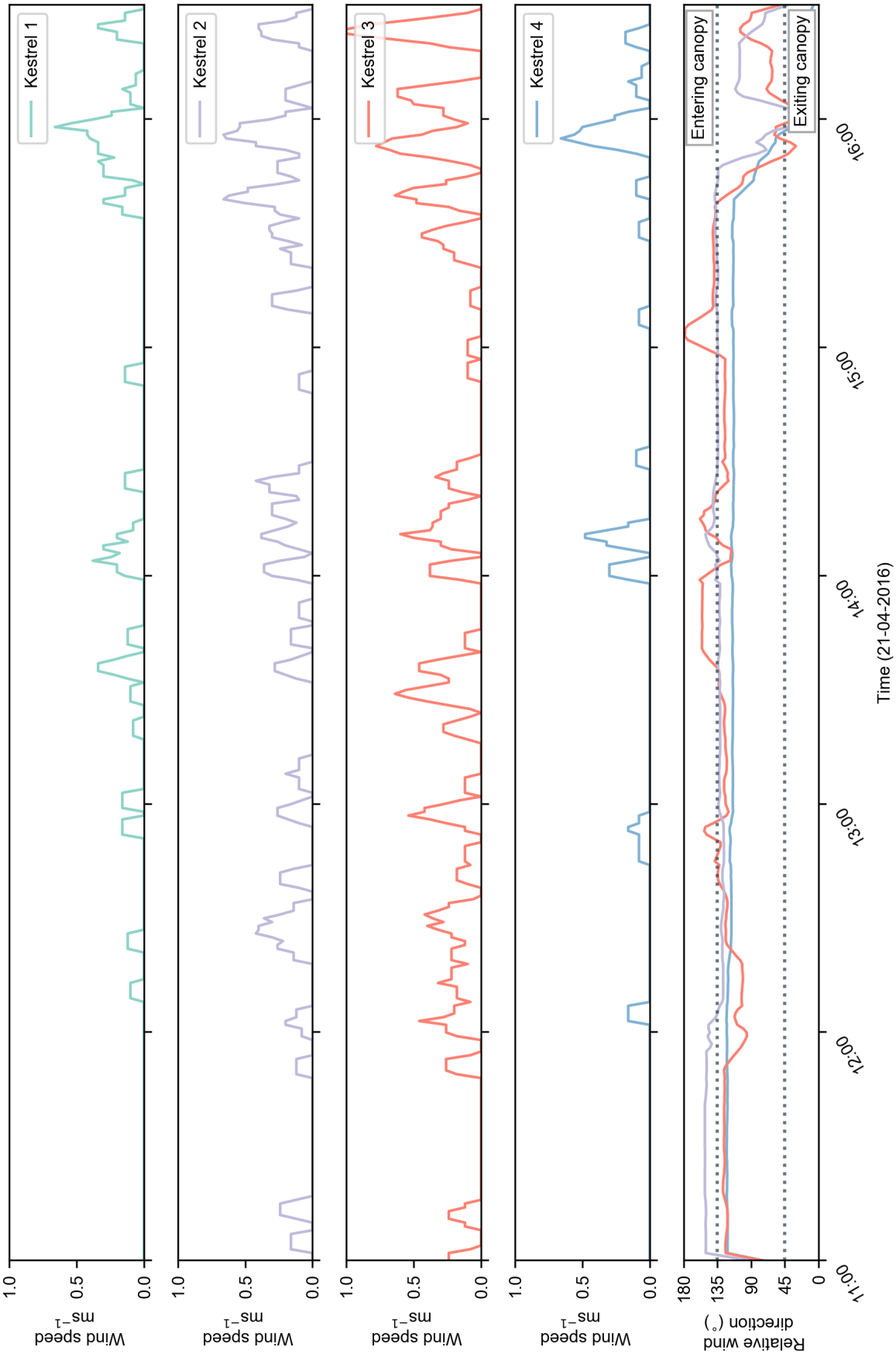

Figure 4.13: Wind speed and direction measured at the Forest track site over a 5.5 hour period on 21st April 2016. Wind speeds at each measurement point are shown separately in the first four panels and represent 5-minute moving averages. Wind directions relative to the main canopy edge are shown together in the bottom panel (directions were not measured by Kestrel 1). A relative direction of 0° corresponds to wind exiting the canopy and a relative direction of 180° corresponds to wind entering the canopy, both flowing perpendicular to the line of the canopy edge.

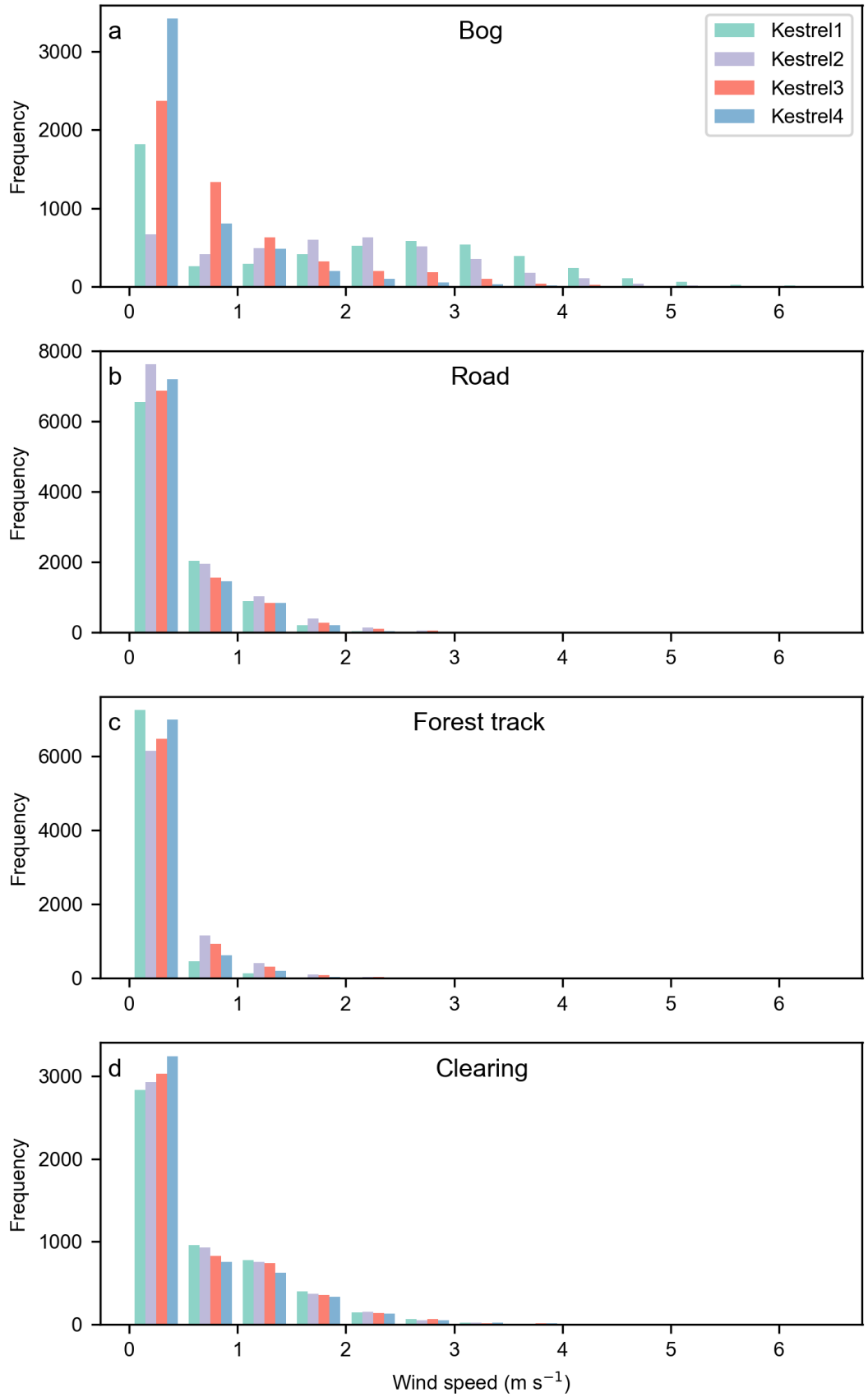

Figure 4.14: Wind speed distributions for the four measurement points (Kestrels 1 – 4) at each of the field sites.

4.3 Results

The final calibrated parameter values are shown in Table 4.3, with the driving wind speed ($utop$) set manually depending on the mean wind speed measured at 48 m by the meteorological mast during the half hour period selected. The values for canopy drag and leaf area density were reached through a process of trial and error; the model was first run with reasonable first approximations of both parameters, based on field observations and typically used values (see Chapter 3.2.2), before an iterative approach was taken until a good model fit was obtained. Figure 4.15 shows both modelled and observed wind speeds for the calibration data set (16:50–17:20 07/04/16). The model produces a good visual fit to the data, which is confirmed by the high R^2 value of 0.98 (see Table 4.4). The RMSE of the model fit is 0.33 m s^{-1} with a bias of -0.31 m s^{-1}; while the model fit the overall pattern of wind speeds, it tended to under-fit the observed data. However, it was not possible to produce higher modelled wind speeds whilst keeping the model parameters within a realistic range or grounded in the meteorological data (specifically the roughness length and driving wind speed parameters).

Parameter	**Calibrated value**
Roughness length (Z_0)	0.001
Canopy height (CNPYHT)	5.82
Canopy displacement height (DISPHT)	4.42
Canopy 1 drag (CNPYCD1)	0.05
Canopy 1 density (CNPYDN1)	0.05
Canopy 2 drag (CNPYCD2)	0.15
Canopy 2 density (CNPYDN2)	0.25

Table 4.3: Final calibrated parameter set. Canopy 1 is the first patch of canopy that the wind flows through, and Canopy 2 is the second patch it flows through. The canopy height and canopy displacement height is constant across both canopy patches.

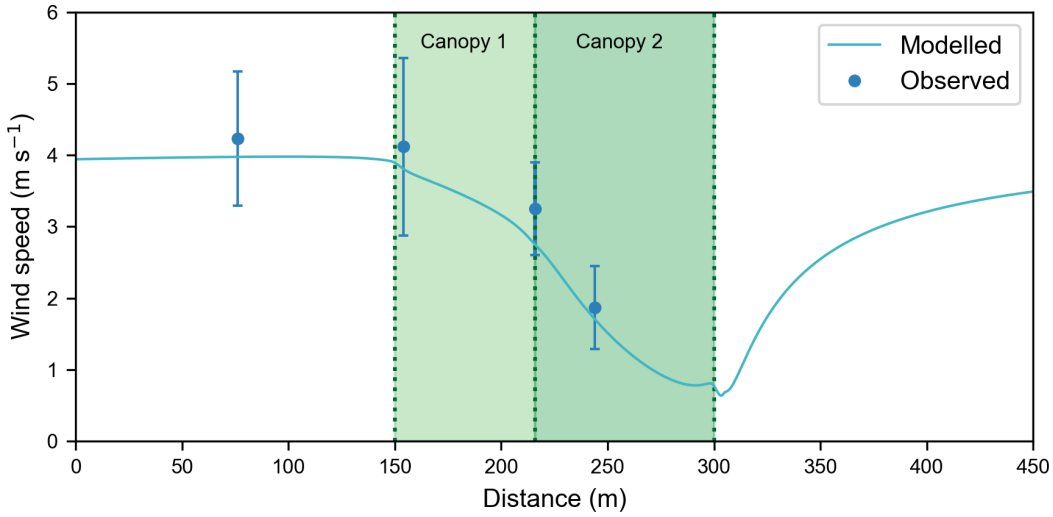

Figure 4.15: Calibrated model run against the calibration data set, which covers the period 16:50–17:20 07/04/16. A driving wind speed of 8 m s^{-1} was prescribed at the upper boundary of the model (z = 100 m), flowing left to right, and is informed by the wind speed measured at the local meteorological mast (5.77 m s^{-1} at z = 48'm). The blue dots represent the mean wind speed measured over the half-hour period at each of the four measurement points and the error bars represent one standard deviation about this mean. Simulated wind speeds are shown by the solid orange line. The canopy extent is shown by the dotted green lines and green shaded areas. Canopy 1 is the first canopy section that the wind flows through and is the sparser of the two canopies.

Following calibration of the Blasius model, its performance was then validated using two further data sets from the bog site: (i) 18:30–19:00 07/04/16; and (ii) 19:30–20:00 07/04/16. The results from these validation runs are presented in Figures 4.16 and 4.17, and again show a good visual fit to the observed wind speeds. In both cases, the R^2 value is high (0.97 and 0.99 respectively) with a relatively low RMSE (0.21 m s^{-1} and 0.32 m s^{-1} respectively) compared to the standard deviation of observed values about their mean (see Table 4.4). The calibrated model performs similarly well with the validation data sets as with the calibration data set.

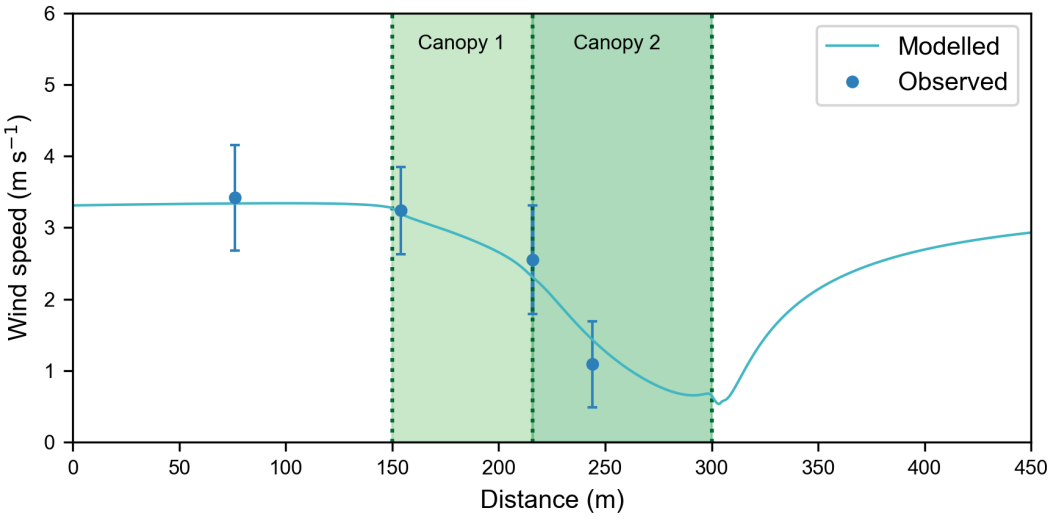

Figure 4.16: Model performance tested against the first validation data set, which covers the period (18:30–19:00 07/04/16). A driving wind speed of 6.71 m s^{-1} was prescribed at the upper boundary of the model ($z = 100$ m), flowing left to right, and is informed by the wind speed measured at the local meteorological mast (4.93 m s^{-1} at $z = 48$ m). The blue dots represent the mean wind speed measured over the half-hour period at each of the four measurement points and the error bars represent one standard deviation about this mean. Simulated wind speeds are shown by the solid orange line. The canopy extent is shown by the dotted green lines and green shaded areas. Canopy 1 is the first canopy section that the wind flows through and is the sparser of the two canopies.

Data set	Kestrel location	Modelled wind speed ($m\ s^{-1}$)	Mean measured wind speed ($m\ s^{-1}$)	Standard deviation (measured) ($m\ s^{-1}$)	R^2	**RMSE**	**Bias**
Calibration	1	3.98	4.23	0.94			
07/04/16	2	3.81	4.12	1.24	0.98	0.33	-0.31
16:50–17:20	3	2.75	3.25	0.65			
	4	1.71	1.87	0.58			
Validation 1	1	3.34	3.42	0.74			
07/04/16	2	3.20	3.24	0.61	0.97	0.21	-0.01
18:30–19:00	3	2.31	2.55	0.76			
	4	1.43	1.09	0.60			
Validation 2	1	2.92	3.21	0.73			
07/04/16	2	2.80	3.21	0.75	0.99	0.32	-0.30
19:30–20:00	3	2.02	2.4	0.54			
	4	1.25	1.38	0.51			

Table 4.4: Summary of the modelled and measured wind speeds for the calibration and validation data sets selected from the Bog site data.

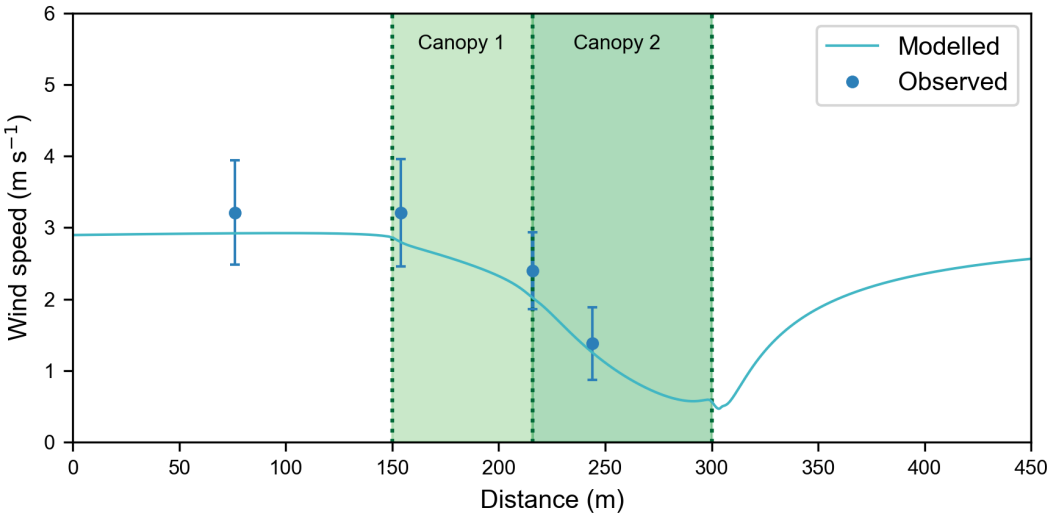

Figure 4.17: Model performance tested against the second validation data set, which covers the period (19:30–20:00 07/04/16). A driving wind speed of 5.86 m s^{-1} was prescribed at the upper boundary of the model ($z = 100$ m), flowing left to right, and is informed by the wind speed measured at the local meteorological mast (4.30 m s^{-1} at $z = 48$ m). The blue dots represent the mean wind speed measured over the half-hour period at each of the four measurement points and the error bars represent one standard deviation about this mean. Simulated wind speeds are shown by the solid orange line. The canopy extent is shown by the dotted green lines and green shaded areas. Canopy 1 is the first canopy section that the wind flows through and is the sparser of the two canopies.

4.4 Discussion

4.4.1 Model calibration

Using observational wind speed data collected across a canopy edge in northern Finland a calibrated parameter set was reached for the BLASIUS wind flow model. The calibrated model was able to successfully capture patterns in wind speed ($R^2 > 0.97$) across the environment that consisted of open bog and a relatively sparse birch/pine canopy.

Whilst producing very good fits to the data collected at the Bog site, this particular calibrated parameter set is most likely to be specific to this environment. Certain values, such as canopy height and LAD, would need to be updated to reflect the canopy characteristics of other forest edge environments. However, it provides a first instance validation that the model is able to reproduce observed patterns in wind speed across a discontinuous canopy. Furthermore, the selected parameter values fall within the ranges used in previous modelling studies (e.g. Ross & Vosper (2005), Ross & Baker (2013), Ross & Harman (2015)) and including the hypothetical canopy scenarios described in Chapter 3. This provides a grounding in real-life data for further wind flow modelling that uses this parameter set as a reference guide to parameter setting.

An important limitation of the BLASIUS model is that it uses a simplified representation of a forest canopy and does not model individual trees, rather a point in the model space is either 'canopy' or 'no canopy'. Therefore, the canopy characteristics are applied uniformly across a vertical column. For instance, the LAD is vertically homogeneous in the canopy patch whereas in real-life it will vary (discussed in further detail in Chapter 3.4). To account for some horizontal variation the modelled canopy was divided into two components (Canopy 1 and Canopy 2) to reflect the sparser

section of canopy on the windward side of the canopy patch with a lower LAD and canopy drag coefficient. A more detailed representation of the canopy that allows for vertical variation would potentially improve the realism of the calibrated model, but in general the simplified scenario considered here seems not to have been an issue with being able to reproduce observed patterns. The measurement points were spaced apart (distances ranged from 28 – 74 m apart) significantly further than the model resolution (0.5 m), so it is challenging to assess the degree to which smaller scale wind flow patterns are able to be reproduced by the calibrated model, but it provides a good first instance reality check on the model capability. In future, closer spacing of measurement points and concentrating measurements on the canopy edge would provide a better constraint on the model calibration, and an interesting insight into the model's ability to pick out finer scale flow patterns. However, this would require significantly more instruments than were available for field data collection here so was not possible for this project.

As demonstrated by the field observations described in this chapter, wind speeds are typically very low at Sodankylä. Furthermore, the field work was conducted over a period of just three weeks in total, which only allowed for a few days of measurements at each site. These factors limited the amount of usable data that was able to be collected for the purpose of calibrating the BLASIUS model. In future, a longer field campaign or multiple field campaigns across a winter season would increase the probability of recording a range of wind conditions, including periods of higher wind speeds and blowing snow events. On reflection, a study site with greater typical wind speeds would also be a more preferable choice for collecting data. For this project, FMI-ARC was chosen on the basis of its long-running monitoring across a range of meteorological and hydrological measurements (which provided a wealth of data particularly for later chapters) and it's accessibility for field work. Forestry and Land Scotland land with coniferous species in Scotland could be an alternative field site option for future work. Although it is not technically boreal forest there are large

areas of land forested with typical boreal species such as Scots pine, much like at FMI-ARC, and with the additional benefit of a greater likelihood of capturing higher wind speeds that those observed at FMI-ARC. The more varied topography of the Scottish landscape would pose a new challenge to the modelling work carried out here though, as this would likely have a significant influence on the wind flow patterns observed (e.g. see Ross & Vosper (2005) and Ross & Baker (2013) for modelling studies of wind flow over forested hills with BLASIUS) and was able to be assumed flat when modelling a site such as those at FMI-ARC.

4.4.2 A simple model relating above-canopy wind speeds to sub-canopy wind speeds and surface friction velocity

The calibrated model can be used to predict expected sub-canopy wind speeds based on above-canopy wind speed measurements. The relationship between these two speeds was applied in further modelling work that is described in Chapters 5 and 7, in which above-canopy meteorological data was used to drive a snow model (a simplified version of FSM2 (Mazzotti et al. 2020a)). The ability to calculate expected sub-canopy wind speeds using a simple mathematical relationship is far more efficient than re-running the BLASIUS model each time the above-canopy wind speed changes.

The calibrated model (presented in Section 4.3) was run with a range of driving wind speeds based on hypothetical wind speeds (every 1 m s^{-1} between 3 – 20 m s^{-1}) at a height of 48 m, which is the height of the wind speed sensor at the FMI-ARC meteorological mast (see Figure 4.1 for mast location). The same method of calculating the driving wind speed ($utop$) as described in Section 4.2.2 was followed here. As an example, Figure 4.18 shows the corresponding wind speeds expected at $z = 1.5$ m. The ratio of each of the modelled wind speeds to the 48 m wind speed

is shown in Figure 4.19. The general convergence of the lines indicates a consistent ratio across the above-canopy wind speeds, which may be used to predict the sub-canopy wind speed given the measured wind speed at $z = 48$ m. As an example, a simple linear regression applied between the 48 m wind speed and the modelled 1.5 m wind speed at x = 0 m produced the following predictive model: $y = 0.46x - 0.02$ ($R^2 > 0.99$) (see Appendix A.4 Figure A.2).

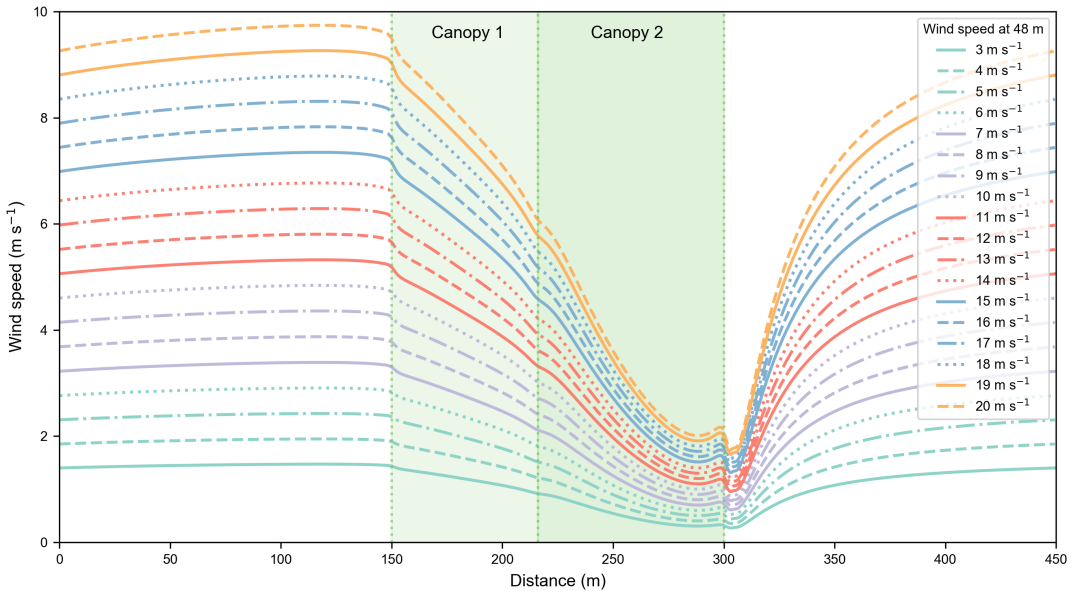

Figure 4.18: Subcanopy wind speeds ($z = 1.5$ m) across the bog site, based on 48 m height wind speeds

Extending this analysis to the full simulation, it is evident that a simple linear emulator can be applied across the full domain. The relationship between the 48 m wind speed and the modelled wind speeds varies spatially across the model domain as the wind flow enters, adjusts to and then exits the canopy (Figure 4.20). The high values of R^2 and relatively low RMSE values across the majority of the domain indicates that the regression model fits the data well. This result is important because it implies that a simple linear model of wind speed can adequately capture the essence of the flow dynamics at a particular point in the model domain. Therefore, a collection of linear models across simulated discontinuities in forest canopies may be used to effectively downscale wind speeds measured at a meteorological mast to sub-canopy levels at a

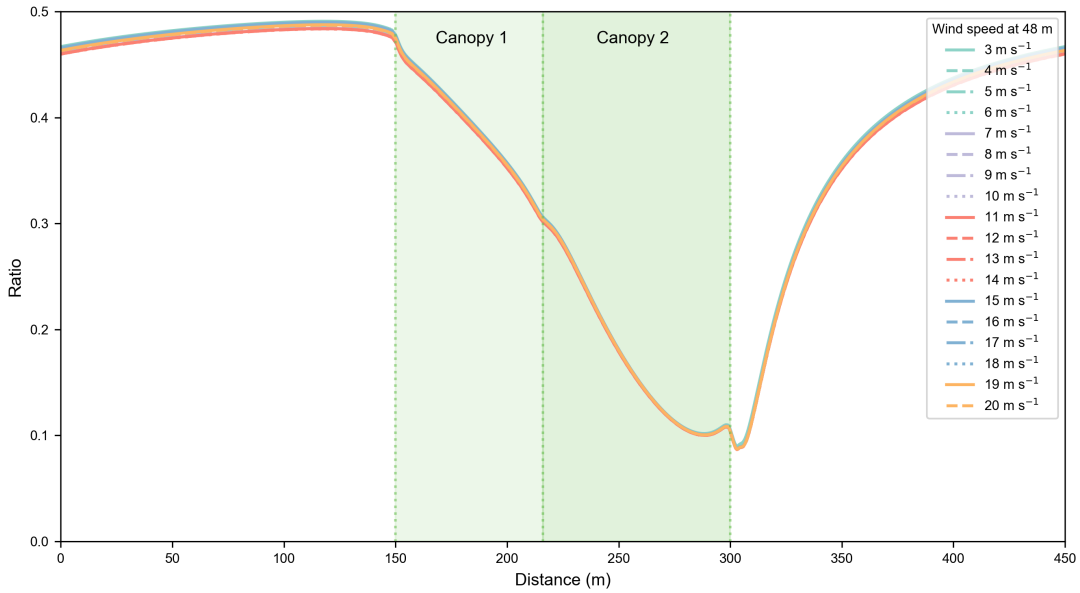

Figure 4.19: Ratio of subcanopy wind speeds ($z = 1.5m$) to 48 m height speeds, across the bog site

given site of interest. Coupling this with a snow model is considerably more efficient than running the full BLASIUS model for every change in the above-canopy wind speed. The above-canopy wind speed may also be scaled to give the modelled surface friction velocity following the same method .

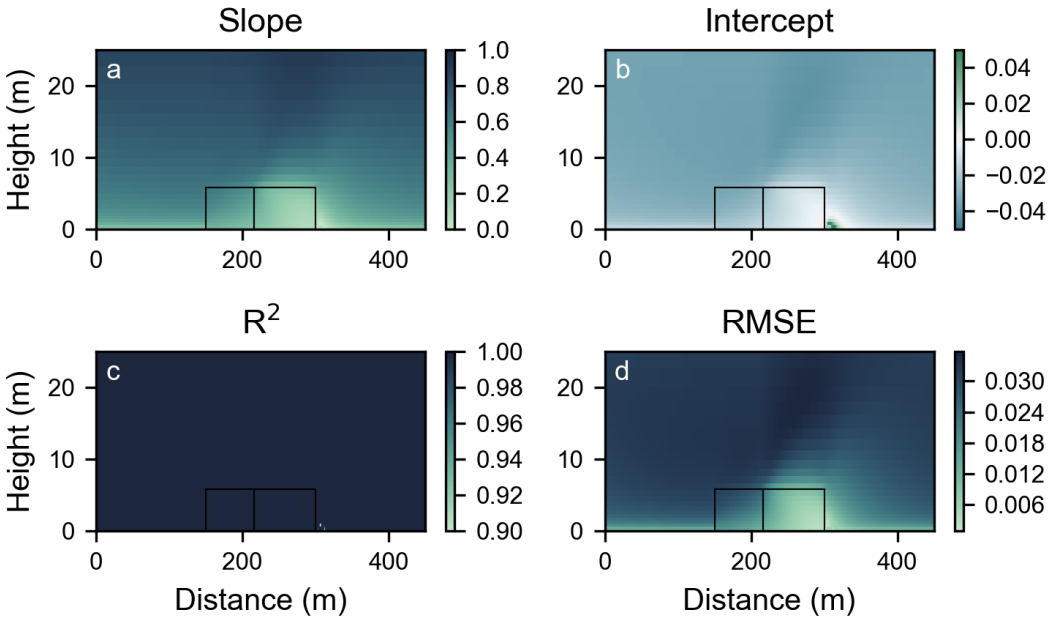

Figure 4.20: Regression coefficients and statistics for modelled wind speeds at the bog site based on a linear relationship with wind speeds measured at 48 m, using the site-calibrated BLASIUS model. The canopy extent is shown by the solid black lines.

4.5 Conclusion

In conclusion, calibration and evaluation of the BLASIUS wind flow model using observational data collected at FMI-ARC in northern Finland demonstrated its ability to reproduce observed patterns of wind speed across a canopy edge. Furthermore, modelled sub-canopy wind speeds and surface friction velocities may be emulated using simple scaling relationships with above-canopy wind speed data. This extends the potential for coupling wind flow results from BLASIUS, which has a relatively long run-time ($\approx$ 1-2 days), with a simplified snow model that runs on a much shorter time frame ($\approx$ seconds).

Chapter 5

Calibration of a simplified snow accumulation model using observational data from forest and open sites

5.1 Introduction

The seasonal accumulation of snowpack is a key process in the hydrology and ecology of boreal forest environments (Bartlett et al. 2006). The depth and mass of the snowpack has an important influence on soil temperature and moisture (Lawrence & Slater 2010, Hardy et al. 2001); biogeochemical cycling (Brooks et al. 2011); timing of melt onset and melt volume (Pomeroy & Granger 1997). Snow accumulation under forest canopies can be spatially heterogeneous, particularly where there are discontinuities arising from clearings in the forest (Golding & Swanson 1986, Pomeroy & Granger 1997, Varhola et al. 2010, Mazzotti et al. 2019). Snowpack within and

adjacent to forest gaps can be more exposed to higher wind speeds than within a closed canopy, and so snow may be redistributed and the snow surface can become more compacted (Stern et al. 2018, Liston et al. 2007). The interface between forest and gap (forest edge) is a transition point between different wind and light conditions and so may be expected to be a point of snow removal or accumulation depending on the relative orientation of the gap.

This chapter focuses on the accumulation of snow on the ground over the winter period, up until the point of maximum snow depth. A simplified model of snow accumulation is calibrated and evaluated using observational data collected between 2007 – 2014 from three different sites in northern Finland: within a large forest clearing; under a closed forest canopy; and on an open bog. These sites are analogues to different situations along a forest-gap transect (below canopy, sheltered and exposed open conditions) and so together can be used to calibrate the model sufficiently to simulate accumulation across forest canopy gaps.

Melting of the snowpack later in the season requires the inclusion of an energy balance sub-model; calibration of this aspect is described in Chapter 7. In Chapter 7, the full calibrated model (capable of modelling both accumulation and melting of snow), will be brought together with the emulated wind model developed in Chapter 4 to investigate hypothetical forest-gap simulations and explore the effects of gap size and orientation on snow accumulation and melt dynamics within a discontinuous boreal forest environment.

5.2 Methodology

5.2.1 Field site and data description

Observational data came from measurements made at the Arctic Research Centre of the Finnish Meteorological Institute (FMI-ARC; see Chapter 4.2.1.1 for a detailed site description). Figure 5.1 provides the geographical context of FMI-ARC within Finland and shows the locations of the measurement sites of interest for this chapter. Driving meteorological data are measured at the Automatic Weather Station (AWS) and snow data for model calibration and evaluation cover three different environments at FMI-ARC: a forest clearing; under forest canopy; and an open bog. The data used in this chapter are described in detail in the following subsections.

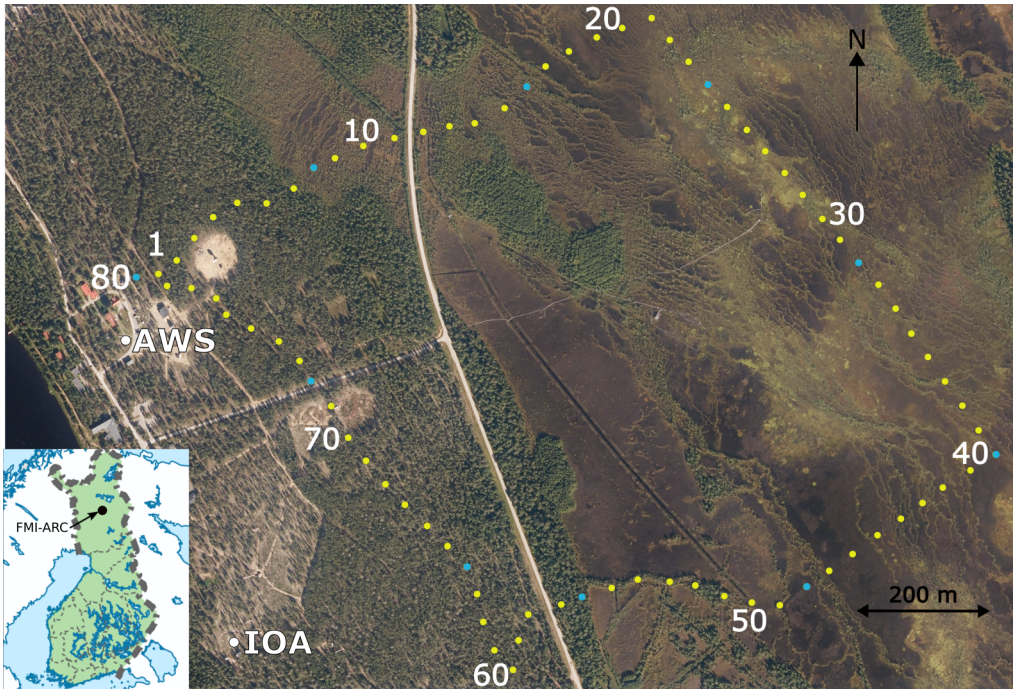

Figure 5.1: Overview map of the snow course (yellow and blue circles) and inset map showing the location of the FMI-ARC research station in northern Finland. The blue circles indicate depth, density and snow water equivalent (SWE) measurement points, and yellow circles indicate depth only measurement points. The measurement points are numbered from 1 – 80, for ease of reference. The locations of the automatic weather station (AWS) and the Intensive Observation Area (IOA) are shown by the white circles and labels.

5.2.1.1 Meteorological data

The snow model used in this chapter requires the following meteorological input data (summarised in Table 5.1): snowfall and rainfall rates, air temperature, relative humidity, wind speed and surface air pressure. This information was provided by a dataset of continuous hourly meteorological measurements from the automatic weather station (AWS; Figure 5.1) at FMI-ARC, which spans a 7-year period from 01/10/2007 – 30/09/2014. The meteorological data are described by Essery et al. (2016) and are available to download alongside the IOA ground-based snow observations (Section 5.2.1.2) at: `https://litdb.fmi.fi/ESMSnowMIP.php`. When temperatures are below 2 °C, precipitation is classed as snow. Winters at FMI-ARC are cold, reaching a minimum of -39.85 °C, and little snow melts before the spring, therefore it is expected that cumulative snowfall during the winter should match the maximum measured snow mass on the ground. The snowfall was scaled by Essery et al. (2016) to ensure consistency with snow accumulation on the ground. Given the sheltered location of the Intensive Observation Area (IOA, see section 5.2.1.2 for further site details), it was treated as a natural snow gauge for this purpose and the snowfall was scaled to match the maximum recorded snow water equivalent (SWE) each winter at this site (see Table 2. in Essery et al. (2016) for the scaling factor applied to each year of snowfall data).

Figure 5.2 shows weekly snowfall and rainfall rates (at 2 m height, snowfall scaled as above), mean weekly air temperature (at 2 m height) and mean weekly wind speed (at 22 m height) as measured at the AWS. Air temperature ranges from a minimum of -39.85 °C in the winter to a maximum of 30.25 °C in the summer. Wind speeds are low and predominantly directed from the south (see Figure 5.3 for the 2011–12 winter period as an example). The mean wind speed over the study period was 2.37 m s^{-1}, although recorded wind speeds reached a maximum of 9.9 m s^{-1}.

Variable	Description	Units	Measurement height
S_f	Snowfall rate	kg m^{-2}s^{-1}	2 m
R_f	Rainfall rate	kg m^{-2}s^{-1}	2 m
T_a	Air temperature	K	2 m
RH	Relative humidity	%	2 m
U_a	Wind speed	m s^{-1}	22 m
p_s	Surface pressure	Pa	1 m

Table 5.1: Input meteorological data

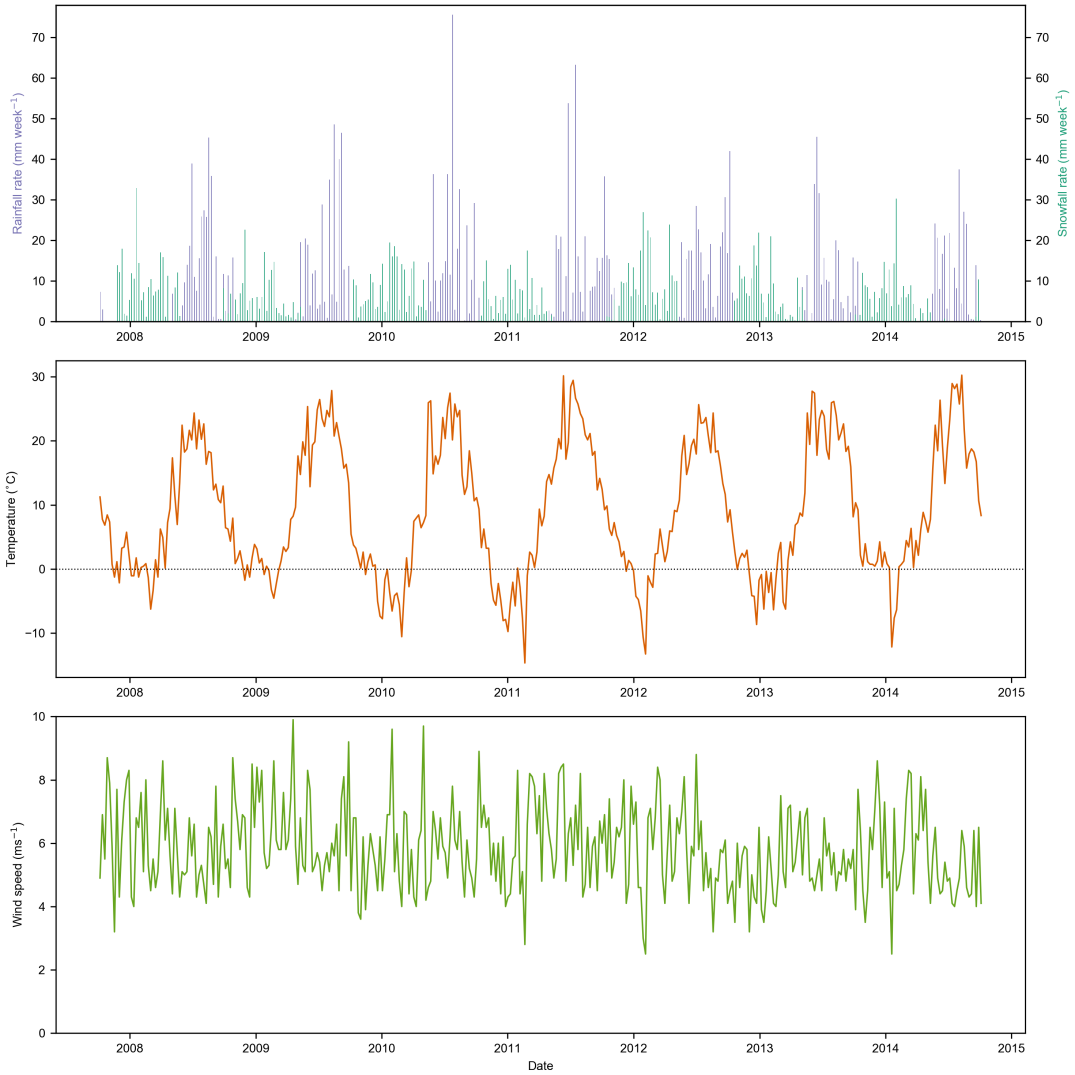

Figure 5.2: Observational precipitation, air temperature and wind speed measurements recorded at the FMI-ARC Automatic Weather Station during the period October 2007 – September 2014 inclusive. For clarity of presentation, the top panel shows weekly snowfall and rainfall rates, the middle panel shows the mean weekly air temperature and the bottom panel shows the mean weekly wind speed. Precipitation and air temperature were measured at a height of 2 m and wind speeds were measured at a height of 22 m.

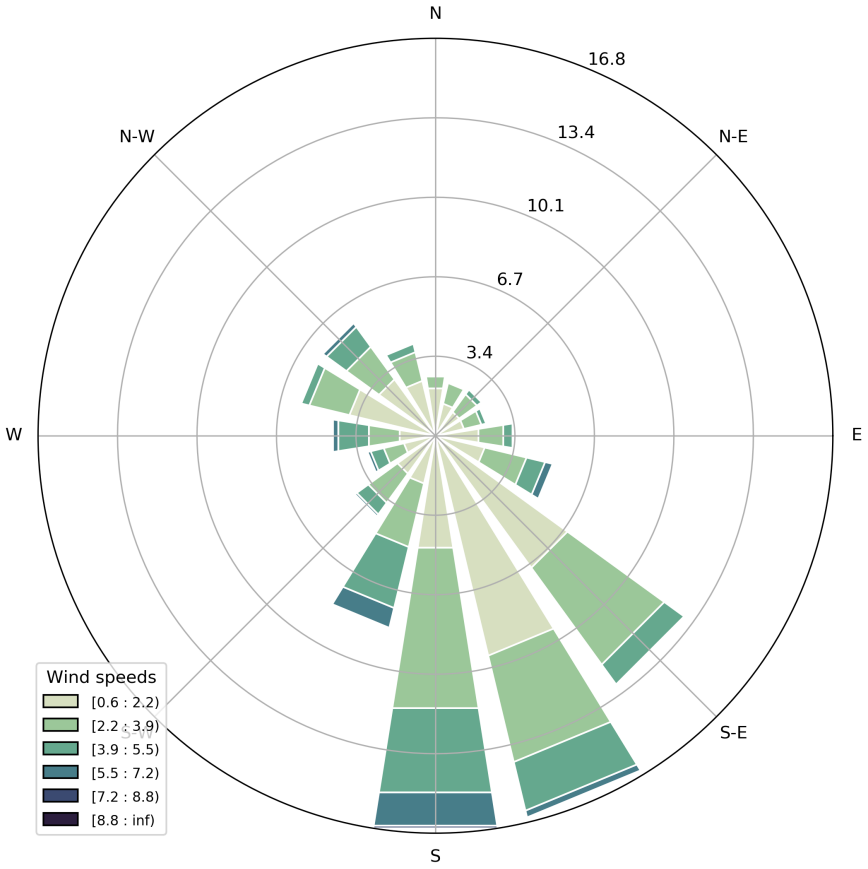

Figure 5.3: Wind rose showing wind directions and speeds measured at the meteorological mast (z=48 m) for the period 01/09/2011 – 31/03/2012

5.2.1.2 Intensive Observation Area point snow measurements

The Intensive Observation Area (IOA) is a ∼40 m diameter forest clearing located 590 m south of the AWS (Figure 5.1) that was established in 2006 for conducting continuous snow and meteorological measurements and experiments (Leppänen et al. 2016, Essery et al. 2016). Snow measurements recorded at the IOA over a period of seven years (01/10/2007 – 30/09/2014 inclusive) were used here to calibrate and evaluate the snow model at a sheltered forest clearing site. The data consists of manual measurements of snow depth, snow density and SWE. As the focus is on snow accumulation only, measurements up to the maximum snow mass recorded each winter were used in this chapter. As the winter climate is typically cold at FMI-ARC, it is a reasonable assumption to separate accumulation and melt processes to simplify

the calibration process.

The IOA was chosen for an initial calibration of the model, as it is surrounded by pine forest and so is relatively sheltered. Essery et al. (2016) measured 2 m height wind speeds at the IOA over the course of a week and found that the average wind speed scaled at 35% of the 22 m height wind speed measured at the AWS. Therefore, it was assumed that very little wind-driven redistribution of snow occurs at the IOA and may be ignored in this instance.

Subsequently, observational transect data covering both enclosed forest areas and exposed open areas (see subsection 5.2.1.3 below) were used to calibrate and evaluate the model in situations where canopy interception and wind processes, respectively, are more important.

5.2.1.3 Snow course data

Snow depth and density data from a snow course located at FMI-ARC (Figure 5.1) were used to calibrate the model and evaluate its performance in both exposed open sites and sheltered canopy sites. The snow course is one of 150 snow measurement courses maintained by the Finnish Environment Institute (SYKE). The snow course data was supplied by Heidi Sjöblom at FMI-ARC. and consists of 80 snow depth and 9 snow density and SWE measurement points co-located along a 4 km circuit that includes forest and open bog environments (Leppänen et al. 2016). Occasionally snow density measurements were recorded at a nearby measurement point to the one indicated on the snow course map.

Manually collected measurements were recorded monthly (approximately in the middle of the month) and this study used data collected over six winter periods (1st September–31st March 2008–09 to 2013–14). Across the six winters used in this study, the annual maximum snow depth varied between 76–86 cm, with a median of 80

cm (Figure 5.4). The annual maximum snow density varied between 229–400 kg m^{-3}, with a median of 287 kg m^{-3}, and the annual minimum snow density varied between 100–171 kg m^{-3}, with a median of 136 kg m^{-3}.

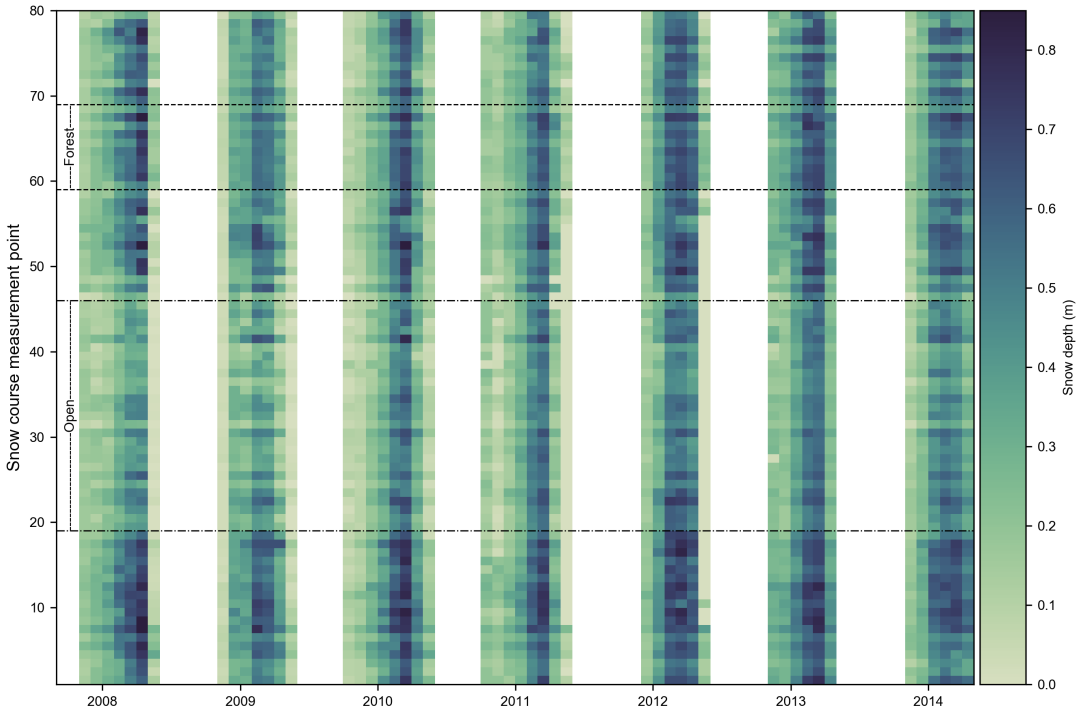

Figure 5.4: Snow depth measurements from the Sodankylä snow course for the six winter study periods (2008–09 to 2013–14). The solid black horizontal line is a broad division of the data into measurement points located in forest or in the open and was determined through visual examination of an aerial photograph of the site and the metadata included with the measurements.

Two subsets of the snow course data were created, representing forest and open sites. Whether a measurement point was located in an open or forest site was determined through visual examination of an aerial photograph of the site and inspection of the metadata included with the snow course measurements (Figure 5.1). To be classed as a forest location, the measurement point had to be located under forest cover and be at least 50 m from the nearest edge in order to minimise potential influence from an adjacent open area. Through this approach, points 19 – 46 were classed as 'open' and points 59 – 69 as 'forest' (see Figure 5.1 for measurement point numbering). Figure 5.5 shows the snow depth, SWE and density data for these two groupings over six years. All measurement points had an associated snow depth observation, and so the

mean of these depths was calculated for each measurement date. At the open sites, 1–2 measurement points had an associated SWE and density observation recorded, and so either a single point measurement or the mean of two point measurements were used for these variables. At the forest site, there was just one SWE and density measurement made each month. Snow under forest is typically deeper than in the open bog. Previous studies have tended to find lower snow depths under forest canopy than in adjacent open areas (e.g. Golding & Swanson (1986)). In this case, the bog site is very exposed and so the lower snow depths are likely due to wind-driven snow transport of snow off the bog and wind-driven compaction of the snowpack. At the forest sites the annual maximum mean snow depth varied between 55–67 cm, with a median of 63 cm, whereas at the open sites the annual maximum mean snow depth varied between 40–56 cm, with a median of 55 cm. The mean snow depths at the forest and open sites are significantly different ($p < 0.05$) for all but a few measurement dates (such as the start of the 2011–12 winter period). The annual maximum snow density at the forest sites varied between 175–223 kg m^{-3} (median = 211 kg m^{-3}), compared to a range of 198–400 kg m^{-3} (median = 246 kg m^{-3}) at the open sites. The annual maximum SWE at the forest sites varied between 104–146 kg m^{-2} (median = 127.5 kg m^{-2}), whereas at the open sites there was a slightly wider range of 92–152.5 kg m^{-2} (median = 119.75 kg m^{-2}).

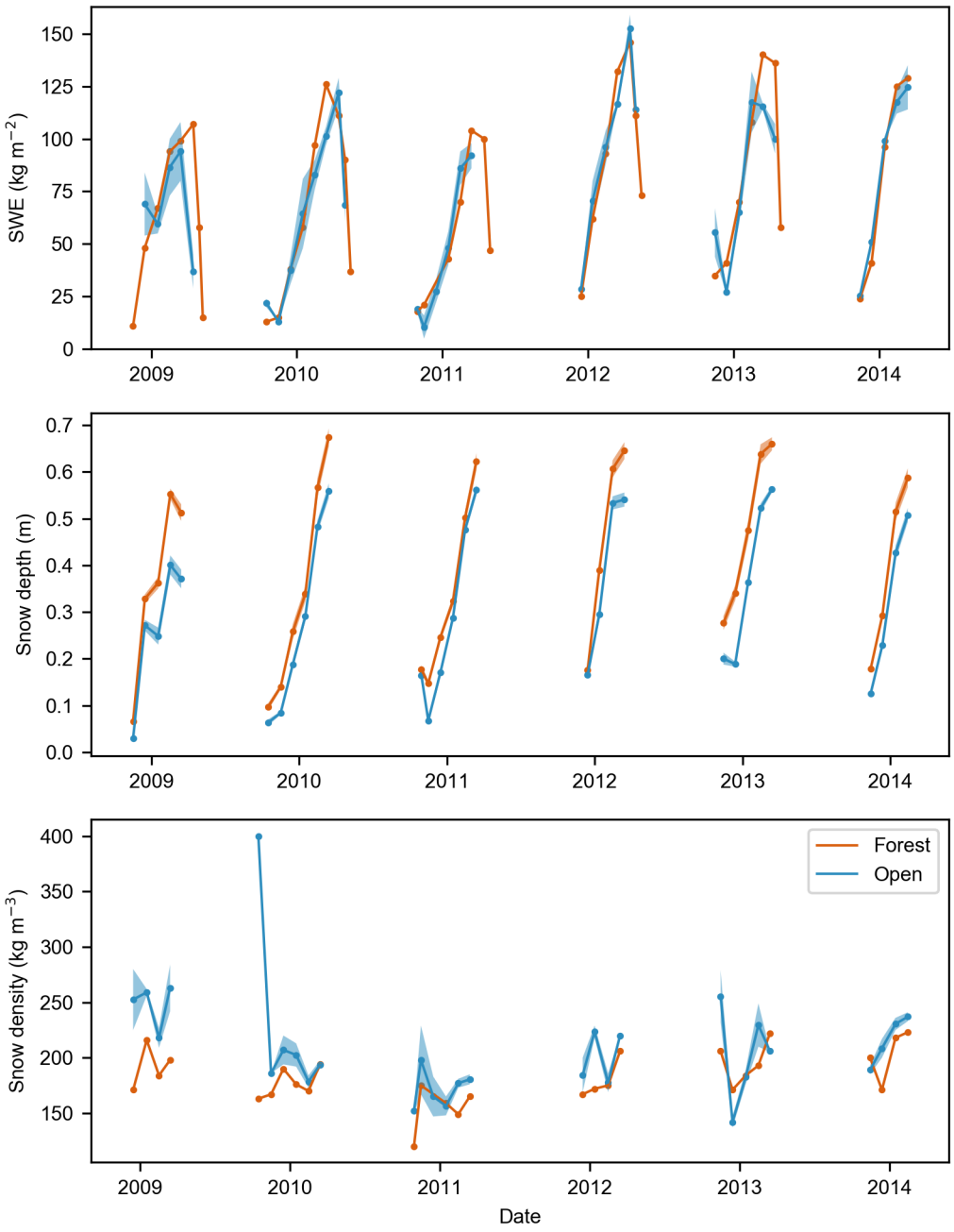

Figure 5.5: SWE (top panel), snow depth (middle panel), and snow density (bottom panel) for open and forest measurement points on the Sodankylä snow course. The snow depths are the mean of all the measurement points classified as either forest or open for a particular measurement date. The forest swe and density values are from a single measurement point. The open swe and density values are the mean of two measurements. The standard error of the mean is shown by the shaded area for both locations, where applicable.

5.2.2 Snow model description

The model used in this thesis is a simplified version of the Flexible Snow Model (FSM2), an open source energy balance snow model that is described in detail by Mazzotti et al. (2020a). The model was written in Fortran, compiled with gfortran and ran on the University of Edinburgh School of GeoSciences linux server. A three-year model run takes less than a second on a single CPU.

As the focus in this chapter is on the accumulation of snow and melting is ignored, only the snow mass balance component is considered. At the IOA site, the simulated snow accumulates with the driving snowfall and the density of the snowpack increases at a rate determined by the density of the freshly fallen snow and the rate of compaction. At the IOA and forest sites, the rate of compaction is influenced by changes in air and snow temperatures. At the bog, which is an open and exposed site, the model additionally includes wind-modified compaction and sublimation rates. At the forest site, it is necessary to also consider the role of the canopy in the mass balance. A fraction of the falling snow is intercepted by the canopy, and removed via sublimation.

For the purposes of calibration, the model was run at a single point for each of the three distinct sites to facilitate calibration of the model parameters with the available data, before considering transects across forest gaps (see Chapter 7), which encompass both forest and open environments and the transition between the two, leading to potentially more complex patterns of snow accumulation.

5.2.2.1 Snow mass balance

The mass balance equations governing overall snow accumulation in the model compartmentalise the snow mass into either snow on the ground or snow in the canopy.

The ground snow mass balance at all three calibration sites is calculated as

$$S_n = S_{n-1} + S_f \delta t - \Delta I \tag{5.1}$$

where S_n is the new snow mass on the ground (kg m^{-2}), S_{n-1} is the existing ground snow mass (kg m^{-2}), S_f is the snowfall rate (kg m^{-2} s^{-1}), δt is the time step (s), and, relevant at the forest site, ΔI is the change in canopy snow load with time (kg m^{-2}) (Eq. 5.3) .

At the forest site, the canopy mass balance is calculated as

$$I_n = I_{n-1} + \Delta I - E_s \delta t \tag{5.2}$$

where I_n is the new canopy snow load (kg m^{-2}), I_{n-1} is the existing snow load on the canopy (kg m^{-2}) and E_s is the sublimation rate of canopy snow (kg m^{-2}) (Eq. 5.4).

5.2.2.2 Interception

The incremental change in canopy snow load with time (ΔI) is from Hedstrom & Pomeroy (1998) as implemented in Essery et al. (2003)

$$\Delta I = 0.7(I_{max} - I_0)\left(1 - e^{-S_f / I_{max}}\right) \tag{5.3}$$

where I_0 is the initial snow load on the canopy (kg m^{-2}), S_f is the snowfall rate (kg m^{-2} s^{-1}), and I_{max} is the maximum intercepted load (kg m^{-2}). Following Essery et al. (2003), the snow interception capacity is estimated as $I_{max} = 4.4LAI$, where LAI is the leaf area index.

The unloading rate of snow from the canopy was set equal to zero, i.e. all intercepted

snow is either held in the canopy or is lost through sublimation (Eq. 5.4).

5.2.2.3 Sublimation of canopy snow

The sublimation of canopy snow is calculated as in Essery et al. (2003). Assuming that the air near the canopy snow surface is saturated at the air temperature, the sublimation rate of snow held in the canopy is

$$E_s = \frac{\rho_a}{r_a + r_c} \left(\frac{I}{I_{max}} \right)^{\frac{2}{3}} (Q_{sat} - Qa) \tag{5.4}$$

where ρ_a is the air density (kg m^{-3}), r_a is the aerodynamic resistance between the canopy air space and the atmosphere (s m^{-1}) (Eq. 5.5), r_c is the aerodynamic resistance between vegetation and the canopy air space (s m^{-1}) (Eq. 5.6), $\frac{I}{I_{max}}$ is the fraction of the canopy with snow cover. The $\frac{2}{3}$ exponent relates to the rate of evaporation of dew on canopies, as given by Deardorff (1978). Q_{sat} is the specific humidity at saturation (Eq. 5.8) and Q_a is the specific humidity of the air (Eq. 5.10).

The aerodynamic resistance between canopy air space and the atmosphere is calculated as

$$r_a = \frac{1}{k u_*} ln \left(\frac{z_{ref} - d_h}{z_0} \right) \tag{5.5}$$

where k is the von Karman constant (0.4), u_* is the friction velocity (Eq. 5.7), z_{ref} is the meteorological measurement height ($=$ 22 m), d_h is the canopy displacement height ($= 0.76h$, where h is the canopy height and $=$ 15 m) and z_0 is the roughness length ($= 0.1h$).

The aerodynamic resistance between the canopy vegetation and air space is calculated as

$$r_c = \frac{20}{LAI u_*^{1/2}} \tag{5.6}$$

The friction velocity is calculated as

$$u_* = \frac{kU_a}{ln(\frac{z_{ref}-d_h}{z_0})} \tag{5.7}$$

Both the aerodynamic resistance equations and the friction velocity equation assume neutral atmospheric stability.

The specific humidity at saturation is calculated as

$$Q_{sat} = 0.622\frac{e_s}{p_s} \tag{5.8}$$

where p_s is the surface pressure (Pa) and e_s is the saturation vapour pressure (Pa)

$$e_s = 611\exp(\frac{22.4422(T_a - 273.15)}{T_a - 0.964}) \tag{5.9}$$

The specific humidity of air is

$$Q_a = Q_{sat}\left(\frac{RH}{100}\right) \tag{5.10}$$

5.2.2.4 Snow compaction

Following Liston et al. (2007), changes in the density of the soft upper snow layer occur through two mechanisms:

1. addition of new snow from falling snow, which has a prescribed 'fresh snow' density

2. the compaction of snow, which is influenced by the air and snow temperatures and the wind speed

The higher wind speeds experienced at the bog site can lead to drifting snow, enhanced

sublimation and snow compaction. Here, the friction velocity ($u_\star$) is compared to the threshold friction velocity ($u_{\star t}$) to determine the onset of snow movement (in contrast to Liston et al. (2007), who use a threshold wind speed of 5 m s^{-1} for the initiation of snow movement). The threshold friction velocity is defined using the following equations.

Snow density can be related to snow strength using the following equation for the variation of hardness (σ), as in Liston et al. (2007) (based on measurements by Abele & Gow (1975))

$$\sigma = 1.36 \exp(0.013 \rho_s) \tag{5.11}$$

where σ is in kPa and ρ_s is the snow density (kg m^{-3}).

Snow hardness can be related to the threshold friction velocity following the equation provided by Liston et al. (2007) (based on data from Kotlyakov (1961))

$$\sigma = 267 u_{\star t} \tag{5.12}$$

Bringing Equations 5.11 and 5.12 together, gives

$$u_{\star t} = 0.005 \exp(0.013 \rho_s), \text{ if } 300 < \rho_s \leq 450 \tag{5.13}$$

A similar equation is used for snow densities between 50 – 300 kg m^{-3}

$$u_{\star t} = 0.10 \exp(0.003 \rho_s), \text{ if } 50 < \rho_s \leq 300 \tag{5.14}$$

These equations allow for a dynamic threshold friction velocity that changes over time as a function of snow density over time. During periods of snowfall and when $u_\star < u_{\star t}$, the snow density (ρ_s) is set to equal the fresh-snow density (ρ_f). During

periods when $u_\star \geq u_{\star t}$, a density offset (ρ_w) is applied, such that

$$\rho_s = \rho_f + \rho_w \tag{5.15}$$

with

$$\rho_w = D_1 + D_2\{1.0 - \exp[-D_3(U_{sub} - 5.0)]\} \tag{5.16}$$

where D_1, D_2 and D_3 are constants. D_1 is the density offset and is set equal to 25.0 kg m^{-3}. D_2 determines the maximum increase in the density due to the wind and equals 250.0 kg m^{-3}. The transition from low to high wind speeds is controlled by D_3, which is set to equal 0.2 m s^{-1}. U_{sub} is the wind speed at a height of 2 m. The change in snow density with time is given by

$$\frac{\delta\rho_s}{\delta t} = CA_1U_{pac}\rho_s \exp[-B(T_f - T_s)] \exp(-A_2\rho_s) \tag{5.17}$$

where $C = 0.10$ and is a non-dimensional constant that determines the rate of change in snow density, A_1 and A_2 are constants equal to 0.0013 m^{-1} and 0.021 m^3 kg^{-1}, respectively, B is a constant set equal to 0.08 K^{-1}, T_f is the freezing temperature (273.15 K) and T_s is the soft snow temperature (assumed to be equal to the air temperature (T_a)). U_{pac} characterises the wind-speed based contribution to the evolution of the snow density and is given by:

$$U_{pac} = \begin{cases} E_1 + E_2\{1.0 - \exp[-E_3(W_t - 5.0)]\}, \text{ if } u_\star \geq u_{\star t} \\ 1.0ms^{-1}, \text{ if } u_\star < u_{\star t} \end{cases} \tag{5.18}$$

where E_1 defines the U_{pac} offset when $u_\star \geq u_{\star t}$ and is set equal to 5.0 m s^{-1}, E_2 defines the maximum increase in U_{pac} due to the wind and is set equal to 15.0 m s^{-1}, and E_3 controls the transition from low to high wind speeds and is set equal to 0.2 m s^{-1}. When the friction velocity is lower than the threshold value, U_{pac} is set equal to 1.0 m s^{-1}. The discontinuity at the threshold point was used by Liston

et al. (2007) to limit any wind-compaction effects to winds most likely to give rise to blowing snow.

5.2.2.5 Snow transport

Initially just saltation — the 'skipping' movement of snow particles across the snow surface — is considered, given the relatively low wind speeds at Sodankylä.

The saltation transport rate is as follows (Pomeroy et al. 1993)

$$Q_s = \frac{C_{salt}\rho u_{\star t}}{u_\star g}(u_\star^2 - u_{\star t}^2) \tag{5.19}$$

where Q_s is the saltation transport rate (kg m^{-1} s^{-1}), C_{salt} is an empirically derived constant that is equal to 0.68 m s^{-1}, ρ is the atmospheric density (kg m^{-1}), g is the acceleration due to gravity (m s^{-2}), $u_\star$ is the friction velocity (m s^{-1}), and $u_{\star t}$ is the friction velocity (shear stress) that is applied to the snow surface at the threshold for transport.

The snow is redistributed following Essery et al. (1999), which gives the developing flux over changing surface conditions as the solution of

$$q_s = Q_s - \frac{F}{3}\frac{dq_s}{dx} \tag{5.20}$$

where F is the fetch length required for the development of blowing snow and has the value $F = 1000$ m, which was fitted to measurements by Takeuchi (1980). Equation 5.20 can be discretised as

$$q_{s,i} \approx Q_{s,i} - \frac{F}{3\Delta x}(q_{s,i} - q_{s,i-1}) \tag{5.21}$$

which can be rearranged as

$$q_{s,i} = fQ_{s,i} + (1-f)q_{s,i-1} \tag{5.22}$$

with $f = (1 + \frac{F}{3\Delta x})^{-1}$.

The rate of change in the snow mass due to redistribution is then

$$\frac{dS}{dt} = -\frac{dq_s}{dx} \tag{5.23}$$

which is discretised as

$$S_n = S_{n-1} + (q_{s,i+1} - q_{s,i})\frac{\delta t}{\Delta x} \tag{5.24}$$

5.2.3 Model calibration

Key model parameters were selected and calibrated using data from three sites representing a range of open and forest environments. Table 5.2 shows the model parameters that were identified, through initial exploratory work, as being the most influential for calibrating the model.

Differences in the environmental conditions and data availability meant that different combinations of parameters were appropriate for calibrating the model at each site.

Parameters A_1, A_2, B and ρ_{ns} all relate to the evolution of the snowpack density over time. An exploratory analysis of the model sensitivity to these parameters showed that A_1 and B had a low influence on the simulated snow depth root mean square error (RMSE) and so they were fixed with the default values used by Liston et al. (2007) (0.0013 and 0.08 K^{-1}, respectively) for the calibration at all three sites. The

Parameter	Description	Default value
A_1	Determines rate of change in snow density (Eq. 5.17)	0.0013 m^{-1} *
A_2	Determines rate of change in snow density (Eq. 5.17)	0.021 m^3 kg^{-1} *
B	Determines rate of change in snow density (Eq. 5.17)	0.08 K^{-1} *
ρ_{ns}	Fresh snow density	100 kg m^{-3} *
E_1	Wind packing offset (Eq. 5.18)	5.0 m s^{-1} *
LAI	Leaf area index	–
z_0	Roughness length	$0.1h$ m

Table 5.2: Model parameters selected for calibration. Asterisks denote parameters from the snow compaction equations in Liston et al. (2007). Canopy height, h, is 15 m.

remaining parameters were calibrated as described below.

There are many different automatic methods for minimising the snow depth RMSE (e.g. in python: `https://docs.scipy.org/doc/scipy/reference/generated/scipy.optimize.minimize.html`). For the calibration process described here, the selected model parameters were calibrated using either a random parameter search if more than one parameter required calibrating at once (e.g. A_2 and ρ_{ns} at the IOA site), or a simple adjustment within a set range for a single parameter (e.g. LAI at the forest site).

The random parameter search works by generating different parameter combinations within a set ranges; the model is then run with each parameter set and the simulations are compared with observations. The random parameter search approach was chosen as it is more time-efficient than manually searching through all possible parameter values and also accounts for potential interactions between parameter effects.The model goodness-of-fit is assessed by calculating the simulated snow depth RMSE. When the model has cycled through the specified number of random parameter combinations, the optimal parameter set is selected based on minimising the snow depth RMSE. Parameter values giving a RMSE < 0.1 were classed as 'good' and used as an ensemble of possible parameter combinations that represent the uncertainty encompassed

by the calibration, given the available data constraints.

5.2.3.1 IOA

The observed snow data from the IOA was subdivided into four years for calibration (covering the period: 01/10/2007 – 05/04/2011) and three years for validation (covering the period: 01/10/2011 – 01/04/2014). A random parameter search was performed with A_2 (0 – 0.063 m^{-3} kg^{-1}) and ρ_{ns} (0 – 300 kg m^{-3}). The upper limits represent three times the Liston et al. (2007) values.

5.2.3.2 Forest

The snow course data cover six years and so were subdivided into a three-year calibration dataset (2008 – 2011) and a three-year evaluation dataset (2011 – 2014). To ensure greater consistency between the snow course measurements, a local snow depth was calculated from the single point measurements of snow density and SWE (using the relationship: snow depth = SWE / snow density).

A two-step process was then taken to calibrate the model at the forest site. First, the value of LAI was adjusted within a realistic range (0 – 4) to minimise the SWE RMSE, as LAI controls the interception of falling snow and therefore also the snow mass accumulating on the ground below.

The A_2 and ρ_{ns} parameters were then calibrated based on minimising the snow depth RMSE following a similar approach to the IOA site. As there was insufficient data at the forest site to constrain both the A_2 and ρ_{ns} parameters, it was assumed that the differences between the snow density in open and forest areas develops as the snow is falling through the canopy rather than when it is on the ground, and that therefore the range of 'good' A_2 values calibrated at the IOA site (relating to compaction of the

ground snowpack) could be used to constrain the parameter space searched during the forest calibration. A random parameter search was performed with A_2 varying within the 'good' range found to give a snow depth RMSE $<$ 0.1 m at the IOA (0.0192 – 0.0629 m^{-3} kg^{-1}) and a range of 0 – 300 kg m^{-3} for ρ_{ns}.

5.2.3.3 Bog

The model was then calibrated to an exposed open site using observational snow data from the bog section of the snow course. The bog survey locations have an upwind fetch of hundreds of metres over which blowing snow can develop (Figure 5.1). Wind therefore has a much more significant role in the snow mass balance than the previous two sites. As with the forest calibration, the snow depth was calculated from the observed SWE and density to ensure consistency between these three related variables. There are two density and SWE measurement points along the snow course classed as 'open bog' environment and the mean value from these two points for each measurement date was used for the calibration. A two-step approach was taken for the calibration process, concentrating first on minimising the RMS error in the simulated SWE and then minimising the RMS error in the simulated snow depth.

Before calibrating the mass balance model at the bog site, it was necessary to modify the snow mass to account for the periodic boundary conditions of the model. This periodicity has the effect that blowing snow is recycled through the model domain, in effect maintaining the amount of snow in the modelled snowpack, whereas in reality the in- and out- fluxes may not be balanced. Excess snow therefore needed to be removed by enhancing sublimation, which was achieved by increasing the roughness length (z_0).

Given the exposed nature of the snow surface at this site, it was assumed that the key parameter to consider for further calibration of the modelled snow depth would

be one that influences the wind-driven compaction of the snow (i.e. D_1, D_2, D_3, E_1, E_2 or E_3 in Equations 5.16 and 5.17). Due to the constraints imposed by limited calibration data (one measurement per month), it was decided to concentrate on just one of these parameters. An initial sensitivity analysis on these parameters showed that the simulated snow depth RMSE is most sensitive to the value of E_1 and so this parameter was chosen for the calibration. The ensemble of 'good' parameter values obtained for A_2 and ρ_{ns} at the IOA calibration site were assumed to be applicable to the open bog site, and the model was run with a sequence of values for E_1 between 0 and 10 m s^{-1} (twice the default Liston et al. (2007) value) for each member of this ensemble.

5.3 Results

5.3.1 Calibration and validation of the IOA site

At the IOA site, the random parameter search found that values of $A_2 = 0.0289$ m^{-3} kg^{-1} and $\rho_{ns} = 119.95$ kg m^{-3} produced the lowest RMS error in the snow depth (RMSE = 0.07 m; Figure 5.6). The calibration plots (Figure 5.6) display broad minima, indicating a range of possible parameter values with very similar quality of fit to the available snow depth observations (a 'good' value range of 0.0192 – 0.0629 m^{-3} kg^{-1} for A_2 and 31.36 – 252.01 kg m^{-3} for ρ_{ns}, as shown by the dark blue points in Figure 5.6). Figure 5.7 highlights the equifinality in the parameterisation of A_2 and ρ_{ns}, governed by the trade-off between the density of fresh snow and the rate of compaction within the snowpack.

The model fits the observed snow depths well (RMSE = 0.07 m), but with some tendency to underestimate the depth in the first half of the winter (Figure 5.8, middle panel). There is a tendency in the calibration dataset for the density of the snow to

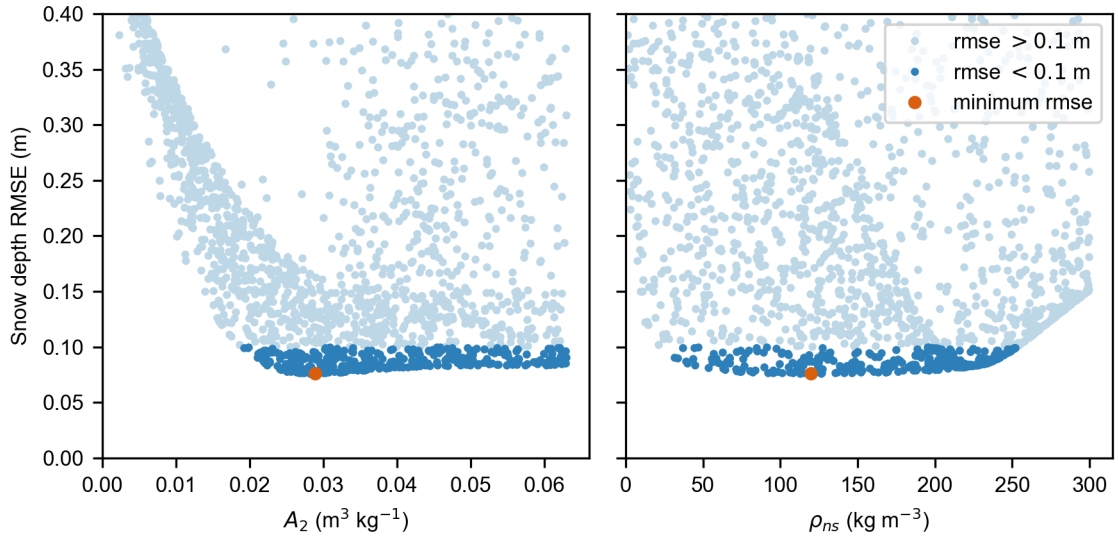

Figure 5.6: IOA calibration results from a random parameter search to find the optimal values for parameters A_2 and ρ_{ns}. Parameter values resulting in a snow depth RMSE $>$ 0.1 m are shown with pale blue points, dark blue points indicate where the depth RMSE is $<$ 0.1 m, and the orange point in each subplot shows the parameter value with the lowest associated error in the modelled snow depth.

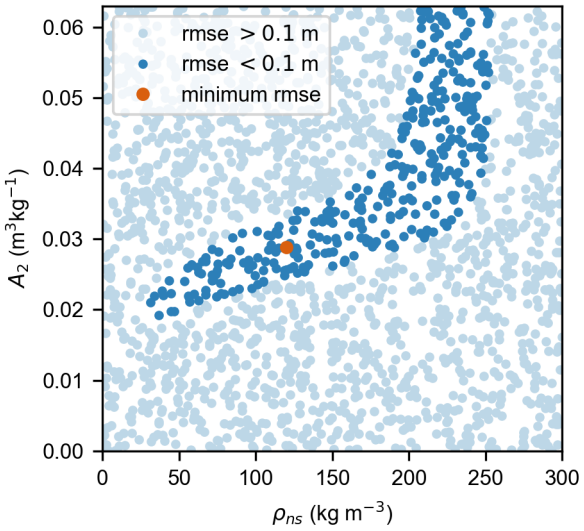

Figure 5.7: IOA calibration: equifinality in the snow density parameters A_2 and ρ_{ns}.

be overestimated by the model, particularly early in the snow season, although the quality of the fit varies between years (overall RMSE = 38.25 kg m^{-3}; Figure 5.8, bottom panel).

When run with the evaluation data sets, the mean ensemble snow depth RMSE is sim-

ilar to the calibration runs (RMSE = 0.08 m) and fits the observations well, although with some notable overestimation between Feb – May 2012 and underestimation between Dec – Feb 2014 (Figure 5.9, middle panel). The snow density RMSE for the mean ensemble is 49.88 kg m^{-3} and the simulations tend to overestimate the observed densities across all three years, an effect that again is particularly noticeable early in the snow accumulation period (Figure 5.9, bottom panel).

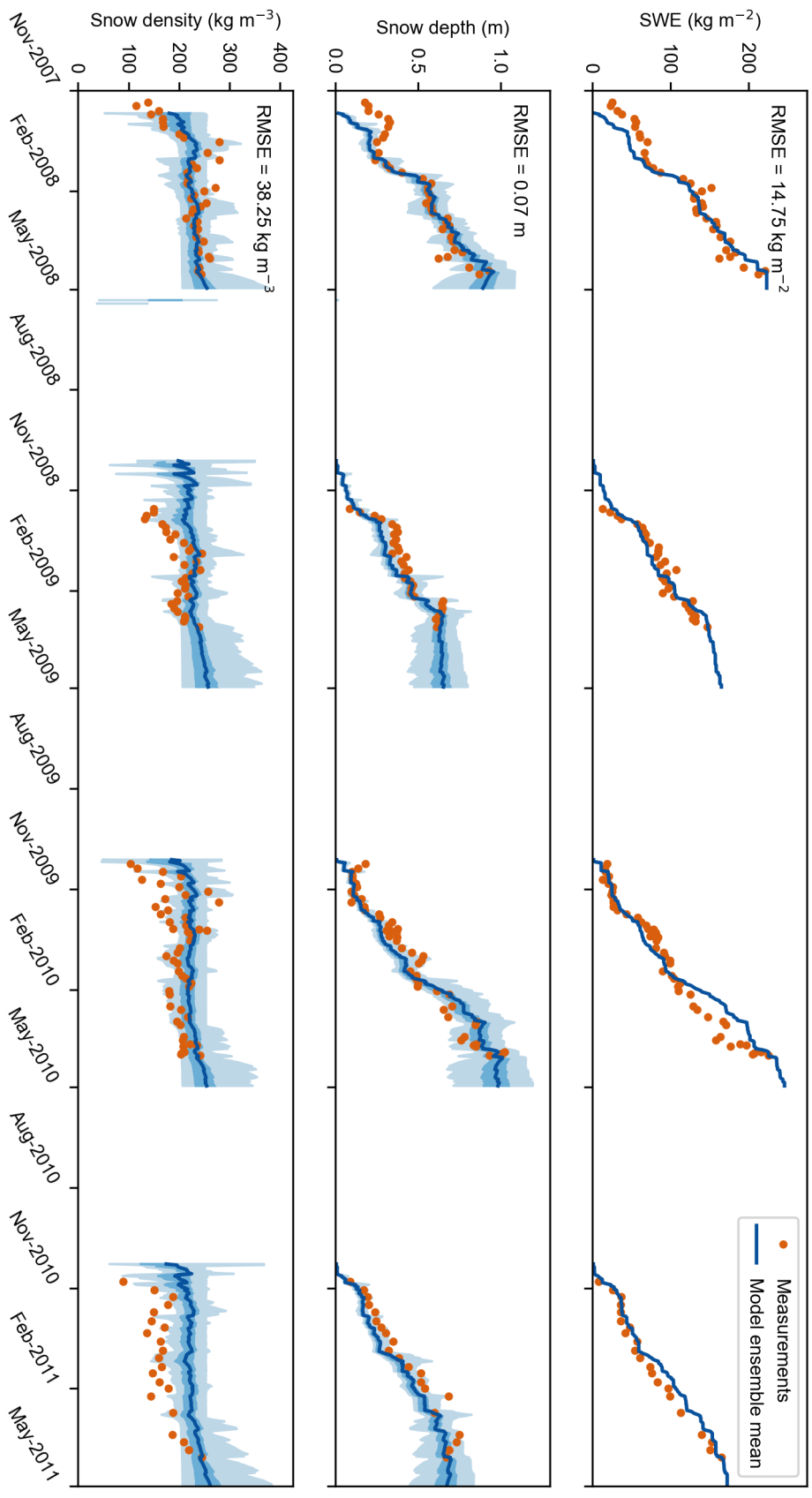

Figure 5.8: Ensemble model run following calibration with the IOA observational snow data (2007 – 2011). The model was run with an ensemble of 'good' value combinations of the snow density parameters A_2 and ρ_{ns} (those that give a depth RMSE < 0.1 m). The mean of this ensemble is shown by the solid blue line, the light blue and dark blue shaded areas represent the full range and inter-quartile range of the model ensemble respectively. The orange dots are the observational snow data. The RMSE of the mean ensemble is given in each panel: simulated SWE RMSE = 14.75 kg m^{-2}; simulated snow depth RMSE = 0.07 m; and simulated snow density RMSE = 38.25 kg m^{-3}.

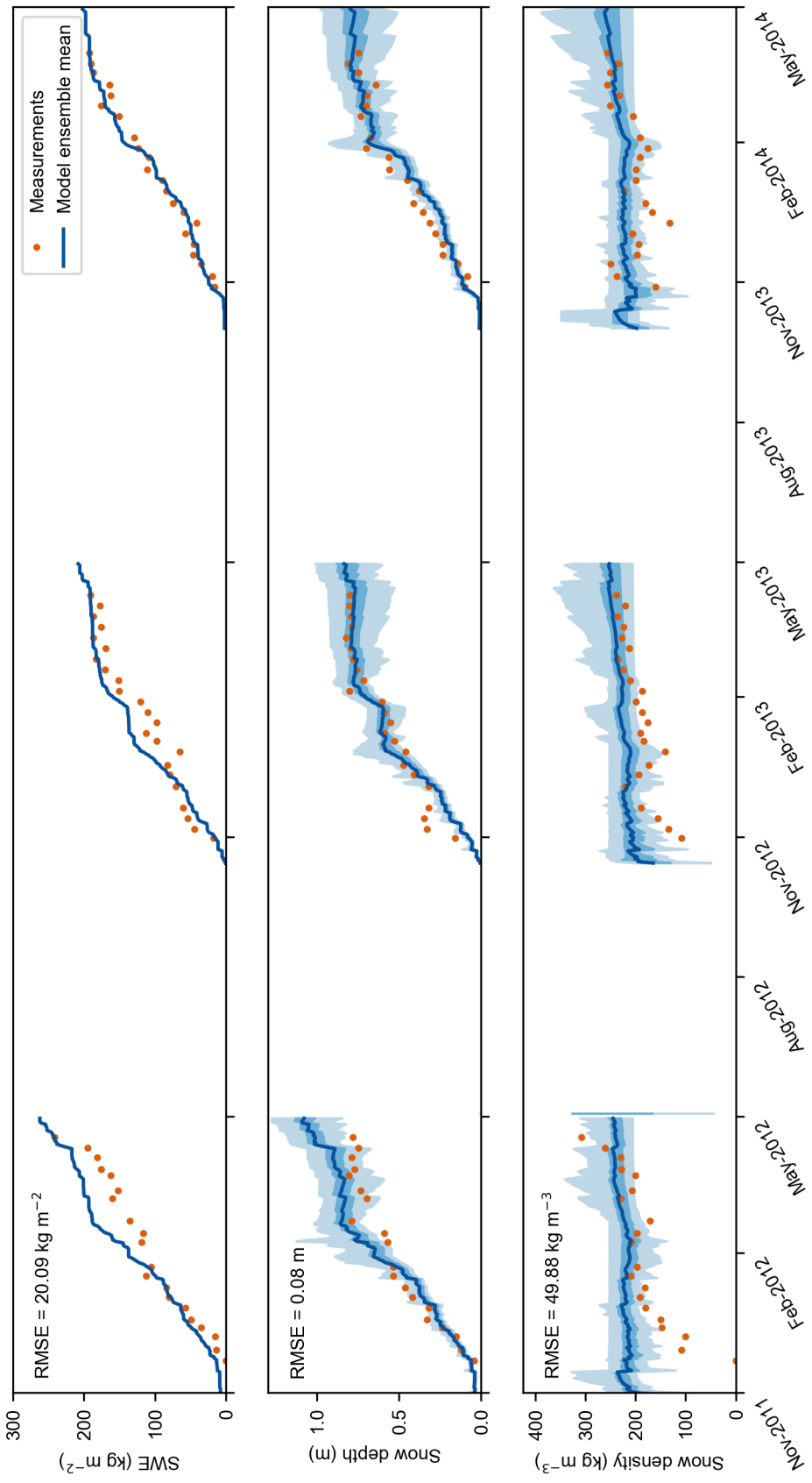

Figure 5.9: Evaluation of the calibrated snow model with observational snow data from the IOA (2011 – 2014). The model was run with an ensemble of 'good' value combinations of the snow density parameters A_2 and ρ_{ns} (those that give a depth RMSE < 0.1 m). The mean of this ensemble is shown by the solid blue line, the light blue and dark blue shaded areas represent the full range and inter-quartile range of the model ensemble respectively. The orange dots are the observational snow data. The RMSE of the mean ensemble is given in each panel: simulated SWE RMSE = 20.09 kg m^{-2}; simulated snow depth RMSE = 0.08 m; and simulated snow density RMSE = 49.88 kg m^{-3}.

5.3.2 Calibration and validation of the forest site

The forest site required a two step calibration process: first calibrating the modelled SWE (via adjustment of the LAI) to account for snow intercepted by the canopy and then calibrating the modelled snow depth (via parameterisation of A_2 and ρ_{ns}). In the first stage, there was a clear minimum in the modelled SWE RMSE with an LAI of 2.20 (RMSE = 12.85 kg m^{-2}), which is a reasonable estimate for the LAI at Sodankylä (Figure 5.10).

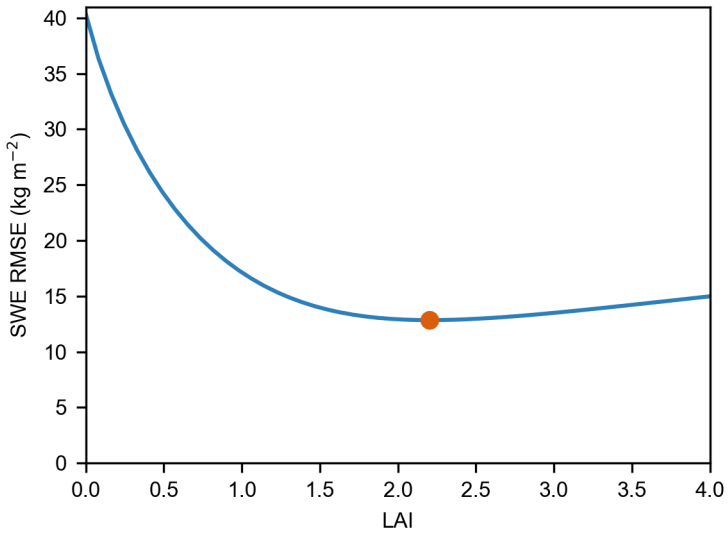

Figure 5.10: Relationship between the RMS error in the simulated SWE at the forest site and the LAI. The orange dot indicates the minimum SWE RMSE, which is 12.85 kg m^{-2} at $LAI = 2.20$.

The RMS error in the snow depth is most strongly controlled by the value of ρ_{ns} (Figure 5.11), with an optimal value for $\rho_{ns} = 48.88$ kg m^{-3} (depth RMSE = 0.08 m). Comparing the time series of snow depths in the calibration period, the RMSE for the mean model ensemble is 0.07 m, with the observed snow depths almost all falling within the uncertainty range of the ensemble depths (Figure 5.12). The RMSE of the ensemble mean snow density is 20.80 kg m^{-3} and matches the observations well but tends to overestimate (Figure 5.12, bottom panel).

The evaluation of the model shows that it continues to perform well under validation

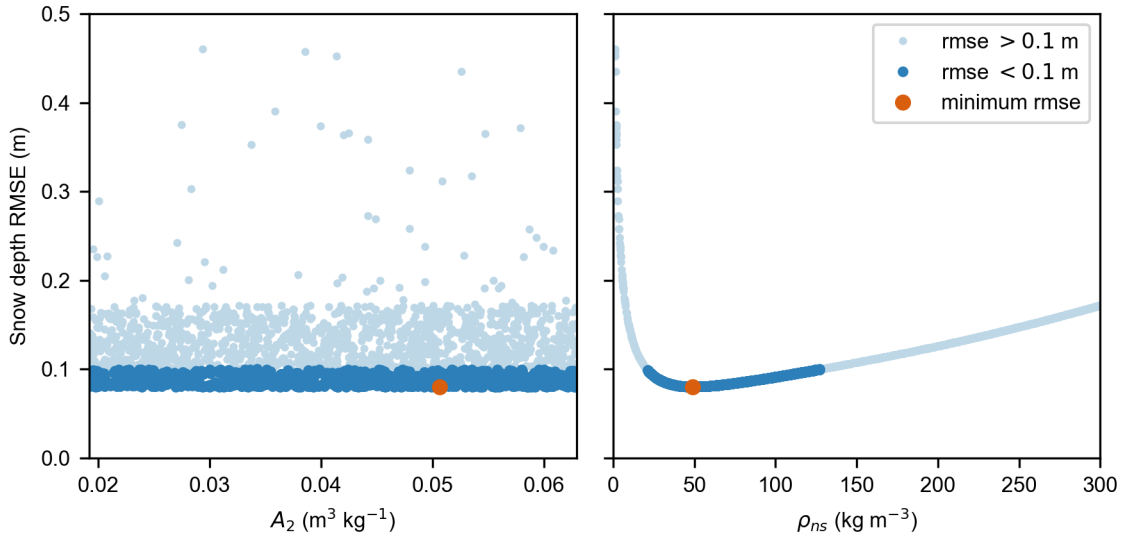

Figure 5.11: Forest calibration results from a random parameter search to find the optimal values for parameters A_2 and ρ_{ns} (value range of A_2 informed by the IOA calibration results). Parameter values resulting in a snow depth RMSE $>$ 0.1 m are shown with pale blue points, dark blue points indicate where the depth RMSE is $<$ 0.1 m, and the orange point in each subplot shows the parameter value with the lowest associated error in the modelled snow depth.

with a new data set. The RMSE in modelled SWE is higher (RMSE $=$ 19.37 kg m^{-2}) and most notably the model overestimates the SWE towards the end of the 2011/12 period and across the middle of the 2012/13 period, while underestimating the SWE for the 2013/14 period (Figure 5.13, top panel). The snow depth RMSE is 0.09 m and the model both matches and overestimates the observed depths in the first two years before tending to underestimate the depths in the final year (Figure 5.13, middle panel). The errors in the simulated snow depth correspond with the model misfit to the observed SWE. The snow density RMSE for the mean model ensemble is 17.37 kg m^{-3}, which is lower than the calibration error (Figure 5.13, bottom panel).

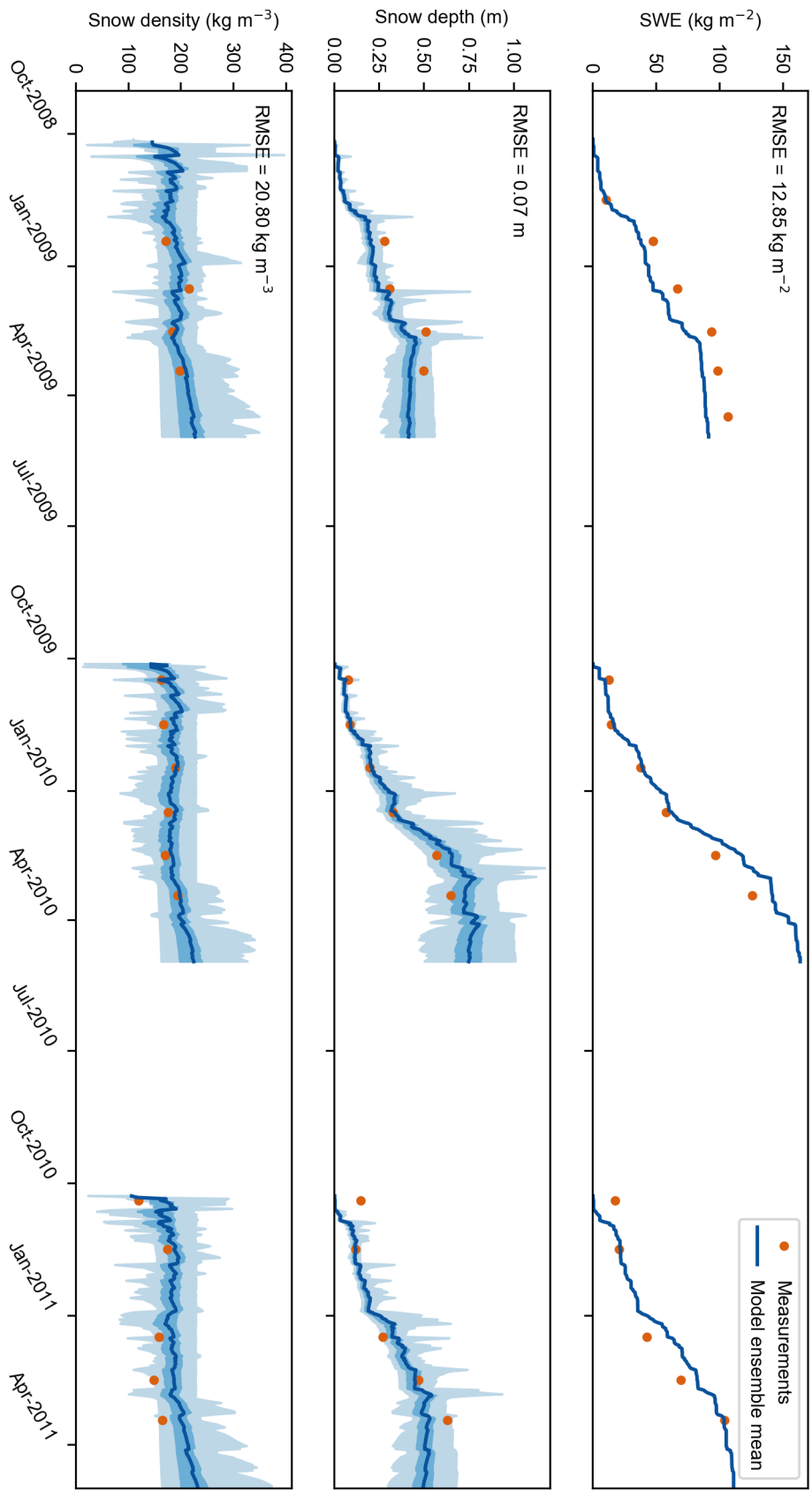

Figure 5.12: Ensemble model run following calibration with the forest site observational snow data (2008 – 2011). The model was run with an ensemble of 'good' value combinations of the snow density parameters A_2 and ρ_{ns} (those that give a depth RMSE < 0.1 m). The mean of this ensemble is shown by the solid blue line, the light blue and dark blue shaded areas represent the full range and inter-quartile range of the model ensemble respectively. The orange dots are the observational snow data. The RMSE of the mean ensemble is given in each panel: simulated SWE RMSE $= 12.85$ kg m^{-2}; simulated snow depth RMSE $= 0.07$ m; and simulated snow density RMSE $= 20.80$ kg m^{-3}.

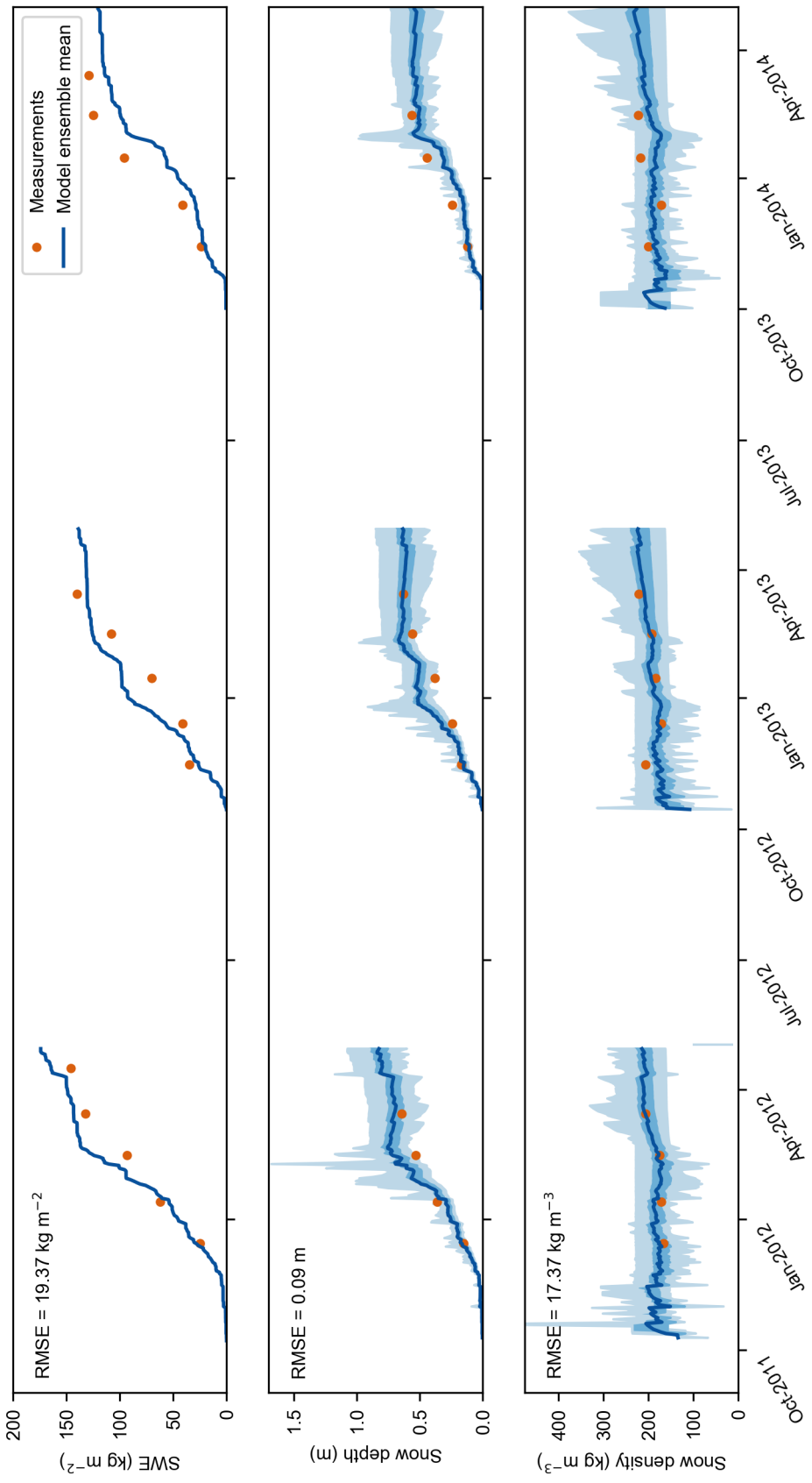

Figure 5.13: Evaluation of the calibrated snow model with observational snow data from the forest site (2011 – 2014). The model was run with an ensemble of 'good' value combinations of the snow density parameters A_2 and ρ_{ns} (those that give a depth RMSE < 0.1 m). The mean of this ensemble is shown by the solid blue line, the light blue and dark blue shaded areas represent the full range and inter-quartile range of the model ensemble respectively. The orange dots are the observational snow data. The RMSE of the mean ensemble is given in each panel: simulated SWE RMSE = 19.37 kg m^{-2}; simulated snow depth RMSE = 0.09 m; and simulated snow density RMSE = 17.37 kg m^{-3}.

5.3.3 Calibration and validation of the bog site

At the bog site, a similar two step calibration process was also required: first calibrating the modelled SWE (via adjustment of z_0) and then calibrating the modelled snow depth (via parameterisation of E_1). In the initial calibration step, the error in the SWE indicated a good constraint for the optimum value of $z_0 = 0.272$ m (Figure 5.14).

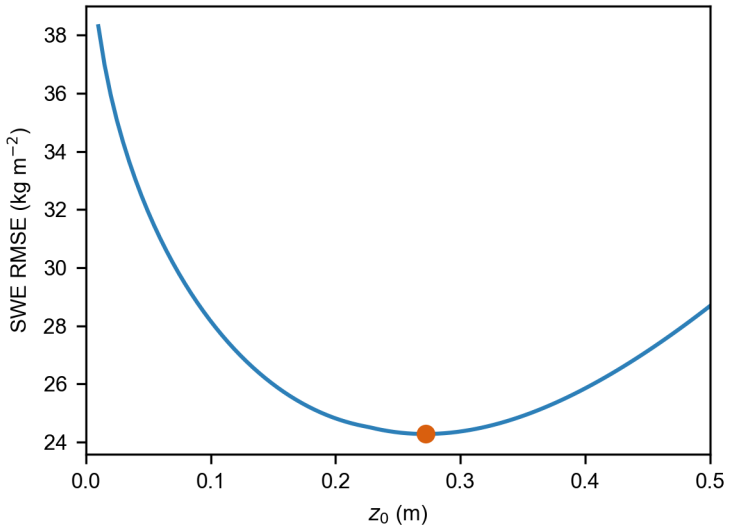

Figure 5.14: Adjustment of the roughness length (z_0) to calibrate the modelled SWE at the bog site. The orange dot indicates the minimum SWE RMSE, which is at $z_0 = 0.272$ m.

Across the tested parameter range for E_1 (0 m s^{-1} – 10 m s^{-1}), the RMSE for the modelled snow depth varied by $<$ 0.5 cm. As the sensitivity of E_1 to the available calibration data was so low, E_1 was set to the default Liston et al. (2007) value of 5 m s^{-1} (the same approach taken with parameters A_1 and B).

Looking first at the calibration period, snow depth RMSE for the mean model ensemble is 0.08 m (Figure 5.15, middle panel). The model underestimates the snow depth in the first period (2008-09) and this mismatch is also seen in the modelled SWE for this period (Figure 5.15, top panel). The model generally fits the observed depths well for the next two snow periods, with some under- and over-estimation outside

of the ensemble uncertainty during the 2010-11 period. The RMSE of the ensemble mean snow density is 70.11 kg m^{-3}. The model matches the measured densities well for the first period (2008 – 09) and overestimates the densities in the subsequent two periods. There is a very high observed density value at the start of the 2009 –10.

Overall the model performs reasonably well with the evaluation data set (Figure 5.16). The snow depth RMSE for the mean model ensemble is 0.10 m and the model matches the observational data particularly well in the first snow period (2011–12), with some over- and under-estimation in the later years. The model continues to tend towards over-estimating the density and the RMSE for the mean ensemble is 46.36 kg m^{-3}. The RMS error in the SWE is 31.31 kg m^{-2} and the model was unable to match the measured values in the 2012–13 and 2013–14 periods in particular.

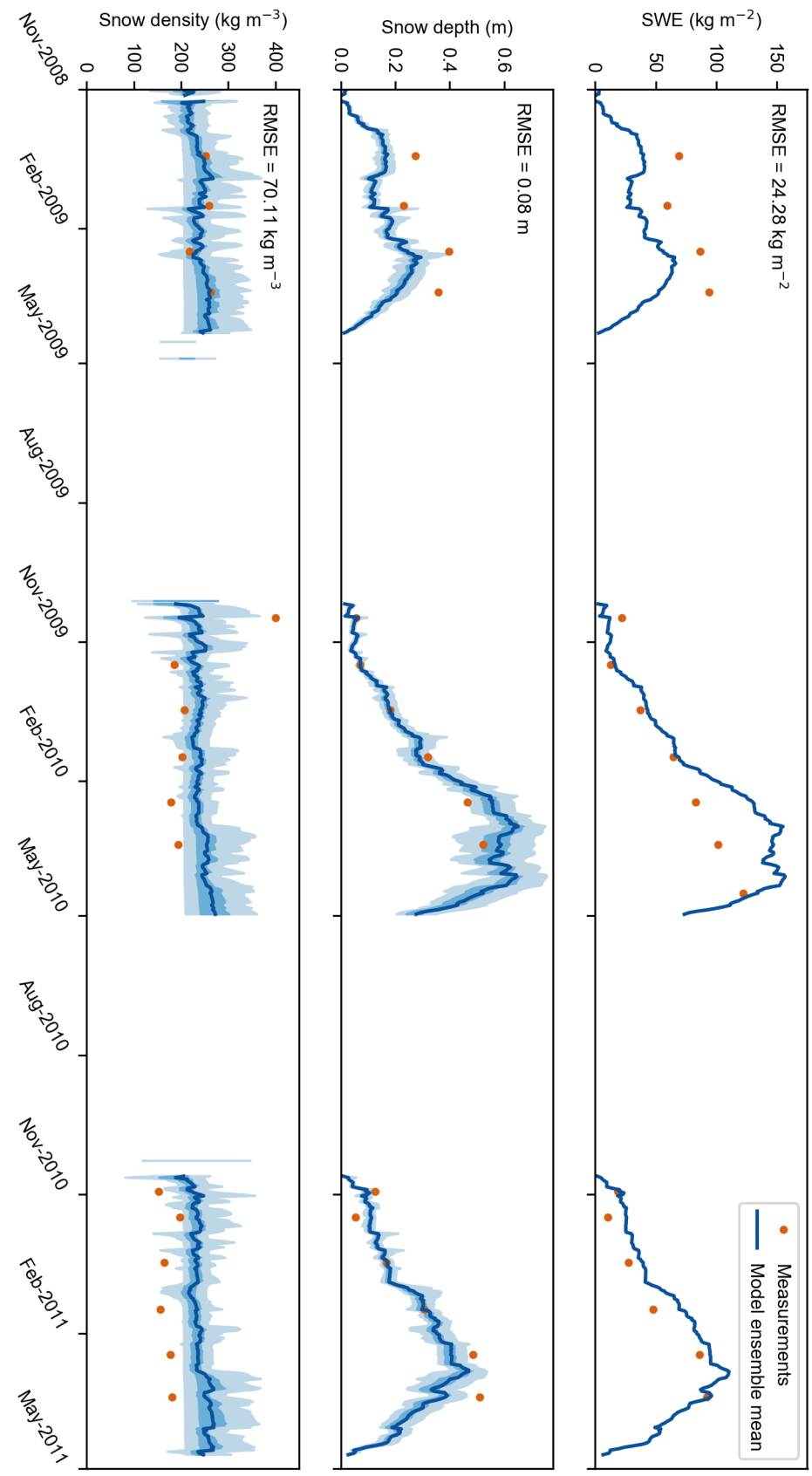

Figure 5.15: Ensemble model run following calibration with the bog site observational snow data (2008 – 2011). The model was run with an ensemble of 'good' value combinations of the snow density parameters A_2 and ρ_{ns} (those that give a depth RMSE < 0.1 m). The mean of this ensemble is shown by the solid blue line, the light blue and dark blue shaded areas represent the full range and inter-quartile range of the model ensemble respectively. The orange dots are the observational snow data. The RMSE of the mean ensemble is given in each panel: simulated SWE RMSE = 24.28 kg m^{-2}; simulated snow depth RMSE = 0.08 m; and simulated snow density RMSE = 70.11 kg m^{-3}.

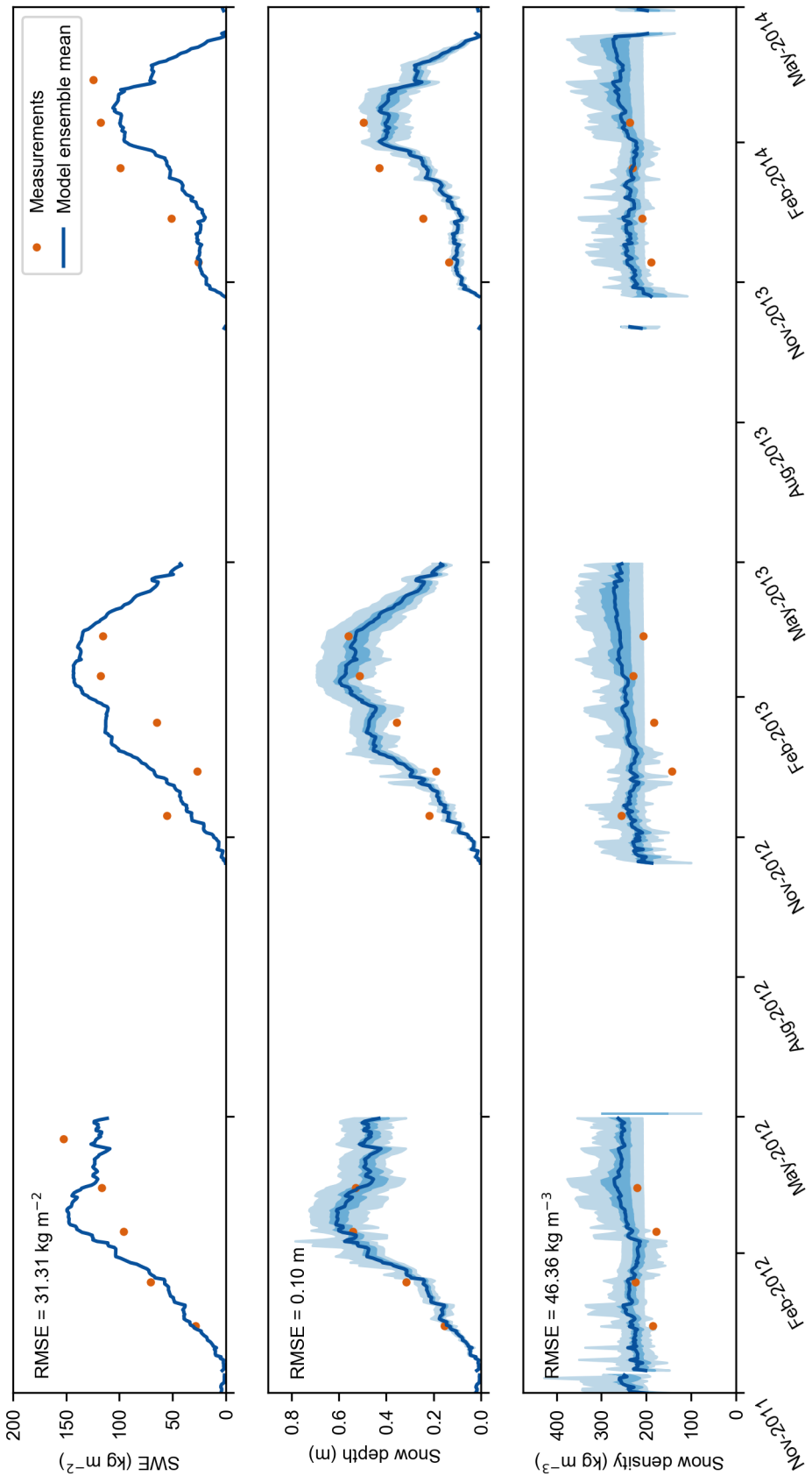

Figure 5.16: Evaluation of the calibrated snow model with observational snow data from the bog site (2011 – 2014). The model was run with an ensemble of 'good' value combinations of the snow density parameters A_2 and ρ_{ns} (those that give a depth RMSE < 0.1 m). The mean of this ensemble is shown by the solid blue line, the light blue and dark blue shaded areas represent the full range and inter-quartile range of the model ensemble respectively. The orange dots are the observational snow data. The RMSE of the mean ensemble is given in each panel: simulated SWE RMSE $= 31.31$ kg m^{-2}; simulated snow depth RMSE $= 0.10$ m; and simulated snow density RMSE $= 46.36$ kg m^{-3}.

5.4 Discussion

Using observational snow data collected at three different sites at FMI-ARC in northern Finland, site-specific calibrated parameter sets were reached for a simple snow accumulation model.

A stepwise procedure was used, making use of the varied characteristics of the three sites to calibrate the different components of the mass balance. However, with the available calibration data it was not possible to provide robust constraints on several of the parameters. Where parameters were insensitive to the available calibration data, it was necessary to refer to published literature values (Liston et al. 2007). At the IOA site, from which there was most available data, it was possible to provide some constraints on the A_2 parameter, which contributes to determining the compaction rate, and the fresh snow density parameter (ρ_{ns}). However, the acceptable parameter ranges were broad, with multiple potential combinations of values that give a snow depth RMSE $<$ 0.1 m. This reflects a trade-off within the parameter space that was not resolvable with the existing survey data. As the measurements are spaced apart by a few days, it is challenging to determine whether the observed snow density is the result of low density snowfall (low ρ_{ns}) and fast compaction (high A_2), or vice versa.

This phenomenon of multiple equally good parameter combinations defines 'equifinality' (e.g. Beven 1993b), which rejects the idea of an optimal (singular) parameter set. Instead, there are many different parameter sets (and model structures) that may produce the observed behaviour of the modelled system to an acceptable degree, and should therefore be included within an assessment of model uncertainty. In this instance, the uncertainty in the model calibration was propagated using an ensemble of 'good' parameter combinations (those which result in misfits to the observed snow depths of $<$ 0.1 m). In many cases this was sufficient to fit the observations within

uncertainty, although the uncertainty ranges were typically large. Large uncertainties in the calibrated models are perhaps inevitable given the limitations imposed by the data available to drive the model and constrain the simulated snow depth and density measurements.

The driving met data for the model was measured at the AWS, which is situated nearby but not exactly co-located with the three snow measurement sites used here. The snowfall data was pre-processed to scale with the IOA (Essery et al. 2016), and required further calibration to account for interception of snow by the canopy at the forest site and loss of snow mass via wind-blown snow at the exposed open bog sites. Errors from the SWE time series propagate through to affect the simulated depths and density (which is calculated from the SWE and depth in the model), which is clear from the temporal correlation in errors across these components in the simulations (Figures 5.9, 5.13 & 5.16). Therefore, as these simulated depths and densities may not be fully representative of the site-specific snowpack at the measurement points, this introduces noise into the calibration that propagates into greater uncertainty in the calibrated parameters.

The availability of observational snow data is a significant limitation of the calibration performed in this chapter. Some of the ranges for 'good' values of the parameters (those value that give a depth RMSE < 0.1 m) were broad and may encompass less realistic values (e.g. as seen by the very flat density simulations on the outer edges of the model ensemble at forest site). These reflect quite high uncertainty in the parameter value ranges resulting from just having a small amount of data to work with. This was a particular issue at the forest and bog sites where the spatial and temporal frequency of measurements was very low (1–2 measurements, approximately once a month). This produces high uncertainty because the measurements may not be very representative of these environments and it is difficult to capture temporal variations in the snow properties when the observations are made so infrequently.

Ideally, daily or sub-daily measurements at all sites would allow for a more detailed examination of the change in snow density over time following a snowfall event and would help reduce the predictive uncertainty of the calibrated model (to an extent, given equifinality).

Furthermore, as the observational snow data used here comes from point measurements at individual sites they are taken to represent specific environmental conditions, e.g. under canopy at the forest site, or with no canopy at the bog site. The purpose of the calibration was to calibrate and validate a model of snow accumulation with the aim to use this model to simulate snow accumulation across a series of hypothetical forest gap scenarios. While the model was shown to perform well at the individual sites, its performance has not been evaluated with transect data across a forest gap. Therefore it has to be assumed that it will bridge the data gap between forest and open environments in later forest gap simulations (Chapter 7). In future, collecting observational snow data from a forest gap transect(s) would be valuable for validating the model.

5.5 Conclusions

Using 6–7 years of observational data from FMI-ARC in northern Finland a simple snow accumulation model was calibrated at three different sites (the IOA (forest clearing), forest site and bog site).

Low availability of observational snow data presented a challenge to constraining the parameters within the calibration process, particularly in cases of low model error sensitivity to a certain parameter. This was particularly an issue at the forest and bog sites, where measurements where made most infrequently (once a month). Together with the effects of equifinality this uncertainty resulted in wide ranges of potential

parameter values for the calibrated model and so an ensemble of all 'good' values were used (those resulting in snow depth errors < 0.10 m). The calibrated ensemble model was shown to perform well across the range of sites, with RMS errors in the simulated snow depth ranging from 0.08 – 0.10 m during the model evaluation stage.

Increasing the spatial and temporal frequency of snow measurements would better capture changes in the observed snow properties over time (particularly during/after snowfall events) and provide further constraints on the calibration of the model parameters. Situating measurement points along a forest gap transect would also provide valuable information about the relationship between the evolution of snow properties over time and the position of the observed snowpack relative to the gap.

The following chapter (Chapter 6) details the approach taken to modelling the direct and diffuse radiation to sub-canopy snow across a forest gap transect.

Chapter 6

Modelling longwave and shortwave radiation to sub-canopy snow

6.1 Introduction

The annual melting of the seasonal snowpack in the spring is a significant hydrological event, with far-reaching influence on water resources in forested watersheds via streamflow timing and amount (Lundquist & Dettinger 2005, Sun et al. 2018), surface albedo and therefore accurate land-surface and climate modelling, biophysical processes such as biogeochemical cycling (Brooks & Williams 1999, Brooks et al. 2011), and vegetation dynamics (Rasmus et al. 2011, Trujillo et al. 2012, Wipf et al. 2009). Net radiation to the snow surface can account for up to 80% of available energy for snowmelt (Link & Marks 1999*a*, Marks & Dozier 1992) and is influenced by a host of factors, including solar angles, canopy characteristics, air temperature, and cloud cover (Musselman et al. 2015, Seyednasrollah et al. 2013).

The presence of a forest canopy modifies the radiative fluxes to the snow surface, producing spatial and temporal variations in the sub-canopy surface energy balance

when compared to adjacent open areas (Seyednasrollah et al. 2013). The canopy casts shadows and so reduces the amount of direct radiation reaching the underlying snow, whereas solar heating of the canopy enhances the longwave radiation to the snow (Sicart et al. 2004). Gaps in the canopy introduce further variability to the patterns of sub-canopy radiation: for example, snow in forest gaps is more exposed to solar radiation than under full canopy but can still receive the enhanced longwave radiation from the surrounding canopy (Bernier & Swanson 1993, Golding & Swanson 1978, Lawler & Link 2011, Musselman et al. 2015, Seyednasrollah & Kumar 2014).

This chapter outlines the approach taken to model the longwave radiation and the direct and diffuse components of the shortwave radiation incident to the sub-canopy snow surface. This work informs the energy-balance sub-model described in the next chapter (Chapter 7), in which the simplified FSM2 snow model described in Chapter 5 is expanded to include simulations of both snow accumulation and melt.

The structure of this chapter is as follows. First, the methods used to calculate the transmission of direct-beam shortwave radiation through the canopy are described and example gap scenarios presented. Next the diffuse shortwave and longwave components of the net radiation to sub-canopy snow are considered, both of which may be related to the sky view fraction (v_s). This section compares three different methods to estimate v_s, including analysis of both hemispherical photographs (from a forest road transect in northern Finland) and synthetic hemispherical images generated using real canopy metrics. Finally, the models of direct and diffuse radiation are evaluated using observational data from a forest clearing transect in northern Finland.

6.2 Modelling direct shortwave radiation

In this sub-section, I outline the methods used to estimate the amount of direct-beam shortwave radiation that is transmitted to the snow surface in a forest-gap environment. This includes a description of how the solar position is calculated (depending on location and time), ray-tracing to determine intersection points between a ray of light and the canopy and the calculation of transmission through the canopy. A selection of gap scenarios are presented as examples of the likely transmission of direct shortwave radiation in linear canopy gaps of different widths and orientations.

6.2.1 Calculating solar positions

This section details the calculation methods used to determine the solar position (which is represented by the angles of solar azimuth, α, and elevation, β, for a specific location at a given time and day in the year, as described in Oke (1978) unless otherwise stated. The azimuth describes the horizontal direction of the sun and the elevation angle is the angle between the sun and a level surface (Figure 6.1).

The solar elevation angle may be calculated as

$$\beta = \arcsin(\sin\phi \sin\delta + \cos\phi \cos\delta \cos\omega) \tag{6.1}$$

where ϕ is the latitude of the location of interest, δ is the solar declination and ω is the hour angle. The solar declination is the angle between the sun's rays and the equatorial plane and depends only upon the day of the year; it may be approximated from Iqbal (1983)

$$\delta = -23.4 \cos(360(t_j + 10)/365) \tag{6.2}$$

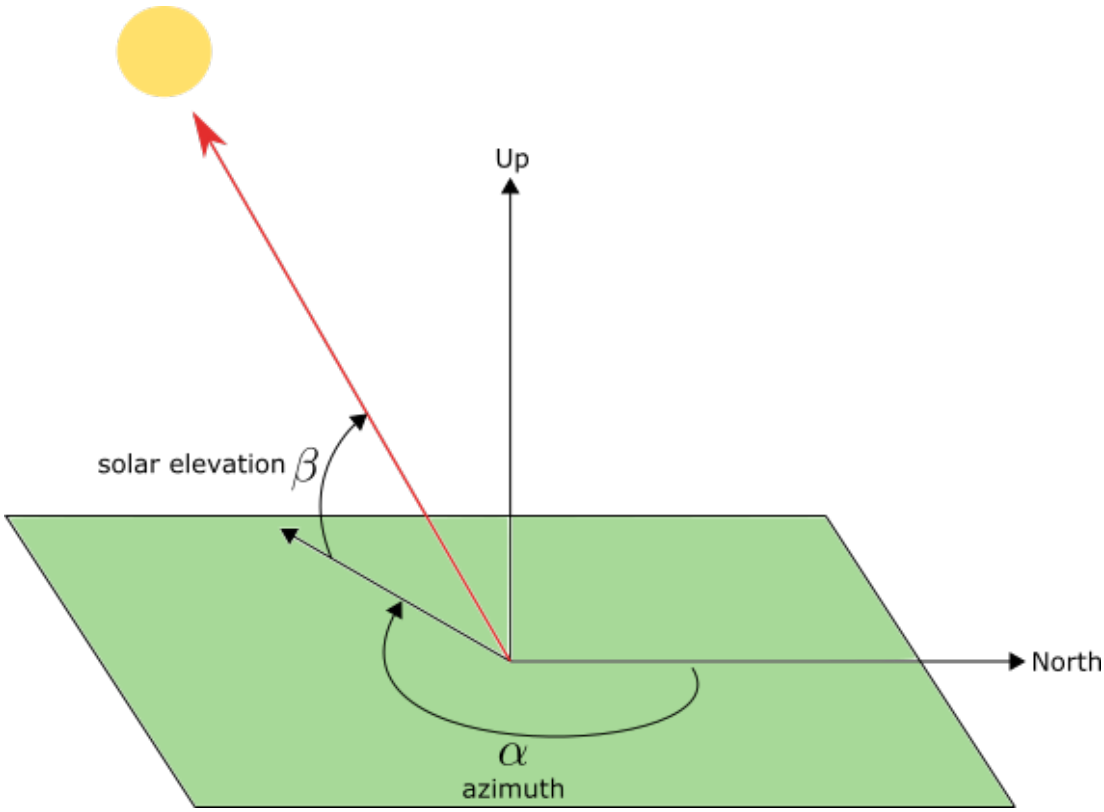

Figure 6.1: Schematic of the solar azimuth and elevation angles

where t_j the number of the day in the year. The hour angle is a function of the time of day and is the angle through which the earth would need to turn in order to bring the meridian (line of longitude) of the location of interest directly under the sun; 1 hour $\approx 15^\circ$ of rotation, and so the hour angle may be given by

$$\omega = 15(12 - t) \tag{6.3}$$

where t is the local apparent solar time (24 hr), which is found by:

(i) calculating the *local mean solar time*; for each degree of longitude the location is east or west of the standard meridian, add or subtract four minutes from local standard time

(ii) adding an *equation of time* correction (Et; Equation 6.4 (Iqbal 1983)) to the

local mean solar time (as calculated in (i))

$$Et = (0.000075 + 0.001868\cos(D) - 0.032077\sin(D) - 0.014615\cos(2D) - 0.040849\sin(2D))(12/\pi) \tag{6.4}$$

where D is the day angle such that: $D = 360(t_j - 1)/365$.

The solar azimuth may be calculated as follows

$$\alpha = \arccos((\sin\delta\cos\phi - \cos\delta\sin\phi\cos\omega)/\sin Z), \quad \text{if } t < 12 \tag{6.5a}$$

$$\alpha = 360 - \arccos((\sin\delta\cos\phi - \cos\delta\sin\phi\cos\omega)/\sin Z), \quad \text{if } t > 12 \tag{6.5b}$$

where Z is the solar zenith angle, the complementary angle to the solar elevation angle; $Z = 90 - \beta$.

As an example, Fig. 6.2 illustrates how the solar azimuth and elevation angles change through the year in Sodankylä (67.368° N, 26.633° E), the location of the FMI-ARC research station, highlighting the summer and winter solstices, and the vernal and autumnal equinoxes. As can be seen, during the summer solstice the sun remains above the horizon throughout the day and night, whereas during the winter solstice the sun remains below the horizon.

6.2.2 Ray trace model to calculate the path length of direct-beam shortwave radiation

The ray trace model presented here is used to calculate the path length, l, of a beam as it travels through a forest canopy, excluding any distance travelled through an idealised rectangular cuboid gap in the canopy, and is informed by the modelling study described by Musselman et al. (2015). For the purposes of the following calculations, the ray is taken to originate at the forest floor and travels in the direction of the sun.

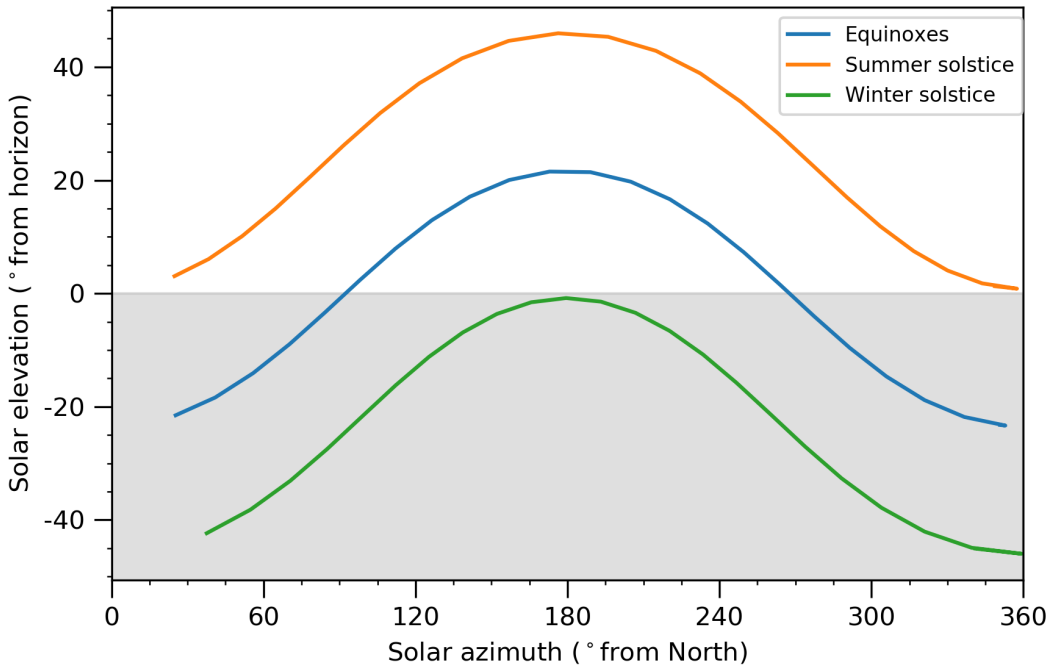

Figure 6.2: Solar azimuth and elevation angles for solstice and equinox days at Sodankylä in 2018

Intersection points between a ray and the gap are determined through an evaluation of the ray's origin, (x_0, y_0, z_0), relative to the gap edges, and the position of the sun in the sky (angles of azimuth, α, and elevation, β). Intersection points refer to points where the ray intersects a gap or canopy edge and are numbered according to their occurrence, for example the first intersection point is at (x_1, y_1, z_1), the second is at (x_2, y_2, z_2) and so on.

Five potential intersection cases between the ray and gap were identified as:

Case 1: The ray originates in a section of canopy and does not intersect the gap edge (Fig. 6.3), i.e. the ray travels through the canopy only.

Case 2: The ray originates in the gap (Fig. 6.4), it intersects with one gap edge (at x_1, y_1, z_1) and exits out the top of the canopy (at x_2, y_2, z_2).

Case 3: The ray originates in the gap and does not intersect the edge (Fig. 6.5), so that $l = 0$ and the beam is fully transmitted.

Case 4: The ray originates in one of the canopy sections, it intersects the gap edge, travels through the gap, intersects the second gap edge, travels through the canopy and then exits out the top of the canopy (see Figure 6.6). The canopy path length is equal to the total path length minus the distance travelled through the gap.

Case 5: The ray originates in one of the canopy sections, it intersects one gap edge and exits out of the top of the gap without travelling through any further canopy (see Figure 6.7). The path length is equal to the distance travelled from the ray's origin on the forest floor to the first intersection point.

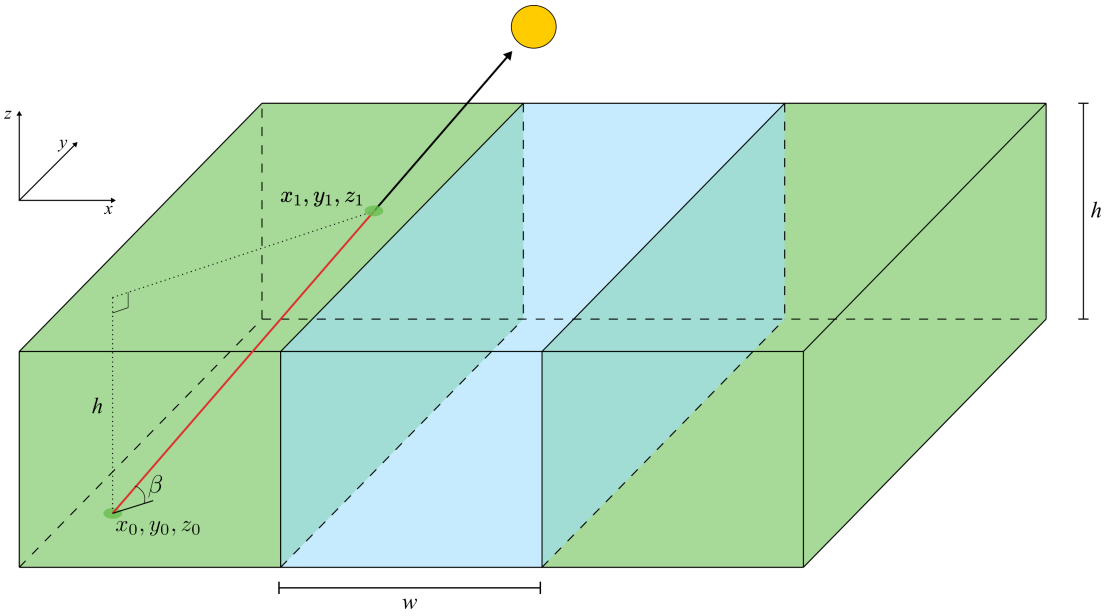

Figure 6.3: Case 1 where the ray travels through the canopy only. h is the canopy height and w is the gap width.

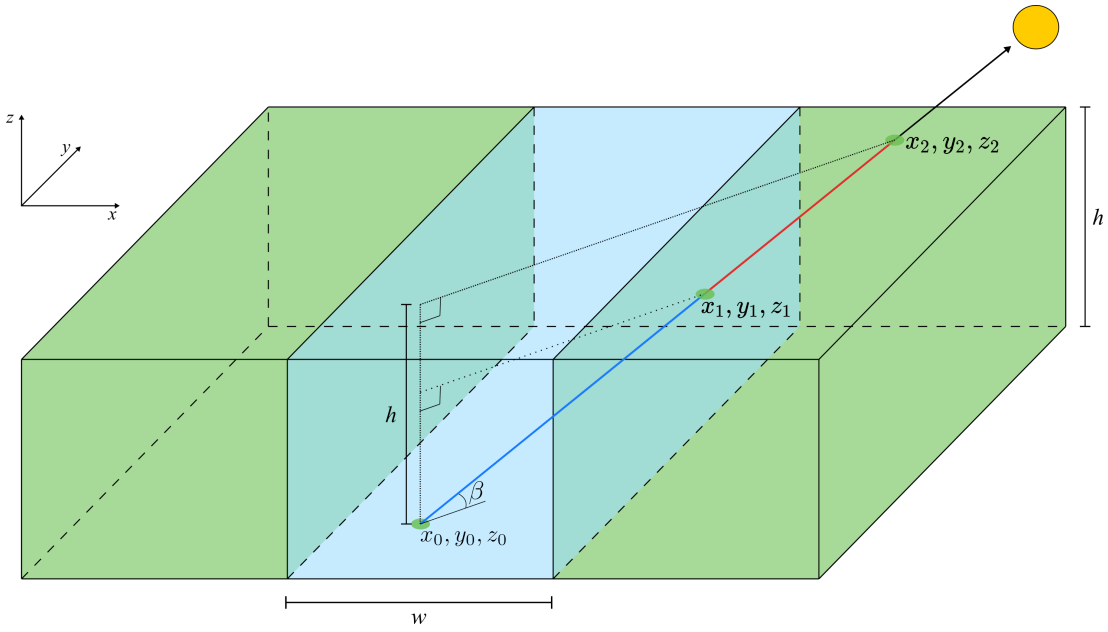

Figure 6.4: Case 2: the ray originates in the gap but travels partially through canopy.

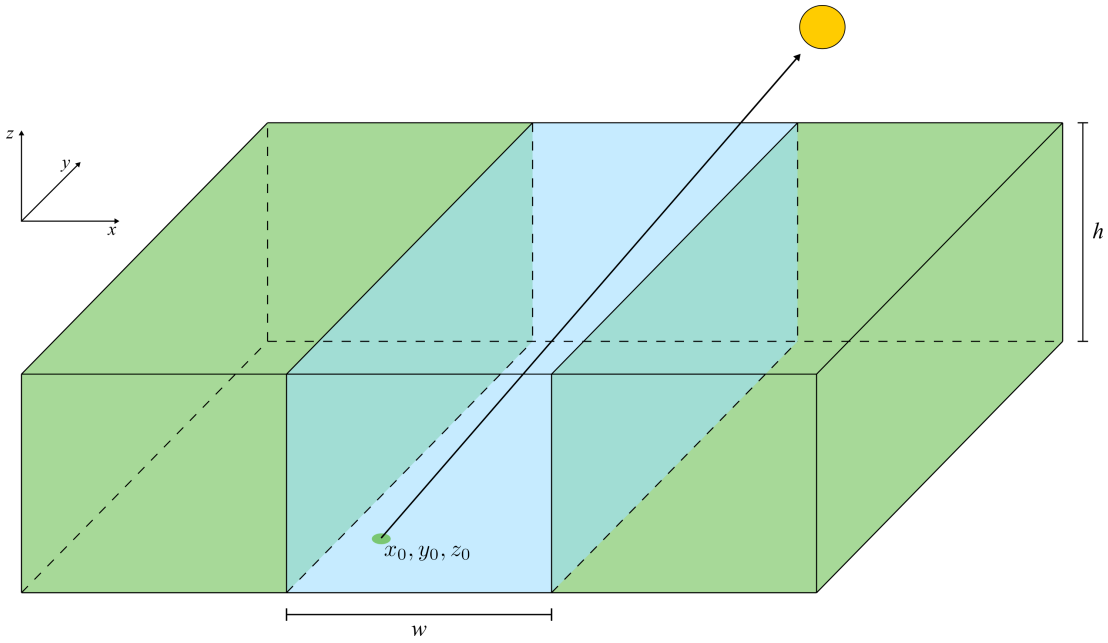

Figure 6.5: Case 3: the ray travels through the gap only.

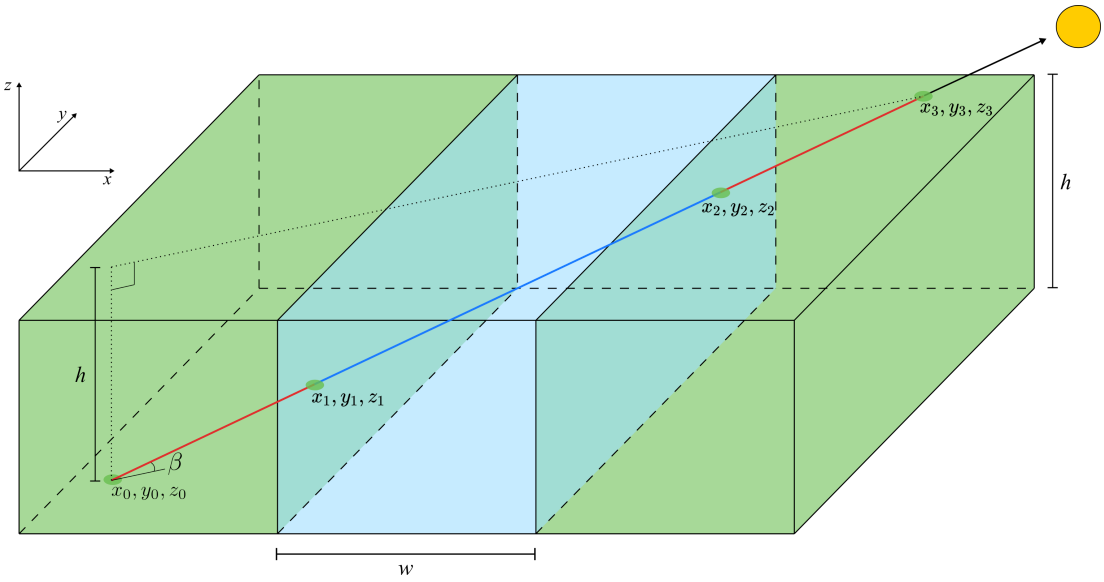

Figure 6.6: Case 4 where the ray travels through the canopy, intersects the gap at two points and then travels through further canopy.

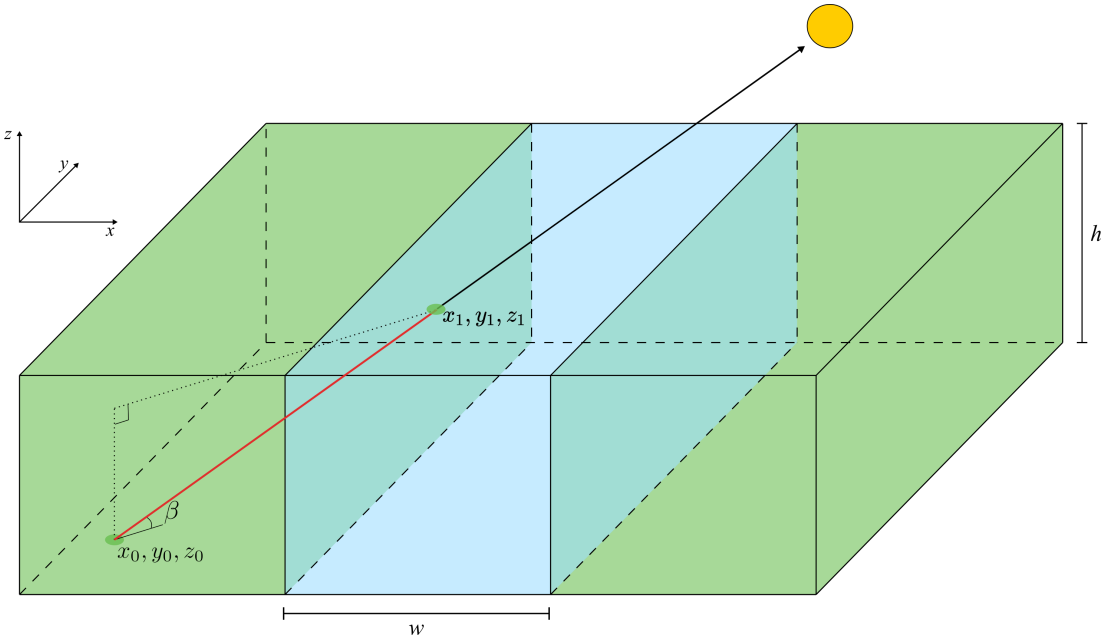

Figure 6.7: Case 5: the ray travels partly through the canopy and exits out the gap.

These five cases can be divided into two subsets:

i The ray originates in the forest (Cases 1, 4 & 5)

ii The ray originates in the gap (Cases 2 & 3)

The path length taken by the ray through forest canopy is then given by the following set of equations, depending on the relevant intersection case.

Take $y_0 = z_0 = 0$ without loss of generality, and take x_0 to be at distance d from the edge of the gap (of width w) that is away from the sun.

If the ray originates from a point in the forest

$$l = \begin{cases} \dfrac{h}{\sin\beta} & \text{case 1} \\ \dfrac{h}{\sin\beta} - \dfrac{w}{\cos\alpha\cos\beta} & \text{case 4} \\ \dfrac{d}{\cos\alpha\cos\beta} & \text{case 5} \end{cases} \tag{6.6}$$

where $h/\sin\beta$ is the total path length between the ground and the height of the canopy, $w/\cos\alpha\cos\beta$ is the distance the ray travels through the gap in case 4 and $d/\cos\alpha\cos\beta$ is the distance the ray travels through the canopy before entering the gap in case 5.

If the ray originates from a point in the gap

$$l = \begin{cases} \dfrac{h}{\sin\beta} - \dfrac{(w-d)}{\cos\alpha\cos\beta} & \text{case 2} \\ 0 & \text{case 3} \end{cases} \tag{6.7}$$

where $(w-d)/\cos\alpha\cos\beta$ is the distance the ray travels through the gap before entering the canopy in case 2.

The transmissivity of direct shortwave radiation through the canopy, τ_{dir}, can then be calculated as in Essery et al. (2007)

$$\tau_{dir} = e^{(-G\lambda l)} \tag{6.8}$$

where G is a projection function of the leaf orientation (assuming a random orientation, $G = 0.5$) and λ is the leaf area density ($LAD = LAI/h$).

6.2.3 Transmission of direct-beam solar radiation to gap and forest floor

The following section provides some example scenarios of the amount of direct solar radiation in gaps of different widths and orientations, using the ray tracing method described above. A surrounding forest canopy with height h = 15 m and LAI = 2 is assumed and is representative of the existing canopy at Sodankylä (Essery et al. 2016). A tree of height h casts a shadow of length $h/\tan\beta$ (Figure 6.8).

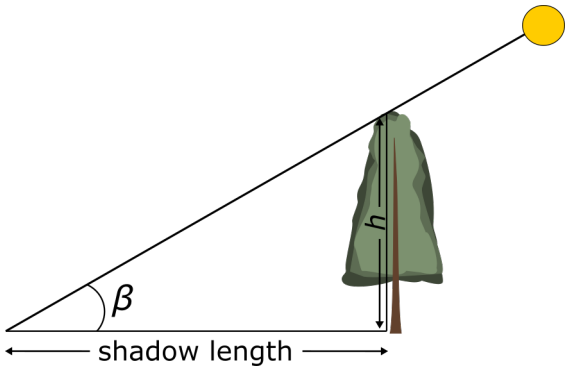

Figure 6.8: A tree of height h casts a shadow of length $h/\tan\beta$.

Figure 6.9 shows how the direct-beam transmissivity changes across forest gaps of widths 20 m and 40 m at noon on the spring equinox (21 March), which is approximately when snow starts to melt at Sodankylä. The solar elevation at this time and location is 22.5° and so the trees cast shadows that are 36 m long. In both gap

scenarios, transmissivity is constant in the forest south of the gap (ray trace case 3). Within the gap, transmissivity starts increasing (case 2) until it either reaches 1 (case 1) or the north edge of the gap. In the forest north of the gap, it either remains constant for a distance equal to the gap width (case 5) before decreasing, or immediately starts decreasing from 1 (case 4). After it decreases to the continuous forest value in distance $h/\tan\beta$, it remains constant (case 3).

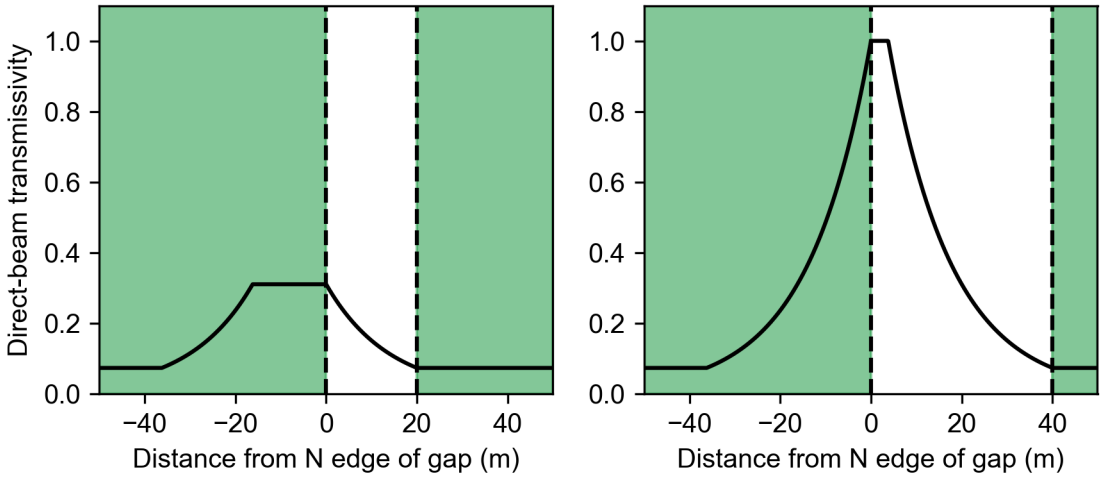

Figure 6.9: Direct-beam transmissivity in a 20 m gap (left) and a 40 m gap (right) with a 15 m high forest canopy on either side of the gap (shown by shaded green areas).

Forest gaps have a multitude of different potential orientations and this has an impact on the amount of direct solar radiation received in the gap and the surrounding canopy. Figure 6.10 provides a diagram of a forest gap of width w, as if looking down from above. The compass direction of the gap is given by the angle Φ, α is the solar azimuth and ϕ is the angle of the sun across the gap, which may be calculated from the first two angles as: $\phi = \alpha + \Phi - \frac{\pi}{2}$. The horizontal distance travelled by a ray of light across the gap is equal to $w/\cos\phi$.

Figure 6.11 shows 5-minute measurements of total and diffuse radiation on a sunny day in Sodankylä on the 21st March 2012. The dashed lines indicate functional fits to the data. The following standard function fits global radiation well without adjustment

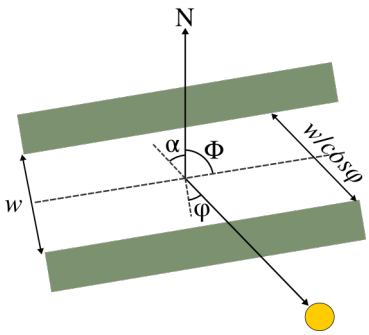

Figure 6.10: Diagram of a gap of width w and compass direction Φ. α is the solar azimuth and ϕ is the angle of the sun across the gap.

$$SW_{\downarrow} = (0.6 + 0.2 \sin \beta) I_0 \sin \beta \tag{6.9}$$

where I_0 is the solar constant ($= 1365$ W m^{-2}). Beer's law is used to fit the transmission of direct-beam solar radiation through the atmosphere

$$S_{dir} = \exp(\frac{-m}{\sin \beta}) I_0 \sin \beta \tag{6.10}$$

The RMSE is minimised with a value of $m = 0.229$. The combination of a good functional fit to direct-beam solar radiation and knowledge of the solar position allows for calculation of the direct-beam transmission for every minute of the day and, therefore, the ability to calculate the fraction of potential radiation that is received within a gap over the entire day.

Figure 6.12 shows the fraction of the total direct solar radiation received by 20 m and 40 m gaps in three different orientations: E-W (top panel); N-S (middle panel); SW-NE (bottom panel). For an E-W gap, the daily transmission values follow a very similar pattern to the noon transmissivity (Figure 6.9). This is because the length of the shadows cast across an E-W gap is almost constant at the equinox. The transmission peaks in the centre of the N-S gaps and on the west side of the SW-NE

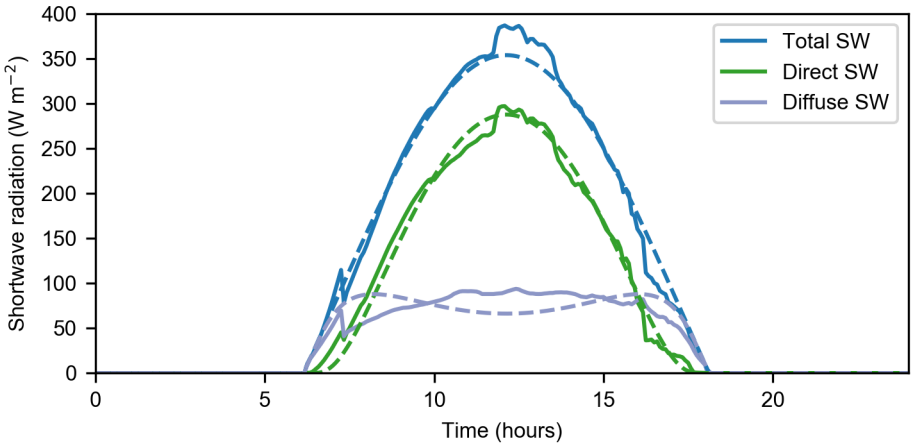

Figure 6.11: 5-minute measurements of total and diffuse radiation on a sunny day in Sodankylä on the 21st March 2012. The dashed lines indicate functional fits to the data. Beer's law is used for the transmission of direct-beam solar radiation.

gaps. The transmission patterns across a NE-SW gap of a given width would mirror that seen with the SW-NE gap of the same width. However, the effect of this on snow melt will differ between the two orientations as the SW-NE gap receives more direct radiation in the afternoon, which is when air temperatures are likely to be higher and so the snow more ready to melt (Figures 6.13 and 6.14). Gaps running N-S receive the most direct solar radiation and E-W gaps the least, with the difference between them being greatest when the gap width is approximately twice the surrounding canopy height (Figure 6.15).

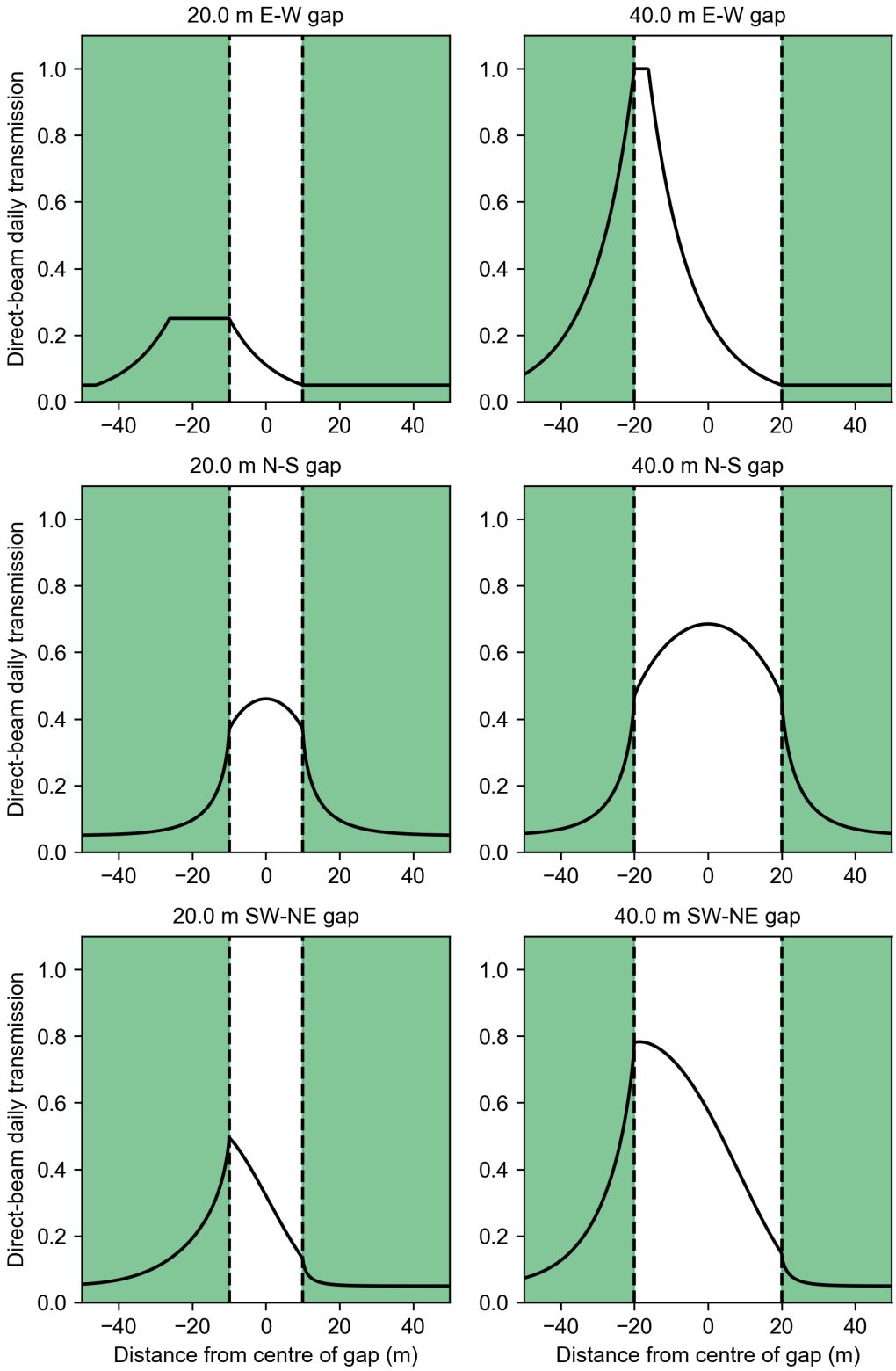

Figure 6.12: The fraction of total direct-beam solar radiation received in gaps of different widths (20 m and 40 m) and orientations(E-W, N-S and SW-NE) on 21st March 2012. There is a 15 m high forest canopy on either side of the gap (shown by the shaded green areas).

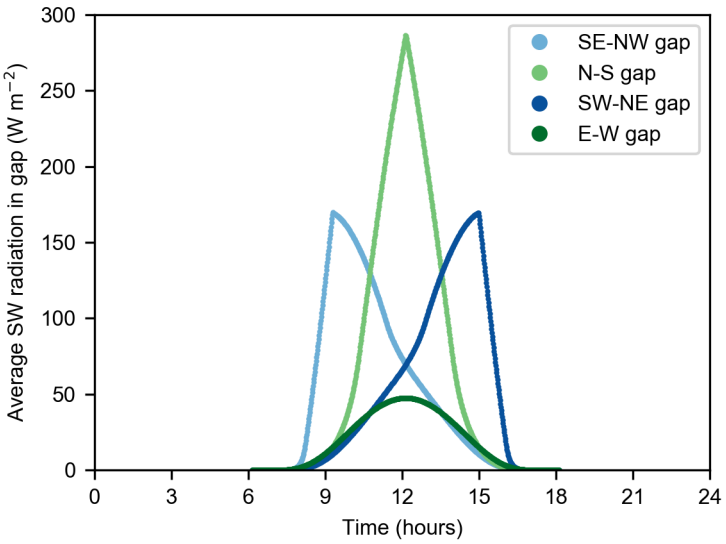

Figure 6.13: Variation with time in direct-beam shortwave radiation averaged across a 20 m gap with different orientations on 21st March 2012

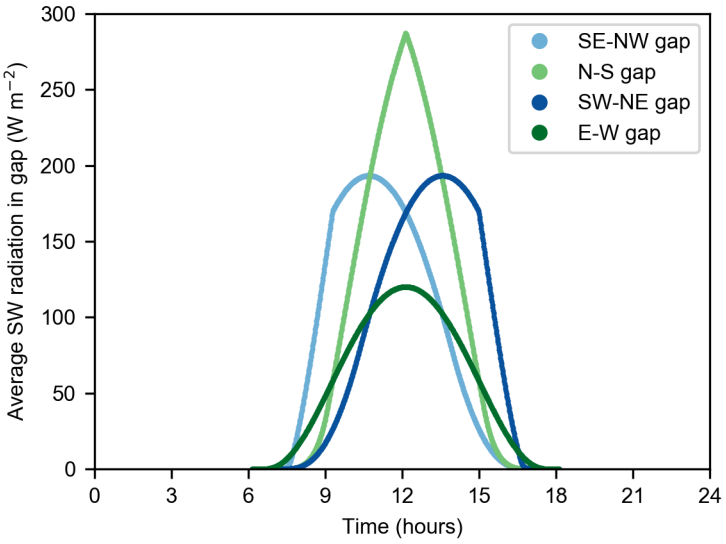

Figure 6.14: Variation with time in direct-beam shortwave radiation averaged across a 40 m gap with different orientations on 21st March 2012

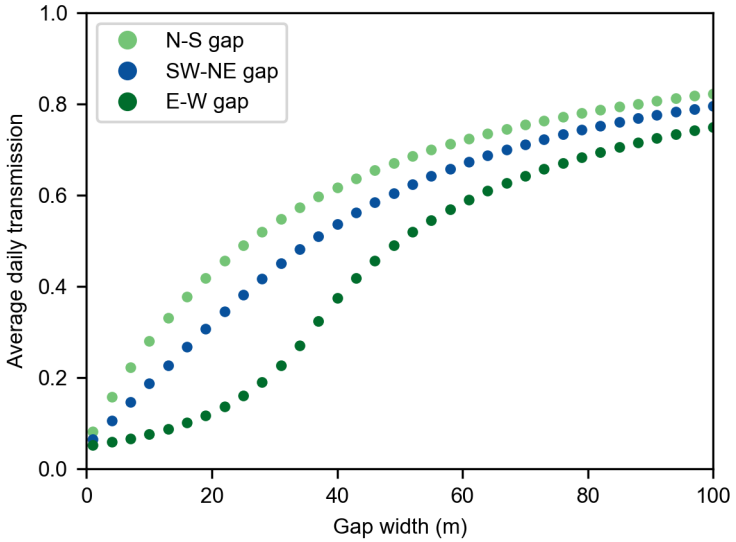

Figure 6.15: Variation in daily transmission of direct-beam shortwave radiation to gaps with different widths and orientations on 21st March 2012

6.3 Modelling diffuse radiation

The amount of diffuse radiation reaching the sub-canopy snow surface depends upon the amount of sky visible from a point on the forest floor. The transmission of diffuse shortwave radiation may be estimated simply as

$$\tau_{diff} = v_s \tag{6.11}$$

and sub-canopy longwave radiation (LW_c) can be calculated as a two-part model that uses the sky view to account for incoming longwave radiation from both the sky and the surrounding canopy

$$LW_c = v_s LW_a + (1 - v_s)\sigma T_c^4 \tag{6.12}$$

where LW_a is the incoming longwave radiation from the sky, σ is the Stefan-Boltzmann constant (5.67 x 10^{-8} W m^{-2} K^{-4}) and T_c is the canopy temperature (canopy emissivity is assumed to equal 1).

This section outlines the estimation of sky view fraction for the transmission of diffuse shortwave and longwave radiation across a forest-gap-forest transect. Three different methods of estimation, using either hemispherical photographs or synthetic hemispherical images from canopy models, are compared and contrasted.

First, the data collection methods are presented for the hemispherical photographs and canopy structure metrics (Subsection 6.3.1). Then the hemispherical photography processing and analysis steps are described (Subsection 6.3.2). In Subsection 6.3.3 the canopy models are introduced, and the creation of an artificial forest and synthetic hemispherical images explained. Finally, the three methods of estimating v_s

are compared and discussed.

6.3.1 Data collection

6.3.1.1 Hemispherical photographs

Upward-looking hemispherical photographs (hereafter referred to as hemiphotos) were taken during two field campaigns at FMI-ARC (see Chapter 4.2.1 for a detailed site description). The first set of hemiphotos were taken in April 2016, at the Road site (Figure 6.16 and see Chapter 4.2.1.3 for site description) when canopy structure measurements were also made (see section 6.3.1.2 for canopy metrics). Hemiphotos were taken of the overlying tree canopy at every wind measurement point along the transect at the Road site (Figure 6.17), using a Nikon Coolpix 4300 camera fitted with a fish eye lens (Nikon FC-E8 0.21x). The camera was mounted on a tripod at breast height (1.3 m), positioned with the lens facing up and with the top of the camera (i.e. where the control buttons are located) orientated to north. Correct and level positioning of the camera was ensured through the use of a spirit level and compass. Photographs were taken on overcast days to avoid glare from the sun, which can reduce the contrast between canopy elements and the sky. A second set of hemiphotos was taken by Richard Essery in April 2019, also at the Road site (Figure 6.18).

6.3.1.2 Forest canopy measurements

Canopy structure metrics of canopy height (h), crown base height (h_c), crown width (CW), diameter at breast height (DBH) and tree stocking density were used to inform the generation of an artificial forest. The following two sets of field measurements were used for this purpose

Figure 6.16: Photographs of the Road site at FMI-ARC showing the view along the road (left) and looking towards the road from within the trees to the north of the road (right).

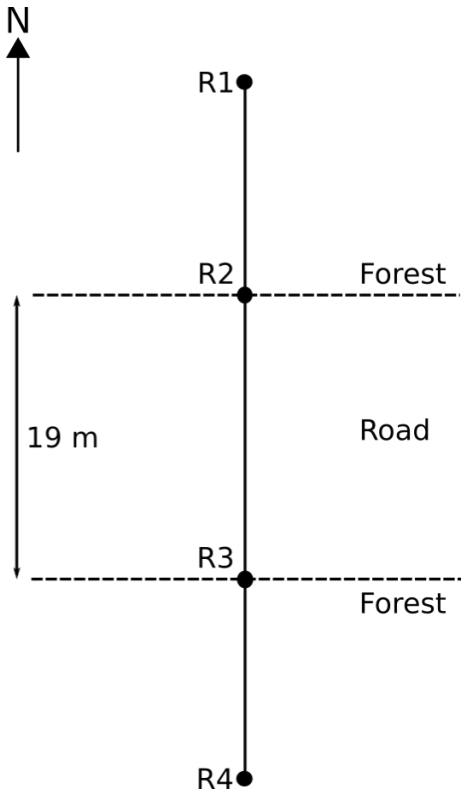

Figure 6.17: Map of hemiphoto locations at the Road site (April 2016).

1. Measurements made during the April 2016 field campaign (methods are described in detail in Chapter 4.2.1.7). Specifically, the data used here were collected at the Road site at FMI-ARC.

2. Measurements made by the Finnish Environment Institute (SYKE) in May 2011.

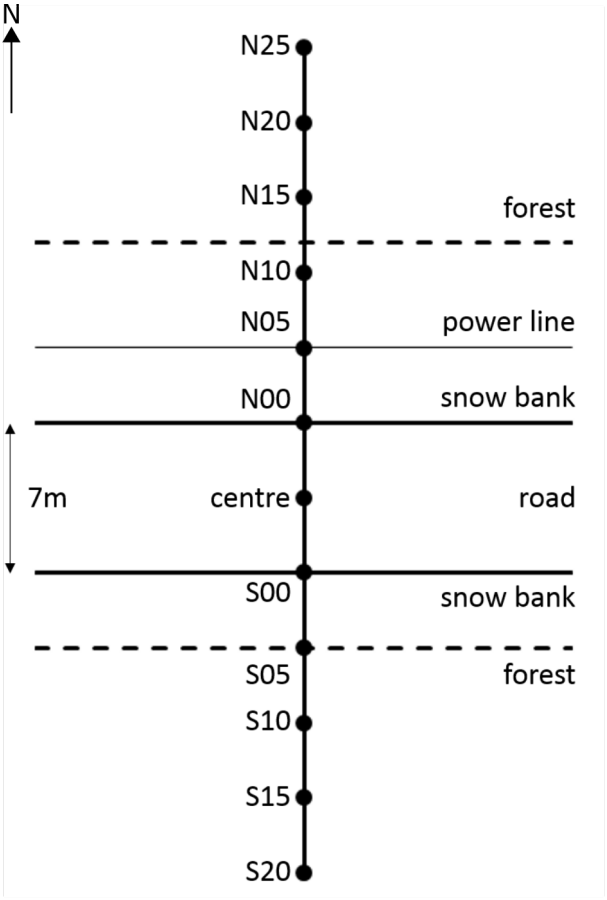

Figure 6.18: Map of hemiphoto locations at the Road site (April 2019).

6.3.2 Processing and analysis of hemispherical photographs

The hemiphotos were processed in python and values of sky view fraction v_s were calculated following Essery et al. (2008) (the code and data used for this are available at: `https://github.com/rmilodowski/thesis_hemiphotos`). First, the pixels in the hemiphoto are classified into two categories: vegetation and sky. This process is called binarization, or thresholding. A brightness threshold based on the grey intensity value is used to produce a binary image which masks the canopy; all pixels above the threshold value are classified as sky, and the remaining pixels are therefore classified as vegetation (e.g. see Figure 6.19.b.). A higher contrast between vegetation and sky filled pixels facilitates their classification. Therefore, the blue colour plane of the photograph is used for this type of analysis as there is low scattering of blue light by

leaves, which increases the contrast between the vegetation and sky.

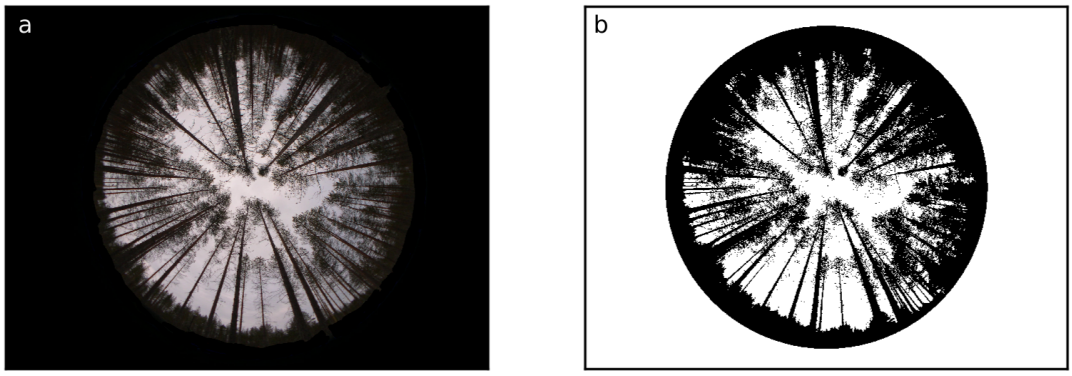

Figure 6.19: (a) Hemiphoto taken at the Road site, in the forest to the north of the road (N20 in Figure 6.18); (b) Corresponding masked image, which separates the sky and canopy according to the brightness threshold

When the threshold is applied to an image, any pixels containing snow will be classified as sky due to its light colour, which would result in overestimates of sky view fraction. To resolve this issue, all ground-level snow was edited out of the image using the open source image editor GIMP (GNU Image Manipulation Program, available to download here: `https://www.gimp.org`) as a pre-processing step prior to analysis. Specifically, the burn tool in GIMP was used to darken any pixels containing ground-level snow (Figure 6.20).

The threshold value used for categorising image pixels can be manually or automatically determined. To reduce subjective error that may be introduced through manual threshold selection, a binarization algorithm was used to automatically select an appropriate threshold value and is described as follows. A histogram of the grey level intensity of the blue colour plane was iteratively smoothed by a moving average function applied over three neighbouring values. This smoothing process was repeated until there was just a single minimum between two modes in the histogram. The bin of this minimum was then used as the threshold value. Glatthorn & Beckschäfer (2014) showed that this is an appropriate approach for the binarization of hemiphotos; in their accuracy assessment of a range of binarization algorithms this "histogram min-

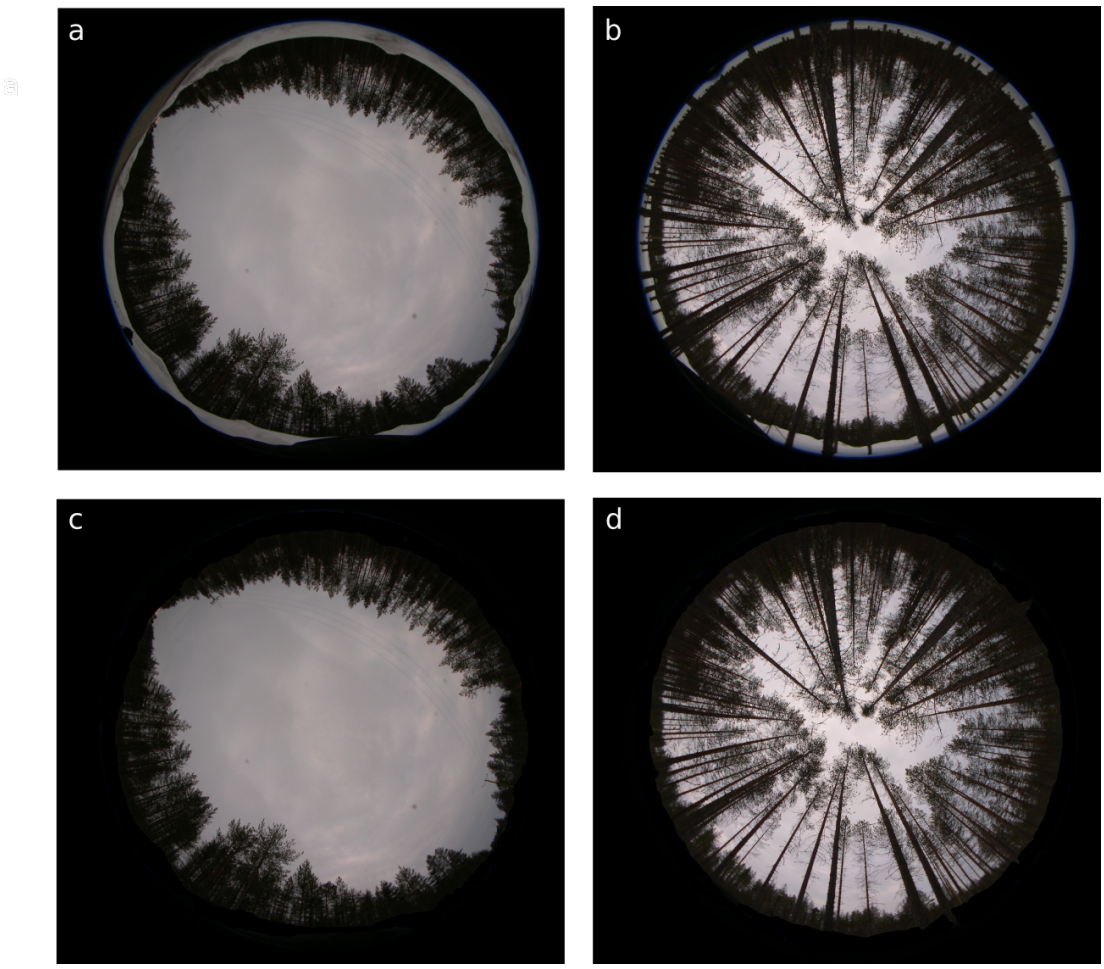

Figure 6.20: Example hemiphotos taken at the Road site: (a) at the road centre; (b) in the forest to the north of the road (N20 in Figure 6.18); (c) and (d) show the same images (a) and (b) (respectively) but with the snow edited out of the image

imum" method was found to be among the most accurate and produced the lowest number of pixel misclassifications.

As an example, figure 6.21 shows the grey level intensity histogram ("Original image") for the blue colour plane of a hemiphoto taken at the Road site (see figure 6.19.a.), in the forest to the north of the road (see Chapter 4.2.1.1 for further site details). The darker blue line is produced following application of the smoothing process ("Smoothed image"). In this case, it took 31 iterations of smoothing until there was a single minimum, which is located at a grey level intensity of 111. This threshold value was then used with the hemispherical analysis software described above to binarize the blue plane image of the photograph. The resulting canopy mask is shown

in Figure 6.19.b. and was used to calculate a value of v_s for this site location. The steps described here were applied to all hemiphotos used in the analysis.

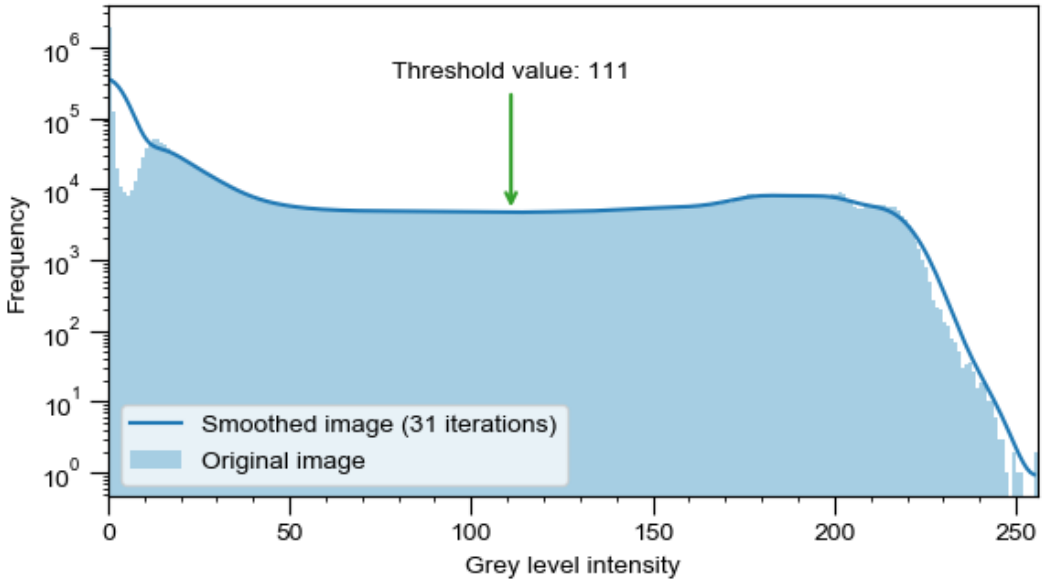

Figure 6.21: Grey value histogram of the blue colour plane of a hemiphoto taken at the Road site (N20 in Figure 6.18), and the smoothed image (using a moving average with window size = 3). The threshold value is located at the single minimum point (at a grey level intensity of 111) found after 31 smoothing iterations.

The sky view fraction v_s was calculated following Essery et al. (2008):

$$v_s = \frac{1}{\pi} \int_0^{\pi/2} d\beta \int_0^{2\pi} d\alpha \sin\beta \cos\beta \tau(\alpha, \beta) \tag{6.13}$$

where α is the azimuth and β is the elevation angle. If the sky is obscured by the canopy or the ground at (β, α) then $\tau = 0$, else $\tau = 1$.

With an equiangular hemispherical lens projection, the direction (β, α) can be mapped onto a point (x, y) on the hemispherical image (measured from the centre), so that:

$$\beta = \frac{\pi}{2} \left[1 - \frac{(x^2 + y^2)^{1/2}}{r} \right] \tag{6.14}$$

and:

$$\alpha = \tan^{-1}\left(\frac{y}{x}\right) \tag{6.15}$$

where r is the radius of the horizon circle on the image. The sky view fraction can then be calculated by dividing the hemispherical view into n_β elevation bands and n_α azimuth bands, and discretising Equation 6.13 as

$$v_s = \frac{\pi}{n_\beta n_\alpha} \sum_{i=1}^{n_\beta} \sum_{j=1}^{n_\alpha} sin\beta_i cos\beta_i c(\beta_i, \alpha_j). \tag{6.16}$$

6.3.3 Generation of synthetic hemispherical images

Taking hemispherical photographs is a manual process that is time consuming for coverage of large areas. Synthetic hemispherical images can be generated from airborne LiDAR (e.g. Webster et al. (2020)) or hypothetical forest gap scenarios.

Here an artificial forest was created as the first step in calculating sky view fraction. The physical characteristics of the artificial forest (such as tree height and stocking density) are based on observational data collected at the Road site at FMI-ARC in April 2016 (Section 6.3.1.2). The artificial forest structure includes a linear gap, representing a road, through its centre. Synthetic hemispherical images were generated from the artificial forest using two different methods – the PRICE model (Essery et al. 2007) and an LiDAR-enhanced methodology (Webster et al. 2020) – and used to calculate v_s across the linear gap. Differences between the two methods of v_s calculation were evaluated and compared against values obtained from the hemiphotos taken at the Road site.

The artificial forest covers a 200 m x 200 m plot (Figure 6.22). v_s values were

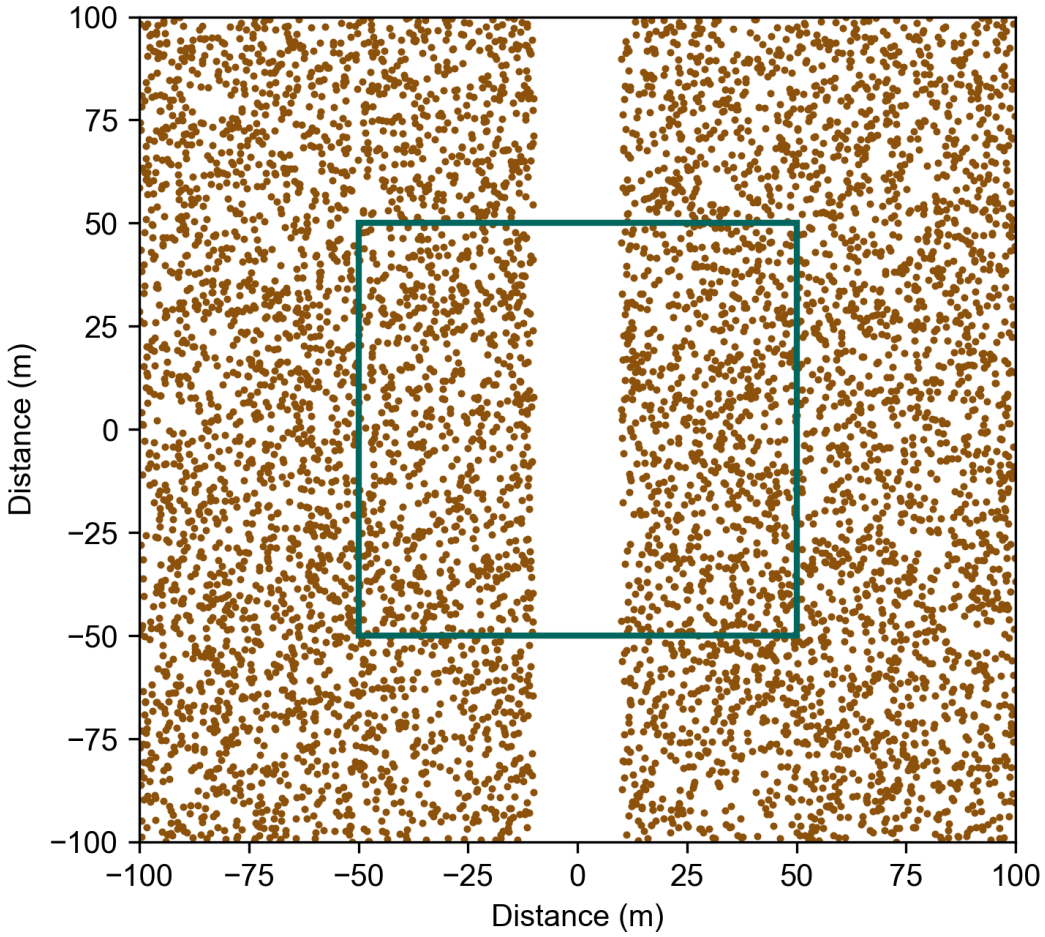

Figure 6.22: Artificial 200 m^2 forest plot with a central 20 m wide road. The location of tree trunks are shown by the brown points and the green box marks a 100 m^2 area centred on the plot, within which v_s values are calculated.

calculated for an inner 100 m^2 area centred on the forest plot centre, to ensure that there were enough surrounding trees to populate the hemispherical image fully. A 20 m wide linear clearing was included to approximate the road at the Road site at FMI-ARC. Trees were assigned randomly generated coordinate locations within the plot. Tree measurements made at the Road site (Appendix A.3) and by the Finnish Environment Institute (SYKE) at Sodankylä were used to approximate relationships between tree height (h) information and other characteristics including diameter at breast height (DBH), crown width (CW), and height to crown base (h_c).

The PRICE model uses simplified tree structures comprising a cylindrical trunk and

ellipsoid crown to populate the artificial forest (Figure 6.23). A binary synthetic hemispherical image is produced by dividing the hemispherical sky into azimuth and elevation cells that are then blanked out where the model indicates that the sky view is blocked by the canopy. The method described in section 6.3.2 (equations 6.13 – 6.16) was used to calculate sky view fraction.

The second approach used an LiDAR–enhanced methodology (similar to that described in Webster et al. (2020)). This method works by identifying local maxima in a LiDAR–derived canopy height model and assigning these as points from tree crowns. Extra points to represent the tree trunk and branches are then added below the tree crown (the 'enhancement'). The trunk is represented by a cylinder between the ground and up to breast height (1.5 m) and then by a linear conical shape up to the height of each individual tree. Branches within the crown are randomly assigned an angle of growth direction based on ranges for Norway spruce trees (a common species in the Swiss Alps, the study area for this methodology development, and in Finland). For the purposes of this research project, LiDAR data from the Swiss Alps was just used as the starting point for constructing an artificial tree from point clouds, meaning that individual trees had a more realistic crown morphology compared to the ellipsoid shape used within the PRICE model. The LiDAR data available for Sodankylä was not sufficiently dense to undertake the full method described by Webster et al. (2020) with in–situ data. As with the PRICE model, the trees were then randomly distributed in space across the 200 m x 200 m forest plot. Synthetic hemispherical images were then created from this artificial forest; the points were converted into a spherical coordinate system in order to replicate the perspective of real-life hemiphotos and v_s calculated following the method described in section 6.3.2 (equations 6.13 – 6.16). The work for this specific method was carried out by Clare Webster.

Figure 6.24 shows the relationships found from data collected at Sodankylä by two

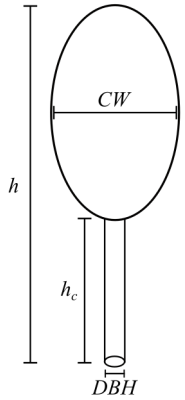

Figure 6.23: Schematic illustration of the simplified tree structure used by the PRICE model to populate an artificial forest. The trunk is conceptualised as a cylinder and the crown as an ellipsoid. Key canopy metrics are labelled as: DBH, the trunk diameter at breast height; h, the canopy height; h_c, the crown base height; CW, the crown width at its widest point.

field campaigns. The 95% confidence intervals (shown by the shaded areas) overlap in many instances, suggesting that these two data sets could be combined and considered as one larger dataset, providing more data points to fit a relationship to. The combined datasets are shown in Figure 6.25.

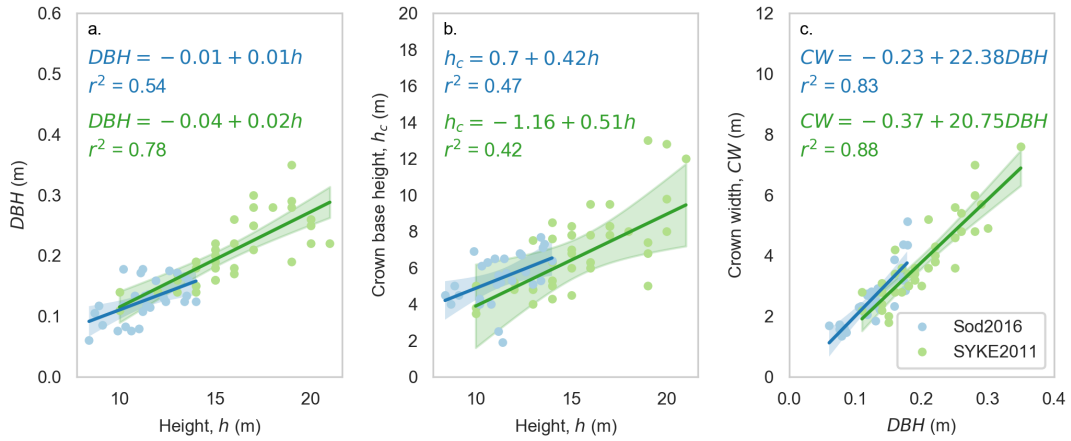

Figure 6.24: Relationships between key canopy metrics for two sets of data, both collected at Sodankylä: Sod2016, collected in 2016 by myself; SYKE2011 collected by the Finnish Environment Institute. Subplots show a) Tree height and DBH; b) Tree height and Crown base height; c) DBH and crown width. Shaded areas indicate 95% confidence intervals

Regression against tree height gives

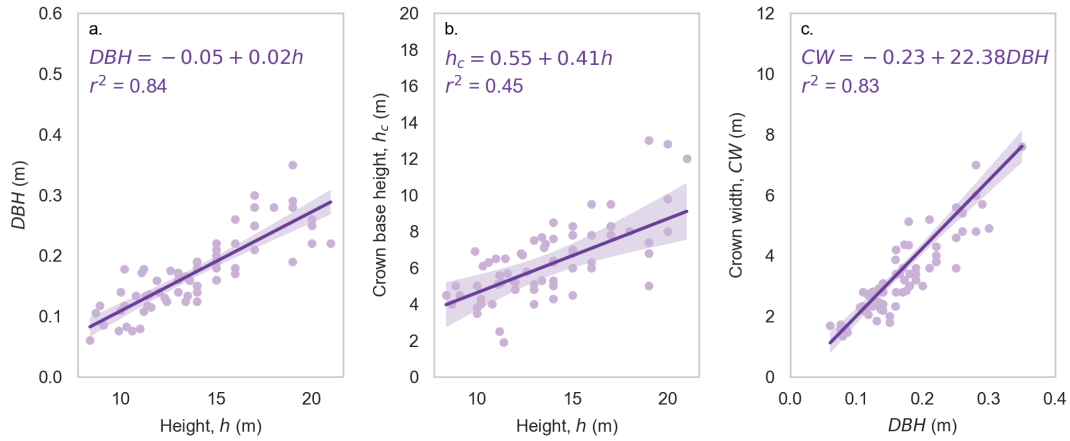

Figure 6.25: Relationships between key canopy metrics for combined sets of data, as described in figure 6.24. Subplots show a) Tree height and DBH; b) Tree height and Crown base height; c) DBH and crown width. Shaded areas indicate 95% confidence intervals

$$DBH = -0.05 + 0.02h \tag{6.17}$$

$$h_c = 0.55 + 0.41h \tag{6.18}$$

and regression against DBH gives

$$CW = -0.23 + 22.38DBH \tag{6.19}$$

Foliage area was not measured in either field campaign and so a different method of relating this variable to a measured characteristic, such as tree height, was required. The foliage area was calculated as

$$FA = h \tag{6.20}$$

This relationship was arrived at following trial and error running tree plots with foliage

area (FA) on different proportions of tree height (h) with the PRICE model (as it is considerably faster to run than the other method) and comparing the sky view fractions at a point in the artificial forest that corresponded with the location a real hemiphoto was taken in the field in 2016 (see section 6.3.1.1 for hemi photo description) until a good match was reached between the two.

To further assess the suitability of this relationship for approximating foliage area, the mean v_s based on a series of 22 synthetic hemispherical images were compared against the mean v_s obtained from a series of 22 hemiphotos taken at Sodankylä by Reid et al. (2014). The hemiphotos were taken during a field campaign in 2012 at various sites in the vicinity of the FMI-ARC research station. These sites were chosen as representative of the canopy cover in the area and comprise high density pine stands of medium-tall height, comparable to those measured by myself in 2016. For further details regarding the collection methods of the hemiphotos please see Reid et al. (2014). The hemiphotos were received pre-processed as binary images: i.e. manual thresholding was already applied to the photograph, which separates the sky and canopy into two distinct components of the image. The synthetic hemispherical images were generated as binary images at 22 different points that were randomly selected within the inner 100 m^2 central area of the artificial forest (as in Figure 6.22 but without the gap).

The average hemispheric view was calculated for both the synthetic forest and the Sodankylä sites, using the synthetic hemi images and the hemiphotos respectively (Figure 6.26). Figure 6.26 shows the mean measured gap fraction as a function of zenith angle.

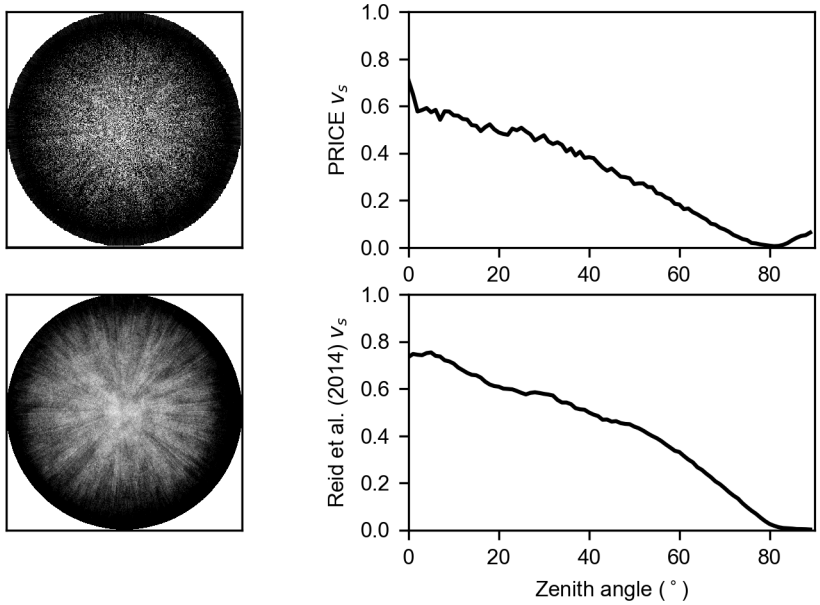

Figure 6.26: Mean sky view fraction as a function of zenith angle from the averaged hemispherical images generated at random points in the synthetic forest using PRICE (upper panel) and from averaged hemiphotos taken by Reid et al. (2014) (lower panel).

6.3.4 Sky view fraction estimates

Three different approaches to estimating v_s were investigated: hemispherical photography, using the PRICE model and using an enhanced LiDAR model of a synthetic forest canopy. They were all used to calculate v_s across the main road running through FMI-ARC (the 'Road site') and the results of these are shown in Figure 6.27. Across the gap there is a high degree of agreement between the three v_s values and less so into the forest. The PRICE model provides a reasonable match to the hemi photo based v_s in the forest to the south of the gap and underestimates it in the northernmost section of forest. In both forest sections the enhanced LiDAR method gives consistently lower values of v_s than those derived from the hemi photos. With this in mind, and given that the PRICE model is a significantly faster method of obtaining v_s estimates, the PRICE model was chosen as the method of calculating v_s in later modelling work.

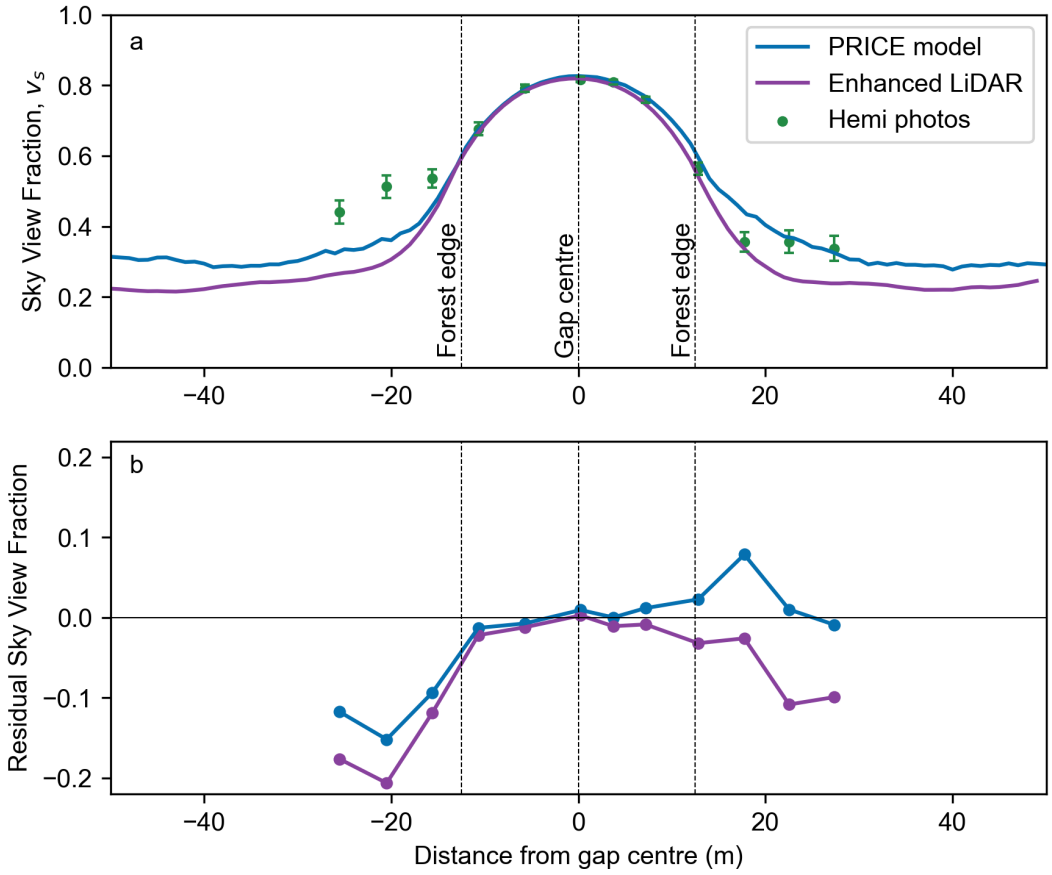

Figure 6.27: (a) Values of sky view fraction across a forest gap estimated from: hemiphotos taken at the Road site and synthetic hemispherical images via the PRICE model and an enhanced LiDAR method. Error bars represent the average change in the sky view fraction when the threshold is varied by ± 10 units on the grey level intensity scale (0–255). (b) Residual sky view fraction values between the hemiphotos and the two synthetic hemispherical image approaches. The northern-most section of forest is to the left of the gap.

6.4 Evaluation of the direct and diffuse radiation models

The combined direct and diffuse radiation models described above were evaluated using observational shortwave and longwave data from a discontinuous Scots pine stand just to the north of the main road at FMI-ARC (described in detail by Mazzotti et al. (2020b)). The data was collected by Mazzotti et al. (2020b) and comprise a line of measurements running 53° west of north across a roughly circular forest gap (diameter = 40 m) and can be seen as the fifth line from the north in Figure 4 of

Mazzotti et al. (2020b). Measurements were made using a gimbal-stabilized handheld setup and data points are approximately 2 m apart along the 80 m transect. There are two sets of observations providing temporal snapshots of the incoming radiation to the sub-canopy snow surface on both a clear-sky day (26/04/2019 between 10:52 and 12:20) and an overcast day (27/04/2019). The data sets also include values of v_s along the transect (Figure 6.28), obtained from hemiphotos that were captured using an upward-pointing camera mounted on the gimbal and then analysed using the radiative transfer model HPEval (Jonas et al. 2020). Observed air temperature was used to approximate the canopy temperature.

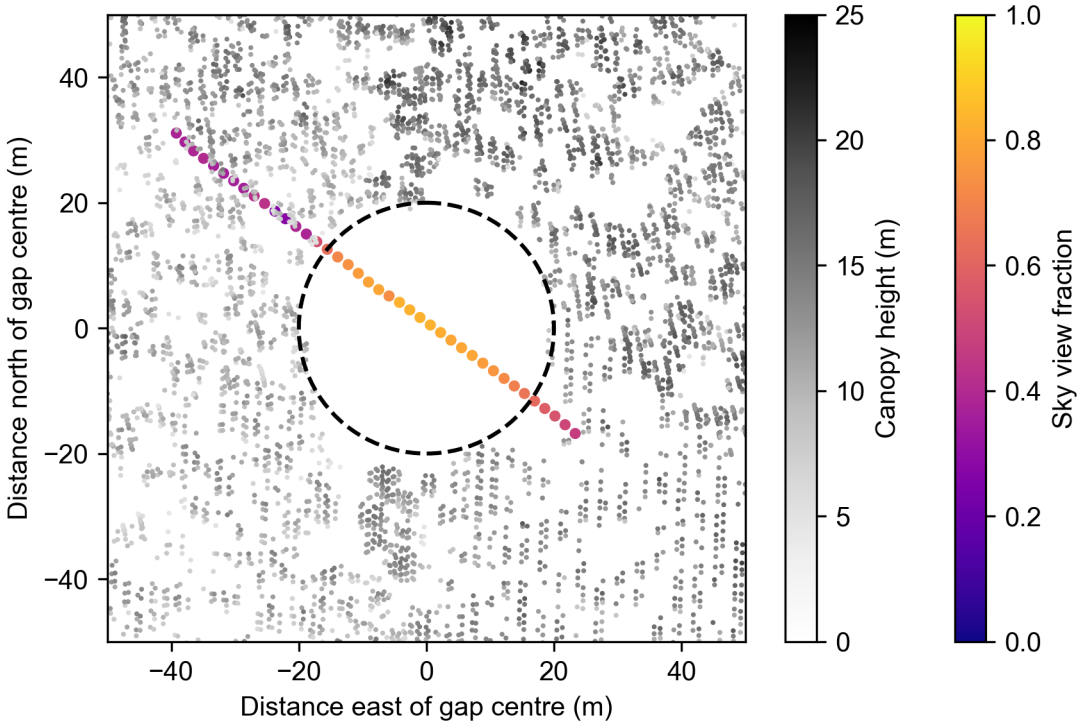

Figure 6.28: LiDAR canopy height and sky view fraction at FMI-ARC, Finland

The combined radiation models approximate the gap as a circular hole in an otherwise homogeneous forest. The ray tracing of tree shadows in a cylindrical gap was informed by the calculations used by Essery et al. (2007) for ray tracing the shadow of a cylindrical trunk and is calculated as follows.

The vector of length l defining a ray from point (x_s, y_s) on the surface towards the

sun at elevation angle β and azimuth angle α is

$$\boldsymbol{r} = (x_s + l\cos\beta\sin\alpha, y_s - l\cos\beta\cos\alpha, l\sin\beta). \tag{6.21}$$

The edge of a canopy gap of radius r_c centred on (0,0) is

$$x^2 + y^2 = r_c^2\ ,\ 0 \leq z \leq h_c \tag{6.22}$$

where h_c is the height of the surrounding canopy. Substituting Equation 6.21 in Equation 6.23 gives a quadratic equation for intersections with the gap edge

$$al^2 + bl + c = 0, \tag{6.23}$$

where

$$a = \frac{\cos^2\beta}{r_c^2}, \tag{6.24}$$

$$b = \frac{2\cos\beta(x_s\sin\alpha - y_s\cos\alpha)}{r_c^2}, \tag{6.25}$$

$$c = \frac{x^2 + y^2}{r_c^2} - 1. \tag{6.26}$$

If $b^2 - 4ac < 0$ the ray does not cross the canopy edge. The path length through the canopy is then equal to $l_h = h_c/\sin\beta$. Real solutions for l only exist if $b^2 - 4ac \geq 0$, in which case there are two solutions

$$l_{\pm} = \frac{-b \pm \sqrt{b^2 - 4ac}}{2a} \tag{6.27}$$

and the ray intersects the canopy edge at heights $h_{\pm} = l_{\pm} \sin \beta$. Intersections at heights less than zero or greater than h_c are neglected. The possible solutions for l_c are then

	$\mathbf{h_- < 0}$	$\mathbf{0 \leq h_- \leq h_c}$	$\mathbf{h_- > h_c}$
$\mathbf{h_+ < 0}$	$l_c = l_h$	–	–
$\mathbf{0 \leq h_+ \leq h_c}$	$l_c = l_h - l_+$	$l_c = l_- + l_h - l_+$	–
$\mathbf{h_+ > h_c}$	$l_c = 0$	$l_c = l_-$	$l_c = l_h$

From equation 6.8, the transmissivity of direct-beam radiation through the canopy is

$$\tau_{dir} = \exp\left(-\frac{l_c LAI}{2h_c}\right). \tag{6.28}$$

From equations 6.9 and 6.10, the direct-beam fraction of the incoming above-canopy shortwave radiation, SW_a, is

$$f_{dir} = \frac{exp(-m/\sin\theta)}{0.6 + 0.2\sin\theta} \tag{6.29}$$

for clear skies and zero for overcast. The model for sub-canopy shortwave radiation is

$$SW_c = [(1 - f_{dir})v_s + f_{dir}\tau]SW_a \tag{6.30}$$

On the overcast day, when direct shortwave radiation is at a minimum, the observed shortwave transmission (SW_c/SW_a) can be approximated by the sky view fraction

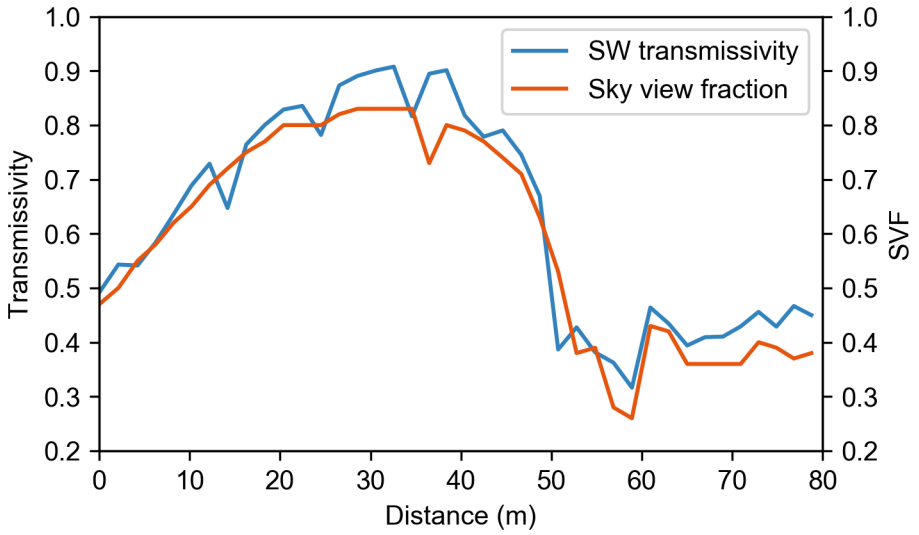

Figure 6.29: Measured shortwave transmissivity and sky view fraction across a circular forest clearing on an overcast day.

(Figure 6.29). The model simulates the observed shortwave radiation observed on the clear-sky day well overall but there are spikes observed in the forest that are not captured by the model (Figure 6.30, left). These are likely caused by sun flecks where the shortwave radiation is able to pass directly through gaps in the overlying canopy. During overcast conditions this is not an issue and the model fits the observed shortwave radiation very well (Figure 6.30, right). The clearly defined spikes seen in the measurements on the cloudy day are also seen in the simulated shortwave radiation as they are due to variations in the above-canopy radiation during the measurement period, rather than being due to variations in transmission through the canopy.

The model of sub-canopy longwave radiation described by Equation 6.12 provides a reasonable fit to the observations, particularly during overcast conditions (Figure 6.31). The clear-sky day shows greater spatial variation in both modelled and observed longwave radiation, with lowest values in the gap and increasing into the forest. The model tends to overestimate the longwave radiation in the gap on the clear-sky day.

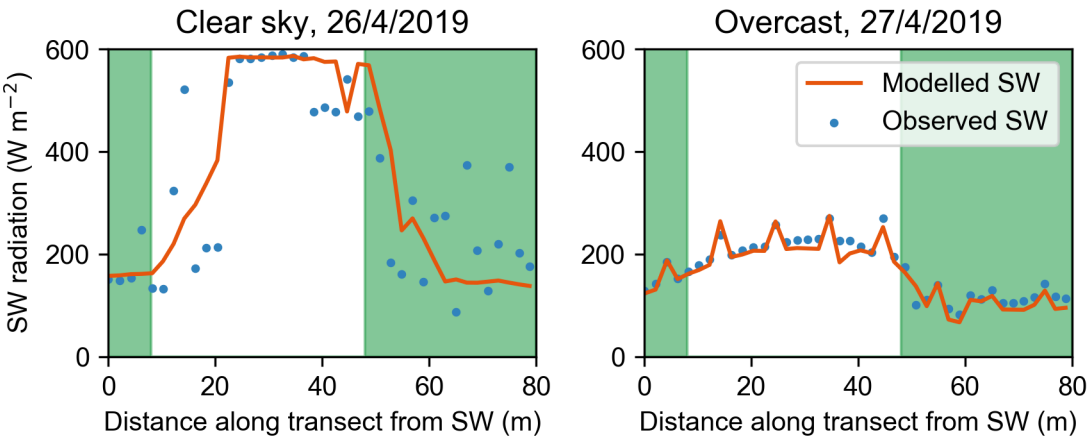

Figure 6.30: Modelled and observed sub-canopy shortwave radiation across a forest clearing on a clear-sky day (left panel) and an overcast day (right panel).

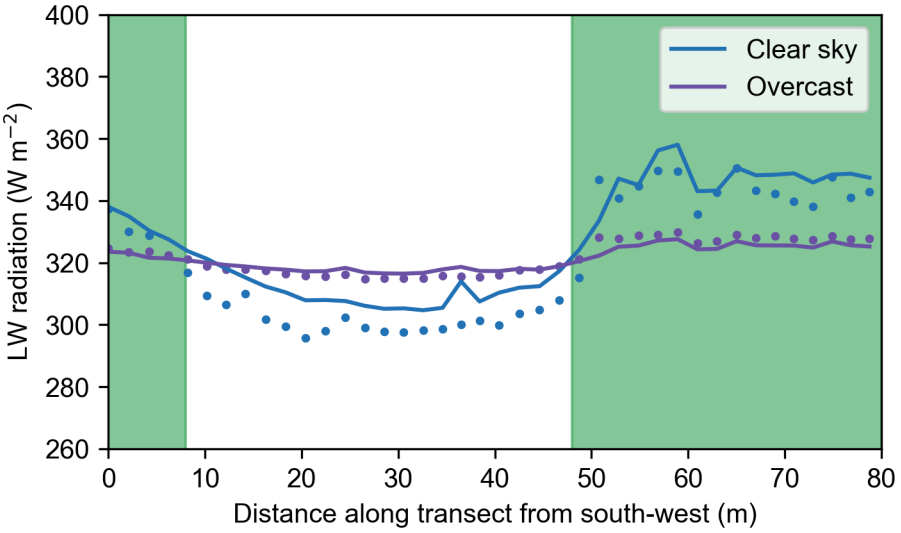

Figure 6.31: Sub-canopy longwave radiation across a forest clearing on a clear-sky day (blue) and on an overcast day (purple). Measurements are shown by dots and simulations by solid lines.

6.5 Discussion and conclusion

This chapter presented methods for modelling shortwave and longwave radiation to the sub-canopy snow surface. A ray-tracing approach to calculating the path length of direct shortwave radiation through the canopy was used to model its transmission and some example scenarios with varying gap widths and orientations were presented. Different methods of obtaining sky view fraction estimates for modelling diffuse radiation were presented and compared. The PRICE model was chosen for calculating v_s as it produced estimates reasonably close to those from hemispherical photographs taken at the Road site and is the fastest method of v_s estimation investigated. The chosen models for shortwave and longwave radiation were then combined and evaluated against observational data from a measurement transect across a forest gap at FMI-ARC collected by Mazzotti et al. (2020b).

The sky view fraction is often used to approximate the transmissivity of diffuse shortwave radiation (e.g. Essery et al. (2007), Link & Marks (1999*a*), Musselman et al. (2015), Pomeroy et al. (2008)). A comparison of v_s values calculated by Mazzotti et al. (2020b) from hemiphotos taken along the measurement transect and the observed transmissivity of shortwave radiation on an overcast day confirmed the suitability of this simple model. Furthermore, under cloudy conditions the modelled shortwave radiation was found to follow the trend of observations across the transect closely. Using measurements obtained on a clear day, when direct shortwave radiation dominates, the model was not able to capture the observed spatial pattern of shortwave radiation as well. It performs well in the gap and matches the observed rise and fall of the shortwave radiation from its peak in the centre of gap. However, the model is unable to match the higher spatial variability seen towards the margins of the gap and into the forest. These variations are likely caused by localised sun flecks (patches of greater direct shortwave radiation, which the model under-predicts) and shadows (patches of lower direct shortwave radiation, which the model over-predicts).

These effects result from the variable and dynamic nature of the transmission of direct shortwave radiation through a forest canopy (Hardy et al. 2004, Pearcy 1990). In this study a simplified representation of the canopy was used where the canopy is represented as homogenous whole, whereas in reality it has a complex and varied structure. For example, the distribution of branches and leaves are not uniform but concentrated in clumps leading to both small gaps and denser sections. Furthermore, movement of the canopy produces variation in the distribution of shortwave radiation on the forest floor, especially so during windy conditions (Reifsnyder et al. 1971). Studies that have captured these fine-scale spatial and temporal variations in direct shortwave radiation have used more complex models of the overlying canopy, for instance using LiDAR data to produce detailed representations of the canopy at the individual tree level (Webster et al. 2020).

The model of longwave radiation, based on the sky view fraction and air temperature (Equation 6.12), also performs best when predicting measurements on an overcast day when there is a low degree of spatial variation. On clear sunny days there are lower levels of downwelling longwave radiation compared to cloudy days, as observed in the gap. There is also greater solar heating of the canopy which enhances longwave fluxes to the forest floor and the gap margins, as seen by the highest levels of measured longwave radiation occurring in the forest sections. When comparing to the data from the clear-sky day, the model is able to pick out this overall trend across the transect with lower levels of longwave radiation in the gap than in the forest. However, across the transect the model tends to over-predict the longwave radiation. This is particularly noticeable in the gap, although the error in the model here is $<5\%$.

In summary, simple models of shortwave and longwave radiation were shown to be able to reproduce the overall patterns of radiative fluxes observed at a measurement site at FMI-ARC. In the following chapter, the full snow model capable of modelling both accumulation and melting of snow will be brought together with the emulated

wind model developed in Chapter 4 to simulate hypothetical forest-gap scenarios and explore the effects of gap width, orientation, and surrounding canopy density on snow accumulation and melt dynamics within a discontinuous boreal forest environment.

Chapter 7

Simulating snow accumulation and melt across linear forest clearings

7.1 Introduction

Snow is fundamental to many aspects of ecosystem function in boreal forest environments. Understanding the spatial and temporal evolution of the snowpack, such as the rate and timing of snow accumulation and melting, is important for predicting and understanding wider ecological and hydrological processes such as biogeochemical cycling (Brooks & Williams 1999, Jones 1999, Brooks et al. 2011), streamflow timing and amount (Lundquist & Dettinger 2005, Sun et al. 2018), vegetation dynamics (Wipf et al. 2009, Rasmus et al. 2011, Trujillo et al. 2012), and also impacts on the earth surface energy balance through surface albedo (Warren 1982, Flanner et al. 2011). Snow processes in open environments are well studied (Pomeroy et al. 1998, Essery et al. 2009). Forest canopy effects on snow accumulation and ablation have also been subject to much study, although it is more challenging to model these dynamics due to the many interacting processes in forest environments (Rutter et al.

2009, Varhola et al. 2010), including the interception and sublimation of snow in the canopy (Wilm & Dunford 1948, Troendle & King 1985, Pomeroy & Schmidt 1993, Hedstrom & Pomeroy 1998, Varhola et al. 2010, Lundquist et al. 2013, Schelker et al. 2013, Moeser et al. 2016, Lundberg et al. 2016), enhanced longwave radiative fluxes and reduced shortwave radiative fluxes (Harding & Pomeroy 1996, Metcalfe & Buttle 1998, Hardy et al. 2004, Sicart et al. 2004, 2006, Talbot et al. 2006, Essery et al. 2008, Lawler & Link 2011, Musselman et al. 2012, Webster et al. 2017, Malle et al. 2019).

Canopy–snow interactions become particularly complex in heterogeneous forests due to fine–scale variability in the canopy structure (Musselman et al. 2015). Discontinuities represent one source of heterogeneity. Discontinuities in boreal forests may be man-made, for example roads, or naturally occurring, for example river stretches. Often, these features are linear or close to linear. As forests worldwide are becoming increasingly fragmented due to human activities (Turner 2010, Haddad et al. 2015), these linear clearings are becoming a more common feature in the landscape (Pickell et al. 2015, Laurance & Arrea 2017, Kuklina et al. 2021). Forest clearings are interesting as they are a transitional zone sitting between the two end states of completely open environments and continuous forest canopy. Within this marginal environment there are a multitude of processes to consider and balance as the snowpack is potentially influenced by both the forest and the opening (Lawler & Link 2011). Furthering our understanding of how snow dynamics in boreal forests are altered by the introduction of a linear canopy clearing is important to further our understanding of the wider environmental impact of increasing forest fragmentation.

This chapter draws together the work across the previous four research chapters, integrating wind (Chapters 3 & 4), snow accumulation (Chapter 5) and radiation (Chapter 6) dynamics across forest gaps to produce simulations of these processes across hypothetical linear forest gaps (Figure 7.1). First, models of the energy fluxes

to snow will be integrated into the simplified snow model described in Chapter 5.2.2 so that the melting of snow may be simulated. Observational meteorological and snow data from northern Finland are used to calibrate the model during periods of snow melt. The final calibrated model will then be used to explore the potential snow accumulation and melting dynamics resulting from different gap scenarios. Of particular interest is how gap width, orientation, and canopy density might influence the observed spatial patterns of snow mass along a transect traversing the canopy gap. Furthermore, the sensitivity of the spatial pattern of snowmelt to radiative and turbulent energy fluxes will be investigated.

The hypotheses guiding this chapter are:

1. Increasing gap width will lead to greater accumulation of snow within gaps due to the decrease in interception. In wider gaps, it is expected that snow will melt more quickly, with melting beginning earlier in the year, due to the increase in exposure to shortwave radiation relative to narrower gaps. However, the effect of gap width on melt dynamics will likely be complex, reflecting the compensating effects of increasing exposure to shortwave radiation and decreasing exposure to longwave radiation as gap width increases (the radiative paradox).

2. As the measured wind speeds at Sodankylä are low, it is expected that the distribution of radiative energy fluxes to the snow surface will dominate melting patterns across the gap, compared to wind-related impacts.

3. Increasing canopy density will reduce the sky view fraction and increase interception at the forest edges and interior. It is therefore expected that a denser canopy would lead to greater fluxes of longwave radiation emitted by the canopy to the snow, reduced transmission of shortwave radiation through the canopy and reduced snow accumulation at the gap edges and within the forest.

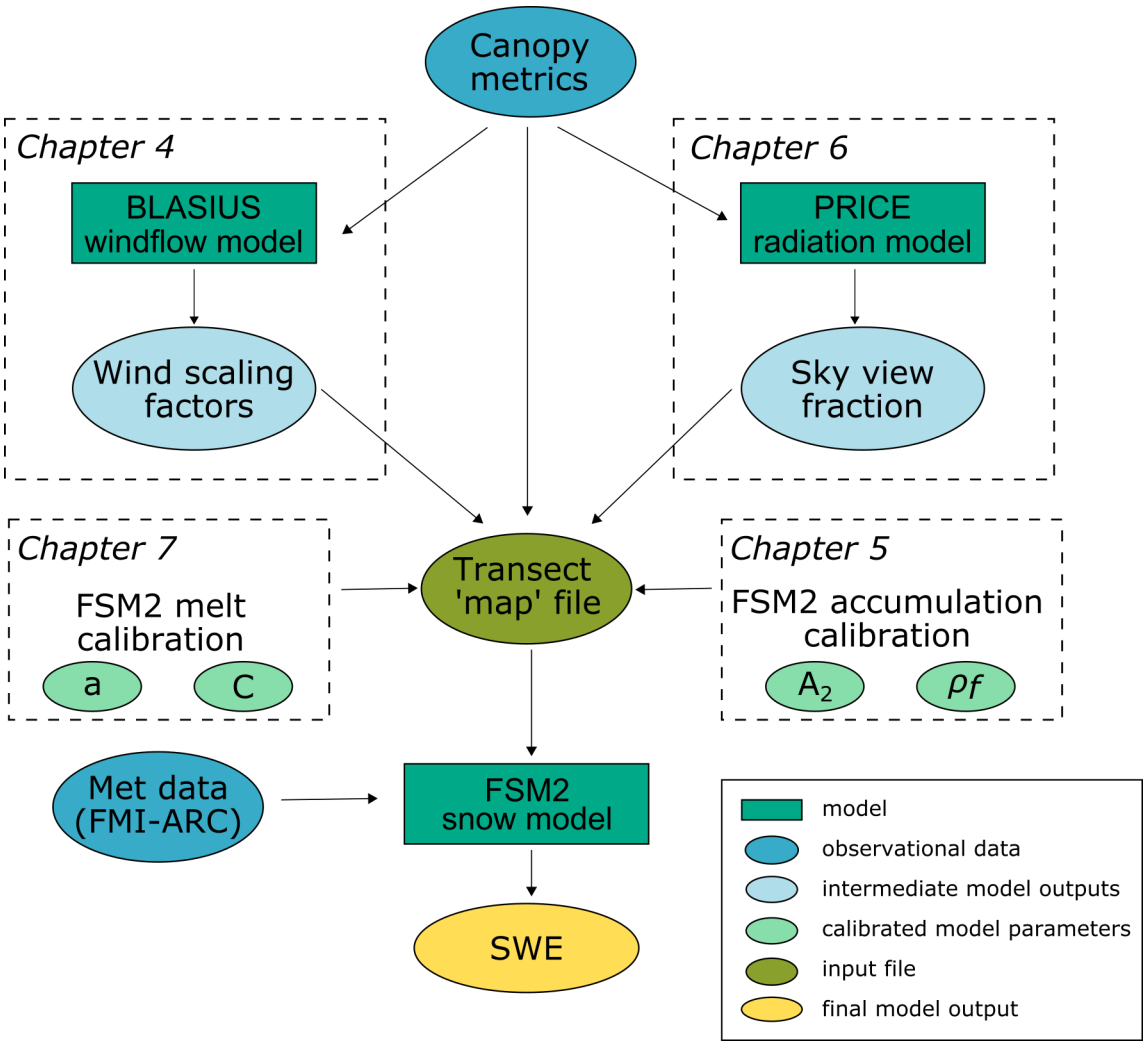

Figure 7.1: A schematic showing how the different models, data and calibrated parameters come together with the FSM2 snow model. The dashed boxes indicate the relevant thesis chapter for further information. The calibration parameter a is the albedo, C is a surface exchange coefficient, A_2 determines the rate of change in snow density and ρ_f is the density of fresh snow. The transect 'map' file allows for the calibrated parameters, wind scaling factors and sky view fraction to be varied according to position along the canopy gap transect. SWE is the snow water equivalent and is the model output used for the different gap scenarios presented in this chapter

4. Changing the orientation of the gap will affect the magnitude of incoming shortwave radiation and the relative wind direction. Snow at south-facing edges will melt sooner and faster than at north-facing edges due to the shading effect of the canopy.

7.2 Methodology

7.2.1 Snow model description

The snow model used in this chapter is as described in Chapter 5.2.2, with the addition of melt energy dynamics (a simplified version of FSM2 (Mazzotti et al. 2020a)).

The surface energy balance equation is

$$G_s = R_n - H - L_s E - L_f M \tag{7.1}$$

where R_n is the net radiation absorbed by the surface (W m^{-2}), H is the sensible heat flux (W m^{-2}), L_s is the latent heat of sublimation for water (J kg^{-1}), E is the sublimation rate (kg m $^{-2}$), L_f is the latent heat of fusion for water (J kg^{-1}) and M is the melt rate (kg m^{-2} s^{-1}). G_s is the ground surface heat flux at the base of the snowpack and is expected to be small due to the low thermal conductivity of snow, so is neglected here. R_n is calculated as

$$R_n = (1-a)SW_{sub} + v_s LW + (1-v_s)\sigma T_a^4 - \sigma T_s^4 \tag{7.2}$$

where a is the snow albedo (the value of this parameter is obtained through the calibration process described in section 7.2.2), SW_{sub} is the incoming shortwave radiation below the canopy (W m^{-2}), v_s is sky view fraction, LW is the above-canopy incoming longwave radiation (W m^{-2}), σ is the Stefan-Boltzmann constant (see Table 7.1), T_a is the air temperature (K) and T_s is the surface temperature (K). SW_{sub} is the sum of the diffuse (SW_{diff}) and direct (SW_{dir}) components of shortwave radiation that reach the snow surface below the canopy

$$SW_{sub} = \upsilon SW_{diff} + \tau_{dir} SW_{dir} \tag{7.3}$$

where τ_{dir} is the transmissivity of direct radiation through the canopy (see Chapter 6.2 for more detail). The incoming shortwave radiation (SW) is split into diffuse and direct components according to $dfrac$, which is the diffuse fraction of SW such that $SW_{diff} = dfrac * SW$ and $SW_{dir} = (1 - dfrac) * SW$. Following Erbs et al. (1982), $dfrac$ is calculated as

$$dfrac = 1 - (0.09Kt), \qquad \text{if } Kt \leq 0.22 \tag{7.4a}$$

$$dfrac = 0.95 - 0.16Kt + 4.39Kt^2 - 16.64Kt^3 + 0.34Kt^4, \qquad \text{if } 0.22 < Kt \leq 0.8 \tag{7.4b}$$

$$dfrac = 0.165, \qquad \text{if } Kt > 0.8 \tag{7.4c}$$

where Kt is the sky clearness parameter and is calculated as

$$Kt = \frac{SW}{I_0 \sin \beta} \tag{7.5}$$

where I_0 is the solar constant (= 1366 W m^{-2}) and β is the solar elevation angle (radians). The sublimation rate (E) of snow on the ground is calculated as (see Chapter 5.2.2.3 for details on the sublimation of snow held in the canopy)

$$E = \rho_a C U_c (Q_{sat} - Q_a) \tag{7.6}$$

where ρ_a is the air density (kg m^{-3}), C is a surface exchange coefficient (the value of this parameter is obtained through the calibration process described in section 7.2.2), U_c is the sub-canopy wind speed (m s^{-1}), Q_{sat} is the specific humidity at saturation and Q_a is the specific humidity of air. The air density is calculated as

$$\rho_a = \frac{P_s}{R_{air} T_a} \tag{7.7}$$

where P_s is the surface pressure (Pa) and R_{air} is the gas constant for dry air (Table 7.1). Q_{sat} is calculated as

$$Q_{sat} = \frac{380.042e^{\frac{22.4422(T_a - T_m)}{T_a - 0.964}}}{P_s} \tag{7.8}$$

where T_m is the melting point of snow (see Table 7.1).

Constant	Value	Description
c_p	1005	Specific heat capacity of air (J K^{-1} kg^{-1})
k	0.4	von Karman constant
L_f	0.334 x 10^6	Latent heat of fusion for water (J kg^{-1})
L_s	2.835 x 10^6	Latent heat of sublimation for water (J kg^{-1})
R_{air}	287	Gas constant for dry air (J K^{-1} kg^{-1})
R_{wat}	462	Gas constant for water vapour (J K^{-1} kg^{-1})
σ	5.67 x 10^{-8}	Stefan-Boltzmann constant (W m^{-2} K^{-4})
T_m	273.15	Melting point (K)

Table 7.1: Physical constants

Q_a is calculated from Q_{sat} as

$$Q_a = Q_{sat}\frac{RH}{100} \tag{7.9}$$

where RH is the observed relative humidity (%). The sensible heat flux (H) between the snow surface and the atmosphere is calculated as

$$H = c_p \rho_a C U_c (T_s - T_a) \tag{7.10}$$

where c_p is the specific heat capacity of air (J K^{-1} kg^{-1}; Table 7.1) The incremental change in temperature for each time step of length δt (3600 s) is found by solving the surface energy balance equation (following Essery (2015)). First, writing

$$T_s^{(n+1)} = T_s^{(n)} + \delta T_s \tag{7.11}$$

then substituting this into equations 7.2, 7.6 and 7.10 and linearising in δT_s gives

$$R_n^{(n+1)} = R_n^{(n)} - 4\sigma T_s^{(n)3} \delta T_s \tag{7.12}$$

$$E^{(n+1)} = E^{(n)} + \rho_a D C U_c \delta T_s \tag{7.13}$$

and

$$H^{(n+1)} = H^{(n)} + c_p \rho_a C U_c \delta T_s \tag{7.14}$$

where

$$D = \frac{dQ_{sat}}{dT_s} = \frac{L_s Q_{sat}}{R_{wat} T_s^2} \tag{7.15}$$

from the Clausius–Clapeyron equation. R_{wat} is the gas constant for water vapour (Table 7.1). Taking equations 7.12, 7.13 and 7.14, and neglecting G_s, equation 7.1 becomes

$$\delta T_s = \frac{R - H - L_s E}{(C_p + L_s D)\rho_a C U_a + 4\sigma {T_{s_i}}^3} \tag{7.16}$$

and it is first assumed that the melt rate, M, = 0. If this gives rise to a surface temperature that exceeds the melting point (T_m = 273.15 K), then the fluxes are recalculated using $T_s = T_m$ and the snow melt rate may be calculated from

$$M = \frac{R_n - H - L_s E}{L_f} \tag{7.17}$$

The modelled snow mass on the ground (SWE) is then equal to the existing snow mass on the ground, plus snowfall and less the change in mass due to sublimation and melt, such that:

$$SWE^{(n+1)} = SWE^{(n)} + Sf\delta t - \delta t(E + M) \tag{7.18}$$

7.2.2 Snow model calibration

7.2.2.1 Field site and data description

The model was calibrated using observational data from the Intensive Observation Area (IOA) at FMI-ARC (see Figure 5.1 for location). The site consists of relatively sparse pine forest ($h \approx 15$ m) surrounding an open clearing in the forest that is approximately 40 m in diameter. Automatic weather stations positioned in the open area (67.361768 N, 26.633857 E; located approximately 5 m into the clearing and away from the southern edge) and in the forest (67.361654 N, 26.634191 E; located approximately 20 m south of the southern edge of the clearing) measure snow depth in addition to air temperature and relative humidity. Snow depth measurements are recorded every ten minutes using a Campbell Scientific SR50 sensor. The input meteorological data are as described in Chapter 5.2.1.1.

The data used for this calibration covered seven winter periods from 2007 – 2014 inclusive. One year was taken as running from the start of October through to the end of September the following year (e.g. 01/10/2007 – 30/09/2008) so as to comfortably cover a full snow season of snow accumulation and melt within each year. This is known as a 'water year' in cold regions hydrology; the snow that falls in October in one calendar year is not available as runoff until the next year.

7.2.2.2 Calibration approach

The model simulates snow accumulation and melting processes along a transect, representing a slice through the IOA clearing. Some model variables, such as canopy height (h), are expected to vary along this transect according to the presence of a forest canopy or not, and so are read in to the model from a 'map' file containing different values for each variable depending on its position along the transect (Table

7.2). For instance, h was assigned a value of 15 m for model grid points in the simulated forest and 0 m in the clearing. The LAI for the forest was set equal to 2.2 following the calibration process described in Chapter 5, which focused on modelling snow accumulation (see section 5.2.3 for further details on this). Values of v_s were estimated using the PRICE model and followed the approach described in Chapter 6.3.3, with the canopy metrics scaled to account for the taller trees surrounding the IOA compared to those at the road site (average h =15 m vs. 11.34 m respectively).

Variable	Description	Value(s)	Source
v_s	Sky view fraction	Varied continuously along the transect	PRICE model (Section 6.3)
h	Canopy height	15 m in forest & 0 m in open	Essery et al. (2016)
LAI	Leaf area index	2.2 in forest & 0 in open	Calibrated value (Section 5.3.2)
f_{scale}	Friction velocity scaling factor	Varied continuously along the transect	BLASIUS model (Chapter 4.4.2)
U_{scale}	Wind speed scaling factor	Varied continuously along the transect	BLASIUS model (Chapter 4.4.2)

Table 7.2: Transect map variable descriptions

Two parameters were identified as being most influential on snowmelt in the updated model and therefore candidates for calibration: a, the albedo, and C, a surface exchange coefficient. Similar to the calibration process described in Chapter 5.2.3, a random parameter search approach was used to reach an optimal parameter value combination that would produce the best model fit to the data (based on minimising the snow depth RMSE). The following value ranges were used for the parameter search and were sampled from 200 times:

- a: 0.4 – 1
- C: 0 – 0.1

The calibration of the snow accumulation model in Chapter 5 found an ensemble of optimal values for the snow density parameters A_2 and ρ_{ns}, which were carried

through to this chapter. The calibration described in this chapter was performed in python and automated to loop through each value combination of the A_2 and ρ_{ns} parameter ensembles for each iteration of the above parameter search. This meant that the model was run with a unique value combination for the four parameters (a, C, A_2 and ρ_{ns}) 12,800 times for the forest site and 7,000 times for the open site.

7.2.3 Hypothetical gap scenarios

Three different gap widths were chosen for the hypothetical gap scenarios: 100 m, 30 m and 10 m. These widths are consistent with those chosen in Chapter 3 for the hypothetical canopy wind flow simulations conducted with BLASIUS and represent likely real-life linear gaps, for example those arising from natural resource extraction or road building. The orientation of the gap relative to north was varied such that the gaps ran E-W (-90°), N-S (0°), NE-SW (45°) and NW-SE (-45°). The snow model was run with one year of meteorological data (see Chapter 5.2.1.1 for detailed description) that covered the period 01/09/2009 – 30/08/2010. For simplification, the single 'best' values of the snow density parameters A_2 and ρ_{ns} were used rather than the full ensemble of 'good' values (see Table 7.3).

For each gap scenario, the BLASIUS model was used to obtain scaling factors for relating sub-canopy wind speed (at a height of 2 m) and surface friction velocity to the observed 22 m height wind speed (see Chapter 4.4.2 for further detail on this methodology). The wind-direction was assumed to be constant and from the south. This meant that for E-W gap orientations the domains were consistent across models as the simulated wind flows perpendicular to the line of the forest edge in both BLASIUS and the snow model. For the N-S gap orientation the wind was scaled by just two factors, depending on whether the transect point is in the canopy or the gap

section. Extra steps were required for wind scaling across the gaps orientated at 45° as the effective gap distance travelled by wind flowing from the south is longer than the gap width in the snow model. For example, for a gap of width 100 m orientated at 45° the wind will flow across an opening of 100 m $/ \cos 45° \approx 141$ m. The wind scaling factors then needed to be projected on to the original gap width and these points interpolated between to produce a transect with even 0.5 m spacing.

Parameter	Forest	Gap
A_2 (m^{-3} kg^{-1})	0.0289	0.0289
ρ_{ns} (kg m^{-3})	48.88	119.95
a	0.92	0.82
C	0.0013	0.0063

Table 7.3: Calibrated parameter values used for the hypothetical gap scenarios

7.3 Results

7.3.1 Calibration results

7.3.1.1 IOA forest site

At the forest measurement site, the random parameter search found that values of $a = 0.92$ and $C = 0.0013$ produced the lowest RMS error in the simulated snow depth (RMSE = 0.064 m; Figure 7.2; Table 7.4).

Parameter	Forest site	Open site
a	0.92	0.82
C	0.0013	0.0063

Table 7.4: Calibrated parameter values

The model was run against the calibration data set (2007 – 2011) with these optimised parameter values for a and C and the ensemble of 'good' value combinations of A_2

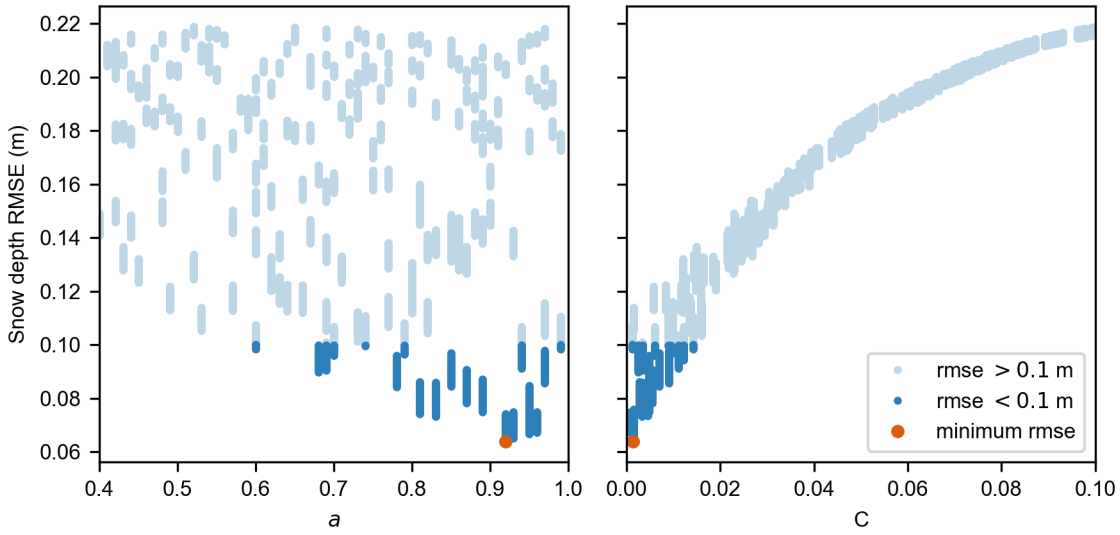

Figure 7.2: IOA forest measurement site calibration results from a random parameter search to find the optimal values for parameters a and C. Parameter values resulting in a snow depth RMSE $>$ 0.1 m are shown with pale blue points, dark blue points indicate where the depth RMSE is $<$ 0.1 m, and the orange point in each subplot shows the parameter value with the lowest associated error in the modelled snow depth.

and ρ_{ns}. The resultant ensemble of snow depth simulations produce a reasonable match to the observed depths 7.3. The ensemble mean underestimates observed snow depths in the first two years but is very close to the observations made in the second half of the calibration period. In all four years the timing of the onset of the main melting period in the spring is predicted accurately and the snow disappearance date is consistent between the simulations and observations. The RMSE of the mean ensemble simulated snow depth is 0.11 m.

As can be seen in Figure 7.4, the model continues to perform well when run against the evaluation data set (2011–2014) with a RMSE of 0.12 m for the ensemble mean. There is a consistent underestimation of the snow depth in the final year, with the observations lying just outside the range of values predicted by the model ensemble. In the first two years, the ensemble encapsulates most of the observed snow depths and the mean model ensemble provides a good match in many instances (e.g. Feb–May 2012). As seen with the calibration data set, the observed timing of the onset of

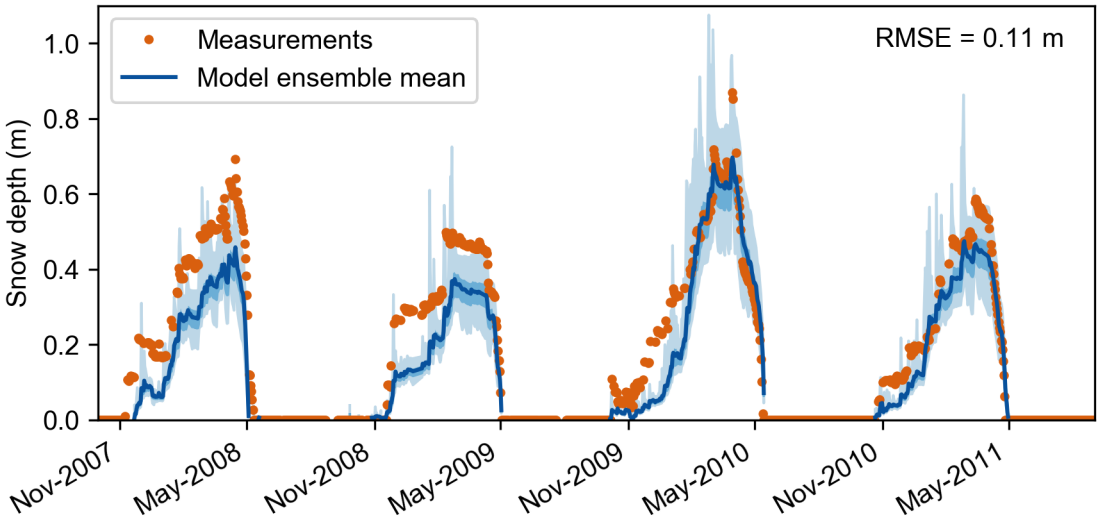

Figure 7.3: Ensemble model run following calibration with the IOA forest site observational snow depth data (2007 – 2011). The model was run with an ensemble of 'good' value combinations of the snow density parameters A_2 and ρ_{ns} (see Chapter 5). The mean of this ensemble is shown by the solid blue line, the light blue and dark blue shaded areas represent the full range and inter-quartile range of the model ensemble respectively. The orange dots are the observed snow depth. The RMSE of the mean ensemble simulated snow depth is 0.11 m.

melting and melt rate is closely matched by the simulated snow behaviour.

7.3.1.2 IOA open site

At the open measurement site, the random parameter search found that values of $a = 0.82$ and $C = 0.0063$ produced the lowest RMS error in the simulated snow depth (RMSE = 0.039 m; Figure 7.5; Table 7.4).

Using these optimised values for a and C, the simulated snow depths closely follow the pattern of observed depths during the calibration period (Figure 7.6). As at the forest site, the calibrated model provides an accurate prediction of the onset and rate of melting in the spring, and the mean model ensemble provides a good match to the observed depths (RMSE = 0.07 m).

The calibrated model continues to perform well under validation with a new data set

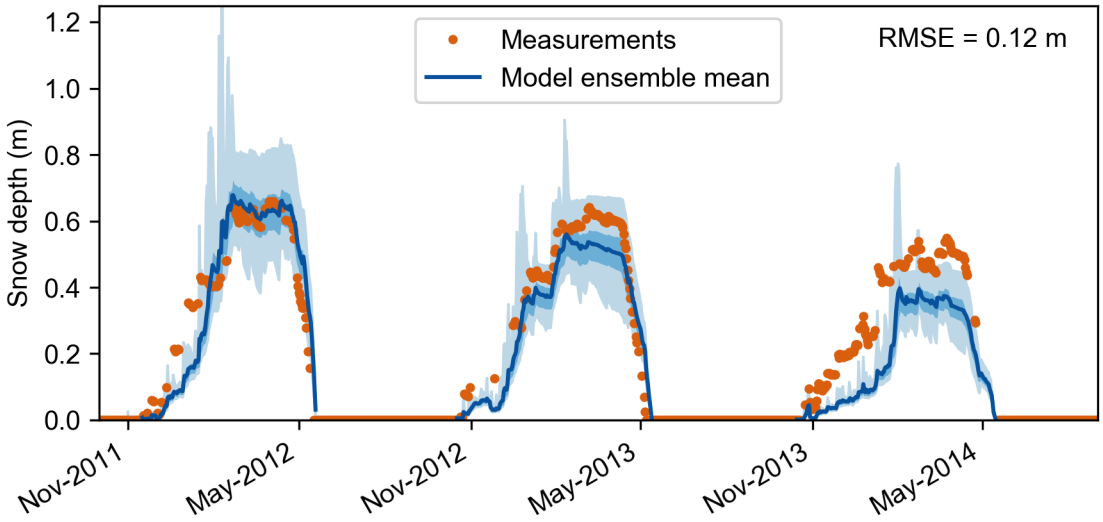

Figure 7.4: Evaluation of the calibrated snow model with observational snow depth data from the IOA forest site (2011 – 2014). The model was run with an ensemble of 'good' value combinations of the snow density parameters A_2 and ρ_{ns} (see Chapter 5). The mean of this ensemble is shown by the solid blue line, the light blue and dark blue shaded areas represent the full range and inter-quartile range of the model ensemble respectively. The orange dots are the observed snow depth. The RMSE of the mean ensemble simulated snow depth is 0.12 m.

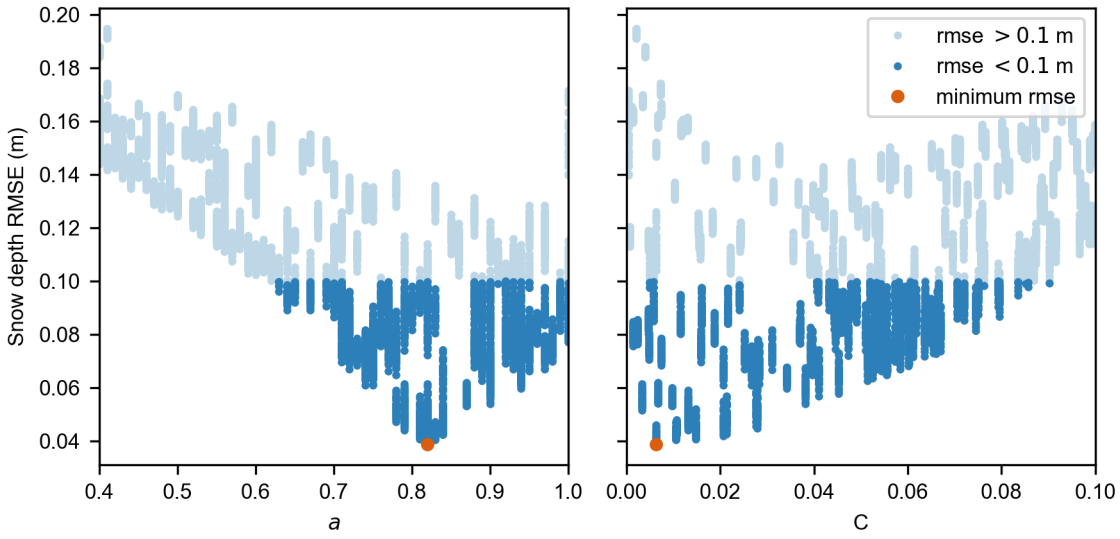

Figure 7.5: IOA open measurement site calibration results from a random parameter search to find the optimal values for parameters a and C. Parameter values resulting in a snow depth RMSE $>$ 0.1 m are shown with pale blue points, dark blue points indicate where the depth RMSE is $<$ 0.1 m, and the orange point in each subplot shows the parameter value with the lowest associated error in the modelled snow depth.

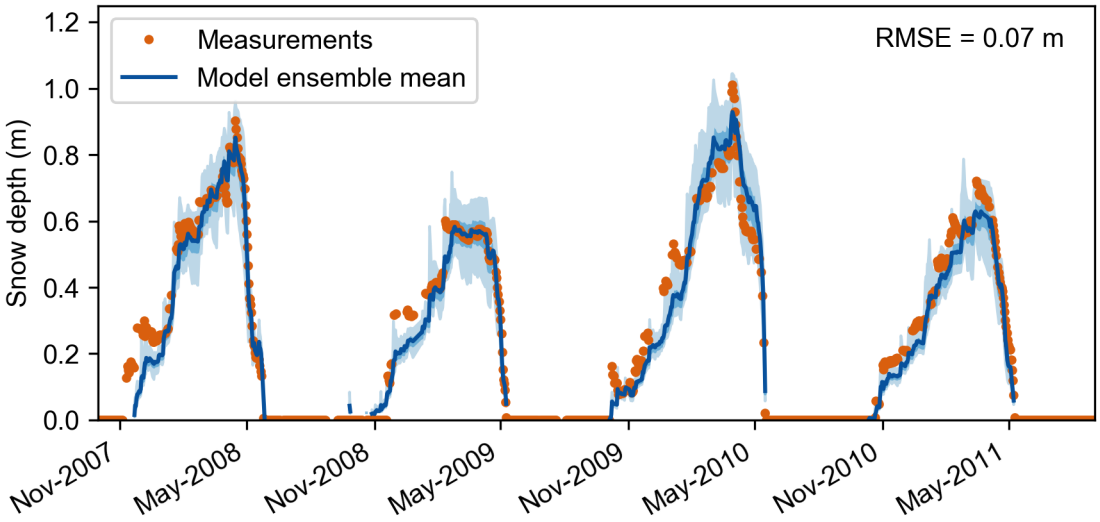

Figure 7.6: Ensemble model run following calibration with the IOA open site observational snow depth data (2007 – 2011). The model was run with an ensemble of 'good' value combinations of the snow density parameters A_2 and ρ_{ns} (see Chapter 5). The mean of this ensemble is shown by the solid blue line, the light blue and dark blue shaded areas represent the full range and inter-quartile range of the model ensemble respectively. The orange dots are the observed snow depth. The RMSE of the mean ensemble simulated snow depth is 0.07 m.

(Figure 7.7). The mean model ensemble RMSE is 0.11 m and the model both over- and under-estimates the observed snow depths across the evaluation time period. There is consistent under-prediction of the depth at the start of each snow season, aside from this the observations generally fall within the ensemble range. The timing and rate of melting in the spring continues to be consistent between model and measurements.

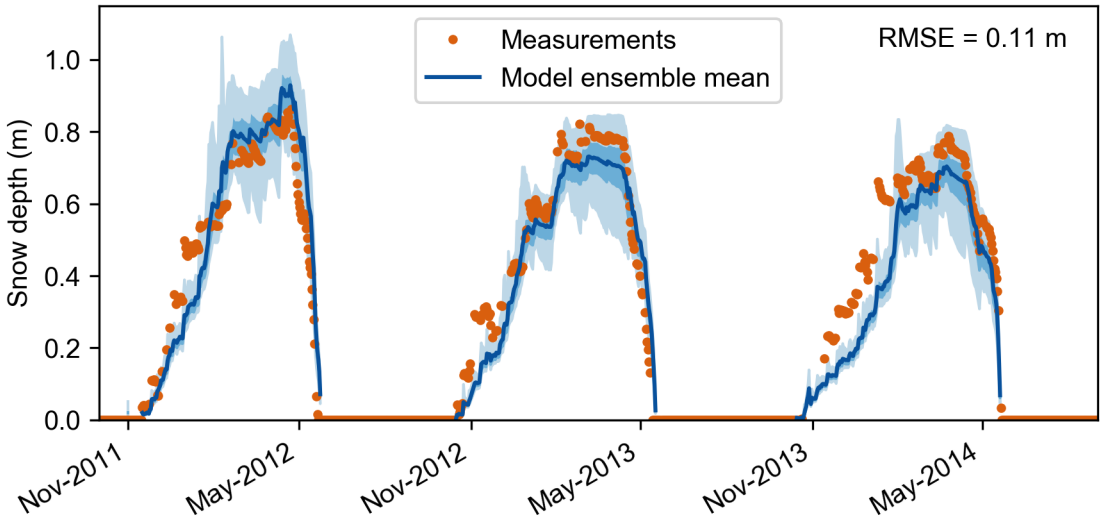

Figure 7.7: Evaluation of the calibrated snow model with observational snow depth data from the IOA open site (2011 – 2014). The model was run with an ensemble of 'good' value combinations of the snow density parameters A_2 and ρ_{ns} (see Chapter 5). The mean of this ensemble is shown by the solid blue line, the light blue and dark blue shaded areas represent the full range and inter-quartile range of the model ensemble respectively. The orange dots are the observed snow depth. The RMSE of the mean ensemble simulated snow depth is 0.11 m.

7.3.2 Forest gap scenarios results

7.3.2.1 Gap width affects spatial distribution of melt patterns

The simulated snow mass accumulates sooner and at a greater rate within the gap compared to under the forest canopy. For example, in the scenario with a 100 m gap running E-W (Figure 7.8.a), the sub-canopy SWE reaches a peak of 121.9 mm in the southern section and 118.9 mm in the northern section at the end of March. In contrast, the maximum snow mass in the gap is higher (227.2 mm) and occurs over a month later on 6th May (Table 7.5). The snow accumulation appears uniform across all three gap widths (Figure 7.8) but in the case of the 100 m gap, the spatial distribution of melting produces an asymmetric pattern with the snow on the northern side of the gap melting soonest and fastest. The sub-canopy snow also melts faster in the northern-most canopy section immediately following the gap, compared to the southern section of forest. The snow persists for longest within the gap on the southern side, with a final snow disappearance date of 20th June approximately 28 m south of the gap centre.

	Max SWE (mm)	Date of max SWE (2010)	Disappearance date (2010)
100 m			
S. canopy	121.9	30th March	16th May
Gap	227.2	6th May	20th June
N. canopy	118.9	30th March	15th May
30 m			
S. canopy	122.0	30th March	16th May
Gap	222.0	3rd May	10th June
N. canopy	120.6	30 March	16th May
10 m			
S. canopy	121.7	30th March	16th May
Gap	219.5	4th April	31st May
N. canopy	121.0	30th March	16th May

Table 7.5: Maximum SWE at three points along the modelled transect: -150 m from the gap centre (South canopy), 150 m from the gap centre (North canopy) and the point in the gap where the maximum SWE occurs (Gap), which varies across each scenario.

The asymmetry in the simulated snow mass across the 100 m gap is not observed to the same extent with the narrower gap scenarios (Figure 7.8b. & c.). The snow in the 30 m gap melts more evenly along the transect although not uniformly (Figure 7.8b.). The melt rate is greatest at the edges of the 30 m gap and the snow persists for longest to the south of the gap centre, although this difference is more subtle than seen with the 100 m gap scenario. Of the three gap widths, the snow melts fastest in the 10 m gap (Figure 7.8c.). There is a gradual transition from the more uniform pattern of melting seen with the 30 m gap, and the wider 100 m gap; Figure A.3 (Appendix A.5) shows further details of this with gap widths of 50, 60, and 70 m.

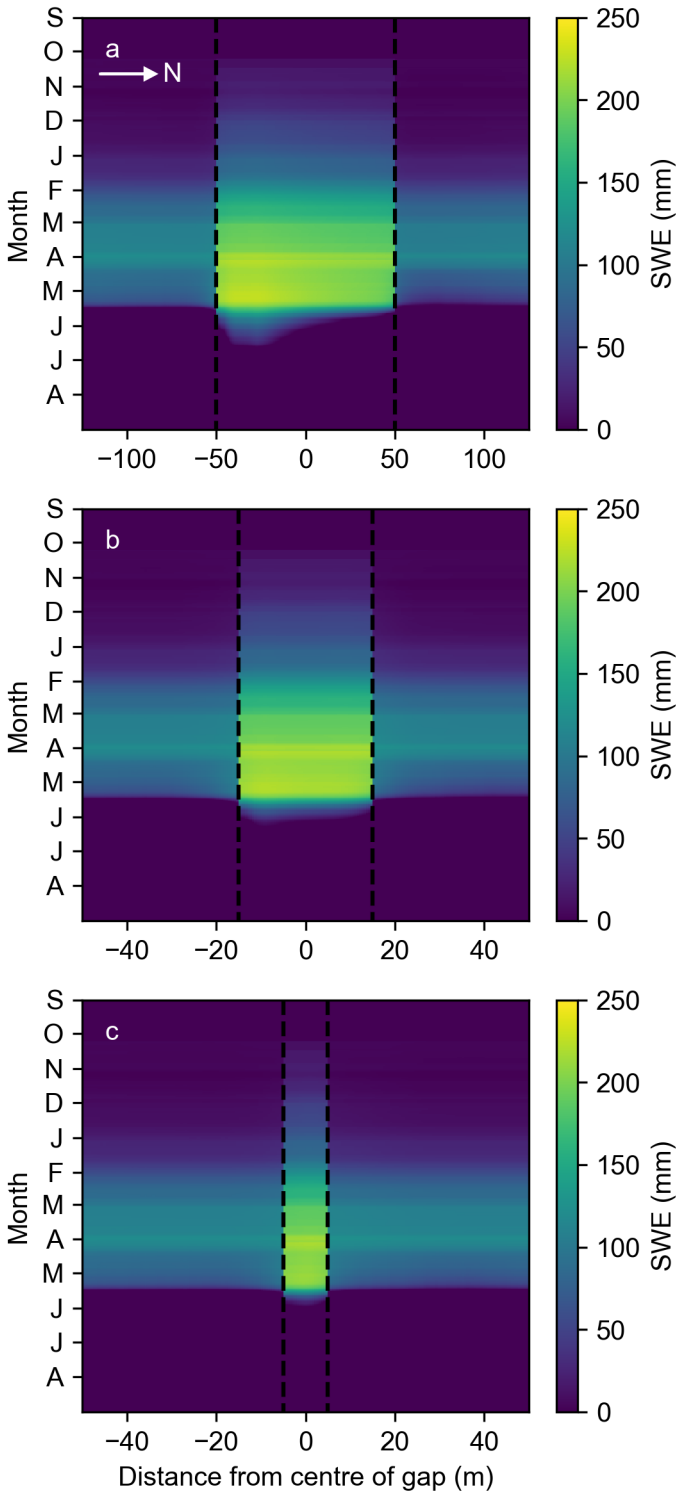

Figure 7.8: Simulated SWE across three forest gaps orientated E-W and with widths of (a) 100 m, (b) 30 m and (c) 10 m. The wind is directed from the south and so flows along the transect from left to right in these panels. The edges between the canopy and gap are shown by the dashed black lines. The horizontal distance is given in terms of distance from the centre of the gap and the horizontal axes are different between the panels for clarity of presentation across different widths.

7.3.2.2 Gap orientation can influence both accumulation and melting of snow

If the 100 m gap is rotated so that it is orientated N-S there is a uniform distribution of snow mass across the gap (Figure 7.9). Less snow accumulates in the gap compared to when the gap is orientated E-W (Maximum SWE of 195.3 mm at the start of April vs. 227.2 mm at the start of May). The sub-canopy snow mass is consistent between the two scenarios, with a peak of 122 mm SWE at the end of March when the gap is orientated N-S. The snow in the N-S gap disappears abruptly and uniformly across the gap in mid-May (19th), almost concurrently with the sub-canopy snow (16th).

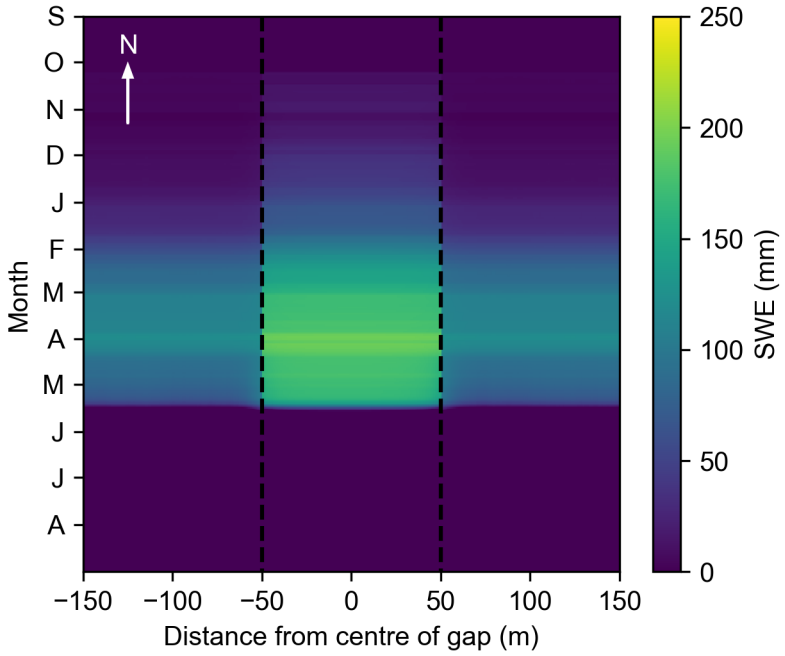

Figure 7.9: Simulated SWE across a 100 m forest gap orientated N-S. The wind is directed from the south and the edges between the canopy and gap are shown by the dashed black lines.

Orientating the 100 m gap 45° (Figure 7.10 a.) and -45° (Figure 7.10 b.) gives very similar spatial patterns of simulated SWE. As with the E-W lying 100 m gap, the greatest snow mass is found on the southern side of the gap (approximately 15 m into the gap from the canopy edge in these scenarios). The simulated snowpack persists

for longest at this location, disappearing on 19th and 20th June for the -45° and 45° scenarios respectively.

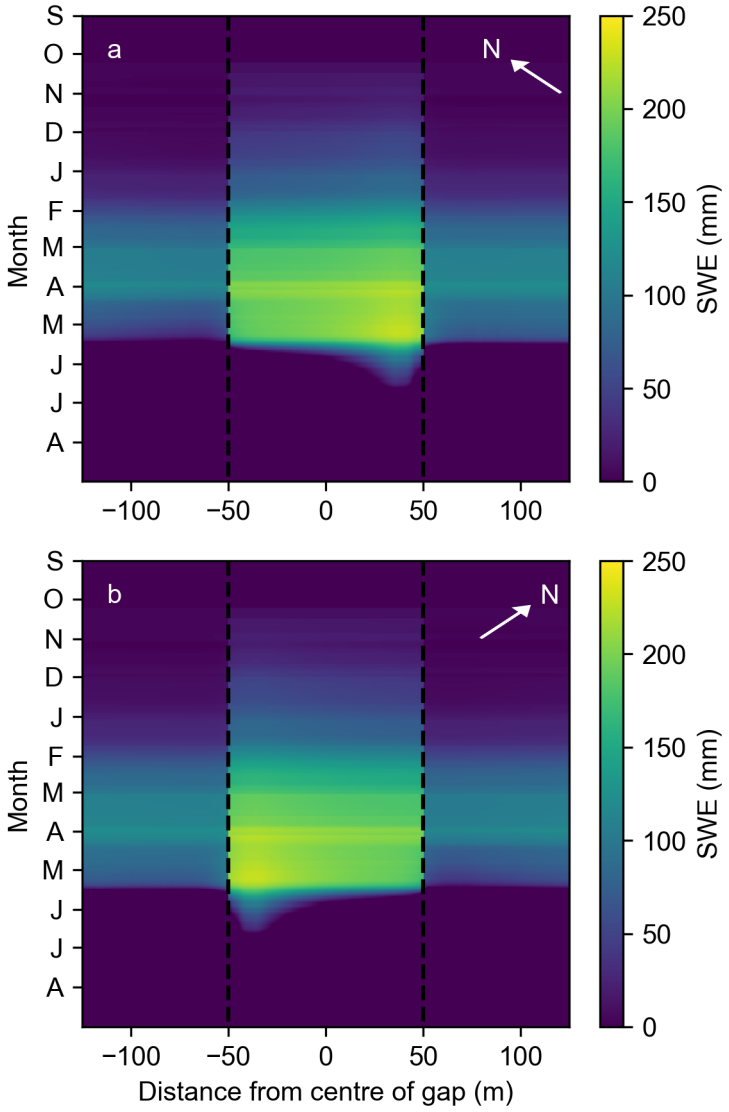

Figure 7.10: Simulated SWE across a 100 m forest gap orientated (a) NE-SW (45°) and (b) NW-SE (-45°). The wind flow direction is from south to north and the gap edges are shown by the black dashed lines.

7.3.2.3 Turbulent fluxes drive the spatial patterns of melt

Setting the surface exchange coefficient (C) to zero effectively stops any turbulent exchange of energy within the model. For example, the 100 m gap (E-W) scenario now looks rather different (Figure 7.11.a vs. Figure 7.8.a). The melt rate becomes

much more uniform across the gap, indicating that the asymmetrical spatial pattern of melt seen in Figure 7.8.a is strongly dependent on the turbulent fluxes across the gap, which are driven by the sub-canopy wind speeds. Figure 7.11.b shows the increase in simulated snow mass when $C = 0$. The dominant effect of removing turbulent fluxes is to slow the melting of the snow in the northern half of the gap so that the melt rate matches the rest of the gap (aside from the snow at the edges of the gap, which melts fastest). The snow mass underlying the canopy to the north of the gap is also greater when $C = 0$, indicating that the influence of the gap extends beyond its edge and into the downwind section of forest. With the narrower gap widths, the effect of setting C to zero is less pronounced, with a maximum difference in SWE of 39.1 mm and 25.5 mm for the 30 m and 10 m gap scenarios respectively (see Appendix A.5, Figures A.4 & A.5).

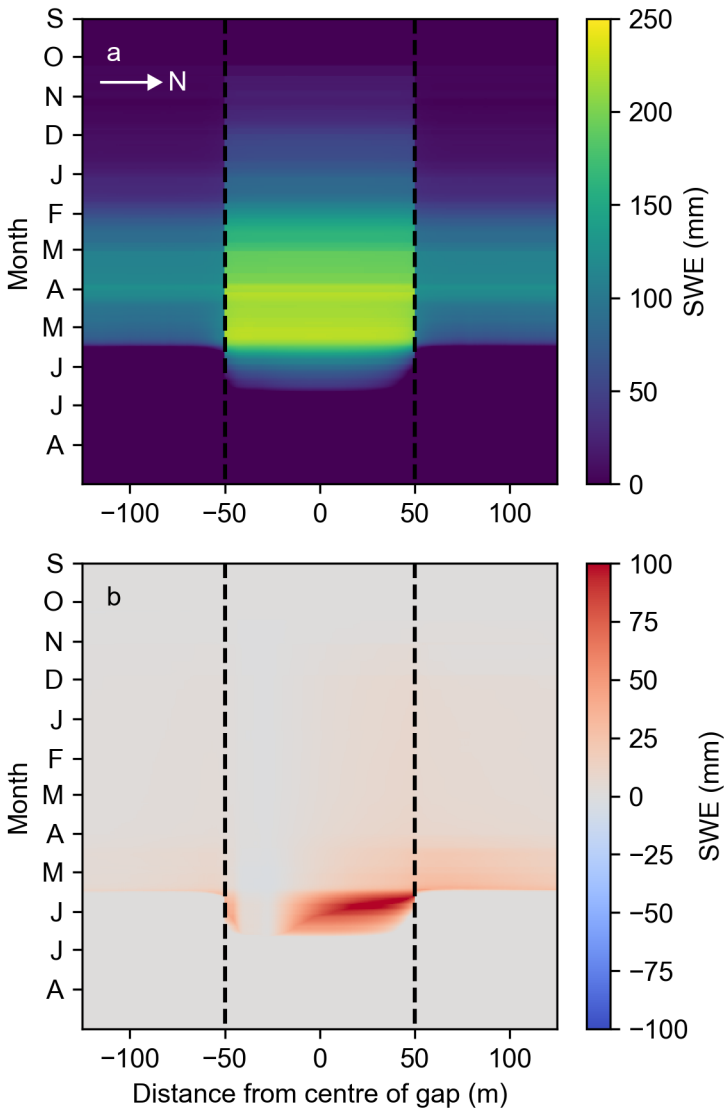

Figure 7.11: (a) Simulated SWE across a 100 m canopy gap orientated E-W with the surface exchange coefficient C = 0. (b) The difference between the 100 m E-W gap scenario with and without the turbulent exchange of energy included within the model. This shows the relative increase in the snow mass if melting due to turbulent fluxes is ignored. The dashed black lines in both panels show the location of the gap edges.

7.3.2.4 Radiative fluxes provide a secondary influence on snow melt

Changing the modelled shortwave radiation to all diffuse ($dfrac = 1$) reduces the snow mass on the southern edge of the gap during the end of the melt period and results in greater amounts of snow at the northern edge of the gap and into the canopy (Figure 7.12). If all shortwave radiation is modelled as direct radiation ($dfrac = 0$),

the situation is reversed and there is greater snow mass at the southern edge of the gap, with lower values of simulated SWE at the northern edge (Figure 7.13). This reflects the shading effect of trees at the southern gap edge and the exposure of snow to direct radiation at the northern edge.

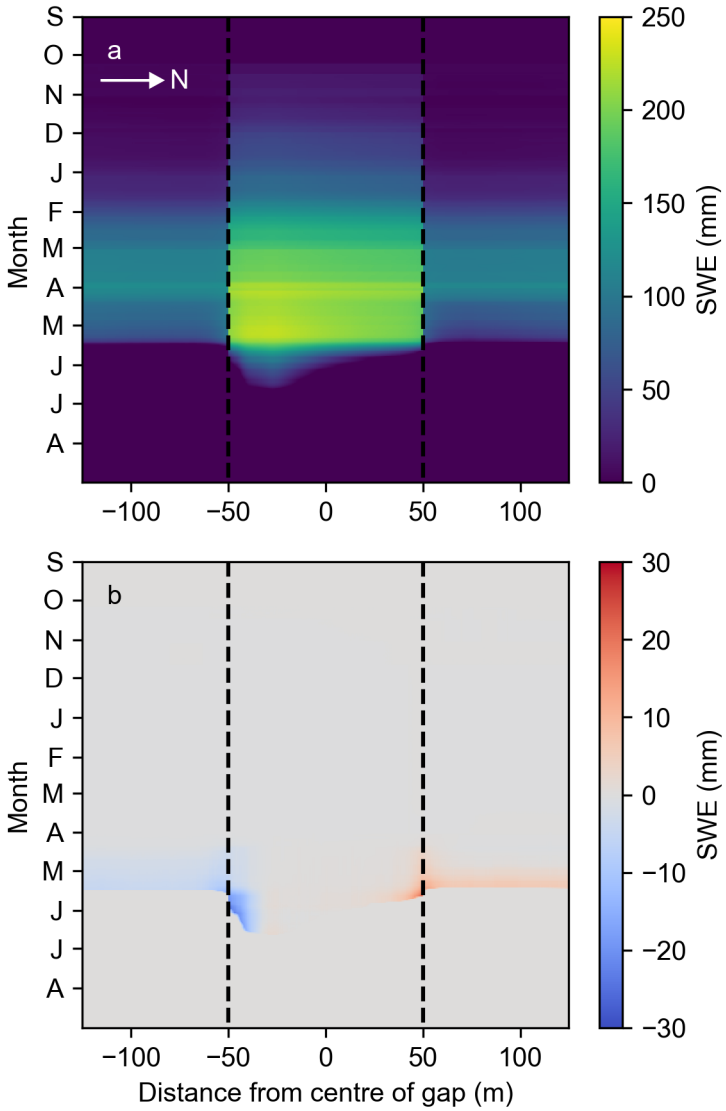

Figure 7.12: (a) Simulated SWE across a forest transect with a 100 m gap orientated E-W, with all shortwave radiation modelled as diffuse radiation. (b) The difference in SWE between the above 'all diffuse' scenario and the original scenario with the shortwave radiation split into diffuse and direct components. A positive SWE value (shown in red) indicates that there is greater snow mass in the 'all diffuse' scenario, and a negative (shown in blue) SWE value means that there is less snow mass (i.e. greater melting) in this scenario. In both panels, the wind flows from the south (left to right) and the canopy edges are shown by the black dashed lines.

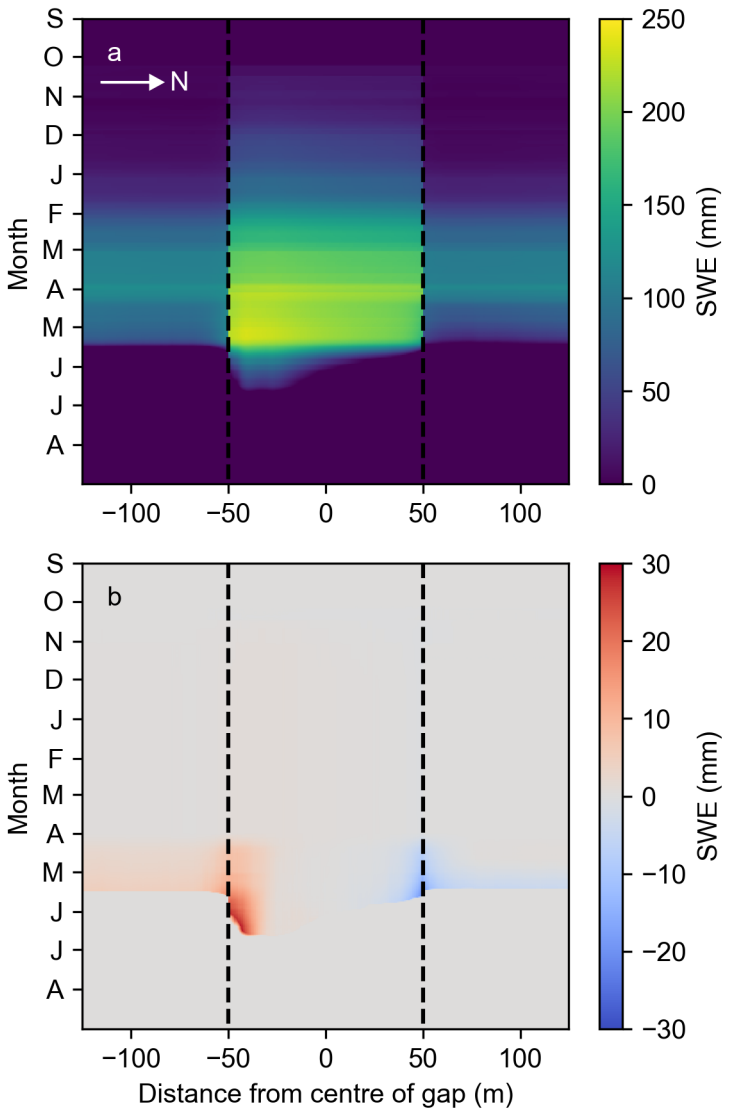

Figure 7.13: (a) Simulated SWE across a forest transect with a 100 m gap orientated E-W, with all shortwave radiation modelled as direct radiation. (b) The difference in SWE between the above 'all direct' scenario and the original scenario with the shortwave radiation split into diffuse and direct components. A positive SWE value (shown in red) indicates that there is greater snow mass in the 'all direct' scenario, and a negative (shown in blue) SWE value means that there is less snow mass (i.e. greater melting) in this scenario. In both panels, the wind flows from the south (left to right) and the canopy edges are shown by the black dashed lines.

Setting the albedo equal to 1 removes the effect of shortwave radiation from the simulations (Figure 7.14). The asymmetrical pattern of snow melt across the gap persists (melt rate is slower on the southern side of the gap) and the snow lasts much longer in the year than when the albedo is lower. Further to the results presented

in section 7.3.2.3 this also shows that the observed spatial pattern of melting is not determined by the shading of trees, although this would act to reinforce the pattern set by the turbulent fluxes.

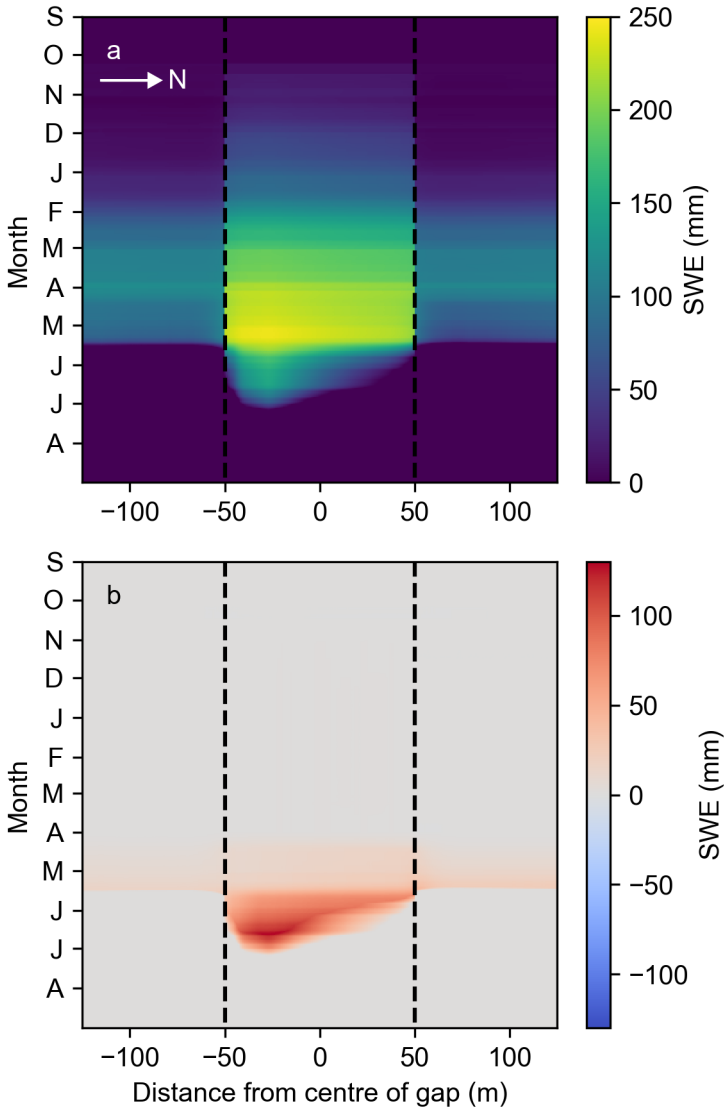

Figure 7.14: (a) Simulated SWE across a forest transect with a 100 m gap orientated E-W, with albedo = 1. (b) The difference in SWE between the above scenario with albedo = 1 and the original scenario with the albedo set to the calibrated values (0.92 in the forest and 0.82 in the gap). A positive SWE value (shown in red) indicates that there is greater snow mass in the albedo = 1 scenario. In both panels, the wind flows from the south (left to right) and the canopy edges are shown by the black dashed lines.

7.3.2.5 Canopy density affects the accumulation and melting of snow

With a narrower gap (width = 30 m), reducing the LAI to 1 gives rise to greater snow mass both under the canopy (due to reduced interception) and within the gap (Figure 7.15.a and Table 7.6). Conversely, increasing the LAI to 4 reduces the snow mass across the transect (Figure 7.15.b). The snow lasts longer when the $LAI = 1$ and the snow in the centre of the gap is most persistent; there is a larger difference between the melt rate at the edges and the centre of the gap than with higher values of LAI. There is less of a marked difference when the $LAI = 4$, although the snow melts fastest at the northern edge of the gap. The higher the LAI, the earlier the snow within the gap finishes melting. The within-gap snow disappears by the 29th May with an LAI of 4, whereas it persists until the 17th June with an LAI of 1 (Table 7.7).

In the 100 m canopy gap (E-W) scenario, an LAI of 1 results in greater snow mass under the canopy but the maximum SWE in the gap is lower compared to the scenarios with a higher canopy density scenarios (Figure 7.16.a and Table 7.6). The snow persists for longest on the southern side of the gap when the $LAI = 1$, whereas this area of more persistent snow is shifted along closer to the gap centre as the LAI increases (Figures 7.16 & 7.16).

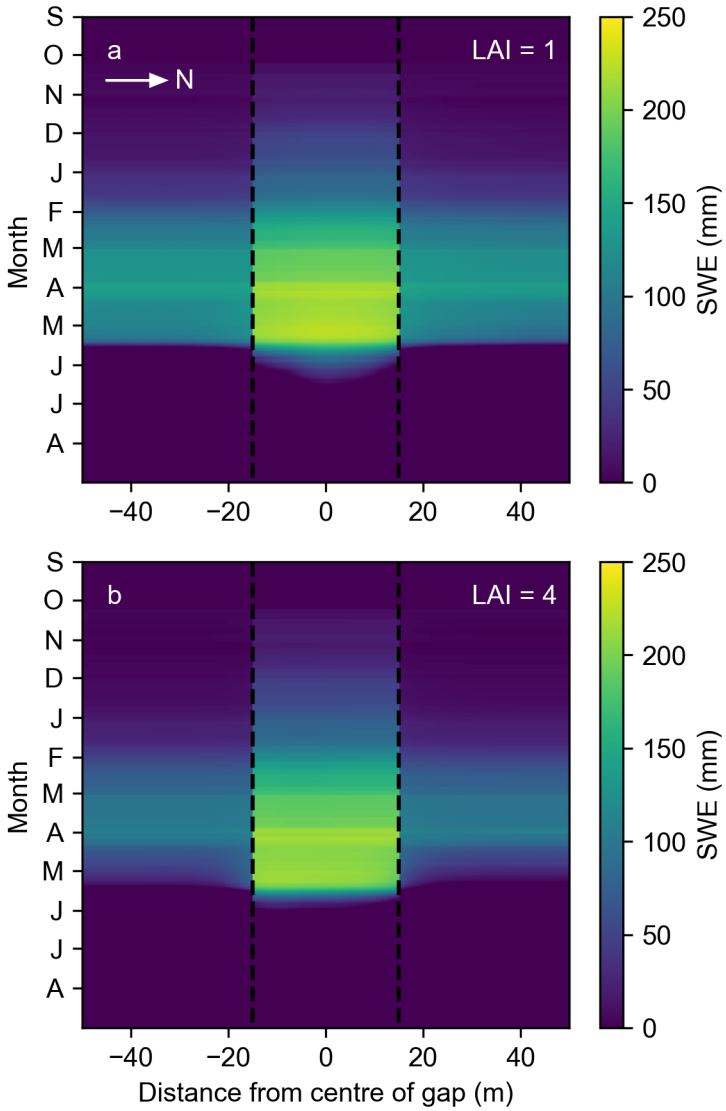

Figure 7.15: Simulated SWE across a 30 m gap in a forest canopy with (a) $LAI = 1$, and (b) $LAI = 4$. In both panels, the wind flows from the south (left to right) and the canopy edges are shown by the black dashed lines.

		Maximum SWE and date of occurance		
Gap width	LAI	South canopy	Gap	North canopy
30 m	1	143.2 mm 30/03/2010	225.8 mm 03/05/2010	141.1 mm 30/03/2010
	2.2	122.0 mm 30/03/2010	222.0 mm 03/05/2010	120.6 mm 30/03/2010
	4	108.1 mm 30/03/2010	217.0 mm 04/04/2010	107.7 mm 30/03/2010
100 m	1	142.7 mm 30/03/2010	221.0 mm 03/05/2010	137.6 mm 30/03/2010
	2.2	121.9 mm 30/03/2010	227.2 mm 06/05/2010	118.9 mm 30/03/2010
	4	108.1 mm 30/03/2010	226.9 mm 06/05/2010	106.7 mm 30/03/2010

Table 7.6: Maximum SWE at three points along the modelled transect: -150 m from the gap centre (South canopy), 150 m from the gap centre (North canopy) and the point in the gap where the maximum SWE occurs (Gap), which varies across each scenario.

		Date of snow disappearance (2010)		
Gap width	LAI	South canopy	Gap	North canopy
30 m	1	18th May	17th June	17th May
	2.2	16th May	10th June	16th May
	4	13th May	29th May	12th May
100 m	1	18th May	12th June	16th May
	2.2	16th May	20th June	15th May
	4	13th May	20th June	11th May

Table 7.7: Date of snow disappearance at three points along the modelled transect: -150 m from the gap centre (South canopy), 150 m from the gap centre (North canopy) and the point in the gap where the snow persists for the longest (Gap), which varies across each scenario.

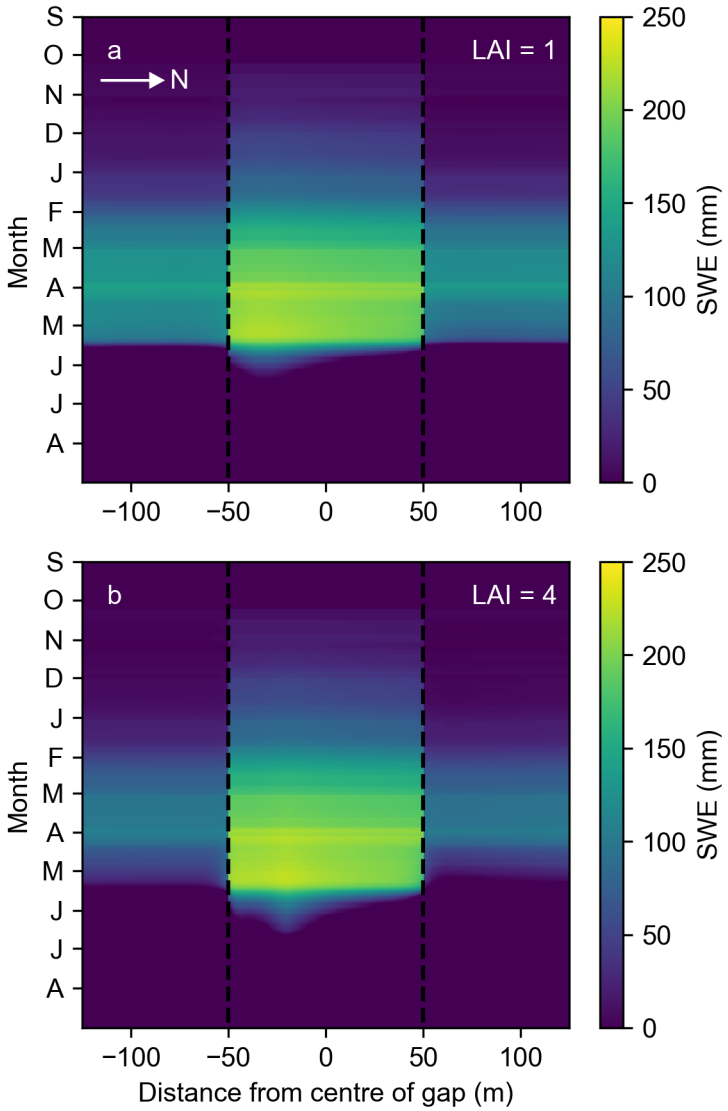

Figure 7.16: Simulated SWE across a 100 m gap in a forest canopy with (a) $LAI = 1$, and (b) $LAI = 4$. In both panels, the wind flows from the south (left to right) and the canopy edges are shown by the black dashed lines.

7.4 Discussion

7.4.1 Calibration

The first section of this chapter addressed the calibration and evaluation of the simplified snow model. This 'final' version of the model had all components present (as detailed in Chapters 5.2.2 and 7.2.1) such that a full winter period of snow accumulation and ablation may be simulated. Observational data from FMI-ARC was utilised for this task, including point measurements of snow depth from both within the clearing and within the adjacent forest at the IOA site, and meteorological data from the AWS (section 7.2.2.1). The calibration process focused on two parameters that influence the modelled snow melt dynamics: albedo (a) and the exchange coefficient C. Optimal values were found for these parameters that minimise the RMS error in the simulated snow depth. The resultant model setup was able to reproduce the snow depths observed at the IOA with an ensemble mean of 0.12 m at the forest site and 0.11 m at the open site when run with the evaluation data sets (section 7.3.1).

Contrary to expectation, the optimal value of sub-canopy albedo in the forest is higher than in the clearing (0.92 vs. 0.82). Natural matter such as tree branches that fall to the forest floor act to reduce the albedo of the sub-canopy snow surface. One would therefore expect the albedo to be higher in the clearing as it is less likely to have debris (Hardy et al. 1998, Melloh et al. 2002). The effect of albedo in the model is to modify the effective shortwave radiation driving melting in the snow pack (see Equation 7.2). Therefore, a higher than expected albedo calibrated at the forest site (or lower than expected albedo at the clearing site) may be compensating for potential differences between the incoming shortwave radiation received at the meteorological station compared to the snow measurement sites, rather than reflecting site-specific differences in the actual reflectance of the snow surface.

As with the calibration of the snow accumulation related parameters, point measurements of snow depth were used for the calibration rather than measurements along a gap transect. Therefore, whilst the model was shown to perform well within a forest setting or open clearing setting, it was not possible to evaluate it's performance in a spatially distributed way. It has to be assumed that the model will simulate the intermediate conditions in a satisfactory way. Evaluation of the shortwave and longwave radiation models with observational data from a measurement transect across a forest gap at FMI-ARC in Chapter 6.4 helped show the suitability of these models used for capturing the key patterns in the radiative fluxes across a forest discontinuity. If this calibration was to be repeated then it would be interesting to obtain a more spatially distributed snow data set rather than just point measurements. Ideally this data set would span the width of a forest gap and into the the canopy either side, with regular measurement points along this. This would enable a better constraint on the model calibration and it's ability to replicate real-life snow melt dynamics across a forest discontinuity.

The calibration of the accumulation-only snow model resulted in an ensemble of 'good' values for the snow density parameters A_2 and ρ_{ns}. However, for the subsequent gap scenario simulations only a single 'best' value was used for these parameters for simplification purposes. With more time, the full ensemble of value combinations for A_2 and ρ_{ns} could be run with the snow model to give a better idea of the uncertainty in the results.

7.4.2 Gap scenarios

I explored sub-canopy snow dynamics within a series of forest gap scenario experiments. Specifically, I tested the impact of radiative and turbulent energy fluxes, gap width and orientation, and canopy density on the accumulation and melting of snow

over the winter season (Figure 7.17).

The spatial distribution of turbulent fluxes across the gap controls the asymmetric pattern of snowmelt observed with the wider gaps (from $\geq$50 m). Removing these fluxes of energy from the model (by setting the turbulent exchange coefficient C to zero) led to a much more even distribution of melt rates across the gap (Figure 7.11 a.). Looking at the difference between the scenarios with and without turbulent fluxes (Figure 7.11 b.), it can be seen that the turbulent exchange of energy reduces the snow mass across the gap from just south of the centre to the northern edge of the gap. It also gives rise to faster melt rates within the northern canopy section compared to the sub-canopy snow to the south of the gap.

Sub-canopy wind speed is a driver of the modelled turbulent fluxes (see Equations 7.6 & 7.10); turbulent heat fluxes will melt more snow where sub-canopy wind speeds are higher. As a result, the spatial pattern of snowmelt follows the variation in wind speed across the wider gaps, which is not symmetrical. As was found in Chapter 3, wind speeds within a 100 m gap increase as the wind flows across the gap and adjusts to the reduction in drag (Figure 3.1 i.). In the 100 m gap scenarios in this chapter, snowmelt occurred sooner on the downwind (northern) side of the gap where the sub-canopy wind speeds are highest (Figure 7.8 a.). Whereas with a narrower canopy opening, such as in the 30 m gap scenario, the wind flow does not have enough space to adjust to the change in boundary conditions as it moves across the gap and so there is not the same degree of variation in the sub-canopy wind speed (Figure 3.1 j.). This is mirrored in the more even pattern of melting across the 30 m and 10 m gaps (Figure 7.8 b. & c.).

In contrast, the shortwave radiative fluxes to the snow provide a secondary influence on snowmelt dynamics, particularly at the northern edge of the gap. It is generally well-established that shade from direct solar radiation provided by trees at the southern edge of a gap acts to preserve the snowpack for longer, whilst snow towards the

northern edge of the gap is exposed to higher levels of direct solar radiation, which acts to advance melt (Lawler & Link 2011, Musselman et al. 2015). This would also be expected to lead to an asymmetric melt pattern. However, we see a more complex interplay of the energy fluxes in the wider gap scenarios presented here. When all shortwave radiation is reflected from the snow surface (by setting albedo equal to one) the asymmetry in melting across the 100 m gap is still observed, supporting the idea that the turbulent fluxes are determining the pattern of melt in this scenario (Figure 7.14 a.). Looking at the difference in SWE as a result of ignoring shortwave radiative fluxes, we see that there is greater snow mass on the ground with no shortwave radiation (Figure 7.14 b.). It could be expected that this increase in mass would be concentrated at the northern side of the gap, where typically there is most melting from direct shortwave radiation, but the increase follows the spatial distribution set by the turbulent fluxes (i.e. most increase in SWE towards the southern edge). Typically cloudy conditions at Sodankylä mean that the incoming shortwave radiation is predominantly diffuse over the melting period, which reduces the influence of direct shading by trees. As the highest wind speeds are at the northern edge of the gap this is where the turbulent heat flux is highest and in this case appears to dominate the melt energy balance, so that removing the melting effect of shortwave radiation does not lead to large increases in snow mass on this side of the gap. Whereas on the southern side of the gap, wind speeds are lower and so the shortwave radiative fluxes account for a greater proportion of the melt energy, hence the larger snow mass gains in this region of the gap from removing shortwave radiation. These findings highlight the importance of turbulent fluxes in setting the melt timings within the gaps modelled here.

The canopy density determines the amount of sub-canopy snow accumulation and modulates the snowmelt patterns set by the energy fluxes across the gap. For instance, increasing the LAI reduces the maximum SWE on the ground in the forest as more snowfall is intercepted by the canopy (Table 7.6). Within the gap it is more complex

due to the interaction of different processes. Adjusting the LAI does not change the broad asymmetrical pattern of snowmelt across the gap, although there are small scale variations in the melt rates, particularly in the southern half of the gap where the most persistent section of snowpack lies. Looking again at the widest gap (100 m E-W), increasing the LAI gives lower wind speeds within the gap (see Chapter 3.3.3), which suppress the turbulent fluxes compared to lower LAI scenarios and results in slower melt rates (Figure 7.16). Increasing the LAI also has the effect of reducing the sky view fraction (v_s) and so decreases the diffuse radiation energy input for melting, particularly towards the edges of the gap where the canopy has the potential to occupy more of the sky view. Both of these effects lead to later snow disappearance dates in the 100 m gap with an LAI of 4, compared to the same gap with lower LAI values (Table 7.7).

Within the model, the balance between turbulent fluxes and radiative fluxes is also set by the parameters C and a (see Equations 7.6, 7.10 & 7.2). For instance the asymmetrical melt pattern would likely become more prominent for larger values of C, and lower values of a would increase the importance of the shortwave radiation. This highlights the importance of getting these parameters within a realistic range via the calibration process. A sensitivity study where the snow model is run with an ensemble of 'good' values for those parameters (e.g. giving snow depth RMSE < 0.1 m) would be interesting to see how the resultant melt patterns differed depending on the value combination of C and a.

The results from the gap scenario simulations presented in this chapter suggest that further work on representing the distribution of turbulent energy exchange and the influence of this on snowmelt patterns across a forest–clearing environment would be a worthwhile endeavour. Often radiative fluxes are considered to be the primary influence on snow melt dynamics in forest settings and so there is a large body of research on this aspect of the energy balance for snowmelt (Link & Marks 1999*a*,

Sicart et al. 2006, Lawler & Link 2011, Musselman et al. 2015). Sub-canopy turbulent fluxes have been studied to a far lesser degree. Lower wind speeds typically found under forest canopies when compared to open environments usually means reduced turbulent exchange. As a result, and because of challenges in making sub-canopy measurements, turbulent fluxes to snow on the forest floor have been considered of minor importance relative to radiative fluxes and so have not been subject to much study (Conway et al. 2018, Hardy et al. 1998, Link & Marks 1999*a*, Marks et al. 2008). This is particularly so in discontinuous forests where there are transitional environments to consider that are neither fully forested nor fully open.

Mazzotti et al. (2020b) introduced simple wind-scaling to the FSM2 modelling framework to improve the representation of sub-canopy wind speeds ('enhanced FSM2'). They found that the difference in the turbulent fluxes between the two versions of the model gave rise to a considerable impact on the timing of melt-out. They highlight a need for more observational data from which to evaluate simulations of sub-canopy turbulent fluxes. As the modelled turbulent fluxes are dependant upon sub-canopy wind speeds and air and surface temperatures (see Equations 7.6 and 7.10), these would be useful variables to collect spatially detailed measurements of. Combined with spatially distributed measurements of snow mass along a forest gap transect spanning the snowmelt period, this would provide a better constraint on the calibration of the model and resultant hypothetical gap scenarios.

7.4.3 Localised solar heating of canopy elements

The simple model used here does not take into account localised heating of canopy elements, for instance solar heating of the exposed trunks at the northern edge of the gap on sunny days. Figure 7.18 shows how the snow melts out fastest on the sunlit side of the clearing at the IOA site. The direct shortwave radiation is at maxima

here and often this can be a localised 'hot spot' where the longwave radiation is also at maxima due to solar heating of the trees at the forest edge (Lawler & Link 2011). This has been found to give trunk temperatures of up to 25°C higher than locally measured air temperatures (Webster et al. 2016). Therefore there is the potential for greater energy to be available for melting snow from longwave radiation emitted by solar-heated trunks than would be simulated by the model for longwave radiation used here. The spatial pattern of snowmelt could also be expected to be altered as it is commonly observed that melting initiates within the snow immediately surrounding trunks, which can lead to greater small-scale variability in melt rates (as seen in Figure 7.18). In order to include the effect of solar heating of the canopy on the northern side of the gap, the modelled canopy would need to be considered as more than one emitting layer and detailed field data on individual trunk temperatures and air temperatures immediately surrounding individual trees would be required to parameterise this, which was beyond the scope of this particular project.

7.4.4 Further limitations

Other limitations to the modelling work presented here are similar to those encountered in previous chapters relating to the use of simplified representations of the forest canopy. For example, the BLASIUS model, which gives the sub-canopy wind speed and friction velocity scaling, represents the canopy on either side of the gap as homogeneous with uniform height and density. The PRICE model uses a more varied artificial forest to generate v_s values, where trees are located randomly in space with varied canopy metrics such as height, crown width and foliage density. However, there is still a simple geometric representation of the tree structure, which in reality would have a more complex and varied canopy architecture. The margin between the canopy and the gap within the models is abrupt but in an actual forest clearing the edge may not be as clearly defined and there may be sections of regrowth blurring the

transition from forest to open environment. This would lead to finer scale variations in the processes modelled here and the resultant spatial patterns of accumulation and melt, particularly at the gap edges. However, the broader scale patterns observed with the gap scenarios can still be held as a general guide to the kind of physical response we might expect from introducing a discontinuity such as a road or track into a boreal forest environment.

7.5 Conclusion

Using 7 years of observational data from FMI-ARC in northern Finland a simple snow model was calibrated at two different sites (the IOA forest site and IOA clearing site). The calibrated model was shown to perform well at both sites, with RMS errors in the simulated snow depth of 0.12 m (forest) and 0.11 m (clearing) during the model evaluation stage.

The calibrated model was then used to undertake a series of hypothetical gap scenario simulations to explore the influence of gap and canopy characteristics on snow accumulation and ablation across a forest gap. The sensitivity of these snow dynamics to the incoming radiative and turbulent fluxes was also investigated.

It was found that the spatial distribution of snowmelt patterns were most sensitive to the modelled turbulent fluxes, which in turn are influenced by factors such as the gap width and the canopy density. The wider gaps ($\geq$50 m) had an asymmetric pattern of snowmelt with melt occurring sooner towards the northern edge of the gap and persisting for up to a month longer towards the southern edge. This asymmetry follows the sub-canopy wind speeds across the gap, with higher speeds leading to greater turbulent heat fluxes and therefore melting. Shortwave radiative fluxes are most influential in the southern half of the 100 m gap, where wind speeds and therefore

turbulent fluxes are low. The canopy density provides a modulating effect on the snow dynamics, enhancing or reducing the snowmelt via changes to the wind speed and sky view fraction.

Scope for further work includes: collecting spatially distributed measurements of sub-canopy wind speeds, air temperature, surface temperature and SWE across a linear forest clearing to better constrain the model calibration, and inclusion of localised solar heating of canopy elements such as tree trunks on the exposed (north) edge of the gap within the model framework.

As forests become increasingly fragmented, improving our ability to represent these processes within a modelling framework will be increasingly valuable to understanding the environmental impact of linear clearings.

	Accumulation		Melting		Notes
	Gap	Canopy	Gap	Canopy	
Increasing gap width					Spatial pattern of melting becomes more asymmetric as gap width increases
Changing orientation E-W to N-S					
E-W to NE-SW /NW-SE					
Remove turbulent fluxes (C=0)					Spatial pattern of melting becomes more uniform across the gap
All diffuse SW					Accumulation increased at northern edge & into canopy (decreased at southern edge/canopy). Melting enhanced at southern edge & into canopy (reduced at northern edge/canopy).
All direct SW					Accumulation decreased at northern edge & into canopy (increased at southern edge/canopy). Melting reduced at southern edge & into canopy (enhanced at northern edge/canopy).
Increase albedo (a=1)					.
Changing LAI					Response varies according to gap width

Increases
Decreases
No/minimal change
Complicated

Figure 7.17: Influence of each factor investigated through the gap scenarios on snow accumulation and melting within the gap and canopy. Green indicates an increase in that snow dynamic (e.g. greater snow accumulation or enhanced melting), red indicates a decrease, yellow indicates no or minimal change in the snow dynamics and blue is used where the response is complicated (e.g. varies in conjunction with gap width).

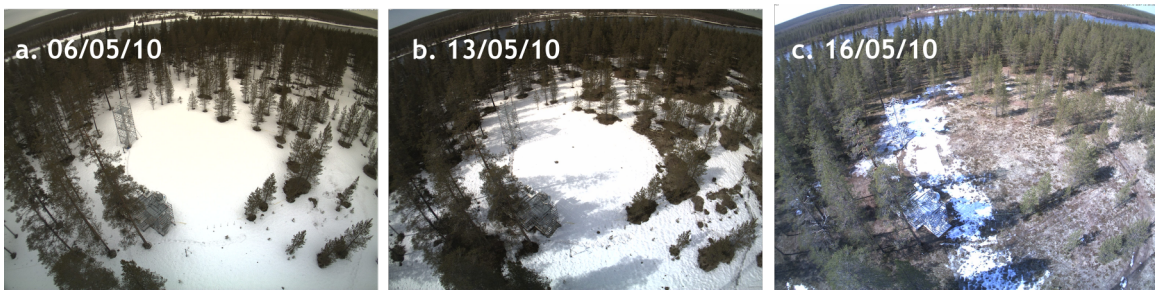

Figure 7.18: Photographs of melting snow cover at the IOA site (06/05 – 16/05 2010). Sub-canopy snow often melts first around the heated trunks of trees, as shown by the progression of images from left to right. Also shown here is the faster melt rate on the north side of the gap (towards the right hand side of each image), which is more exposed to direct solar radiation than the shaded southern edge. Images were taken at 12:00 from the 48 m high tower at the IOA. These and more recent images are available at: `https://litdb.fmi.fi/ioa0010_data.php/`

Chapter 8

Conclusion

8.1 Summary of findings

The aims for this thesis were to explore how patterns of sub-canopy wind flow and radiative fluxes vary across linear forest gaps, and the impact of these on the spatial and temporal distribution of snow accumulation and melt processes.

The objectives for achieving these aims were to:

- Explore how sub-canopy wind flow is modified by linear clearings within the forest canopy and investigate how gap width and canopy characteristics, such as height and density, may influence these flow patterns (**Chapter 3**).

- Calibrate and evaluate the ability of a Reynolds-Averaged Navier Stokes wind flow model (BLASIUS (Wood & Mason 1993, Wood 1995)) to capture observed wind behaviour across a canopy edge (**Chapter 4**).

- Produce a simple linear model relating sub-canopy wind speeds and friction velocities to above-canopy wind speed measurements in order to facilitate the

integration of these variables into a snow model for accumulation and melting.(**Chapter 4**).

- Calibrate and evaluate a simplified forest snow model (FSM2 (Mazzotti et al. 2020a)) to represent snow accumulation and melting in a boreal forest setting (**Chapters 5, 6 & 7**).

- Bring the simple wind and snow models together to simulate snow accumulation and melting processes across hypothetical forest gaps of varying width, orientation and canopy density (**Chapter 7**).

The work in this thesis utilised observational data from the FMI-ARC research station in northern Finland. This site has a flat topography and is characterised by a mixture of boreal forest (typically Scots pine and birch tree species) and some open bog. The data came from a variety of sources: my own measurements (collected in April 2016), long-running observations at FMI-ARC (spanning 2007–2014), data collected by other researchers such as Reid et al. (2014) and Mazzotti et al. (2020b).

The main findings from this thesis were:

1. Sub-canopy wind flow is modified by the presence of a forest gap, as the wind adjusts to the change in the lower boundary conditions. Notable features of the wind flow within the widest gap (100 m wide) include a general increase in wind speeds below the canopy height as the wind flows across the gap and a zone of recirculating air as the wind enters the gap (**Chapter 3**).

2. Of the gap sizes investigated, only the widest gap (100 m wide) was wide enough for the air flow to adjust fully to the new boundary condition. For narrower gaps, the perturbation to the flow was smaller. Canopy characteristics have a secondary influence on sub-canopy wind flow. Taller trees accentuate the region of reversed wind flow and faster flowing air above the canopy is not

drawn down as deeply down into the gap. A denser forest canopy results in greater vertical velocities at the canopy edges. Reducing the canopy density results in higher overall wind speeds across the domain. (**Chapter 3**).

3. It was possible to use simple linear models to relate sub-canopy wind speeds and friction velocities across the model domain to above-canopy wind speed observations (**Chapter 4**).

4. Considering snow dynamics across forest gaps, I found that in general, greater snow accumulation occurs within the gaps and that this snow persisted for longer when compared to the sub-canopy snowpack (**Chapter 7**).

5. Turbulent fluxes drive the spatial pattern of snowmelt across a gap. They can lead to an asymmetric distribution of melting across wider gaps ($\geq$ 50 m), with greater melting towards the exposed downwind edge and a patch of persistent snow towards the sheltered upwind edge (**Chapter 7**).

6. Simulated snowmelt patterns correlate with the sub-canopy wind speeds across the gap (**Chapter 7**). Higher wind speeds mean greater fluxes of sensible heat, which leads to greater melting. Narrower gaps ($\leq$ 30 m) are not wide enough for the wind flow to adjust to the gap in the canopy, so there is not the same increase in speeds across the gap as in the wider scenarios, hence turbulent fluxes are lower, and the melting is more evenly distributed across the narrower gap transects.

7. Radiative fluxes provide a secondary influence on simulated snow melt (**Chapter 7**). Sub-canopy shortwave radiation was most influential in the windward side of the gap where the turbulent fluxes are lower due to low wind speeds.

8.2 Importance and wider implications for boreal hydrology and ecology

These findings demonstrate that gaps in forest canopies impact both local wind flow and snow dynamics. There is a global trend towards increasingly fragmented forests (Haddad et al. 2015, Watson et al. 2018), often linked to human development such as the creation of road networks (Kuklina et al. 2021). As a result, linear clearings may become increasingly prevalent within these landscapes. Other modes of disturbance, such as fire and wind-throw events, can also create large canopy gaps that will alter local meteorological conditions (McCarthy 2001). Understanding the role that gaps play in modifying the local environment of these disturbances is important for future forest management aiming to mitigate as far as possible any negative impacts of future fragmentation.

Forest gaps are generally associated with greater snow mass that persists for longer in the melting season, particularly in the parts of the gap that are sheltered from the prevailing wind direction (Chapter 7). The persistence of snow has the potential to impact on local streamflow, in terms of the rate and timing of melt. A single isolated road through an otherwise undisturbed forest may not have a notable influence on the local hydrology beyond its immediate location. However, where there are networks of road or access tracks the cumulative effect could be more significant. Patches of persistent snow within a clearing will also act to increase the surface albedo relative to continuous canopy. Within heavily fragmented landscapes, particularly if the clearings are wide, this could contribute towards regionally significant changes in the surface energy balance during the spring melting period.

The downwind edge of a wide forest gap is exposed to higher wind speeds (Chapter 3). Although wind speeds at Sodankyla are typically low, other sites of interest may be more prone to high wind speeds and gusts. As a result, trees at this exposed edge

are more vulnerable to wind damage compared to those further within the forest (Burton 2002, Gardiner 2021). This is particularly the case if the clearing has been recently created, as the trees at the edge may not have had time to adjust to the new conditions (Gardiner et al. 2016). The modelling work in Chapter 3 also showed a downward movement of air from above the canopy as the air flows into the gap and an upward movement of air as it re-enters the canopy. This could affect other natural processes such as the spread of fire (Kiefer et al. 2016), particularly as there may be greater plant material on the ground at gap edges (e.g. from wind-snapped branches or leftover from the gap creation). Seed and pollen dispersal are also depend on vertical movements of air to lift them in and out of the canopy (Nathan et al. 2002).

Gap size is an important determinant of the temporal and spatial patterns of snowmelt (Chapter 7). Keeping clearings as narrow as possible is likely to be the most impactful way of reducing the extent to which they modify their surrounding environment. Another consideration is the effect that gap orientation relative to the prevailing wind direction can have on the fetch across the gap. A narrow gap orientated parallel or almost-parallel to the prevailing wind direction would have much higher sub-canopy wind speeds than if it were orientated perpendicular to the wind direction. As well as affecting the turbulent flux of energy to snow via wind-speed, the gap width and orientation can also affect the amount of radiation received by snow on the ground, both of which are important for melt dynamics.

At Sodankylä, I found that snowmelt patterns were principally controlled by turbulent fluxes. The transferability of modelling results is a key factor to consider when thinking about their wider implications. The models used in this thesis were calibrated and run with data from FMI-ARC, Sodankylä. Findings presented here are therefore applicable to this particular site, but may still be broadly applicable to other topographically flat boreal forest landscapes. However, the relative importance of

turbulent fluxes and insolation may vary in other settings. Atmospheric conditions are typically cloudy at Sodankylä. In a landscape where clear-sky days are more common, radiative fluxes may be more influential on the sub-canopy snow dynamics within forest gaps. Sodankylä is also characterised by low wind speeds. There may be greater spatial variation in snow accumulation across a gap at winder sites where sub-canopy friction velocities may be high enough to initiate wind-driven movement of snow. As discussed before, the effective length of gap travelled by the wind can be lengthened according to the gap orientation relative to the wind direction. As such, at windier sites even a narrow gap could modify snow accumulation and melt patterns, depending on its relative orientation.

8.3 Simple models vs. complex models

Forests are intricately varied ecosystems populated with trees of varying age, height and species. The structure of the canopy is spatially variable and characteristics such as foliage area and crown size vary from tree to tree. Branches and leaves grow in varied directions and orientations to produce complex and unique spatial arrangements of these canopy elements. Furthermore, forest canopies are dynamic living systems; the position of branches change on the time scale of seconds as they sway in the wind, and over larger time scales, the space occupied by individual trees will expand as they grow and will open up as a result of damage and mortality.

In this thesis, the modelled forest canopy sections are simplified versions of actual canopies, for example represented by simplistic tree geometries and by canopy metrics. Some of the natural variation within a forest could be captured within the PRICE model (used to estimate sky view fraction), in which trees were randomly positioned within the forest plot and assigned varied canopy metrics based on field observations. Within the BLASIUS wind flow model canopy characteristics were applied uniformly

in space. The limitation of applying canopy metrics uniformly across a forest section, or using a simplistic representation of tree form, is that finer scale variations are not captured. For example, models with a simplified canopy structure are not able to replicate the movement of sun flecks and shadows across the forest floor, or finer scale variations of wind flow around canopy elements.

Using LiDAR data, it is possible to capture the finer-scale detail of a canopy structure (Webster et al. 2020). This information can be used to drive more complicated representations of the canopy within a snow modelling framework. A more complex model that can capture finer scale processes has the potential to produce accurate predictions of snow accumulation and melting and be able to hone in on the key processes and study them in finer detail. However, complex models are computationally expensive to run and need greater amounts of data to calibrate the larger number of parameters that are required. More complex models may only provide more accurate predictions if there is sufficient data to calibrate them with (Famiglietti et al. 2021). Otherwise, the high number of poorly constrained parameters results in high levels of model uncertainty, with equifinality potentially becoming increasingly important.

Complex models calibrated at intensively monitored sites may not transfer well to other locations. Other sites may have more limited data sets available for calibration or none at all, and the same complex model may not perform equally well across multiple sites with varying characteristics. In many practical cases, a model-user may be principally interested in the broad patterns and trends rather than requiring the full complexity of the modelled processes. Furthermore, a stakeholder may not have the technical knowledge or processing capability to obtain the required information from a more complex model when an understanding of the higher level response of the modelled system is sufficient for their needs. With this in mind, there is still a need and value in having simpler models that can predict snow accumulation and

melt patterns to a reasonable degree, require far fewer parameters to be calibrated, are quicker to run, more straightforward to quantify model uncertainty and easier to understand.

8.4 Data limitations

Field measurements of sub-canopy wind speeds across linear clearings were collected during April 2016 at FMI-ARC (Chapter 4). The intention was to use this data for the calibration of the BLASIUS wind flow model. However, the observed speeds were very low and with a relatively high degree of variation, and so unsuitable for use in the calibration process. The open bog site was the only location at FMI-ARC where suitable data could be collected, and even at this site speeds are quite low. This meant that it was not possible to evaluate the ability of BLASIUS to replicate real-life flow patterns across a forest gap scenario (instead, data across a canopy edge at the open bog site was used). In the future, selecting another field site with typically windier conditions would provide a better source of data from which to calibrate and evaluate a model of sub-canopy wind speeds across forest discontinuities.

A common limitation within the thesis is related to the low availability of observational snow data, which posed a challenge to constraining the calibration and evaluation of the snow model. This was a particular issue at the forest and bog sites along the snow course (Chapter 5), where the spatial and temporal frequency of measurements was very low (1–2 measurements, approximately once a month). This produces high levels of uncertainty in the calibrated parameters as these measurements may not be very representative of their environment and it is difficult to capture temporal variations in the snow properties when the observations are made so infrequently.

The next section outlines the scope for further work, to both address some of the

thesis limitations and to build upon the findings from this thesis.

8.5 Scope for future work: recommendations and future research priorities

8.5.1 Consider heterogeneities and multiple discontinuities within forest canopies

The wind flow modelling suggested that horizontal variations in the forest at the scale of individual trees are unlikely to have notable impacts on sub-canopy wind speeds. However, it would be interesting to consider how larger patches of canopy (on the scale of 10 m+) with differing canopy metrics might influence wind flow patterns. In addition, it would be interesting to explore the wind dynamics that might arise from the presence of multiple forest gaps, for instance where natural resource extraction has created networks of linear clearings through forests.

8.5.2 Collect wind speed data at windier sites

It would be beneficial to consider collecting sub-canopy wind speeds across a forest clearing transect. Wind speeds at Sodankylä were very low and, except at the most exposed site, were never sufficient to move settled snow. Future studies at alternative sites with higher average wind speeds would be beneficial because it would allow for the collection of better quality data set within forest gaps, rather than only in open environments. Observations of sub-canopy wind speeds across forest gaps, which was the specific interest of this thesis, would provide a better constraint on the model calibration. Secondly, a longer field campaign or multiple campaigns would increase

the probability of recording a range of wind conditions, including higher wind speeds and blowing snow events. Finally, increasing the number of measurement points by having more anemometers would help better constrain the spatial distribution of wind speeds. Ensuring that the edges are well observed would also be valuable for furthering our understanding of this marginal environment. Ideally this work would be carried out across a selection of gap widths and/or across a number of sites to enable greater transferability of the findings.

8.5.3 Increase spatial and temporal frequency of snow data collection

Obtaining a spatially distributed data set of sub-canopy snow depth and mass, incoming radiation, air and canopy temperatures along a forest gap transect would help to overcome some of the limitations with the model calibration. Taking daily or sub-daily measurements would allow for a more detailed examination of the change in snow properties over time and help reduce the predictive uncertainty of the calibrated model. Taking a particular focus on data collection at the forest edge would help increase our understanding of the key processes and fluxes in this marginal environment.

8.5.4 Include localised solar heating of canopy elements

Studies have shown that air temperature cannot always be used to approximate canopy temperature (Webster et al. 2017). Solar heating of canopy elements, such as trunks, can result in localised temperatures that far exceed air temperature (Webster et al. 2016). Including this effect within the snow model would provide a more realistic representation of the longwave energy emitted by the canopy to the snow surface,

and enable more accurate predictions of snow melt timing and runoff rates. This could be achieved by treating the canopy as more than one emitting layer and would require detailed canopy and air temperature field observations to parameterise the model.

8.5.5 Further research into sub-canopy turbulent fluxes across forest gaps

This thesis primarily focused on the radiative fluxes in the snow melt energy balance as these are typically the dominant sources of energy to the snowpack in forest environments. My findings showed that while the radiative input to snowmelt is influential, the turbulent fluxes are key to the observed asymmetrical pattern of melting across the gap in the wider scenarios ($\geq$ 50 m). Therefore this is a topic deserving further research, particularly as turbulent fluxes in forest clearings have been subject to far less attention than their radiative counterparts. Measurements of sub-canopy turbulent fluxes can be challenging but observational data of sub-canopy wind speeds and temperatures could help evaluate the models of turbulent fluxes used here. Conducting a more detailed sensitivity study into the melt parameters a and C and how the balance between radiative and turbulent fluxes vary across the range of potential value combinations for these parameters would also be informative for the gap scenarios in this thesis.

8.6 Conclusion

The dynamics of forest snow are a fundamental component of the wider hydrology and ecology of boreal forests. The rate and timing of snow accumulation and melting are key controls on streamflow timing and magnitude, surface albedo, soil temperatures

(and therefore soil microbial activity), vegetative productivity and the availability of nutritious food for herbivores. Understanding how forest snow dynamics are modified by the presence of gaps in the canopy, through the interactions of the disturbed canopy with wind flow and energy fluxes, is therefore critical for understanding the wider impacts of forest disturbance in boreal environments. Models able to capture these relationships provide useful tools that can help managers identify and mitigate these impacts, which will become increasingly important as forest disturbance and fragmentation continue in the future.

Appendix A

Appendix

A.1 Wind speed profiles: modelled vs. theoretical

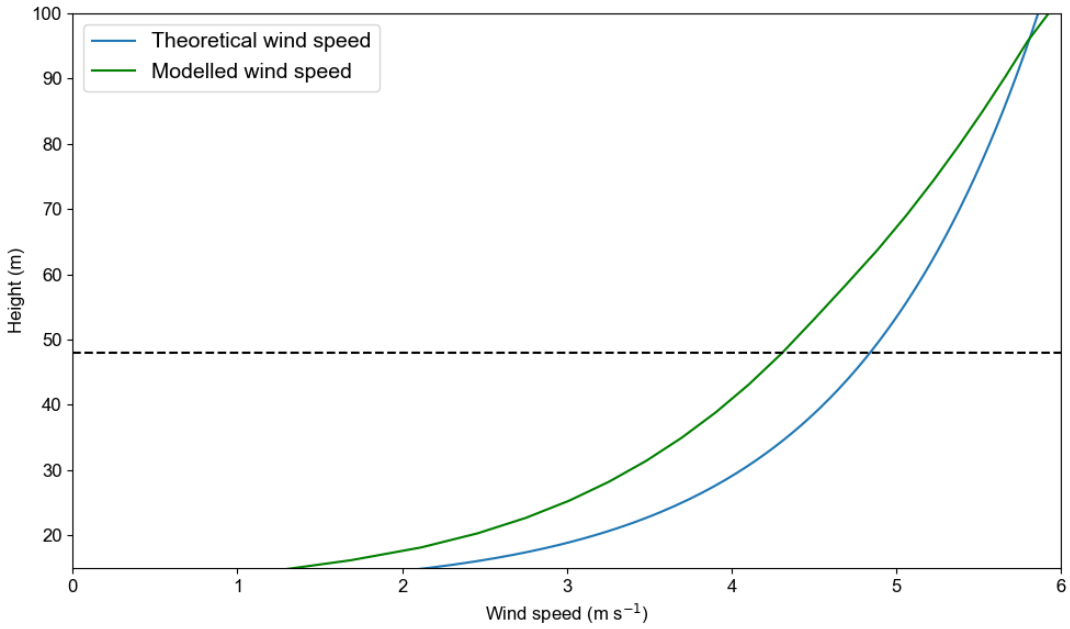

Figure A.1: An example of the difference between the modelled wind profile and expected log-law wind profile.

A.2 Canopy measurements: Bog site

Tree species	**h1**	**h2**	**h3**	**h4**	**h (average)**
Birch	6.2	6.2	6.3	6.3	6.3
Birch	7.6	7.8	7.7	7.8	7.7
Birch	6.2	6.0	6.0	6.0	6.1
Pine	5.7	5.7	5.7	5.7	5.7
Pine	5.9	5.9	6	5.9	5.9
Birch	8.0	8.0	7.9	8.0	8.0
Birch	4.2	4.2	4.2	4.2	4.2
Pine	3.5	3.5	3.5	3.5	3.5
Birch	5.1	5.0	5.1	5.0	5.1
Average for sample					5.82

Table A.1: Measured and averaged tree heights for the main canopy at the bog site (taken from a random sample in the field)

Tree species	**h1**	**h2**	**h3**	**h4**	**h (average)**
Pine	6.1	6.1	6.1	6.2	6.1
Pine	4.0	4.0	4.1	4.1	4.1
Birch	5.7	5.9	5.8	5.8	5.8
Pine	4.4	4.4	4.4	4.4	4.4
Pine	3.3	3.3	3.3	3.3	3.3
Birch	6.1	6.1	6.1	6.1	6.1
Birch	6.3	6.3	6.4	6.4	6.4
Pine	7.7	7.7	7.7	7.8	7.7
Pine	6.9	7.0	7.0	7.1	7.0
Birch	4.7	4.7	4.8	4.8	4.8
Average for sample					5.56

Table A.2: Measured and averaged tree heights for the sparse canopy at the bog site (taken from a random sample in the field)

A.3 Canopy measurements: Road site

Tree ID	h_1 **(m)**	h_2 **(m)**	h_3 **(m)**	h_4 **(m)**	h_5 **(m)**	h_6 **(m)**	h_{mean} **(m)**	**DBH (m)**
T01	13.25	13.45	13.35	13.45	13.25	13.35	13.35	0.390
T02	11.15	11.25	11.15	11.25	11.15	11.15	11.18	0.335
T03	12.25	12.45	12.35	12.35	12.35	12.35	12.35	0.386
T04	13.45	13.45	13.45	13.45	13.45	13.45	13.45	0.420
T05	13.40	13.50	13.50	13.50	13.20	13.50	13.43	0.524
T06	13.40	13.50	13.70	13.60	13.90	13.70	13.63	0.500
T07	11.35	11.45	11.45	11.45	11.55	11.65	11.48	0.430
T08	8.30	8.30	8.40	8.50	8.40	8.50	8.40	0.188
T09	10.00	9.80	9.90	9.80	10.00	9.80	9.88	0.242
T10	11.75	12.05	11.95	11.85	12.15	11.85	11.93	0.500
T11	13.90	14.70	14.10	13.70	13.70	13.80	13.98	0.394
T12	10.75	10.85	10.75	10.85	10.75	10.75	10.78	0.422
T13	11.40	11.40	11.50	11.40	11.40	11.50	11.43	0.368
T14	10.43	10.23	10.23	10.03	10.13	10.23	10.21	0.370
T15	10.37	10.27	10.27	10.37	10.37	10.27	10.32	0.264
T16	9.00	9.10	9.10	9.10	9.20	9.10	9.10	0.270
T17	12.58	12.68	12.58	12.58	12.58	12.58	12.60	0.546
T18	11.25	11.25	11.45	11.25	11.25	11.25	11.28	0.418
T19	11.00	11.00	11.00	11.00	11.10	11.10	11.03	0.248
T20	10.60	10.50	10.60	10.60	10.50	10.70	10.58	0.244
T21	8.77	8.77	8.87	8.77	8.67	8.57	8.74	0.328
T22	13.01	12.71	12.91	13.01	13.11	13.01	12.96	0.540
T23	11.54	11.44	11.64	11.74	11.84	11.54	11.62	0.356
T24	8.85	9.05	8.55	9.15	8.95	9.05	8.93	0.366
T25	12.15	12.15	12.35	12.25	12.35	12.25	12.25	0.414
T26	11.00	11.10	11.10	11.20	11.40	11.1	11.15	0.564
T27	11.00	11.00	11.00	11.10	11.10	11.10	11.05	0.540
T28	10.26	10.16	10.26	10.36	10.16	10.26	10.24	0.556
Mean							11.33	0.397

Table A.3: Measured tree heights and values of DBH for the road site (all trees within 2.5 m either side of the transect line were measured)

Tree ID	h_{c1} **(m)**	h_{c2} **(m)**	h_{c3} **(m)**	h_{c4} **(m)**	h_{c5} **(m)**	h_{c6} **(m)**	**mean** h_c **(m)**	**CW (E-W) (m)**	**CW (N-S) (m)**
T01	4.9	4.9	4.9	4.9	5.0	5.0	4.9	2.50	2.15
T02	5.3	5.3	4.9	5.1	5.3	5.4	5.2	1.90	2.75
T03	6.4	6.2	6.2	6.4	6.5	6.4	6.4	2.75	2.50
T04	6.7	6.7	6.7	6.6	6.6	6.6	6.7	2.15	2.50
T05	7.3	7.3	7.3	7.5	7.2	7.3	7.3	3.20	3.60
T06	7.0	7.0	7.0	6.9	7.0	6.9	7.0	2.15	2.50
T07	6.0	6.0	6.0	6.1	6.1	6.1	6.1	2.10	2.35
T08	4.0	4.1	4.2	4.1	4.1	4.1	4.1	1.55	1.85
T09	6.8	6.7	6.8	6.8	6.8	6.8	6.8	1.45	1.70
T10	5.3	5.3	15.3	5.3	5.3	5.2	5.3	3.75	4.00
T11	6.3	6.3	6.3	6.3	6.3	6.4	6.3	3.40	2.25
T12	4.0	4.0	4.0	4.0	4.0	4.0	4.0	3.10	2.75
T13	1.8	1.8	1.8	1.8	1.8	1.5	11.8	2.35	1.75
T14	3.8	3.8	3.8	3.9	3.9	3.9	3.9	2.50	3.00
T15	5.9	5.9	5.9	5.9	5.9	6.0	5.9	1.70	1.50
T16	4.2	4.2	4.2	4.2	4.2	4.2	4.2	1.30	1.65
T17	6.3	6.5	6.4	6.4	6.4	6.4	6.4	3.10	2.60
T18	4.9	4.9	4.7	4.7	4.8	4.8	4.8	1.95	3.00
T19	6.1	6.2	6.1	6.1	6.2	6.2	6.2	1.20	1.50
T20	5.9	6.0	5.9	5.9	6.0	5.9	5.9	1.60	1.85
T21	3.6	3.6	3.5	3.6	3.6	3.6	3.6	2.25	2.35
T22	4.6	4.6	4.7	4.8	4.7	4.7	4.7	3.30	3.10
T23	5.2	5.4	5.4	5.2	5.4	5.2	5.3	1.95	2.60
T24	4.8	4.8	4.5	4.8	4.6	4.6	4.7	2.90	2.50
T25	6.6	6.5	6.5	6.5	6.5	6.5	6.5	1.75	1.95
T26	2.2	2.3	2.2	2.3	2.2	2.2	2.3	5.20	3.50
T27	4.8	4.8	4.8	4.8	4.8	4.8	4.8	5.00	3.75
T28	3.7	3.8	3.7	3.7	3.8	3.8	3.8	5.30	4.95
Mean							5.15	2.49	2.55

Table A.4: Measured crown base heights (h_c) and crown widths (CW) at the road site (all trees within 2.5 m either side of the transect line were measured). The crown widths were measured both in the E-W direction and the N-S direction to give a sense of its radial extent.

A.4 Wind scaling

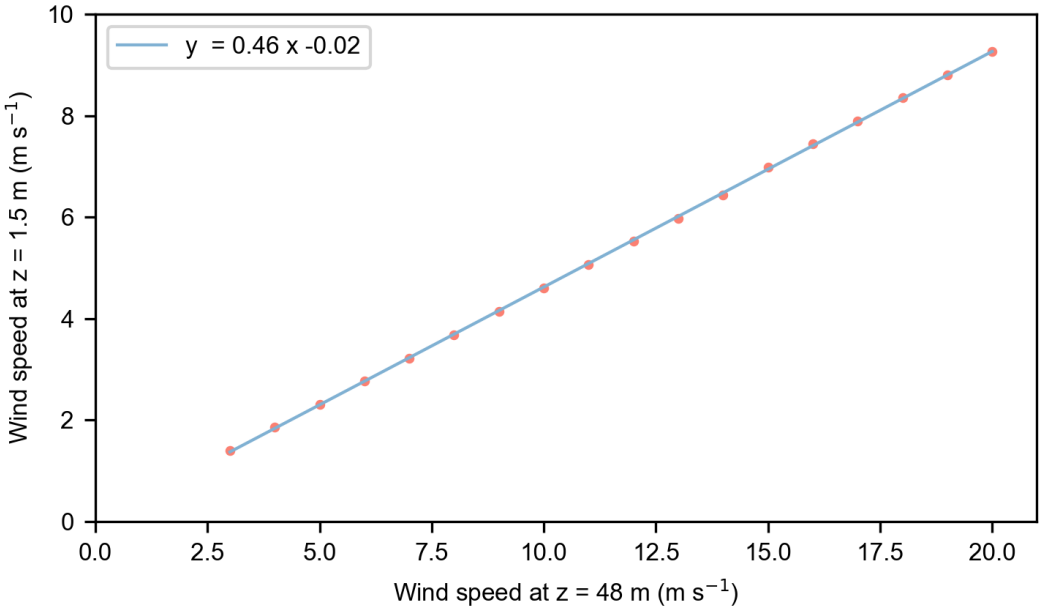

Figure A.2: Ratio of wind speeds in the open (at $x = 0$m, $z = 1.5$ m) to 48 m height speeds

A.5 Chapter 7: Gap scenarios

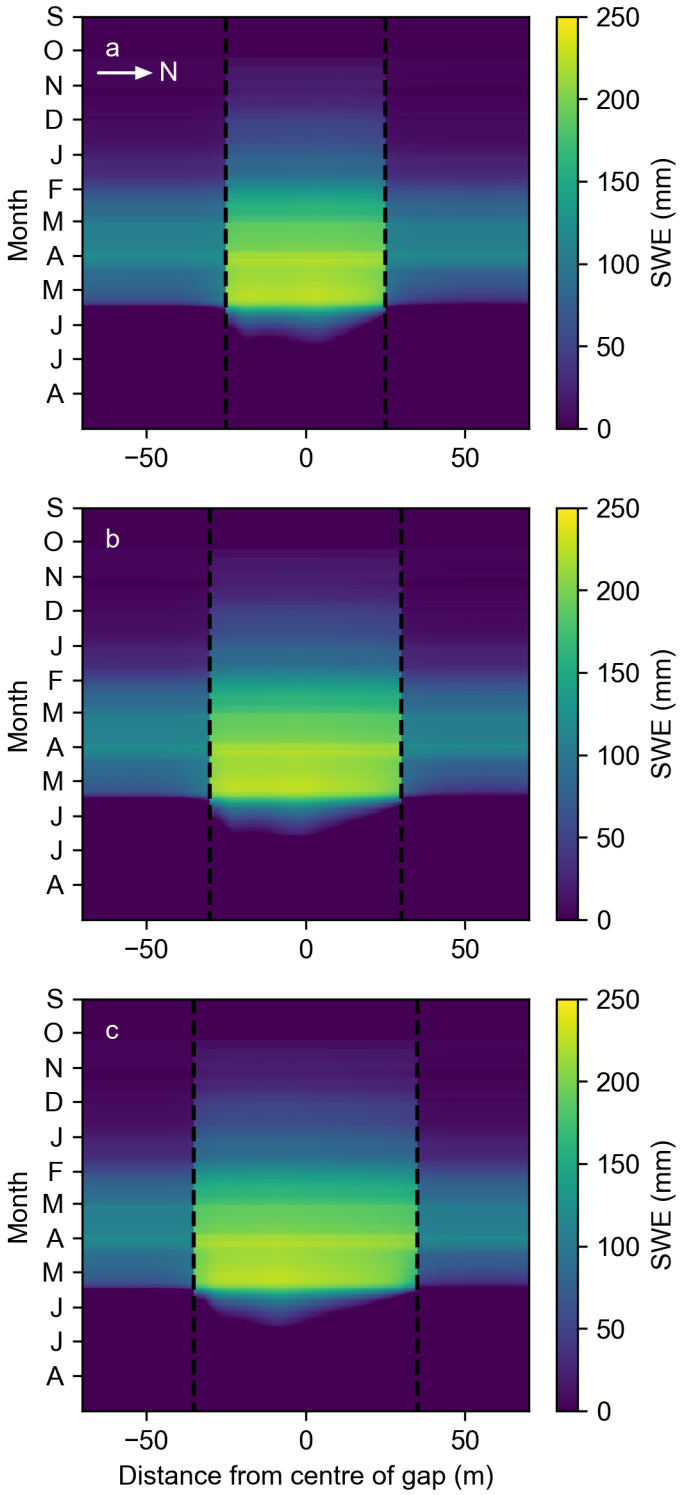

Figure A.3: Three gap scenarios orientated E-W with widths of 50 m (a), 60 m (b) and 70 m (c). The wind is directed from the south and so flows along the transect from left to right in these panels. The edges between the canopy and gap are shown by the dashed black lines.

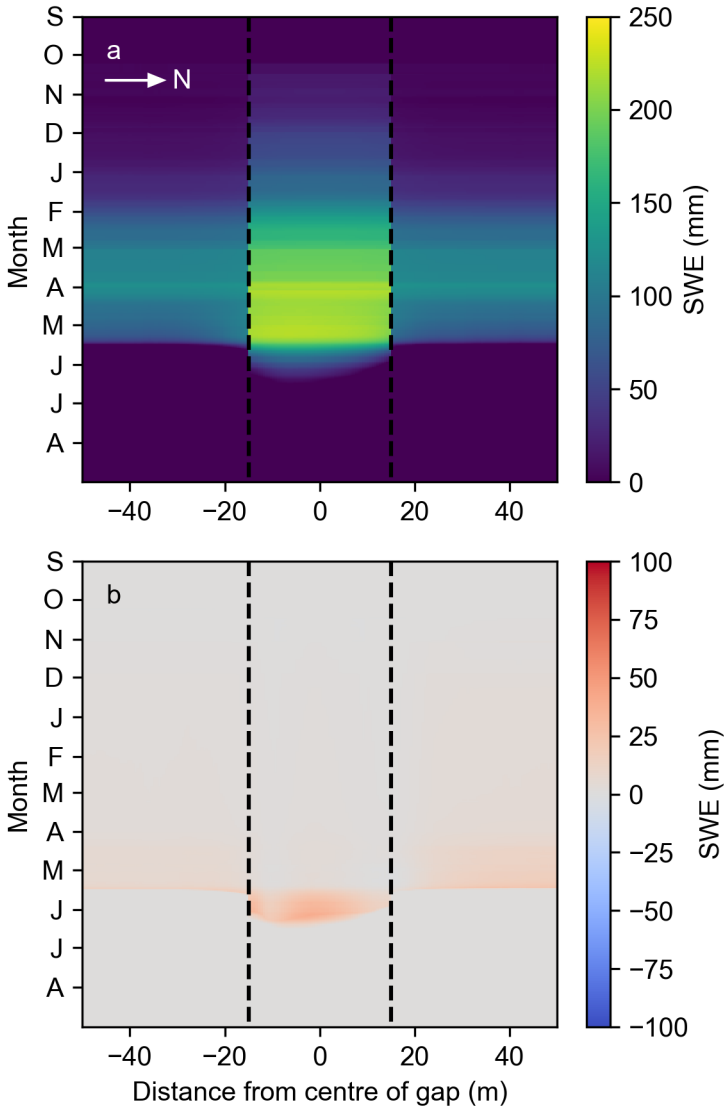

Figure A.4: (a) Simulated SWE across a 30 m canopy gap orientated E-W with the surface exchange coefficient $C = 0$. (b) The difference between the 30 m E-W gap scenario with and without the turbulent exchange of energy included within the model. This shows the relative increase in the snow mass if melting due to turbulent fluxes is ignored. The dashed black lines in both panels show the location of the gap edges.

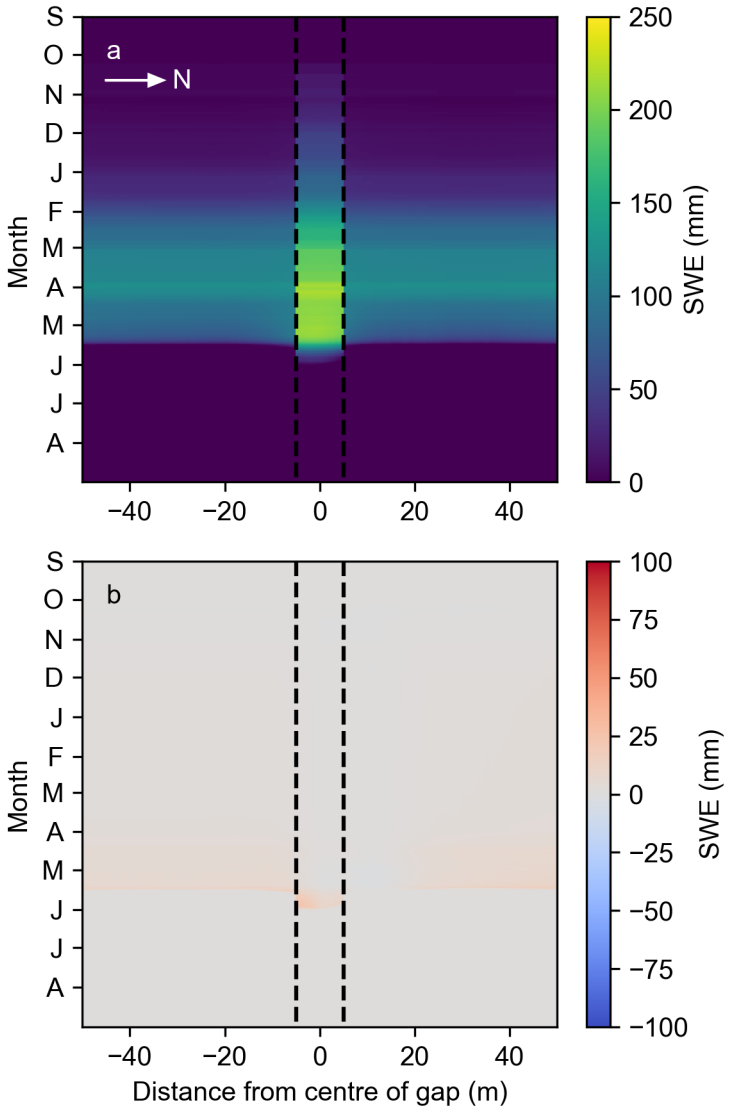

Figure A.5: (a) Simulated SWE across a 10 m canopy gap orientated E-W with the surface exchange coefficient C = 0. (b) The difference between the 10 m E-W gap scenario with and without the turbulent exchange of energy included within the model. This shows the relative increase in the snow mass if melting due to turbulent fluxes is ignored. The dashed black lines in both panels show the location of the gap edges.

Bibliography

Abele, G. & Gow, A. J. (1975), Compressibility characteristics of undisturbed snow, Technical report, Cold Regions Research And Engineering Lab Hanover NH.

Ahmed, H. F., Helgason, W., Barr, A. & Black, A. (2021), 'Characterization of spring thaw and its relationship with carbon uptake for different types of southern boreal forest', *Agricultural and Forest Meteorology* **307**, 108511.

Amiro, B. (1990), 'Comparison of turbulence statistics within three boreal forest canopies', *Boundary-Layer Meteorology* **51**(1-2), 99–121.

Arnqvist, J., Segalini, A., Dellwik, E. & Bergström, H. (2015), 'Wind statistics from a forested landscape', *Boundary-Layer Meteorology* **156**(1), 53–71.

Ayotte, K. W. (2008), 'Computational modelling for wind energy assessment', *Journal of Wind Engineering and Industrial Aerodynamics* **96**(10), 1571–1590.

Baldocchi, D. D. & Meyers, T. P. (1988), 'Turbulence structure in a deciduous forest', *Boundary-Layer Meteorology* **43**(4), 345–364.

Baldocchi, D., Kelliher, F. M., Black, T. A. & Jarvis, P. (2000), 'Climate and vegetation controls on boreal zone energy exchange', *Global Change Biology* **6**(S1), 69–83.

Banerjee, T., Katul, G., Fontan, S., Poggi, D. & Kumar, M. (2013), 'Mean flow near edges and within cavities situated inside dense canopies', *Boundary-layer meteorology* **149**(1), 19–41.

Barichivich, J., Briffa, K. R., Myneni, R., Schrier, G. V. d., Dorigo, W., Tucker, C. J., Osborn, T. J. & Melvin, T. M. (2014), 'Temperature and snow-mediated moisture controls of summer photosynthetic activity in northern terrestrial ecosystems between 1982 and 2011', *Remote Sensing* **6**(2), 1390–1431.

Barnett, T. P., Adam, J. C. & Lettenmaier, D. P. (2005), 'Potential impacts of a warming climate on water availability in snow-dominated regions', *Nature* **438**(7066), 303–309.

Barr, A., Griffis, T., Black, T., Lee, X., Staebler, R., Fuentes, J., Chen, Z. & Morgenstern, K. (2002), 'Comparing the carbon budgets of boreal and temperate deciduous forest stands', *Canadian Journal of Forest Research* **32**(5), 813–822.

Bartlett, P. A., MacKay, M. D. & Verseghy, D. L. (2006), 'Modified snow algorithms in the canadian land surface scheme: Model runs and sensitivity analysis at three boreal forest stands', *Atmosphere-Ocean* **44**(3), 207–222.

Baskent, E. Z. & Jordan, G. A. (1995), 'Characterizing spatial structure of forest landscapes', *Canadian Journal of Forest Research* **25**(11), 1830–1849.

Bayne, E. M., Van Wilgenburg, S. L., Boutin, S. & Hobson, K. A. (2005), 'Modeling and field-testing of ovenbird (seiurus aurocapillus) responses to boreal forest dissection by energy sector development at multiple spatial scales', *Landscape Ecology* **20**(2), 203–216.

Becknell, J. M., Desai, A. R., Dietze, M. C., Schultz, C. A., Starr, G., Duffy, P. A., Franklin, J. F., Pourmokhtarian, A., Hall, J., Stoy, P. C. et al. (2015), 'Assessing interactions among changing climate, management, and disturbance in forests: a macrosystems approach', *BioScience* **65**(3), 263–274.

Belcher, S. E., Harman, I. N. & Finnigan, J. J. (2012), 'The wind in the willows: flows in forest canopies in complex terrain', *Annual Review of Fluid Mechanics* **44**, 479–504.

Belcher, S., Jerram, N. & Hunt, J. (2003), 'Adjustment of a turbulent boundary layer to a canopy of roughness elements', *Journal of Fluid Mechanics* **488**, 369–398.

Bergen, J. (1975), 'Air movement in a forest clearing as indicated by smoke drift', *Agricultural Meteorology* **15**, 165–179.

Bergeron, Y., Chen, H. Y., Kenkel, N. C., Leduc, A. L. & Macdonald, S. E. (2014), 'Boreal mixedwood stand dynamics: ecological processes underlying multiple pathways', *The Forestry Chronicle* **90**(2), 202–213.

Bernier, P. Y. & Swanson, R. (1993), 'The influence of opening size on snow evaporation in the forests of the alberta foothills', *Canadian Journal of Forest Research* **23**(2), 239–244.

Berry, G. & Rothwell, R. (1992), 'Snow ablation in small forest openings in southwest alberta', *Canadian Journal of Forest Research* **22**(9), 1326–1331.

Betts, A. K. & Ball, J. H. (1997), 'Albedo over the boreal forest', *Journal of Geophysical Research: Atmospheres* **102**(D24), 28901–28909.

Black, T., Chen, W., Barr, A., Arain, M., Chen, Z., Nesic, Z., Hogg, E., Neumann, H. & Yang, P. (2000), 'Increased carbon sequestration by a boreal deciduous forest in years with a warm spring', *Geophysical Research Letters* **27**(9), 1271–1274.

Bokhorst, S., Pedersen, S. H., Brucker, L., Anisimov, O., Bjerke, J. W., Brown, R. D., Ehrich, D., Essery, R. L., Heilig, A., Ingvander, S. et al. (2016), 'Changing arctic snow cover: A review of recent developments and assessment of future needs for observations, modelling, and impacts', *Ambio* **45**(5), 516–537.

Bonan, G. (2015), *Turbulent Fluxes*, 3 edn, Cambridge University Press, pp. 209–217.

Bonan, G. B. & Shugart, H. H. (1989), 'Environmental factors and ecological processes in boreal forests', *Annual review of ecology and systematics* **20**(1), 1–28.

Boon, S. (2012), 'Snow accumulation following forest disturbance', *Ecohydrology* **5**(3), 279–285.

Boudreault, L.-É., Dupont, S., Bechmann, A. & Dellwik, E. (2017), 'How forest inhomogeneities affect the edge flow', *Boundary-Layer Meteorology* **162**(3), 375–400.

Brandt, J. P. (n.d.), 'The extent of the north american boreal zone', *Environmental Reviews* **17**.

Brooks, P. D., Grogan, P., Templer, P. H., Groffman, P., Öquist, M. G. & Schimel, J. (2011), 'Carbon and nitrogen cycling in snow-covered environments', *Geography Compass* **5**(9), 682–699.

Brooks, P. D., McKnight, D. & Elder, K. (2005), 'Carbon limitation of soil respiration under winter snowpacks: potential feedbacks between growing season and winter carbon fluxes', *Global Change Biology* **11**(2), 231–238.

Brooks, P. D. & Williams, M. W. (1999), 'Snowpack controls on nitrogen cycling and export in seasonally snow-covered catchments', *Hydrological processes* **13**(14-15), 2177–2190.

Brooks, P. D., Williams, M. W. & Schmidt, S. K. (1996), 'Microbial activity under alpine snowpacks, niwot ridge, colorado', *Biogeochemistry* **32**(2), 93–113.

Bründl, M., Bartelt, P., Schneebeli, M. & Flühler, H. (1999), 'Measuring branch deflection of spruce branches caused by intercepted snow load', *Hydrological processes* **13**(14-15), 2357–2369.

Budd, W. (1966), 'The drifting of non-uniform snow particles', *Studies in Antarctic Meteorology* pp. 59–70.

Burton, P. J. (2002), 'Effects of clearcut edges on trees in the sub-boreal spruce zone of northwest-central british columbia', *Silva Fennica* **36**(1), 329–352.

Cadenasso, M. & Pickett, S. (2000), 'Linking forest edge structure to edge function: mediation of herbivore damage', *Journal of Ecology* **88**(1), 31–44.

Cadenasso, M., Traynor, M. & Pickett, S. T. (1997), 'Functional location of forest edges: gradients of multiple physical factors', *Canadian Journal of Forest Research* **27**(5), 774–782.

Cameron, E. K., Bayne, E. M. & Clapperton, M. J. (2007), 'Human-facilitated invasion of exotic earthworms into northern boreal forests', *Ecoscience* **14**(4), 482–490.

Caners, R. T. & Lieffers, V. J. (2014), 'Divergent pathways of successional recovery for in situ oil sands exploration drilling pads on wooded moderate-rich fens in alberta, canada', *Restoration ecology* **22**(5), 657–667.

Cassiani, M., Katul, G. & Albertson, J. (2008), 'The effects of canopy leaf area index on airflow across forest edges: large-eddy simulation and analytical results', *Boundary-layer meteorology* **126**(3), 433–460.

Chahine, A., Dupont, S., Sinfort, C. & Brunet, Y. (2014), 'Wind-flow dynamics over a vineyard', *Boundary-layer meteorology* **151**(3), 557–577.

Chen, J., Franklin, J. F. & Spies, T. A. (1993), 'Contrasting microclimates among clearcut, edge, and interior of old-growth douglas-fir forest', *Agricultural and forest meteorology* **63**(3-4), 219–237.

Chen, J. M. & Black, T. (1992), 'Defining leaf area index for non-flat leaves', *Plant, Cell & Environment* **15**(4), 421–429.

Chen, J. M., Rich, P. M., Gower, S. T., Norman, J. M. & Plummer, S. (1997), 'Leaf area index of boreal forests: Theory, techniques, and measurements', *Journal of Geophysical Research: Atmospheres* **102**(D24), 29429–29443.

Coen, J. L. (2005), 'Simulation of the big elk fire using coupled atmosphere–fire modeling', *International Journal of Wildland Fire* **14**(1), 49–59.

Colbeck, S. C. (1987), *Snow Metamorphism and Classification*, Springer Netherlands, Dordrecht, pp. 1–35.

Conan, B., Aubrun, S., Coudour, B., Chetehouna, K. & Garo, J.-P. (2015), 'Contribution of coherent structures to momentum and concentration fluxes over a flat vegetation canopy modelled in a wind tunnel', *Atmospheric environment* **107**, 329–341.

Conklin, M. H. & Bales, R. C. (1993), 'SO_2 uptake on ice spheres: Liquid nature of the ice-air interface', *Journal of Geophysical Research: Atmospheres* **98**(D9), 16851–16855.

Conway, J. P., Pomeroy, J. W., Helgason, W. D. & Kinar, N. J. (2018), 'Challenges in modeling turbulent heat fluxes to snowpacks in forest clearings', *Journal of Hydrometeorology* **19**(10), 1599–1616.

Currier, W. R. & Lundquist, J. D. (2018), 'Snow depth variability at the forest edge in multiple climates in the western united states', *Water Resources Research* **54**(11), 8756–8773.

Dabros, A., Hammond, H. J., Pinzon, J., Pinno, B. & Langor, D. (2017), 'Edge influence of low-impact seismic lines for oil exploration on upland forest vegetation in northern alberta (canada)', *Forest Ecology and Management* **400**, 278–288.

Dabros, A., Pyper, M. & Castilla, G. (2018), 'Seismic lines in the boreal and arctic ecosystems of north america: environmental impacts, challenges, and opportunities', *Environmental Reviews* **26**(2), 214–229.

Dale, V. H., Joyce, L. A., McNulty, S., Neilson, R. P., Ayres, M. P., Flannigan, M. D., Hanson, P. J., Irland, L. C., Lugo, A. E., Peterson, C. J. et al. (2001), 'Climate change and forest disturbances', *BioScience* **51**(9), 723–734.

Deardorff, J. W. (1978), 'Efficient prediction of ground surface temperature and moisture, with inclusion of a layer of vegetation', *Journal of Geophysical Research: Oceans* **83**(C4), 1889–1903.
URL: *https://agupubs.onlinelibrary.wiley.com/doi/abs/10.1029/JC083iC04p01889*

Dellwik, E., Bingöl, F. & Mann, J. (2014), 'Flow distortion at a dense forest edge', *Quarterly Journal of the Royal Meteorological Society* **140**(679), 676–686.

Detto, M., Katul, G. G., Siqueira, M., Juang, J.-Y. & Stoy, P. (2008), 'The structure of turbulence near a tall forest edge: The backward-facing step flow analogy revisited', *Ecological Applications* **18**(6), 1420–1435.

DeWalle, D. R. & Rango, A. (2008), *Principles of snow hydrology*, Cambridge University Press.

Dickerson-Lange, S. E., Vano, J. A., Gersonde, R. & Lundquist, J. D. (2021), 'Ranking forest effects on snow storage: a decision tool for forest management', *Water Resources Research* p. e2020WR027926.

Dupont, S., Bonnefond, J.-M., Irvine, M. R., Lamaud, E. & Brunet, Y. (2011), 'Long-distance edge effects in a pine forest with a deep and sparse trunk space: in situ and numerical experiments', *Agricultural and forest meteorology* **151**(3), 328–344.

Dupont, S. & Brunet, Y. (2006), 'Simulation of turbulent flow in an urban forested park damaged by a windstorm', *Boundary-Layer Meteorology* **120**(1), 133–161.

Dupont, S. & Brunet, Y. (2008*a*), 'Edge flow and canopy structure: a large-eddy simulation study', *Boundary-Layer Meteorology* **126**(1), 51–71.

Dupont, S. & Brunet, Y. (2008*b*), 'Impact of forest edge shape on tree stability: a large-eddy simulation study', *Forestry* **81**(3), 299–315.

Dupont, S., Brunet, Y. & Finnigan, J. (2008), 'Large-eddy simulation of turbulent

flow over a forested hill: Validation and coherent structure identification', *Quarterly Journal of the Royal Meteorological Society* **134**(636), 1911–1929.

Dupont, S., Brunet, Y. & Jarosz, N. (2006), 'Eulerian modelling of pollen dispersal over heterogeneous vegetation canopies', *Agricultural and Forest Meteorology* **141**(2), 82–104.

Dupont, S., Pivato, D. & Brunet, Y. (2015), 'Wind damage propagation in forests', *Agricultural and Forest Meteorology* **214**, 243–251.

Dwyer, M. J., Patton, E. G. & Shaw, R. H. (1997), 'Turbulent kinetic energy budgets from a large-eddy simulation of airflow above and within a forest canopy', *Boundary-Layer Meteorology* **84**(1), 23–43.

Dyer, S. J., O'Neill, J. P., Wasel, S. M. & Boutin, S. (2001), 'Avoidance of industrial development by woodland caribou', *The Journal of Wildlife Management* pp. 531–542.

Dyer, S. J., O'neill, J. P., Wasel, S. M. & Boutin, S. (2002), 'Quantifying barrier effects of roads and seismic lines on movements of female woodland caribou in northeastern alberta', *Canadian journal of Zoology* **80**(5), 839–845.

Ellis, C. R., Pomeroy, J. W., Essery, R. L. & Link, T. E. (2011), 'Effects of needleleaf forest cover on radiation and snowmelt dynamics in the canadian rocky mountains', *Canadian Journal of Forest Research* **41**(3), 608–620.

Ellis, C. R., Pomeroy, J. W. & Link, T. E. (2013), 'Modeling increases in snowmelt yield and desynchronization resulting from forest gap-thinning treatments in a northern mountain headwater basin', *Water Resources Research* **49**(2), 936–949.

Erbs, D., Klein, S. & Duffie, J. (1982), 'Estimation of the diffuse radiation fraction for hourly, daily and monthly-average global radiation', *Solar energy* **28**(4), 293–302.

Essery, R. (2015), 'A factorial snowpack model (fsm 1.0)', *Geoscientific Model Development* **8**(12), 3867–3876.

Essery, R., Bunting, P., Rowlands, A., Rutter, N., Hardy, J., Melloh, R., Link, T., Marks, D. & Pomeroy, J. (2007), 'Radiative transfer modeling of a coniferous canopy characterized by airborne remote sensing', *Journal of Hydrometeorology* **9**(2), 228–241.

Essery, R., Kontu, A., Lemmetyinen, J., Dumont, M. & Ménard, C. B. (2016), 'A 7-year dataset for driving and evaluating snow models at an arctic site (sodankylä, finland)', *Geoscientific Instrumentation, Methods and Data Systems* **5**(1), 219–227.

Essery, R., Li, L. & Pomeroy, J. (1999), 'A distributed model of blowing snow over complex terrain', *Hydrological processes* **13**(14-15), 2423–2438.

Essery, R. & Marks, D. (2007), 'Scaling and parametrization of clear-sky solar radiation over complex topography', *Journal of Geophysical Research: Atmospheres* **112**(D10), n/a–n/a. D10122.

Essery, R. & Pomeroy, J. (2004), 'Vegetation and topographic control of wind-blown snow distributions in distributed and aggregated simulations for an arctic tundra basin', *Journal of Hydrometeorology* **5**(5), 735–744.

Essery, R., Pomeroy, J., Ellis, C. & Link, T. (2008), 'Modelling longwave radiation to snow beneath forest canopies using hemispherical photography or linear regression', *Hydrological Processes* **22**(15), 2788–2800.

Essery, R., Pomeroy, J., Parviainen, J. & Storck, P. (2003), 'Sublimation of snow from coniferous forests in a climate model', *Journal of Climate* **16**(11), 1855–1864.

Essery, R., Rutter, N., Pomeroy, J., Baxter, R., Stähli, M., Gustafsson, D., Barr, A., Bartlett, P. & Elder, K. (2009), 'Snowmip2: An evaluation of forest snow process simulations', *Bulletin of the American Meteorological Society* **90**(8), 1120–1135.

Famiglietti, C. A., Smallman, T. L., Levine, P. A., Flack-Prain, S., Quetin, G. R., Meyer, V., Parazoo, N. C., Stettz, S. G., Yang, Y., Bonal, D. et al. (2021), 'Optimal model complexity for terrestrial carbon cycle prediction', *Biogeosciences* **18**(8), 2727–2754.

FAO (2016), State of the world's forests 2016, Technical report, Food and Agriculture Organization of the United Nations (FAO).

Finnigan, J. (2000), 'Turbulence in plant canopies', *Annual review of fluid mechanics* **32**(1), 519–571.

Finnigan, J. J., Shaw, R. H. & Patton, E. G. (2009), 'Turbulence structure above a vegetation canopy', *Journal of Fluid Mechanics* **637**, 387–424.

Flanner, M. G., Shell, K. M., Barlage, M., Perovich, D. K. & Tschudi, M. (2011), 'Radiative forcing and albedo feedback from the northern hemisphere cryosphere between 1979 and 2008', *Nature Geoscience* **4**(3), 151–155.

Flesch, T. K. & Wilson, J. D. (1999), 'Wind and remnant tree sway in forest cutblocks.: I. measured winds in experimental cutblocks', *Agricultural and Forest Meteorology* **93**(4), 229–242.

Forestry Commission (2014*a*), *NFI Survey Manual: 15.0 Diameter (DBH) assessments*.

URL: *https://www.forestry.gov.uk/pdf/15-Diameter-DBH-Assessments-June-2014.pdf/$FILE/15-Diameter-DBH-Assessments-June-2014.pdf*

Forestry Commission (2014*b*), *NFI Survey Manual: 16.0 Height and crown diameter assessments*.

URL: *https://www.forestry.gov.uk/pdf/16-Height-and-Crown-Diameter-Assessments-June-2014.pdf/$FILE/16-Height-and-Crown-Diameter-Assessments-June-2014.pdf*

Forman, R. T. (1995), *Land Mosaics: The Ecology of Landscapes and Regions*.

Gardiner, B. (2021), 'Wind damage to forests and trees: a review with an emphasis on planted and managed forests', *Journal of Forest Research* **26**(4), 248–266.

Gardiner, B., Berry, P. & Moulia, B. (2016), 'Wind impacts on plant growth, mechanics and damage', *Plant Science* **245**, 94–118.

Gardiner, B., Schuck, A. R. T., Schelhaas, M.-J., Orazio, C., Blennow, K. & Nicoll, B. (2013), *Living with storm damage to forests*, European Forest Institute Joensuu.

Garvelmann, J., Pohl, S. & Weiler, M. (2013), 'From observation to the quantification of snow processes with a time-lapse camera network', *Hydrology and Earth System Sciences* **17**(4), 1415.

Gash, J. (1986), 'Observations of turbulence downwind of a forest-heath interface', *Boundary-Layer Meteorology* **36**(3), 227–237.

Gauthier, S., Bernier, P., Kuuluvainen, T., Shvidenko, A. & Schepaschenko, D. (2015), 'Boreal forest health and global change', *Science* **349**(6250), 819–822.

Gelfan, A., Pomeroy, J. & Kuchment, L. (2004), 'Modeling forest cover influences on snow accumulation, sublimation, and melt', *Journal of Hydrometeorology* **5**(5), 785–803.

Glatthorn, J. & Beckschäfer, P. (2014), 'Standardizing the protocol for hemispherical photographs: Accuracy assessment of binarization algorithms', *PLOS ONE* **9**(11), 1–19.
URL: *https://doi.org/10.1371/journal.pone.0111924*

Golding, D. L. & Swanson, R. H. (1978), 'Snow accumulation and melt in small forest openings in alberta', *Canadian Journal of Forest Research* **8**(4), 380–388.

Golding, D. L. & Swanson, R. H. (1986), 'Snow distribution patterns in clearings and adjacent forest', *Water Resources Research* **22**(13), 1931–1940.

Gower, S. T., Kucharik, C. J. & Norman, J. M. (1999), 'Direct and indirect estimation of leaf area index, fapar, and net primary production of terrestrial ecosystems', *Remote sensing of environment* **70**(1), 29–51.

Grant, E. R., Ross, A. N., Gardiner, B. A. & Mobbs, S. D. (2015), 'Field observations of canopy flows over complex terrain', *Boundary-layer meteorology* **156**(2), 231–251.

Gray, D. M. & Male, D. H. (1981), *Handbook of snow: principles, processes, management & use*, Pergamon Press.

Gray, J. & Morland, L. (1995), 'The compaction of polar snow packs', *Cold Regions Science and Technology* **23**(2), 109 – 119.

Haddad, N. M., Brudvig, L. A., Clobert, J., Davies, K. F., Gonzalez, A., Holt, R. D., Lovejoy, T. E., Sexton, J. O., Austin, M. P., Collins, C. D. et al. (2015), 'Habitat fragmentation and its lasting impact on earth's ecosystems', *Science advances* **1**(2), e1500052.

Haglöf Sweden (n.d.), *Users' Guide Vertex III and Transponder T3*, Haglöf Sweden, Långsele, Sweden.
URL: *https://www.forestrytools.com.au/VertexIII%20users%20guide.pdf*

Harding, R. J. & Pomeroy, J. W. (1996), 'The energy balance of the winter boreal landscape', *Journal of Climate* **9**(11), 2778–2787.

Hardy, J., Davis, R., Jordan, R., Ni, W. & Woodcock, C. E. (1998), 'Snow ablation modelling in a mature aspen stand of the boreal forest', *Hydrological Processes* **12**(10-11), 1763–1778.

Hardy, J., Melloh, R., Koenig, G., Marks, D., Winstral, A., Pomeroy, J. & Link, T. (2004), 'Solar radiation transmission through conifer canopies', *Agricultural and Forest Meteorology* **126**(3–4), 257 – 270.

Hardy, J. P., Groffman, P. M., Fitzhugh, R. D., Henry, K. S., Welman, A. T., Demers, J. D., Fahey, T. J., Driscoll, C. T., Tierney, G. L. & Nolan, S. (2001), 'Snow depth manipulation and its influence on soil frost and water dynamics in a northern hardwood forest', *Biogeochemistry* **56**(2), 151–174.

Harper, K. A., Macdonald, S. E., Burton, P. J., Chen, J., Brosofske, K. D., Saunders, S. C., Euskirchen, E. S., Roberts, D., Jaiteh, M. S. & Esseen, P.-A. (2005), 'Edge influence on forest structure and composition in fragmented landscapes', *Conservation Biology* **19**(3), 768–782.

Hasselquist, E. M., Lidberg, W., Sponseller, R. A., Ågren, A. & Laudon, H. (2018), 'Identifying and assessing the potential hydrological function of past artificial forest drainage', *Ambio* **47**(5), 546–556.

Hay, J. E. (1976), 'A revised method for determining the direct and diffuse components of the total short-wave radiation', *Atmosphere* **14**(4), 278–287.

He, S. & Ohara, N. (2017), 'A new formula for estimating the threshold wind speed for snow movement', *Journal of Advances in Modeling Earth Systems* **9**(7), 2514–2525.

Hedstrom, N. & Pomeroy, J. (1998), 'Measurements and modelling of snow interception in the boreal forest', *Hydrological Processes* **12**(10), 1611–1625.

Iqbal, M. (1983), 'An introduction to solar radiation'.

Irvine, M., Gardiner, B. & Hill, M. (1997), 'The evolution of turbulence across a forest edge', *Boundary-Layer Meteorology* **84**(3), 467–496.

Jackson, P. (1981), 'On the displacement height in the logarithmic velocity profile', *Journal of fluid mechanics* **111**, 15–25.

James, A. R. & Stuart-Smith, A. K. (2000), 'Distribution of caribou and wolves in relation to linear corridors', *The Journal of Wildlife Management* pp. 154–159.

Jarvis, P., James, G. & Landsberg, J. (1976), Coniferous forest, *in* J. Monteith, ed., 'Vegetation and the Atmosphere', Academic Press, London, chapter 7, pp. 171–236.

Jarvis, P. & Linder, S. (2000), 'Constraints to growth of boreal forests', *Nature* **405**(6789), 904–905.

Johnson, E. A. & Miyanishi, K. (2010), *Plant disturbance ecology: the process and the response*, Academic Press.

Johnson, E. A. & Miyanishi, K. (2012), 'The boreal forest as a cultural landscape', *Annals of the New York Academy of Sciences* **1249**(1), 151–165.

Jonas, T. & Essery, R. (2011), Snow cover and snowmelt in forest regions, *in* V. P. Singh, P. Singh & U. K. Haritashya, eds, 'Encyclopedia of Snow, Ice and Glaciers', Springer Netherlands, Dordrecht, pp. 1033–1036.

Jonas, T., Webster, C., Mazzotti, G. & Malle, J. (2020), 'Hpeval: A canopy shortwave radiation transmission model using high-resolution hemispherical images', *Agricultural and Forest Meteorology* **284**, 107903.

Jones, H. (1999), 'The ecology of snow-covered systems: a brief overview of nutrient cycling and life in the cold', *Hydrological processes* **13**(14-15), 2135–2147.

Kaimal, J. C. & Finnigan, J. J. (1994), *Atmospheric boundary layer flows: their structure and measurement*, Oxford university press.

Katul, G. G., Mahrt, L., Poggi, D. & Sanz, C. (2004), 'One-and two-equation models for canopy turbulence', *Boundary-Layer Meteorology* **113**(1), 81–109.

Kiefer, M. T., Heilman, W. E., Zhong, S., Charney, J. J. & Bian, X. (2016), 'A study of the influence of forest gaps on fire–atmosphere interactions', *Atmospheric Chemistry and Physics* **16**(13), 8499–8509.

Kivi, R., Kyrö, E., Turunen, T., Ulich, T. & Turunen, E. (1999), 'Atmospheric trends above finland: Ii. troposphere and stratosphere', *Geophysica* **35**(1-2), 71–85.

Kobayashi, D. (1972), 'Studies of snow transport in low-level drifting snow', *Contrib. Inst. Low Temp. Sci., Ser. A* **24**, 1–58.

Kobayashi, D. (1987), 'Snow accumulation on a narrow board', *Cold Regions Science and Technology* **13**(3), 239–245.

Kojola, S., Ahtikoski, A., Hökkä, H. & Penttilä, T. (2012), 'Profitability of alternative management regimes in scots pine stands on drained peatlands', *European Journal of Forest Research* **131**(2), 413–426.

Kotlyakov, V. (1961), 'Results of a study of the processes of formation and structure of the upper layer of the ice sheet in eastern antarctica', *IASH Publ* **55**, 88–99.

Kuklina, V., Bilichenko, I., Bogdanov, V., Kobylkin, D., Petrov, A. N. & Shiklomanov, N. (2021), 'Informal road networks and sustainability of siberian boreal forest landscapes: case study of the vershina khandy taiga', *Environmental Research Letters* **16**(11), 115001.

Langham, E. J. (1981), Physics and properties of snow covers, *in* D. M. Gray & D. H. Male, eds, 'Handbook of Snow: Principles, Processes, Management, and Use', Pergamon Press, New York, pp. 275–337.

Lankau, H., Bayne, E. & Machtans, C. (2013), 'Ovenbird (seiurus aurocapilla) territory placement near seismic lines is influenced by forest regeneration and conspecific density', *Avian Conservation and Ecology* **8**(1).

Latham, A. D. M., Latham, M. C., Boyce, M. S. & Boutin, S. (2011), 'Movement responses by wolves to industrial linear features and their effect on woodland caribou in northeastern alberta', *Ecological Applications* **21**(8), 2854–2865.

Latimer, Christopher, E. & Zuckerberg, B. (2017), 'Forest fragmentation alters winter microclimates and microrefugia in human-modified landscapes', *Ecography* **40**(1), 158–170.

Laurance, W. F. & Arrea, I. B. (2017), 'Roads to riches or ruin?', *Science* **358**(6362), 442–444.

Laurance, W. F., Goosem, M. & Laurance, S. G. (2009), 'Impacts of roads and linear clearings on tropical forests', *Trends in Ecology & Evolution* **24**(12), 659–669.

Lawler, R. R. & Link, T. E. (2011), 'Quantification of incoming all-wave radiation in discontinuous forest canopies with application to snowmelt prediction', *Hydrological Processes* **25**(21), 3322–3331.

Lawrence, D. M. & Slater, A. G. (2010), 'The contribution of snow condition trends to future ground climate', *Climate dynamics* **34**(7-8), 969–981.

Leblond, M., Dussault, C. & Ouellet, J.-P. (2013), 'Avoidance of roads by large herbivores and its relation to disturbance intensity', *Journal of zoology* **289**(1), 32–40.

Lee, P. & Boutin, S. (2006), 'Persistence and developmental transition of wide seismic lines in the western boreal plains of canada', *Journal of Environmental Management* **78**(3), 240–250.

Leppänen, L., Kontu, A., Hannula, H.-R., Sjöblom, H. & Pulliainen, J. (2016), 'Sodankylä manual snow survey program', *Geoscientific Instrumentation, Methods and Data Systems* **5**(1), 163–179.

Li, L. & Pomeroy, J. W. (1997), 'Estimates of threshold wind speeds for snow transport using meteorological data', *Journal of Applied Meteorology* **36**(3), 205–213.

Link, T. E. & Marks, D. (1999*a*), 'Point simulation of seasonal snow cover dynamics

beneath boreal forest canopies', *Journal of Geophysical Research: Atmospheres* **104**(D22), 27841–27857.

Link, T. E., Marks, D. & Hardy, J. P. (2004), 'A deterministic method to characterize canopy radiative transfer properties', *Hydrological processes* **18**(18), 3583–3594.

Link, T. & Marks, D. (1999*b*), 'Distributed simulation of snow cover mass- and energy-balance in the boreal forest', *Hydrological Processes* **13**(14-15), 2439–2452.

Linke, J., Franklin, S. E., Huettmann, F. & Stenhouse, G. B. (2005), 'Seismic cutlines, changing landscape metrics and grizzly bear landscape use in alberta', *Landscape Ecology* **20**(7), 811–826.

Liston, G. E. & Elder, K. (2006), 'A distributed snow-evolution modeling system (snowmodel)', *Journal of Hydrometeorology* **7**(6), 1259–1276.

Liston, G. E., Haehnel, R. B., Sturm, M., Hiemstra, C. A., Berezovskaya, S. & Tabler, R. D. (2007), 'Simulating complex snow distributions in windy environments using snowtran-3d', *Journal of Glaciology* **53**(181), 241–256.

Lohmus, A., Remm, L. & Rannap, R. (2015), 'Just a ditch in forest? reconsidering draining in the context of sustainable forest management', *BioScience* **65**(11), 1066–1076.

Lopes da Costa, J., Castro, F., Palma, J. & Stuart, P. (2006), 'Computer simulation of atmospheric flows over real forests for wind energy resource evaluation', *Journal of Wind Engineering and Industrial Aerodynamics* **94**(8), 603–620.

Lundberg, A., Ala-Aho, P., Eklo, O., Klöve, B., Kværner, J. & Stumpp, C. (2016), 'Snow and frost: implications for spatiotemporal infiltration patterns–a review', *Hydrological processes* **30**(8), 1230–1250.

Lundberg, A. & Halldin, S. (2001), 'Snow interception evaporation. review of measurementtechniques, processes, and models', *Theoretical and Applied Climatology* **70**(1), 117–133.

Lundquist, J. D. & Dettinger, M. D. (2005), 'How snowpack heterogeneity affects diurnal streamflow timing', *Water Resources Research* **41**(5).

Lundquist, J. D., Dickerson-Lange, S. E., Lutz, J. A. & Cristea, N. C. (2013), 'Lower forest density enhances snow retention in regions with warmer winters: A global framework developed from plot-scale observations and modeling', *Water Resources Research* **49**(10), 6356–6370.

MacFarlane, A. K. (2003), 'Vegetation response to seismic lines: Edge effects and on-line succession.'.

Machtans, C. S. (2006), 'Songbird response to seismic lines in the western boreal forest: a manipulative experiment', *Canadian Journal of Zoology* **84**(10), 1421–1430.

Maeno, N., Naruse, R., Nishimura, K., Takei, I., Ebinuma, T., Kobayabhi, S., NIshlmura, H., Kaneda, Y. & Ishida, T. (1985), 'Wind-tunnel experiments on blowing snow', *Annals of Glaciology* **6**(1), 63–67.

Mahat, V., Tarboton, D. G. & Molotch, N. P. (2013), 'Testing above-and below-canopy representations of turbulent fluxes in an energy balance snowmelt model', *Water Resources Research* **49**(2), 1107–1122.

Male, D. & Granger, R. (1981), 'Snow surface energy exchange', *Water Resources Research* **17**(3), 609–627.

Malle, J., Rutter, N., Mazzotti, G. & Jonas, T. (2019), 'Shading by trees and fractional snow cover control the subcanopy radiation budget', *Journal of Geophysical Research: Atmospheres* **124**(6), 3195–3207.

Malle, J., Rutter, N., Webster, C., Mazzotti, G., Wake, L. & Jonas, T. (2021), 'Effect of forest canopy structure on wintertime land surface albedo: Evaluating clm5 simulations with in-situ measurements', *Journal of Geophysical Research: Atmospheres* **126**(9), e2020JD034118.

Mammarella, I., Dellwik, E. & Jensen, N. O. (2008), 'Turbulence spectra, shear stress and turbulent kinetic energy budgets above two beech forest sites in denmark', *Tellus B* **60**(2), 179–187.

Mårell, A., Hofgaard, A. & Danell, K. (2006), 'Nutrient dynamics of reindeer forage species along snowmelt gradients at different ecological scales', *Basic and Applied Ecology* **7**(1), 13–30.

Markfort, C., Porté-Agel, F. & Stefan, H. (2014), 'Canopy-wake dynamics and wind sheltering effects on earth surface fluxes', *Environmental Fluid Mechanics* **14**(3), 663–697.

Marks, D. & Dozier, J. (1992), 'Climate and energy exchange at the snow surface in the alpine region of the sierra nevada: 2. snow cover energy balance', *Water Resources Research* **28**(11), 3043–3054.

Marks, D., Winstral, A., Flerchinger, G., Reba, M., Pomeroy, J., Link, T. & Elder, K. (2008), 'Comparing simulated and measured sensible and latent heat fluxes over snow under a pine canopy to improve an energy balance snowmelt model', *Journal of Hydrometeorology* **9**(6), 1506–1522.

Marsh, C. B., Pomeroy, J. W. & Spiteri, R. J. (2012), 'Implications of mountain shading on calculating energy for snowmelt using unstructured triangular meshes', *Hydrological Processes* **26**(12), 1767–1778.

Marsh, P. & Pomeroy, J. W. (1996), 'Meltwater fluxes at an arctic forest-tundra site', *Hydrological Processes* **10**(10), 1383–1400.

Matlack, G. R. (1993), 'Microenvironment variation within and among forest edge sites in the eastern united states', *Biological conservation* **66**(3), 185–194.

Mayhead, G. (1973), 'Some drag coefficients for british forest trees derived from wind tunnel studies', *Agricultural Meteorology* **12**, 123–130.

Mazzotti, G., Currier, W. R., Deems, J. S., Pflug, J. M., Lundquist, J. D. & Jonas, T. (2019), 'Revisiting snow cover variability and canopy structure within forest stands: Insights from airborne lidar data', *Water Resources Research* **55**(7), 6198–6216.

Mazzotti, G., Essery, R., Moeser, C. D. & Jonas, T. (2020a), 'Resolving small-scale forest snow patterns using an energy balance snow model with a one-layer canopy', *Water Resources Research* **56**(1), e2019WR026129.

Mazzotti, G., Essery, R., Webster, C., Malle, J. & Jonas, T. (2020b), 'Process-level evaluation of a hyper-resolution forest snow model using distributed multisensor observations', *Water Resources Research* **56**(9), e2020WR027572.

McCarthy, J. (2001), 'Gap dynamics of forest trees: a review with particular attention to boreal forests', *Environmental reviews* **9**(1), 1–59.

Melloh, R. A., Hardy, J. P., Bailey, R. N. & Hall, T. J. (2002), 'An efficient snow albedo model for the open and sub-canopy', *Hydrological Processes* **16**(18), 3571–3584.

Metcalfe, R. & Buttle, J. (1998), 'A statistical model of spatially distributed snowmelt rates in a boreal forest basin', *Hydrological processes* **12**(10-11), 1701–1722.

Mitchell, S. (2013), 'Wind as a natural disturbance agent in forests: a synthesis', *Forestry: An International Journal of Forest Research* **86**(2), 147–157.

Moeser, D., Mazzotti, G., Helbig, N. & Jonas, T. (2016), 'Representing spatial variability of forest snow: Implementation of a new interception model', *Water Resources Research* **52**(2), 1208–1226.

Moeser, D., Morsdorf, F. & Jonas, T. (2015), 'Novel forest structure metrics from airborne lidar data for improved snow interception estimation', *Agricultural and Forest Meteorology* **208**, 40–49.

Mortensen, D. A., Rauschert, E. S., Nord, A. N. & Jones, B. P. (2009), 'Forest roads facilitate the spread of invasive plants', *Invasive Plant Science and Management* **2**(3), 191–199.

Mott, R., Vionnet, V. & Grünewald, T. (2018), 'The seasonal snow cover dynamics: review on wind-driven coupling processes', *Frontiers in Earth Science* **6**, 197.

Murray, C. & Buttle, J. (2003), 'Impacts of clearcut harvesting on snow accumulation and melt in a northern hardwood forest', *Journal of Hydrology* **271**(1-4), 197–212.

Musselman, K. N., Molotch, N. P., Margulis, S. A., Kirchner, P. B. & Bales, R. C. (2012), 'Influence of canopy structure and direct beam solar irradiance on snowmelt rates in a mixed conifer forest', *Agricultural and Forest Meteorology* **161**, 46–56.

Musselman, K. N., Pomeroy, J. W. & Link, T. E. (2015), 'Variability in shortwave irradiance caused by forest gaps: Measurements, modelling, and implications for snow energetics', *Agricultural and Forest Meteorology* **207**, 69 – 82.

Nakai, Y., Sakamoto, T., Terajima, T., Kitahara, H. & Saito, T. (1994), 'Snow interception by forest canopies: Weighing a conifer tree, meteorological observation and analysis by the penman-monteith formula', **223**, 227–236.

Nathan, R., Katul, G. G., Horn, H. S., Thomas, S. M., Oren, R., Avissar, R., Pacala, S. W. & Levin, S. A. (2002), 'Mechanisms of long-distance dispersal of seeds by wind', *Nature* **418**(6896), 409–413.

Nickling, W. G. (1988), 'The initiation of particle movement by wind', *Sedimentology* **35**(3), 499–511.

Nijssen, B. & Lettenmaier, D. P. (1999), 'A simplified approach for predicting shortwave radiation transfer through boreal forest canopies', *Journal of Geophysical Research: Atmospheres* **104**(D22), 27859–27868.

NK (n.d.), *Kestrel 4000 series Weather & Environmental Meters: Instruction Manual*, Nielsen-Kellerman, Boothwyn, Pennsylvania, U.S.A.
URL: *https://kestrelmeters.com/pages/kestrel-downloads-and-manuals*

Oke, T. R. (1978), *Boundary layer climates*, Routledge.

Paine, R. T., Tegner, M. J. & Johnson, E. A. (1998), 'Compounded perturbations yield ecological surprises', *Ecosystems* **1**(6), 535–545.

Pan, Y., Birdsey, R. A., Fang, J., Houghton, R., Kauppi, P. E., Kurz, W. A., Phillips, O. L., Shvidenko, A., Lewis, S. L., Canadell, J. G. et al. (2011), 'A large and persistent carbon sink in the worlds forests', *Science* **333**(6045), 988–993.

Panferov, O. & Sogachev, A. (2008), 'Influence of gap size on wind damage variables in a forest', *Agricultural and forest meteorology* **148**(11), 1869–1881.

Parajka, J., Haas, P., Kirnbauer, R., Jansa, J. & Blöschl, G. (2012), 'Potential of time-lapse photography of snow for hydrological purposes at the small catchment scale', *Hydrological Processes* **26**(22), 3327–3337.

Pasher, J., Seed, E. & Duffe, J. (2013), 'Development of boreal ecosystem anthropogenic disturbance layers for canada based on 2008 to 2010 landsat imagery', *Canadian Journal of Remote Sensing* **39**(1), 42–58.

Paterson, W. S. B. (1994), *Physics of glaciers*, Butterworth-Heinemann.

Pattison, C. A., Castley, J. G. & Catterall, C. P. (2020), 'Seismic linear clearings alter mammal abundance and community composition in boreal forest landscapes', *Forest Ecology and Management* **462**, 117936.

Pearcy, R. W. (1990), 'Sunflecks and photosynthesis in plant canopies', *Annual review of plant biology* **41**(1), 421–453.

Penczykowski, R. M., Connolly, B. M. & Barton, B. T. (2017), 'Winter is changing: trophic interactions under altered snow regimes', *Food Webs* **13**, 80–91.

Pickell, P. D., Andison, D. W., Coops, N. C., Gergel, S. E. & Marshall, P. L. (2015), 'The spatial patterns of anthropogenic disturbance in the western canadian boreal forest following oil and gas development', *Canadian Journal of Forest Research* **45**(6), 732–743.

Pomeroy, J., Ellis, C., Rowlands, A., Essery, R., Hardy, J., Link, T., Marks, D. & Sicart, J. E. (2008), 'Spatial variability of shortwave irradiance for snowmelt in forests', *Journal of Hydrometeorology* **9**(6), 1482–1490.

Pomeroy, J. & Goodison, B. (1997), *Winter and snow*, McGill-Queen's University Press Montreal, pp. 68–100.

Pomeroy, J. & Granger, R. (1997), 'Sustainability of the western canadian boreal forest under changing hydrological conditions. i. snow accumulation and ablation', *IAHS Publication* **240**, 237–242.

Pomeroy, J. & Gray, D. (1990), 'Saltation of snow', *Water resources research* **26**(7), 1583–1594.

Pomeroy, J. & Gray, D. (1995), 'Snowcover accumulation, relocation and management', *Bulletin of the International Society of Soil Science no* **88**(2).

Pomeroy, J., Gray, D., Hedstrom, N. & Janowicz, J. (2002), 'Prediction of seasonal snow accumulation in cold climate forests', *Hydrological Processes* **16**(18), 3543–3558.

Pomeroy, J., Gray, D. & Landine, P. (1993), 'The prairie blowing snow model: characteristics, validation, operation', *Journal of Hydrology* **144**(1-4), 165–192.

Pomeroy, J., Gray, D., Shook, K., Toth, B., Essery, R., Pietroniro, A. & Hedstrom, N. (1998), 'An evaluation of snow accumulation and ablation processes for land surface modelling', *Hydrological Processes* **12**(15), 2339–2367.

Pomeroy, J. & Li, L. (2000), 'Prairie and arctic areal snow cover mass balance using a blowing snow model', *Journal of Geophysical Research* **105**(D21), 26619–26634.

Pomeroy, J. & Male, D. (1992), 'Steady-state suspension of snow', *Journal of Hydrology* **136**(1-4), 275–301.

Pomeroy, J., Marsh, P. & Gray, D. (1997), 'Application of a distributed blowing snow model to the arctic', *Hydrological processes* **11**(11), 1451–1464.

Pomeroy, J. & Schmidt, R. (1993), The use of fractal geometry in modeling intercepted snow accumulation and sublimation, *in* 'Proceedings of the Eastern Snow Conference', Vol. 50, pp. 1–10.

Pomeroy, J. W. & Dion, K. (1996), 'Winter radiation extinction and reflection in a boreal pine canopy: Measurements and modelling', *Hydrological Processes* **10**(12), 1591–1608.

Pomeroy, J. W., Gray, D. M., Brown, T., Hedstrom, N. R., Quinton, W. L., Granger, R. J. & Carey, S. K. (2007), 'The cold regions hydrological model: a platform for basing process representation and model structure on physical evidence', *Hydrological Processes* **21**(19), 2650–2667.

Pomeroy, J. W., Marks, D., Link, T., Ellis, C., Hardy, J., Rowlands, A. & Granger, R. (2009), 'The impact of coniferous forest temperature on incoming longwave radiation to melting snow', *Hydrological Processes* **23**(17), 2513–2525.

Price, A. & Petzold, D. (1984), 'Surface emissivities in a boreal forest during snowmelt', *Arctic and Alpine Research* **16**(1), 45–51.

Pulliainen, J., Aurela, M., Laurila, T., Aalto, T., Takala, M., Salminen, M., Kulmala, M., Barr, A., Heimann, M., Lindroth, A. et al. (2017), 'Early snowmelt significantly enhances boreal springtime carbon uptake', *Proceedings of the National Academy of Sciences* **114**(42), 11081–11086.

Queck, R., Bernhofer, C., Bienert, A., Eipper, T., Goldberg, V., Harmansa, S., Hildebrand, V., Maas, H.-G., Schlegel, F. & Stiller, J. (2014), 'Turbefa: an interdisciplinary effort to investigate the turbulent flow across a forest clearing', *Meteorol. Z* **23**, 637–659.

Rasmus, S., Lundell, R. & Saarinen, T. (2011), 'Interactions between snow, canopy, and vegetation in a boreal coniferous forest', *Plant Ecology & Diversity* **4**(1), 55–65.

Raupach, M. (1979), 'Anomalies in flux-gradient relationships over forest', *Boundary-Layer Meteorology* **16**(3), 467–486.

Raupach, M., Coppin, P. & Legg, B. (1986), 'Experiments on scalar dispersion within a model plant canopy part i: The turbulence structure', *Boundary-Layer Meteorology* **35**(1), 21–52.

Raupach, M., Finnigan, J. & Brunet, Y. (1996), Coherent eddies and turbulence in vegetation canopies: the mixing-layer analogy, *in* 'Boundary-Layer Meteorology 25th Anniversary Volume, 1970–1995', Springer, pp. 351–382.

Raupach, M., Gillette, D. & Leys, J. (1993), 'The effect of roughness elements on wind erosion threshold', *Journal of Geophysical Research: Atmospheres* **98**(D2), 3023–3029.

Reid, T., Essery, R., Rutter, N. & King, M. (2014), 'Data-driven modelling of shortwave radiation transfer to snow through boreal birch and conifer canopies', *Hydrological processes* **28**(6), 2987–3007.

Reifsnyder, W. E., Furnival, G. & Horowitz, J. (1971), 'Spatial and temporal distribution of solar radiation beneath forest canopies', *Agricultural Meteorology* **9**, 21–37.

Revel, R. D., Dougherty, T. D. & Downing, D. J. (1984), *Forest growth and revegetation along seismic lines*, University of Calgary Press, Calgary, Alberta.

Rodrigo, J. S., Van Beeck, J. & Dezsö-Weidinger, G. (2007), 'Wind tunnel simulation of the wind conditions inside bidimensional forest clear-cuts. application to wind turbine siting', *Journal of wind engineering and industrial aerodynamics* **95**(7), 609–634.

Rominger, J. T. & Nepf, H. M. (2011), 'Flow adjustment and interior flow associated with a rectangular porous obstruction', *Journal of Fluid Mechanics* **680**, 636–659.

Ross, A. N. (2008), 'Large-eddy simulations of flow over forested ridges', *Boundary-Layer Meteorology* **128**(1), 59–76.

Ross, A. N. & Baker, T. P. (2013), 'Flow over partially forested ridges', *Boundary-Layer Meteorology* **146**(3), 375–392.

Ross, A. N. & Harman, I. N. (2015), 'The impact of source distribution on scalar transport over forested hills', *Boundary-Layer Meteorology* **156**(2), 211–230.

Ross, A. N. & Vosper, S. B. (2005), 'Neutral turbulent flow over forested hills', *Quarterly Journal of the Royal Meteorological Society* **131**(609), 1841–1862.

Ruck, B. & Adams, E. (1991), 'Fluid mechanical aspects of the pollutant transport to coniferous trees', *Boundary-Layer Meteorology* **56**(1), 163–195.

Rutter, N., Essery, R., Pomeroy, J., Altimir, N., Andreadis, K., Baker, I., Barr, A., Bartlett, P., Boone, A., Deng, H. et al. (2009), 'Evaluation of forest snow processes models (snowmip2)', *Journal of Geophysical Research: Atmospheres* **114**(D6).

Sanderson, L., McLaughlin, J. & Antunes, P. (2012), 'The last great forest: a review of the status of invasive species in the north american boreal forest', *Forestry* **85**(3), 329–340.

Schelhaas, M.-J., Nabuurs, G.-J. & Schuck, A. (2003), 'Natural disturbances in the european forests in the 19th and 20th centuries', *Global Change Biology* **9**(11), 1620–1633.

Schelker, J., Kuglerová, L., Eklöf, K., Bishop, K. & Laudon, H. (2013), 'Hydrological effects of clear-cutting in a boreal forest–snowpack dynamics, snowmelt and streamflow responses', *Journal of Hydrology* **484**, 105–114.

Schlegel, F., Stiller, J., Bienert, A., Maas, H.-G., Queck, R. & Bernhofer, C. (2012), 'Large-eddy simulation of inhomogeneous canopy flows using high resolution terrestrial laser scanning data', *Boundary-layer meteorology* **142**(2), 223–243.

Schlegel, F., Stiller, J., Bienert, A., Maas, H.-G., Queck, R. & Bernhofer, C. (2015), 'Large-eddy simulation study of the effects on flow of a heterogeneous forest at sub-tree resolution', *Boundary-layer meteorology* **154**(1), 27–56.

Schmidt, R. (1972), 'Sublimation of wind-transported snow–a model', *USDA Forest Service research paper RM-United States, Rocky Mountain Forest and Range Experiment Station* .

Schmidt, R. (1980), 'Threshold wind-speeds and elastic impact in snow transport', *Journal of Glaciology* **26**, 453–467.

Schmidt, R. (1981), 'Estimates of threshold windspeed from particle sizes in blowing snow', *Cold regions science and technology* **4**(3), 187–193.

Schmidt, R. (1986), 'Transport rate of drifting snow and the mean wind speed profile', *Boundary-Layer Meteorology* **34**(3), 213–241.

Schmidt, R. A. (1982*a*), 'Properties of blowing snow', *Reviews of Geophysics* **20**(1), 39–44.

Schmidt, R. A. (1982*b*), 'Vertical profiles of wind speed, snow concentration, and humidity in blowing snow', *Boundary-Layer Meteorology* **23**(2), 223–246.

Schmidt, R. & Gluns, D. R. (1991), 'Snowfall interception on branches of three conifer species', *Canadian Journal of Forest Research* **21**(8), 1262–1269.

Schmidt, R. & Pomeroy, J. (1990), 'Bending of a conifer branch at subfreezing temperatures: implications for snow interception', *Canadian Journal of Forest Research* **20**(8), 1251–1253.

Schmidt, R. & Troendle, C. A. (1992), *Sublimation of intercepted snow as a global source of water vapor*, Colorado State University.

Schwartz, N. B., Uriarte, M., DeFries, R., Bedka, K. M., Fernandes, K., Gutiérrez-Vélez, V. & Pinedo-Vasquez, M. A. (2017), 'Fragmentation increases wind disturbance impacts on forest structure and carbon stocks in a western amazonian landscape', *Ecological Applications* .

Seidl, R., Schelhaas, M.-J., Rammer, W. & Verkerk, P. J. (2014), 'Increasing forest disturbances in europe and their impact on carbon storage', *Nature Climate Change* **4**(9), 806–810.

Seidl, R., Spies, T. A., Peterson, D. L., Stephens, S. L. & Hicke, J. A. (2016), 'Searching for resilience: addressing the impacts of changing disturbance regimes on forest ecosystem services', *Journal of applied ecology* **53**(1), 120–129.

Seyednasrollah, B. & Kumar, M. (2014), 'Net radiation in a snow-covered discontinuous forest gap for a range of gap sizes and topographic configurations', *Journal of Geophysical Research: Atmospheres* **119**(17), 10,323–10,342. 2014JD021809.

Seyednasrollah, B., Kumar, M. & Link, T. E. (2013), 'On the role of vegetation density on net snow cover radiation at the forest floor', *Journal of Geophysical Research: Atmospheres* **118**(15), 8359–8374.

Sicart, J. E., Essery, R. L. H., Pomeroy, J. W., Hardy, J., Link, T. & Marks, D. (2004), 'A sensitivity study of daytime net radiation during snowmelt to forest canopy and atmospheric conditions', *Journal of Hydrometeorology* **5**(5), 774–784.

Sicart, J. E., Pomeroy, J. W., Essery, R. L. H. & Bewley, D. (2006), 'Incoming longwave radiation to melting snow: observations, sensitivity and estimation in northern environments', *Hydrological Processes* **20**(17), 3697–3708.

Slatyer, R. A., Umbers, K. D. & Arnold, P. A. (2021), 'Ecological responses to variation in seasonal snow cover', *Conservation Biology* .

Sommerfeld, R. & LaChapelle, E. (1970), 'The classification of snow metamorphism', *Journal of Glaciology* **9**(55), 3–18.

Sorensen, T., McLoughlin, P. D., Hervieux, D., Dzus, E., Nolan, J., Wynes, B. & Boutin, S. (2008), 'Determining sustainable levels of cumulative effects for boreal caribou', *Journal of Wildlife Management* **72**(4), 900–905.

Stern, E. R., Riva, F. & Nielsen, S. E. (2018), 'Effects of narrow linear disturbances on light and wind patterns in fragmented boreal forests in northeastern alberta', *Forests* **9**(8), 486.

Stewart, B. P., Nelson, T. A., Laberee, K., Nielsen, S. E., Wulder, M. A. & Stenhouse, G. (2013), 'Quantifying grizzly bear selection of natural and anthropogenic edges', *The Journal of Wildlife Management* **77**(5), 957–964.

Storck, P., Lettenmaier, D. P. & Bolton, S. M. (2002), 'Measurement of snow interception and canopy effects on snow accumulation and melt in a mountainous maritime climate, oregon, united states', *Water Resources Research* **38**(11).

Sturm, M., Goldstein, M. A. & Parr, C. (2017), 'Water and life from snow: A trillion dollar science question', *Water Resources Research* **53**(5), 3534–3544.

Sturm, M., Holmgren, J., McFadden, J. P., Liston, G. E., III, F. S. C. & Racine, C. H. (2001), 'Snowshrub interactions in arctic tundra: A hypothesis with climatic implications', *Journal of Climate* **14**(3), 336–344.

Sun, N., Wigmosta, M., Zhou, T., Lundquist, J., Dickerson-Lange, S. & Cristea, N. (2018), 'Evaluating the functionality and streamflow impacts of explicitly modelling forest–snow interactions and canopy gaps in a distributed hydrologic model', *Hydrological processes* **32**(13), 2128–2140.

Sun, R., Krueger, S. K., Jenkins, M. A., Zulauf, M. A. & Charney, J. J. (2009), 'The importance of fire–atmosphere coupling and boundary-layer turbulence to wildfire spread', *International Journal of Wildland Fire* **18**(1), 50–60.

Takeuchi, M. (1980), 'Vertical profile and horizontal increase of drift-snow transport', *Journal of Glaciology* **26**(94), 481–492.

Talbot, J., Plamondon, A., Levesque, D., Aube, D., Prevos, M., Chazalmartin, F. & Gnocchini, M. (2006), 'Relating snow dynamics and balsam fir stand characteristics, montmorency forest, quebec', *Hydrological Processes: An International Journal* **20**(5), 1187–1199.

Thom, D. & Seidl, R. (2016), 'Natural disturbance impacts on ecosystem services and biodiversity in temperate and boreal forests', *Biological Reviews* **91**(3), 760–781.

Tigner, J., Bayne, E. M. & Boutin, S. (2014), 'Black bear use of seismic lines in northern canada', *The Journal of Wildlife Management* **78**(2), 282–292.

Troendle, C. A. & King, R. M. (1985), 'The effect of timber harvest on the fool creek watershed, 30 years later', *Water Resources Research* **21**(12), 1915–1922.

Trujillo, E., Molotch, N. P., Goulden, M. L., Kelly, A. E. & Bales, R. C. (2012), 'Elevation-dependent influence of snow accumulation on forest greening', *Nature Geoscience* **5**(10), 705.

Turner, M. G. (2010), 'Disturbance and landscape dynamics in a changing world', *Ecology* **91**(10), 2833–2849.

Valentini, R., Matteucci, G., Dolman, A., Schulze, E.-D., Rebmann, C., Moors, E., Granier, A., Gross, P., Jensen, N., Pilegaard, K. et al. (2000), 'Respiration as the main determinant of carbon balance in european forests', *Nature* **404**(6780), 861–865.

Van Rensen, C. K., Nielsen, S. E., White, B., Vinge, T. & Lieffers, V. J. (2015), 'Natural regeneration of forest vegetation on legacy seismic lines in boreal habitats in alberta's oil sands region', *Biological Conservation* **184**, 127–135.

Varhola, A., Coops, N. C., Alila, Y. & Weiler, M. (2013), 'Exploration of remotely sensed forest structure and ultrasonic range sensor metrics to improve empirical snow models', *Hydrological processes* **28**(15), 4433–4448.

Varhola, A., Coops, N. C., Weiler, M. & Moore, R. D. (2010), 'Forest canopy effects on snow accumulation and ablation: An integrative review of empirical results', *Journal of Hydrology* **392**(3), 219–233.

Wang, Z., Zeng, X. & Decker, M. (2010), 'Improving snow processes in the noah land model', *Journal of Geophysical Research: Atmospheres* **115**(D20). D20108.

Warren, S. G. (1982), 'Optical properties of snow', *Reviews of Geophysics* **20**(1), 67–89.

Watson, J. E., Evans, T., Venter, O., Williams, B., Tulloch, A., Stewart, C., Thompson, I., Ray, J. C., Murray, K., Salazar, A. et al. (2018), 'The exceptional value of intact forest ecosystems', *Nature ecology & evolution* **2**(4), 599–610.

Webster, C., Mazzotti, G., Essery, R. & Jonas, T. (2020), 'Enhancing airborne lidar data for improved forest structure representation in shortwave transmission models', *Remote Sensing of Environment* **249**, 112017.

Webster, C., Rutter, N. & Jonas, T. (2017), 'Improving representation of canopy temperatures for modeling subcanopy incoming longwave radiation to the snow surface', *Journal of Geophysical Research: Atmospheres* **122**(17), 9154–9172.

Webster, C., Rutter, N., Zahner, F. & Jonas, T. (2016), 'Modeling subcanopy incoming longwave radiation to seasonal snow using air and tree trunk temperatures', *Journal of Geophysical Research: Atmospheres* **121**(3), 1220–1235. 2015JD024099.

Weiss, A. & Allen Jr, L. (1976), 'Air-flow patterns in vineyard rows', *Agricultural Meteorology* **16**(3), 329–342.

Wells, J. V., Dawson, N., Culver, N., Reid, F. A. & Morgan Siegers, S. (2020), 'The state of conservation in north america's boreal forest: issues and opportunities', *Frontiers in Forests and Global Change* **3**, 90.

Whittington, J., Hebblewhite, M., DeCesare, N. J., Neufeld, L., Bradley, M., Wilmshurst, J. & Musiani, M. (2011), 'Caribou encounters with wolves increase near roads and trails: a time-to-event approach', *Journal of Applied Ecology* **48**(6), 1535–1542.

Williams, M. W. & Melack, J. M. (1991), 'Solute chemistry of snowmelt and runoff in an alpine basin, sierra nevada', *Water Resources Research* **27**(7), 1575–1588.

Williams, T. J., Quinton, W. L. & Baltzer, J. L. (2013), 'Linear disturbances on discontinuous permafrost: implications for thaw-induced changes to land cover and drainage patterns', *Environmental Research Letters* **8**(2), 025006.

Wilm, H. G. & Dunford, E. (1948), 'Effect of timber cutting on water available for stream flow from a lodgepole pine forest', *Methods* **1**, 2.

Winkler, R. & Moore, R. (2006), 'Variability in snow accumulation patterns within forest stands on the interior plateau of british columbia, canada', *Hydrological processes* **20**(17), 3683–3695.

Wipf, S., Stoeckli, V. & Bebi, P. (2009), 'Winter climate change in alpine tundra: plant responses to changes in snow depth and snowmelt timing', *Climatic change* **94**(1-2), 105–121.

Wood, N. (1995), 'The onset of separation in neutral, turbulent flow over hills', *Boundary-Layer Meteorology* **76**(1), 137–164.

Wood, N. & Mason, P. (1993), 'The pressure force induced by neutral, turbulent flow over hills', *Quarterly Journal of the Royal Meteorological Society* **119**(514), 1233–1267.

Yang, B., Raupach, M. R., Shaw, R. H., Morse, A. P. et al. (2006), 'Large-eddy simulation of turbulent flow across a forest edge. part i: flow statistics', *Boundary-layer meteorology* **120**(3), 377–412.

Zeng, H., Peltola, H., Väisänen, H. & Kellomäki, S. (2009), 'The effects of fragmentation on the susceptibility of a boreal forest ecosystem to wind damage', *Forest Ecology and Management* **257**(3), 1165–1173.

Zhang, T. (2005), 'Influence of the seasonal snow cover on the ground thermal regime: An overview', *Reviews of Geophysics* **43**(4).